Discovering Protein-Glycolipid Interactions Using Electrospray Ionization Mass Spectrometry

by

Jianing Li

A thesis submitted in partial fulfillment of the requirements for the degree of

Master of Science

Department of Chemistry
University of Alberta

Abstract

This thesis focuses on the development and application of electrospray ionization mass spectrometry (ESI-MS) based techniques to detect and quantify proteins interactions with carbohydrates or glycolipids in model membranes.

In Chapter 2, the native ESI-MS based direct/competitive binding assay and catch-and-release electrospray ionization mass spectrometry (CaR-ESI-MS) assay were employed to investigate the ganglioside specificities of a series of anti-GD2 monoclonal antibodies (mAbs) and their antigen binding fragments (Fabs). First, the affinities of anti-GD2 antibodies including hu3F8 and its double mutant E1K/D32H Fabs and 14G2a mAb to a library of fourteen ganglioside oligosaccharides were quantified using the direct ESI-MS assay. The binding data revealed that the anti-GD2 antibodies were ranked in order of affinity: hu3F8 E1K/D32H Fab ($K_{a,GD2os}$ = (22 ± 1.5) x 10^5 M^{-1}) > hu3F8 Fab ($K_{a,GD2os}$ = (4.3 ± 0.1) x 10^5 M^{-1}) > 14G2a mAb ($K_{a1,app}$ = (1.2 ± 0.9) x 10^5 M^{-1}, $K_{a2,app}$ = (4.1 ± 0.4) x 10^4 M^{-1} and $K_{a,int,GD2os}$ = (7.0 ± 0.2) x 10^4 M^{-1} (per binding site). Measurements performed on other ganglioside oligosaccharides indicated that all of the ganglioside oligosaccharides tested were recognized by these antibodies, although with lower affinities, in the 2.0 x 10^2 M^{-1} - 5.8 x 10^3 M^{-1} range. In addition, the hu3F8 Fab exhibits better specificity to $GD2_{os}$ than the hu3F8 E1K/D32H Fab and 14G2a mAb. The CaR-ESI-MS assay implemented with model membrane nanodiscs (NDs) to solubilize gangliosides, was then used to screen mixtures of gangliosides against different types of anti-GD2 antibodies including hu3F8 and its double mutant E1K/D32H and 14G2a mAbs. As expected, GD2 was found to be the dominant ligand of these anti-GD2 antibodies. However, CaR-ESI-MS also revealed 14G2a mAb has measurable binding to GM3 and GM4. Finally, the competitive binding ESI-MS assays were applied to quantify affinities of the hu3F8 and its double mutant E1K/D32H Fabs and 14G2a mAb

for GD2 incorporated into NDs. The binding data revealed the extent of GD2 binding to these antibodies was found to be sensitive to ganglioside content of the NDs.

In Chapter 3, the membrane anchor-assisted electrospray ionization mass spectrometry approach was introduced for detecting low affinity interactions between glycan binding proteins (GBPs) and glycospingolipids (GSLs) presented in model membranes. The method involves covalent cross-linking the GBP to the model membrane through a modified lipid. The resulting membrane anchor serves to enhance the local concentration of GBP on the surface of the membrane and enhance binding to GSL ligands. The implementation and reliability of this new approach was demonstrated using three human galectins, C-terminal fragment of human galectin-3, recombinant human galectin-1 and recombinant human galectin-7, and their interactions with gangliosides presented in nanodiscs. The results of this study were validated using binding data measured for the corresponding ganglioside oligosaccharides.

Preface

Chapter 2 is under preparation as manuscript. I was responsible for all the experiments, data analysis, as well as writing of the manuscript. Modified $GM2_{os}$-CUPRA, $GM3_{os}$-CUPRA, $GD2_{os}$-CUPRA and $GD3_{os}$-CUPRA compounds were synthesized by Pavel I. Kitov. In addition, I and Pavel I. Kitov together produced modified $GM4_{os}$-CUPRA ligand.

Chapter 3 is under preparation as manuscript. I was responsible for performing all the ESI-MS experiments, processing experimental data and writing. I and Elena N. Kitova together performed experiments for detection of hGal-7 interactions with GM3 ganglioside ligand presented in azide-PE POPC ND using membrane anchor-assisted CaR-ESI-MS assay.

The supervisory author, Prof. John S. Klassen, was involved throughout all the projects in concept formation and manuscript composition.

Acknowledgement

I would like to express my sincere gratitude to my supervisor, Professor John S. Klassen, for the continuous support of my graduate study and research, for his patience, enthusiasm and inspiration. His friendly guidance and expert suggestion have been invaluable throughout all stages of the work. Besides my supervisor, I would also like to thank other members of my supervisory and defense committee, Prof. Liang Li, Prof. Robert Campbell and Prof. Matthew Macauley, for their insightful comments and valuable suggestions which have contributed greatly to the improvement of my research and the thesis.

I would also wish to express my gratitude to my collaborators, Prof. Kenneth Ng and research assistant Julia Savtchouk from University of Calgary for generously providing us hu3F8 and hu3F8 E1K/D32H Fabs for anti-GD2 antibodies related projects and helpful suggestions. I would like to thank Prof. Nai-Kong Cheung and Dr. Brian Santich at Memorial Sloan Kettering Cancer Center who provided hu3F8 and hu3F8 E1K/D32H mAbs. I am thankful to Prof. Christopher Cairo for providing us with the human galectin-3, Prof. Todd L. Lowary for providing $GM4_{os}$, Prof. S. Sato from Université Laval for providing human galectin-1, Prof. Yves St-Pierre from INRS-Institut Armand-Frappier for providing human galectin-7 and Prof. Matthew Macauley for providing a fragment of human Siglec-1. I also thank Blake Zheng for his assistance in biological analysis.

It is my pleasure to have worked with previous and present excellent colleagues in the Klassen group. I would like to thank Dr. Elena N. Kitova, Dr. Pavel I. Kitov, Dr. Lin Han and Dr. Jun Li for their technical supports, expert guidance and productive suggestions during my research. Moreover, I also wish to acknowledge the support, encouragement and friendship from other colleagues (previous and present) in Klassen group: Dr. Heajin Park, Dr. Mickey Richards, Dr.

Amr El-hawiet, Yajie Chen, Hong Lin, Yilin Wang, Zhixiong Li, Erick Baez Bolivar, Linh Nguyen, Md Reazul Islam, Anantha Ealeswarapu and Km Shams-Ud-Doha.

I would like to thank the financial support provided by the Department of Chemistry, University of Alberta.

Finally, I am deeply thankful to my parents and my boyfriend, Yingnan Zhang, for their continuous encouragement and spiritual support.

Table of Contents

Chapter 1 Discovering Protein-Glycolipid Interactions Using Electrospray Ionization Mass Spectrometry 1

1.1 Introduction 1

1.1.1 Composition of membranes 1

1.1.2 Protein-glycolipid interactions 3

1.2 Electrospray Ionization (ESI)/Matrix Assisted Laser Desorption Ionization (MALDI) Mass Spectrometry 7

1.2.1 ESI mechanisms 7

1.2.2 Nanoflow ESI-MS 11

1.2.3 MALDI mechanism 11

1.2.4 MS instrumentation 13

1.2.4.1 Hybrid quadrupole-ion mobility separation-time of flight mass spectrometer 13

1.2.4.1.1 Quadrupole 14

1.2.4.1.2 Travelling wave 17

1.2.4.1.3 TOF mass analyzer 19

1.2.4.2 Orbitrap mass spectrometer 20

1.2.4.2.1 Orbitrap mass analyzer 22

1.2.4.3 Fourier transform ion cyclotron resonance (FT-ICR) mass spectrometer 24

1.2.4.3.1 FT-ICR mass analyzer 25

1.3 ESI-MS Based Methods 27

1.3.1 Direct ESI-MS assay 27

1.3.2 *Proxy Ligand* ESI-MS assay 30

1.3.3 Catch and Release (CaR)-ESI-MS assay 32

1.4 The Present Work 33

1.5 References 35

Chapter 2 Glycan Binding Properties of Anti-GD2 Antibodies Studied by Electrospray Ionization Mass Spectrometry 49

2.1 Introduction 49

2.2 Experimental Section 51

2.2.1 Proteins 51

2.2.2 Lipids and Glycolipids 52

2.2.3 Oligosaccharides 56

2.2.4 Preparation of nanodiscs 59

2.2.5 Nanodisc concentration determination 60

2.2.6 Mass spectrometry 60

2.2.6.1 Direct ESI-MS assay 61

2.2.6.2 *Proxy Ligand* ESI-MS assay 63

2.2.6.3 Competitive universal proxy receptor assay (CUPRA)-*Proxy Ligand* ESI-MS method 64

2.2.6.4 Catch and Release (CaR)-ESI-MS assay 66

2.2.6.5 Quantifying ganglioside content of nanodiscs using MALDI-MS 66

2.3 Results and Discussion 67

2.3.1 Affinities of ganglioside oligosaccharides for anti-GD2 antibodies 67

2.3.2 Screening ganglioside-containing NDs against anti-GD2 antibodies 77

2.3.3 Investigating binding properties of GD2-containing nanodiscs for anti-GD2 antibodies 84

2.3.3.1 Quantifying GD2 incorporation efficiency in NDs 84

2.3.3.2 Affinities of GD2-containing nanodiscs for hu3F8 and hu3F8 E1K/D32H Fabs 87

2.3.3.3 Affinities of GD2-containing nanodiscs for 14G2a mAb 91

2.4 Conclusions 93

2.5 References 95

Chapter 3 Elusive Protein-Glycosphingolipid Interactions Revealed by Membrane Anchor-Assisted Catch-and-Release Electrospray Ionization Mass Spectrometry 99

3.1 Introduction 99

3.2 Experimental Section 102

3.2.1 Proteins 102

3.2.2 Lipids and Glycospingolipids 103

3.2.3 Oligosaccharides 106

3.2.4 Preparation of nanodiscs 108

3.2.5 Protein labeling (NHS ester reaction chemistry) and copper-free click chemistry reaction 109

3.2.6 Mass spectrometry 111

3.2.6.1 Direct ESI-MS assay 112

3.2.6.2 GSL binding measurements 113

3.3 Results and Discussion 113

3.3.1 Affinities of ganglioside oligosaccharides of hGal-3C 114

3.3.2 hGal-3C binding to POPC NDs containing a single ganglioside 118

3.3.3 Detecting hGal-3C interactions with low affinity GSL ligands by membrane anchor-assisted CaR-ESI-MS assay 120

3.3.4 Detecting hGal-1 and hGal-7 interactions with low affinity GM3 ligand by membrane anchor-assisted CaR-ESI-MS assay 131

3.4 Conclusions 137

3.5 References 138

Chapter 4 Conclusions and Future Work 142

4.1 Conclusions 142

4.2 Future work 144

4.3 References 150

List of References 152

List of Tables

Table 2.1. Association constants K_a (M^{-1}) for anti-GD2 antibodies binding to ganglioside oligosaccharides measured by ESI-MS in 200 mM aqueous ammonium acetate solutions (pH 6.8, 25 °C)……...76

Table 2.2. Composition of lipids including phospholipid and glycolipid in *Library 1-10*……..77

Table 3.1. Association constants (K_a, units 10^3 M^{-1}) for hGal-3C binding to the oligosaccharides of eight gangliosides measured in an aqueous ammonium acetate solution (200 mM, pH 6.8 and 25 ºC) using the direct ESI-MS assay……117

List of Figures

Figure 1.1. Schematic illustration of the ESI process performed in positive ion mode, adapted from reference 51……...…….....8

Figure 1.2. Different ESI models proposed for gas-phase ion generation. (a) IEM, (b) CRM and (c) CEM. Figure 1.2 is adapted from reference 63…….10

Figure 1.3. Schematic illustration of the process of MALDI in positive ion mode, adapted from reference 87……..12

Figure 1.4. A schematic diagram of the Waters Synapt G2-S Q-IMS-TOF mass spectrometer, adapted from Waters user's manual……...14

Figure 1.5. (a) Stability diagram of a quadrupole analyzer for ions with different mass (m) values ($m_1 < m_2 < m_3$), adapted from reference 95. (b) Schematic representation of the quadrupole used in Waters Synapt mass spectrometer……..16

Figure 1.6. Illustration of the operation of a Triwave SRIG, adapted from reference 97……18

Figure 1.7. Schematic diagram of the Thermo Fisher Q Exactive ultra high mass range (UHMR) Orbitrap mass spectrometer, adapted from Thermo Fisher user's manual…….22

Figure 1.8. A cut-away model of the Orbitrap mass analyzer. (a) a central electrode; (b) an outer electrode, split in half by an insulating ceramic ring; (c) complex orbital path of an ion. Figure 1.8 is adapted from reference 112…….....23

Figure 1.9. Schematic diagram of the Bruker 15 Tesla SolariX-XR FT-ICR Mass spectrometer, adapted from the Bruker user's manual.……25

Figure 1.10. Principles of FTICR-MS illustrated in ion excitation, image current detection and generation of mass spectrum, adapted from reference 117.……...27

Figure 2.1. Structures of the gangliosides Fucosyl GM1, GM1, GM2, GM3, GM4, GD1a, GD1b,

GD2, GD3, GT1a, GT1b and POPC…….56

Figure 2.2. Structures of the gangliosides oligosaccharides $GM1a_{os}$, $GM1b_{os}$, $GM2_{os}$, $GM3_{os}$, $GM4_{os}$, $GD2_{os}$, $GD1a_{os}$, $GD1b_{os}$, $GD3_{os}$, $GT1b_{os}$, $GT1a_{os}$, $GT1c_{os}$, $GT2_{os}$ and $GT3_{os}$...59

Figure 2.3. Schematic for competitive CUPRA-*proxy ligand* ESI-MS assay……..64

Figure 2.4. ESI mass spectra in positive ion mode for a 200 mM aqueous ammonium acetate solution (pH 6.8, 25 °C) of (a) hu3F8 Fab (4 μM) and with (b) $GD2_{os}$ (8 μM), (c) $GD3_{os}$ (50 μM) and (d) $GT3_{os}$ (70 μM) using scFv as P_{ref}.……69

Figure 2.5. ESI mass spectra in positive ion mode for a 200 mM aqueous ammonium acetate solution (pH 6.8, 25 °C) of (a) hu3F8 E1K/D32H Fab (3.5 μM) and with (b) $GD2_{os}$ (3 μM), (c) $GD3_{os}$ (50 μM) and (d) $GT3_{os}$ (50 μM) using scFv as P_{ref}.……70

Figure 2.6. ESI mass spectra in positive ion mode for a 200 mM aqueous ammonium acetate solution (pH 6.8, 25 °C) of (a) 14G2a mAb (1.5 μM) and with (b) $GD2_{os}$ (15 μM), (c) $GM1a_{os}$ (35 μM) and (d) $GT2_{os}$ (25 μM) using huNoV Saga P dimer as P_{ref}.……..71

Figure 2.7. Plots of fraction of ligand-bound hu3F8 Fab versus ligand concentration measured for (a) $GM1a_{os}$, (b) $GM1b_{os}$, (c) $GM2_{os}$, (d) $GM3_{os}$, (e) $GM4_{os}$, (f) $GD1a_{os}$, (g) $GD1b_{os}$, (h) $GD2_{os}$, (i) $GD3_{os}$, (j) $GT1a_{os}$, (k) $GT1b_{os}$, (l) $GT1c_{os}$, (m) $GT2_{os}$ and (n) $GT3_{os}$. Plot of fraction of ligand-bound hu3F8 E1K/D32H Fab versus ligand concentration measured for (o) $GD2_{os}$. The solid curves correspond to the best fit of eq1.12 to the experimental data and the error bars correspond to one standard derivation……...74

Figure 2.8. (a) ESI mass spectrum acquired in negative ion mode for an aqueous ammonium acetate solution (200 mM, pH 6.8) of *Library 1* (8 μM, 1% of each ganglioside). (b) - (f) CID mass spectra of ions with m/z > 6400, produced by ESI in negative ion mode for aqueous ammonium acetate solutions (200 mM, pH 6.8) of *Library 1* to *Library 5*,

respectively, using a collision energy (in Trap) of 150 V……...79

Figure 2.9. ESI mass spectra acquired in negative ion mode for a 200 mM aqueous ammonium acetate solution (pH 6.8) containing 14G2a mAb (2.5 μM) and (a) *Library 1* (1.5 μM of each ganglioside) and (b) *Library 2* (1.5 μM of each ganglioside). (c) and (d) CID mass spectra acquired in the Trap region for the $(P + L)^{22-}$ ions using a collision energy of 100 V……80

Figure 2.10. ESI mass spectra acquired in negative ion mode for a 200 mM aqueous ammonium acetate solution (pH 6.8) containing 14G2a mAb (2.5 μM) and (a) *Library 6* (1.5 μM of each ganglioside) and (b) *Library 7* (1.5 μM of each ganglioside). (c) and (d) CID mass spectra acquired in the Trap region for the $(P + L)^{22-}$ ions using a collision energy of 100 V……81

Figure 2.11. ESI mass spectra acquired in negative ion mode for a 200 mM aqueous ammonium acetate solution (pH 6.8) containing 14G2a mAb (2.5 μM) and (a) *Library 1* (4 μM of each ganglioside) and (b) *Library 2* (4 μM of each ganglioside). (c) and (d) CID mass spectra acquired in the Trap region for the $(P + L)^{22-}$ ions using a collision energy of 100 V…….....82

Figure 2.12. ESI mass spectra acquired in negative ion mode for a 200 mM aqueous ammonium acetate solution (pH 6.8) containing 14G2a mAb (2.5 μM) and (a) *Library 6* (4 μM of each ganglioside) or (b) *Library 7* (4 μM of each ganglioside). (c) and (d) CID mass spectra acquired in the Trap region for the $(P + L)^{22-}$ ions using a collision energy of 100 V……....83

Figure 2.13. (a) Representative MALDI mass spectrum acquired in negative ion mode for mixture of ganglioside GD2 (5 μM), empty ND (1.7 μM) with GD1b (3.33 μM) after

preparation with matrix. (b) Plot of the total abundance (*Ab*) ratio of GD2-to-GD1b ions versus the corresponding concentration ratio in solution; the concentration of ganglioside GD2 was 5 μM in all cases. The error bars corresponding to one standard deviation and the solid line corresponds to linear fit to the experimental data; also shown was slope and R^2 value from the linear fitting……...84

Figure 2.14. Representative MALDI mass spectra acquired in negative ion mode for (a) mixture of 3.3 μM of 5% GD2 ND with 5.5 μM GD1b, (b) mixture of 3.6 μM of 5% GD2 ND with 5 μM GD1b, (c) mixture of 4 μM of 5% GD2 ND with 4.4 μM GD1b after preparation with matrix. (d) Plot of the total abundance (*Ab*) ratio of GD2-to-GD1b ions versus the ratio of $[GD2]_{norminal}$-to-[GD1b]. The error bars corresponding to one standard deviation and the solid line corresponds to linear fit to the experimental data; also shown is slope and R^2 value from the linear fitting……86

Figure 2.15. ESI mass spectra acquired in positive ion mode for hu3F8 Fab (4 μM), $GD2_{os}$ (L_{proxy}, 8 μM) without (a) and with (b) 5% GD2 POPC ND (3 μM)……..89

Figure 2.16. Plots of R_{proxy} (≡ *Ab*(hu3F8 Fab + $GD2_{os}$)/*Ab*(hu3F8 Fab)) versus (a) 1% GD2 POPC ND concentration, (b) 5% GD2 POPC ND concentration, (c) 10% GD2 POPC ND concentration measured by ESI-MS. (d) Bar graph of $K_{a,GD2}$ values measured for hu3F8 Fab binding to different percentages (1%, 5% and 10%) of GD2 in NDs……..89

Figure 2.17. ESI mass spectra acquired in positive ion mode for hu3F8 E1K/D32H Fab (3.5 μM), GD2os (L_{proxy}, 3 μM) without (a) and with (b) 5% GD2 POPC ND (2 μM)……...90

Figure 2.18. Plots of R_{proxy} (≡ *Ab*(hu3F8 E1K/D32H Fab + GD2os)/*Ab*(hu3F8 Fab)) versus (a) 1% GD2 POPC ND concentration, (b) 5% GD2 POPC ND concentration, (c) 10% GD2 POPC ND concentration measured by ESI-MS. (d) Bar graph of K_a values measured

for hu3F8 E1K/D32H Fab binding to different percentages (1%, 5% and 10%) of GD2 in NDs……...90

Figure 2.19. ESI mass spectra in positive ion mode of (a) hCA (5 μM) and with (b) $GD2_{os}$-CL (8 μM)……...92

Figure 2.20. Plots of R_{proxy} (≡ *Ab*(hCA + $GD2_{os}$-CL)/*Ab*(hCA)) versus 14G2a mAb concentration measured for (a) 1% GD2 POPC ND, (b) 5% GD2 POPC ND, (c) 10% GD2 POPC ND. (d) Bar graph of $K_{a,GD2}$ values measured for 14G2a mAb binding to different percentages (1%, 5% and 10%) of GD2 in NDs……93

Figure 3.1. Structures of the gangliosides GM1, GM2, GM3, GD1a, GD1b, GD2, GT1a, GT1b, POPC and azidocaproyl PE…….106

Figure 3.2. Structures of the gangliosides oligosaccharides $GM1_{os}$, $GM2_{os}$, $GM3_{os}$, $GD2_{os}$, $GD1a_{os}$, $GD1b_{os}$, $GT1a_{os}$, $GT1b_{os}$…….108

Figure 3.3. Schematic representation of the membrane anchor-assisted CaR-ESI-MS assay applied for detecting weak GBP-GSL interactions. The labeled GBP (light blue) and model membrane [e.g., nanodisc (ND) with surrounding membrane scaffold protein (purple)] containing GSL (yellow), azide-PE (dark bule/dark green) and POPC phospholipid (orange) are incubated for a certain time. Conformationally strained alkyne conjugated with receptor GBP first reacts with azide-terminated phospholipid incorporated in MM via a "click chemistry" reaction, thus, anchoring the GBP to the membrane surface. Then, non-covalent interactions between GBP and GSL becomes intramolecular and more entropically favorable. Finally, the labeled GBP-azide-PE-GSL-MM whole complexes are transferred into gas phase by ESI and the labeled GBP-azide-PE-GSL complexes are released in source for MS detection…..……110

Figure 3.4. (a) Protein labeling NHS ester reaction chemistry and (b) Copper free click chemistry……111

Figure 3.5. ESI mass spectra acquired in positive ion mode for aqueous ammonium acetate solutions (200 mM, pH 6.8) of hGal-3C (4 μM), BCA (P_{ref}, 4 μM), and the ganglioside oligosaccharide (a) $GM1_{os}$ (70 μM), (b) $GM2_{os}$ (70 μM), (c) $GM3_{os}$ (30 μM), (d) $GD1a_{os}$ (50 μM), (e) $GD1b_{os}$ (30 μM), (f) $GD2_{os}$ (50 μM), (g) $GT1a_{os}$ (40 μM) and (h) $GT1b_{os}$ (30 μM)……..115

Figure 3.6. Plots of the fraction of ligand-bound hGal-3C (i.e., R/(R+1)) versus ligand concentration measured for the ganglioside oligosaccharides (a) $GM1_{os}$, (b) $GM3_{os}$, (c) $GD1a_{os}$, (d) $GD1b_{os}$, (e) $GT1a_{os}$ and (f) $GT1b_{os}$. The direct ESI-MS binding measurements were carried out on 200 mM aqueous ammonium acetate solutions containing hGal-3C (4 μM), BCA (P_{ref}, 4 μM and each ganglioside oligosaccharide at three different concentrations ranging from 30 to 70 μM. The error bars correspond to one standard derivation and the solid curves corresponding to the best fit of eq3.3 to the experimental data……116

Figure 3.7. ESI mass spectra acquired in positive ion mode for aqueous ammonium acetate solutions (200 mM, pH 6.8) of hGal-3C (4 μM) with (a) 8 μM 10% GM1 POPC ND, (b) 8 μM 5% GM2 POPC ND, (c) 8 μM 5% GM3 POPC ND (d) 10 μM 1% GD1a POPC ND, (e) 10 μM 1% GD1b POPC ND, (f) 8 μM 10% GD2 POPC ND, (g) 10 μM 1% GT1a POPC ND and (h) 10 μM 1% GT1b POPC ND……...119

Figure 3.8. ESI mass spectra acquired in positive ion mode for aqueous ammonium acetate solutions (200 mM, 25 °C, and pH 6.8) containing (a) hGal-3C labeled with DBCO-PEG_4 (2.8 μM) and (b) hGal-3C labeled with DBCO-PEG_4 (2.8 μM) with 20% PE

POPC ND (10 μM) incubated for 17 h at 4 °C. Inset show the normalized distribution of (hGal-3C + qDBCO-PEG$_4$) measured for solutions described in (a), where q = 0-6……..121

Figure 3.9. ESI mass spectra acquired in positive ion mode for aqueous ammonium acetate solutions (200 mM, 25 °C, and pH 6.8) containing labeled hGal-3C (2.8 μM) with (a) 10% GM3 20% PE POPC ND (10 μM), (b) 10% GM1 20% PE POPC ND (10 μM) (c) 10% GD1a 20% PE POPC ND (10 μM), (d) 10% GD1b 20% PE POPC ND (10 μM), (e) 10% GT1a 20% PE POPC ND (10 μM), (f) 10% GT1b 20% PE POPC ND (10 μM) and (g) 10% GM2 20% PE POPC ND (10 μM) and (h) 10% GD2 20% PE POPC ND (10 μM) incubated for 17 h at 4 °C. Insets show the corresponding fractions of (hGal-3C + qDBCO-PEG$_4$ + qPE) and (hGal-3C + qDBCO-PEG$_4$ + qPE + GSL) measured for solutions described in (a) to (h), where q = 0-5……..127

Figure 3.10. Plots of fraction of GSL complexes versus incubation time (7 h, 17 h and 40 h) measured by ESI-MS for solutions of labeled hGal-3C (2.8 μM) and NDs produced from: 10% GM1 20% PE POPC ND (10 μM); 10% GM2 20% PE POPC ND (10 μM); 10% GM3 20% PE POPC ND (10 μM); 10% GD1a 20% PE POPC ND (10 μM); 10% GD1b 20% PE POPC ND (10 μM); 10% GD2 20% PE POPC ND (10 μM); 10% GT1a 20% PE POPC ND (10 μM) and 10% GT1b 20% PE POPC ND (10 μM). The error bars correspond to one standard deviation……129

Figure 3.11. Plots of fraction of GSL complexes versus GSL PE POPC ND concentrations (3 μM, 6 μM and 10 μM) measured by ESI-MS for solutions of labeled hGal-3C (2.8 μM) and NDs produced from: 10% GM1 20% PE POPC ND; 10% GM2 20% PE POPC ND; 10% GM3 20% PE POPC ND; 10% GD1a 20% PE POPC ND; 10% GD1b 20% PE

POPC ND; 10% GD2 20% PE POPC ND; 10% GT1a 20% PE POPC ND and 10% GT1b 20% PE POPC ND incubated for 17 h. The error bars correspond to one standard deviation…….130

Figure 3.12. ESI mass spectra acquired in positive ion mode for aqueous ammonium acetate solutions (200 mM, 25 °C, and pH 6.8) containing (a) hGal-1 labeled with DBCO-PEG_4 (3 μM) and (b) hGal-7 labeled with DBCO-PEG_4 (8 μM). Insets show the normalized distributions of (P_2 + qDBCO-PEG_4) measured for solutions described in (a) and (b), where q = 0-4……..133

Figure 3.13. ESI mass spectrum acquired in positive ion mode for aqueous ammonium acetate solutions (200 mM, 25 °C, and pH 6.8) containing (a) hGal-1 labeled with DBCO-PEG_4 (3 μM) with 20% PE POPC ND (12 μM) and (b) hGal-7 labeled with DBCO-PEG_4 (8 μM) with 20% PE POPC ND (5 μM) incubated for 15 h at 4 °C……..134

Figure 3.14. ESI mass spectra acquired in positive ion mode for aqueous ammonium acetate solutions (200 mM, 25 °C, and pH 6.8) containing (a) labeled hGal-1 (3 μM) with 10% GM3 20% PE POPC ND (13 μM) incubated for 15 h and (b) labeled hGal-7 (3.5 μM) with 10% GM3 20% PE POPC ND (3 μM) incubated for 3.5 h. Insets show the corresponding fractions of (P_2 + 1DBCO-PEG_4 + 1PE) and (P_2 + 1DBCO-PEG_4 + 1PE + GM3) measured for solutions described in (a) and (b)…….135

Figure 3.15. Plots of fraction of GM3 complexes versus GM3 PE POPC ND concentration measured by ESI-MS for solutions of (a) labeled hGal-1 (3 μM) and 10% GM3 20% PE POPC ND (10 μM, 13 μM and 15 μM) incubated for 15h; (b) labeled hGal-7 (3.5 μM) and 10% GM3 20% PE POPC ND (2 μM, 3 μM, 4 μM and 7 μM). The error bars correspond to one standard deviation……..136

Figure 4.1. ESI mass spectra acquired in positive ion mode for aqueous ammonium acetate solutions (200 mM, pH 6.8) of (a) fragment of human siglec-1 (3 μM) and with (b) 8 μM 10% GM1 POPC ND, (c) 8 μM 5% GM2 POPC ND, (d) 8 μM 5% GM3 POPC ND……..146

Figure 4.2. ESI mass spectra acquired in positive ion mode for aqueous ammonium acetate solutions (200 mM, 25 °C, and pH 6.8) containing fragment of human Siglec-1 labeled with DBCO-PEG_4 (0.5 μM). Inset show the normalized distribution of (Siglec-1 + qDBCO-PEG_4) measured from the mass spectrum, where q = 0-4……..147

Figure 4.3. ESI mass spectra acquired in positive ion mode for aqueous ammonium acetate solutions (200 mM, 25 °C, and pH 6.8) containing labeled fragment of human Siglec-1 (0.5 μM) with (a) 10% GM1 20% PE POPC ND (3 μM), (b) 10% GM2 20% PE POPC ND (2 μM) (c) 10% GM3 20% PE POPC ND (2.5 μM) incubated for 2 h…...……149

Figure 4.4. Structures of the modified lipids azidoethyl PC and azidoethyl SM……..149

List of Abbreviations

Ab	Abundance of gas-phase ions
AGC	Automatic gain control
azide-PE	16:0 azidocaproyl PE
BCA	Bovine carbonic anhydrase
CaR	Catch-and-release
CEM	Chain injection model
ch3F8	Chimeric 3F8
ch14.18	Chimeric14.18
CHCA	α-cyano-4-hydroxycinnamic acid
CID	Collision-induced dissociation
CRM	Charged residue model
CTB_5	Cholera toxin B subunit homopentamer
CUPRA	Competitive universal proxy receptor assay
cytoc	Cytochrome c
Da	Dalton
DBCO-PEG_4-NHS ester	Dibenzocyclooctyne-PEG_4-*N*-hydroxysuccinimidyl ester
DC	Direct current
DMSO	Dimethyl sulfoxide
EDTA	Ethylenediaminetetraacetic acid
ELISA	Enzyme-linked immunosorbent assay
ESI	Electrospray ionization
ESI-MS	Electrospray ionization mass spectrometry
FDA	Food and drug administration
FFT	Fast fourier transform
f_{GSL}	Fraction of glycospingolipid complexes

FID	Free induction decay
FT	Fourier transform
FT-ICR	Fourier transform ion cyclotron resonance
GalNAc	N-acetylgalactosamine
GBP	Glycan binding protein
$GD2_{os}$	GD2 oligosaccharide
$GD2_{os}$-CL	GD2 oligosaccharide-CUPRA ligand
GL	Glycolipid
GSL	Glycosphingolipid
hCA	Human carbonic anhydrase
HCD	Higher energy collisional dissociation
hGal-1	Recombinant human galectin-1
hGal-3C	C terminal fragment of human galectin-3
hGal-7	Recombinant human galectin-7
HMOs	Human milk oligosaccharides
HRAM	High resolution accurate-mass
hu3F8	Humanized 3F8 wild type
hu3F8 Fab	Fab fragment of humanized 3F8 wild type
hu3F8 E1K/D32H	Humanized 3F8 E1K/D32H mutant
hu3F8 E1K/D32H Fab	Fab fragment of humanized 3F8 E1K/D32H mutant
huNoV	Human noroviruse
hu14.18	Humanized 14.18
IE	Incorporation efficiency
IEM	Ion evaporation model
IgG	Immunoglobulin
IgG2a	Immunoglobulin G2a
IgG3	Immunoglobulin G3

IMS	Ion mobility separation
IS	Internal standard
ITC	Isothermal titration calorimetry
K_a	Association constant
$K_{a,app}$	Apparent association constant
$K_{a,q}$	Association constant for stepwise ligand binding
$K_{a,int}$	Intrinsic association constant
L	Ligand
L_{proxy}	Proxy ligand
Lys	Lysine
m3F8	Mouse immunoglobulin G3 antibody 3F8
m/z	Mass-to-charge ratio
mAbs	Monoclonal antibodies
MALDI	Matrix-assisted laser desorption ionization
MD	Molecular dynamic
MMs	Model membranes
MS	Mass spectrometry
MS/MS	Tandem mass spectrometry
MSP	Membrane scaffold protein
MW	Molecular weight
nanoESI	Nanoflow electrospray ionization
NaCl	Sodium chloride
NBs	Neuroblastomas
NDs	Nanodiscs
NMR	Nuclear magnetic resonance
OS	Oligosaccharides
P	Protein

P_{proxy}	Proxy protein
P_{ref}	Reference protein
PA	Phosphatidic acid
PBS	Phosphate-buffered saline
PC	Phosphatidylcholine
PDs	Picodiscs
P dimer	Dimer of the norovirus P domain protein
P domain	Protruding domain of the norovirus capsid protein
PE	Phosphatidylethanolamine
PG	Phosphatidylglycerol
PI	Phosphatidylinositol
PL	Protein-ligand complex
POPC	1-palmitoyl-2-oleoyl-sn-glycero-3-phosphocholine
PS	Phosphatidylserine
R	Abundance ratio
RF	Radio frequency
RF	Response factor
SapA	Saposin A
scFv	Single chain variable fragment
SF_6	Sulfur hexafluoride
Siglecs	Sialic-acid-binding-immunoglobulin-like lectins
SPR	Surface plasmon resonance
SRIG	Stacked ring ion guide
TLC	Thin layer chromatography
TOF	Time-of-flight
TrisHCl	Tris(hydroxymethyl) aminomethane hydrochloride
T-wave	Travelling-wave

TWIMS	Travelling wave ion mobility spectrometry
UHMR	Ultra-high mass range
2,5-DHB	2,5-Dihydroxybenzoic acid
14G2a mAb	Mouse monoclonal anti-GD2 14G2a antibody

Chapter 1

Discovering Protein-Glycolipid Interactions Using Electrospray Ionization Mass Spectrometry

1.1 Introduction

1.1.1 Composition of membranes

Cellular membranes contain a wide variety of lipids which are known for their amphipathic nature and their capacity to form membrane bilayers. There are four main classes of lipids found in biomembranes according to their distinct chemical backbones: glycerophospholipids, sphingolipids, sterols and glycolipids (GLs).[1] The amount of each lipid depends largely upon the cell type and organelle. Generally, the most abundant class is the glycerophospholipids, also known as phospholipids.[2] They consist of a diacylglycerol, which contains fatty acid chains that can differ in length and in its level of unsaturation (helps to identify membrane thickness and fluidity), as well as a hydrophilic phosphate-containing head group that interfaces with the aqueous phase and can serve as a signaling hub.[3] In phospholipids, based on the head group, they are divided into phosphatidic acid (PA), phosphatidylcholine (PC), phosphatidylethanolamine (PE), phosphatidylglycerol (PG), phosphatidylserine (PS) and phosphatidylinositol (PI). Among them, PC accounts for > 50% of the phospholipids in most eukaryotic membranes.[2] Sphingolipids are derived from sphingosine and constitute the second major lipid class. They are composed of the amino group of the sphingosine backbones linked to a fatty acid by an amide bond and a hydrophilic head group at the primary hydroxyl. Sphingolipids are found in essentially all eukaryotes and some prokaryotic organisms and viruses, where they affect cell structure, signaling and interactions with the extracellular environment.[4] Sterols, the major non-polar lipids of cell

membranes, consist of four fused cycloalkane rings possessing an alcohol group on one ring. Cholesterol is the predominant sterols present in mammalian cells and generally accounts for approximately 30% of the animal cell membranes.[2,5] Moreover, cholesterol is capable of regulating the fluidity of the membrane in a concentration-dependent manner due to its planar and rigid structure.[6]

GLs are sugar-containing lipids consisting of a hydrophilic carbohydrate head group exposed to the aqueous phase, which can be recognized by glycan binding proteins (GBPs) and other glycan-recognizing molecules, linked to a hydrophobic lipid that anchors the GL in cell membranes. Two main classes of GLs, glycoglycerolipids and glycosphingolipids (GSLs), are distinguished by their lipid moieties, diacylglycerol and ceramide, respectively. The most abundant and diverse class of GLs in animals are GSLs, whereas glycerol-based GLs are most abundant in microbes and plants.[7] So far, approximately 400 different types of glycol(sphingo and glycerol)lipids are known, based on the list of glycans at the Lipid Maps Consortium website.[8] Most GSLs are classified on the basis of carbohydrate composition: 1) neutral species of GSLs that contain one or more uncharged sugars; 2) acidic species of GSLs that have ionized functional groups (phosphate or sulfate) linked to neutral sugars or charged sugar residues; 3) basic GSLs and 4) amphoteric GSLs.[1,9] Particularly, gangliosides, which are acidic GSLs with one or more sialic acids linked on the sugar chain, are found predominantly in the plasma membrane of nerve cells, where they constitute 5 - 10% of the total lipids.[10] Although only small amount of GLs are present in the cell membrane, they are involved in many cellular processes, including cell recognition, cell adhesion, signaling and bacterial and viral infection, through interactions with proteins.[11,12]

1.1.2 Protein-glycolipid interactions

Carbohydrate moieties of GLs, the most prominently exposed on the surface of cells of many living organisms, with many potential binding sites are specifically recognized by other biomolecules (e.g. proteins). For example, many bacteria and viruses possess GBPs specific for the GL receptors of the target cell, and these interactions result in the occurrence of infection. In addition, it is known that anti-ganglioside antibodies directed against the tumor-associated gangliosides can be used as therapeutics for certain types of cancer, since expression levels of certain gangliosides differ significantly between normal and tumor cells.[13] In general, the noncovalent interactions between the binding sites of proteins and carbohydrate moieties of GLs are primarily by the formation of hydrogen bond and van der Waals contacts.[14] Because protein interactions with individual carbohydrates typically tend to be weak (association constants (K_a) < 10^4 M^{-1}), multivalency is often required to generate biologically relevant binding.[15,16]

Due to the fundamentally biological importance, investigating the molecular basis of GBP-GL recognition, binding affinity and specificity have attracted extensive attention. Currently, although the GL ligands of many GBPs are known, it is widely believed that the vast majority of these interactions have yet to be identified.[17] The extremely limited availability of purified GLs, relative insoluble nature of GLs in aqueous solution and the shortcomings in existing analytical techniques associated with detection of low affinity monovalent GBP-GL interactions are the significant barrier to the discovery of GBP-GL binding. Alternatively, one strategy to overcome these limitations is to study the interactions between GBPs and water soluble analogs of GLs (i.e., GL oligosaccharides).

There are a number of surfaced-based analytical methods available to analyze biologically relevant GBP-carbohydrate interactions, such as enzyme-linked immunosorbent assay (ELISA),

surface plasmon resonance (SPR) spectroscopy and glycan microarray screening. ELISA is a commonly used analytical tool for measuring GBP-carbohydrate interactions with moderately high sensitivity.[18] While there are several ways of performing ELISA, this assay typically involves the immobilization of carbohydrate ligands on a solid support (usually a polystyrene microplate), followed by incubating with solutions containing the target protein which is linked to an enzyme. In the final step, the enzyme's substrates are added to produce a detectable signal, most commonly a color change. Since the multiple washing steps are required, ELISA assay is limited to measure relatively high affinity interactions. SPR allows for the direct and rapid measurements of association and dissociation rate constants and the affinities of GBP-carbohydrate interactions without the need for protein labelling.[19] Normally, carbohydrate ligands are immobilized on the surface of sensor chips, which are glass slides that are coated with a very thin layer of gold. The recruitment of an interacting protein by the carbohydrate changes the refractive index at the surface of the chip. This information is recorded for analysis of GBP-carbohydrate interactions. Glycan microarray assay is generally high-throughput manner for screening carbohydrate libraries against target GBPs.[20] This microarray technique involves application of a small volume of buffer containing target GBPs to a microarray consisted of a library of carbohydrates, and then the specific GBP-carbohydrate interactions are qualitatively detected through fluorescence of either the fluorescently labeled GBP or a secondary reagent that binds to the GBP. Although these surfaced-based analytical techniques have uncovered hundreds of new GBP-carbohydrate interactions, the orientation of the carbohydrate, carbohydrate density, the nature of immobilization and the loss of mobility of the immobilized carbohydrates may potentially affect the nature of the binding interaction.[21,22]

In addition, the common solution-based techniques used for GBP-carbohydrate interactions

studies include isothermal titration calorimetry (ITC) and electrospray ionization mass spectrometry (ESI-MS). ITC is a powerful label-free technique, which is generally considered as the "gold standard" for studying thermodynamics of GBP-carbohydrate interactions in solution. It is a quantitative method that can determine the binding affinity (K_a), enthalpy and entropy changes. Since conventional ITC instruments suffer from low sensitivity and low throughput, the large amount of protein and ligand (~ mg) are required for each analysis and each measurement is time-consuming (hours).[23,24] ESI-MS has emerged as an important technique for the identification and quantification of GBP-carbohydrate interactions in vitro.[25-27] ESI allows noncovalent GBP-carbohydrate complexes to be transferred intact from solution to the gas phase for MS detection. The analytical advantages of ESI-MS assay include simplicity (labeling and immobilization free), speed (individual measurement normally can be completed within a few minutes), low sample consumption (~ 10 pmol of sample consumed per analysis for nanoflow ESI-MS). Most of all, the ESI-MS assay enables to directly measure binding stoichiometry and multiple equilibria simultaneously.[28] The detailed description of implementing ESI-MS assay is described in sections 1.3.

GBP-GL interactions can also be probed directly by using surface-based techniques such as ELISA, SPR spectroscopy, thin layer chromatography (TLC) and microarray.[7,29,30] In these assays, the GLs are readily immobilized on a solid support, where they remain stably attached in aqueous solution. Shotgun microarrays were recently developed to aid in the discovery of GL receptors. Natural GLs and glycoprotein-derived glycans extracted from cells, organism or tissue were derivatized with a hetero-bifunctional fluorescent tag suitable for covalent immobilization on a glass slide.[29] However, those GL immobilization based assays is limited by unnatural presentation and lack of mobility of GL on surfaces, which will affect the nature of protein interactions.

Recent methodological advances have led to development of new analytical approaches to GBP-GL interactions using membrane mimetic systems for solubilization of GLs. These include micelles, nanodiscs (NDs), picodiscs (PDs), liposomes, bicelles and supported lipid bilayer.[31-34] Micelles are detergent molecules that form a spherical arrangement in aqueous solutions. The hydrophilic head groups are in contact with surrounding solvent, while the hydrophobic tails are in the micelle center. Nanodiscs are ~ 150 kDa water-soluble discoidal phospholipid bilayers surrounded by two copies of an amphipathic membrane scaffold protein (MSP). Picodiscs are the lipid-transferring macromolecular complexes, which are composed of two copies of the human sphingolipid activator protein saposin A (SapA) and a small number of (8 - 12) of phospholipids. Liposomes are lipid bilayer rolled up into a hollow spherical shell, enclosing a small region of water. Bicelles are formed from mixed phospholipids that can assemble into bilayer-like structures. They mainly consist of long-chain phospholipids that make up the bilayer-like region and either detergent or short-chain phospholipids that compose flanking rims. Supported lipid bilayer is a planar lipid bilayer structure localized on a solid support. The incorporation of GLs into these model membranes (MMs) provides a native-like membrane environment, which allows GBP-GL binding to be comprehensively studied.

Several conventional binding methods have been adapted to probe GBP binding to GLs incorporated into the MMs, including fluorescence microscopy, SPR spectroscopy, nuclear magnetic resonance (NMR) spectroscopy.[35-38] More recently, a silver nanocube biosensor technology was developed to investigate multivalent protein-GL recognition, which combines localized SPR and a supported lipid bilayer on the Ag@SiO2 core-shell nanocube (~ 110 nm).[39,40] In addition, the combination of ESI-MS with MMs has been reported for probing GBP-GL interactions in aqueous solution.[41-43] In particular, catch-and-release (CaR)-ESI-MS assay,

implemented with either NDs or PDs has been used to screen GLs against GBPs to identify specific interactions.[44] This thesis mainly focuses on the development and application of either ESI-MS or CaR-ESI-MS methods combined with NDs to discover and quantitatively evaluate protein-GL interactions.

1.2 Electrospray Ionization (ESI)/Matrix Assisted Laser Desorption Ionization (MALDI) Mass Spectrometry

1.2.1 ESI mechanisms

Electrospray ionization (ESI) is a mild ionization technique that was first pioneered in the late 1960s by Malcolm Dole[45,46] and later advanced by John B.Fenn.[47] It is a versatile method that not only allows analytes present in a solution to be transferred into the gas phase as ions without fragmentation, but also maintains the noncovalent interactions, including those involved in protein-ligand complexes. Subsequently, the gas phase ions can be detected by mass spectrometer. Remarkably, ESI could handle a variety of analytes from small inorganic or organic species to polymers, nucleic acids, peptides and proteins that have a molecular mass ranging from kilo to hundreds of mega Daltons.[48] ESI occurs at atmospheric pressure.[49] The ESI process, as described by Kebarle and Tang,[50] involves three major steps, as shown in Figure 1.1.[47,51,52]

(a) Production of charged droplet

Using the positive ion mode as an example, analyte solution is flowed through a metallic capillary that is held at high electrical potential. At the tip of the capillary, the applied potential causes a numbers of positive charges to accumulate preferentially at the tip, forming a "Taylor cone".[50,53,54] At the narrow end of the cone, where the electrostatic forces overcome the surface tension of the solution, the liquid cone becomes unstable and a liquid filament forms.[50] At some distance downstream, the liquid filament becomes unstable and result in the emission of highly positive

charged droplets, generally on the order of several micrometers in diameter.[55] A coaxial gas flow generally assists in this spraying process.[49]

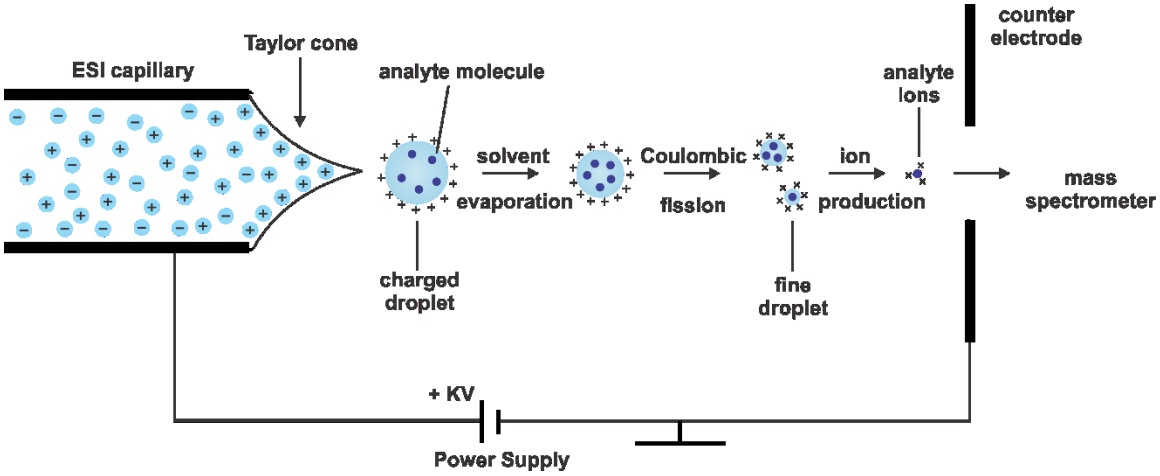

Figure 1.1. Schematic illustration of the ESI process performed in positive ion mode, adapted from reference 51.

(b) Shrinkage of charged droplets and repeated droplet disintegrations

The positive charged droplets emitted from the Taylor cone undergo rapid shrinkage due to solvent evaporation. As the droplet size continues reduction, droplet fission occurs, termed the "Rayleigh limit", where the Coulombic repulsion forces between the increasingly crowded charges become sufficient to overcome surface tension forces holding the droplet together.[51,52,56] At this Rayleigh limit, the limiting charge on a droplet (Q_R) is given by eq1.1.[57]

$$Q_R = 8\pi\sqrt{\varepsilon_0 \gamma R^3} \qquad (1.1)$$

Where ε_0 is the electrical permittivity of a vacuum, γ is the solvent surface tension and R is the droplet radius. The smaller and positive charged offspring droplets are generated from the parent droplets at the Rayleigh limit via jet fission. Typically, the offspring droplets carry off approximately 2% of the parent's mass and 15% of the charge of the parent droplet.[58-60]

Subsequently, the droplets go through repeated solvent evaporation and disintegration events until ultimately the highly positive charged droplets with radii with a few nanometers are produced.

(c) Generation of gas phase ions

Three different ion release mechanisms including ion evaporation model (IEM), charged residue model (CRM) and chain ejection model (CEM) have been proposed to elucidate the formation of gas phase ions from the highly charged nanodroplets, as show in Figure 1.2.

(i) Ion evaporation model (IEM): Iribarne and Thomoson proposed this ion evaporation model that is experimentally supported for small organic and inorganic ions.[61,62] When solvent evaporation and Coulomb droplet fissions have shrunk the size of the charged droplets to a very small radius ($R < 10$ nm), direct ejection of the small ions from the surface of charged nanodroplets into the gas phase will occur. At this point, the ion evaporation process replaces Coulomb fission and the evaporation of ions still continues until small analyte ions are produced.

(ii) Charged residue model (CRM): The dominant mechanism of ion formation during ESI process is charged residue model, introduced by Dole and coworkers, for the release of macromolecules.[45,63] This model proposes that evaporation and Coulombic fission occur until the highly charged nanodroplets containing a single analyte molecule are formed. Complete evaporation of the solvent containing this nanodroplet eventually yields a "naked" gas phase analyte ion whose charge comes from the charges at the surface of the vanished nanodroplet.[52] There is considerable evidence that the gas phase ions of large globular species such as natively folded globular proteins are produced by CRM.[45,52,64,65] During the entire shrinkage process, the CRM nanodroplets keep close to the Rayleigh limit, which means that the nanodroplet sheds charge as its radius gradually decreases.[63]

(iii) Chain ejection model (CEM): This model, introduced by Konermann and coworkers, has been proposed to account for unfolded proteins where the macromolecular chains are disordered, generally hydrophobic, which was demonstrated by molecular dynamic (MD) simulations.[63,66-68] In a Rayleigh-charged nanodroplet, the unfolded protein chains immediately migrate from the droplet interior to the surface of the droplet. Subsequently, one chain terminus is expelled into the gas phase. As the unfolded protein is gradually ejected, the protruding tail experiences charge equilibration with the droplet via H^+ migration. Finally, the protein separates from the nanodroplet as a highly charged unfolded gas phase ion.[63,66]

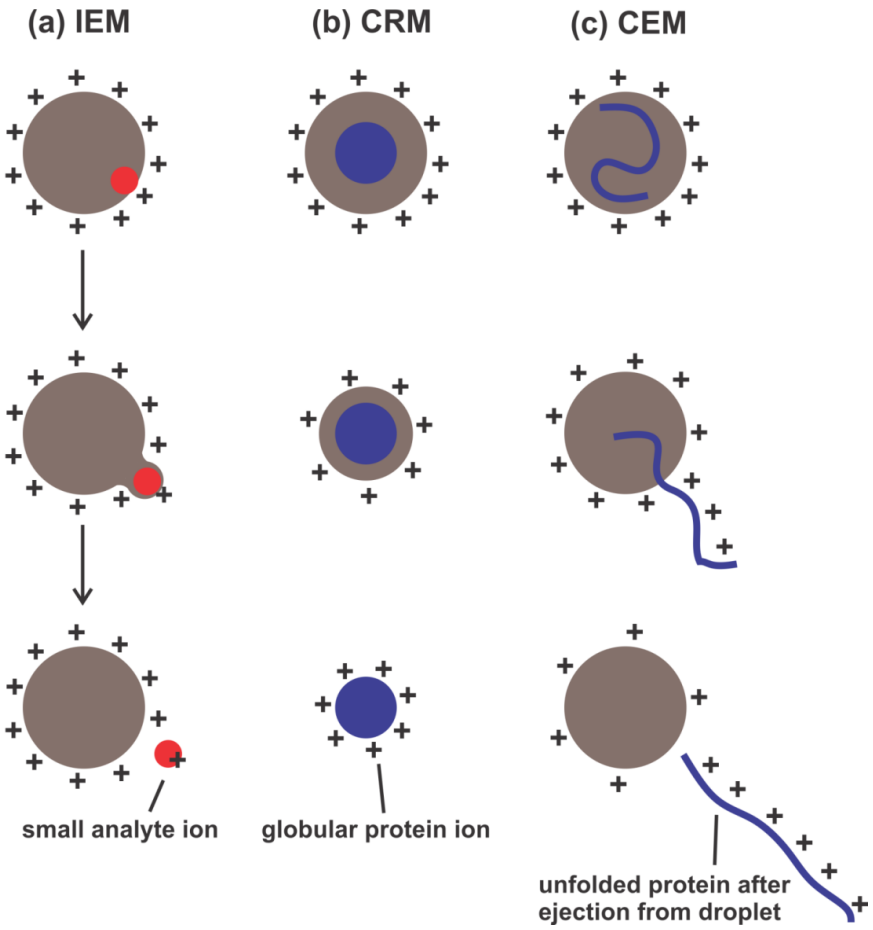

Figure 1.2. Different ESI models proposed for gas-phase ion generation. (a) IEM, (b) CRM and (c) CEM. Figure 1.2 is adapted from reference 63.

1.2.2 Nanoflow ESI-MS

The conventional ESI apparatus uses a metallic capillary on the order of 0.5 mm in diameter.[56] The flow rates of conventional ESI require μL/min to maintain the stable Taylor cone necessary for droplet formation and the diameters of the initially produced droplets are in the μm range.[50,69,70] Consequently, it is generally required to have at least ~ 50 μL of sample solution for most ESI-MS analysis. In contrast, the nanoflow ESI (nanoESI), introduced by Wilm and Mann in 1994, is typically performed by using glass or quartz capillaries which have been pulled to a fine tip (~ 1 μm inner diameter).[71-73] The flow rates in nanoESI (without external pumping) is typically in the range of ~ 1 nL/min to several tens of nL/min. Therefore, approximately 1-5 μL of solution containing pmol of analyte is required for an analysis, resulting in low sample consumption.[73,74] Additionally, a very low flow rate in nanoESI leads to very small droplet sizes (less than 200 nm).[72] A higher number of droplets produced in nanoESI will generate more ions that are available for MS since smaller initial droplets accelerate the solvent evaporation process. Due to the higher concentration of excess charge on the droplet, the ionization efficiency is enhanced.[75] Moreover, there are fewer analyte molecules in each nanoESI droplet, which may reduce the formation of nonspecific binding during the ESI process.[72,73,75,76] In this thesis, nanoESI was used.

1.2.3 MALDI mechanism

Matrix-assisted laser desorption ionization (MALDI), invented by Karas and Hillenkamp in late 1980s, is a soft ionization method that uses a laser energy absorbing matrix to create ions from large biomolecules and organic molecules, such as proteins, peptides and polymers with minimal fragmentation.[77-81] Shown in Figure 1.3 is a schematic illustration of the process of MALDI in positive ion mode. The basic principle of MALDI is to mix thermally unstable, nonvolatile analytes

with matrix molecules, which are highly photo-absorbing organic compounds, in a solution. A small droplet of mixed solution is taken and deposited onto a metal plate to form a solid sample. The metal plate is inserted into a mass spectrometer. Subsequently, a pulsed laser beam (e.g., 337 nm from a nitrogen gas laser and 355 nm frequency-tripled Nd:YAG solid-state laser) is applied to strike the solid sample.[82] The matrix molecules absorb the laser's photons or energy and they can be desorbed, shooting off the surface and expanding into the gas phase. Meanwhile, analyte molecules can be left into the gas phase as well. Some matrix molecules become ionized by photons from the laser pulse during the expansion process. The ionized matrix molecules collide with the analyte molecules already in the gas phase to convert the neutral analyte molecules into analyte ions, in cases where the analyte molecules can gain a photon from the matrix ions to become protonated analyte molecules in ion-molecule reactions. The protonated ions are then accelerated at a fixed potential and detected by a mass spectrometer.[82-87]

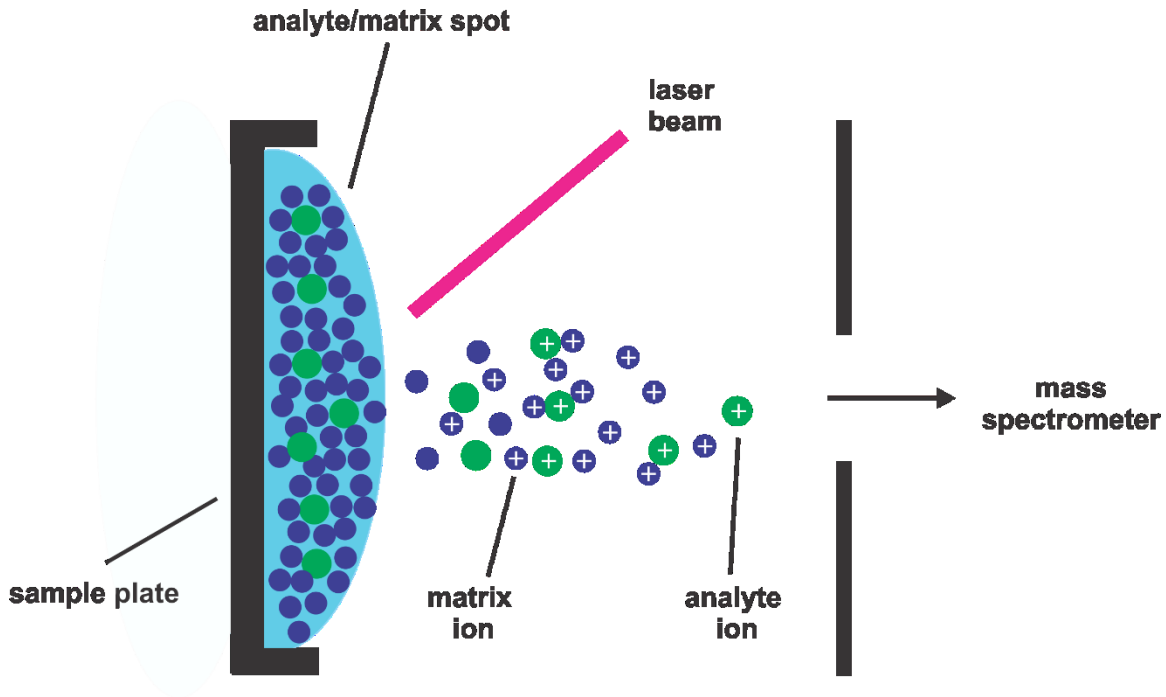

Figure 1.3. Schematic illustration of the process of MALDI in positive ion mode, adapted from

reference 87.

The selection of matrix is a pivotal parameter for MALDI mass analysis. A number of organic compounds have been used as matrices for MALDI-MS. For microbiological applications, α-cyano-4-hydroxycinnamic acid (CHCA), 2,5-dihydroxybenzoic acid (2,5-DHB) and 3,5-dimethoxy-4-hydroxycinnamic acid (sinapinic acid) have been found to be the most useful.[88-90] A good matrix is necessary to have a sufficient absorption coefficient at the applied laser wavelength, and could transfer the absorbed photon energy into thermal energy efficiently for desorption of both matrix and analyte molecules.[82,91] In the present work, the MALDI-MS measurements described in Chapter 2 were performed on quantifying the amount of GLs in a given ND preparation and 2,5-DHB was used as matrix.

1.2.4 MS instrumentation

1.2.4.1 Hybrid quadrupole-ion mobility separation-time of flight mass spectrometer

A Synapt G2-S quadrupole-ion mobility separation-time of flight (Q-IMS-TOF) mass spectrometer (Waters UK Ltd., Manchester, UK) equipped with a nanoESI source was used in Chapter 2 & 3. Shown in Figure 1.4 is a schematic diagram of the Waters Synapt G2-S Q-IMS-TOF mass spectrometer, which consists of four principal components: Z-spray source with StepWave ion guide, quadrupole, a travelling wave device containing Trap, IMS and Transfer (Triwave) and quantitative TOF-reflectron mass analyzer (QuanTOF). The highly charged analyte nanodroplets produced by nanoESI are introduced into the mass spectrometer through a Z-spray source, which reduces the transfer of the neutral contamination and improves the signal-to-noise ratio. The resulting ion beam passes into the entrance of a two-stage StepWave transfer optics, which can efficiently capture ions in the expanded beam. Ions are focused in the first stage and then easily directed to the second stage, a narrow bore ion guide. The StepWave ion transfer optics

employs an off-axis design, which guarantees that any neutral contaminants are actively extracted from the system. The focused ions then enter the quadrupole, where ions of interest are filtered according to *m/z* ratio. The mass-separated ions are transmitted through Trap collision cell, IMS cell and Transfer collision cell, where they can undergo collision-induced dissociation (CID). Finally, transmitted ions are detected by an orthogonal acceleration reflectron TOF mass analyzer. A brief description of the quadrupole, Triwave and TOF parts of the instruments will be given below.

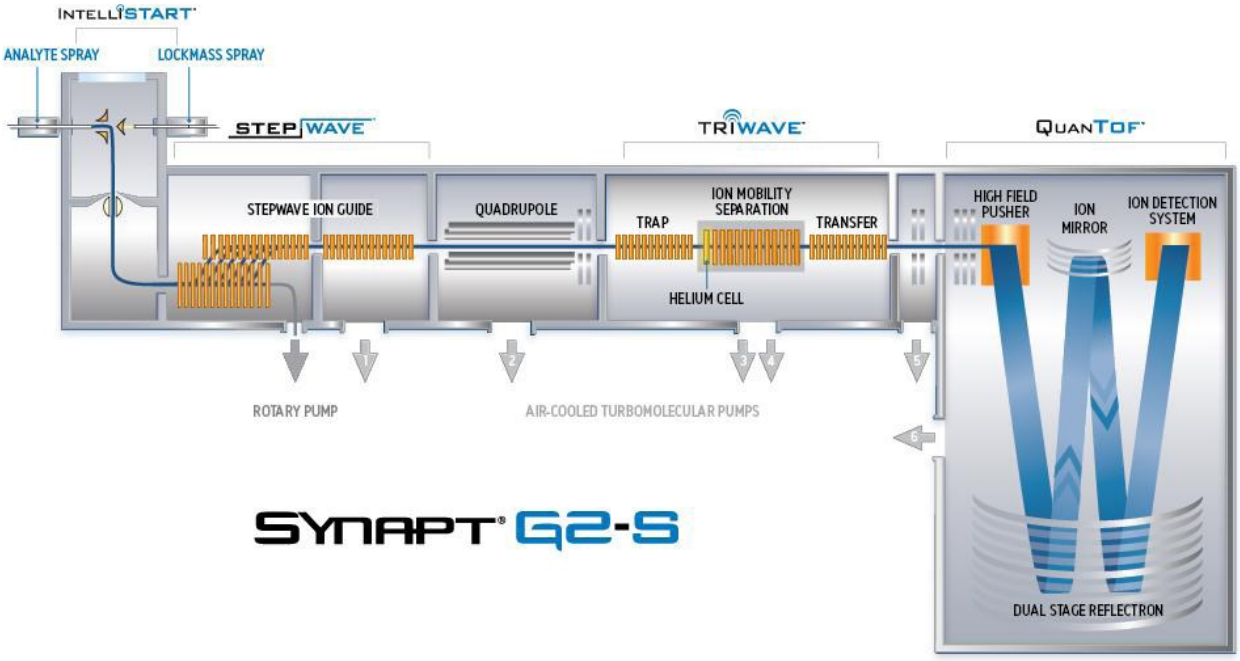

Figure 1.4. A schematic diagram of the Waters Synapt G2-S Q-IMS-TOF mass spectrometer, adapted from Waters user's manual.

1.2.4.1.1 Quadrupole

A quadrupole mass analyzer uses four cylindrically shaped rod electrodes extending in the z-direction to create a hyperbolic field.[92-94] One pair of opposite rods have an applied potential of (U + Vcos(ωt)) and the other pair of opposite rods have a potential of -(U + Vcos(ωt)), where U is a

direct current (DC) voltage and Vcos(ωt) is a radio frequency (RF) voltage, with a "zero-to-peak" amplitude of the RF voltage V and angular frequency ω. The applied voltages can affect the trajectory of ions traveling through the flight path centered between the rods. The stability of the ion trajectory in a quadrupole analyzer is dependent on the ion's a_u and q_u values defined by eq1.2 and 1.3:[92]

$$a_u = \frac{8ezU}{mr_0^2\omega^2} \qquad (1.2)$$

$$q_u = \frac{4ezV}{mr_0^2\omega^2} \qquad (1.3)$$

where u represents position along the coordinate axes (x or y), e is the charge on an electron and r is the effective radius between electrodes. By plotting the parameter *a* versus *q*, the stability diagram of the two-dimentional quadrupole field can be obtained, which is used to determine the stability of several ions with different masses (Figure 1.5). In this diagram, any *a* and *q* point with in stable region represents DC and RF voltages where the ion can traverse the quadrupole with a stable trajectory, whereas any point outside the stable region (unstable region) represent the situations where the ions will be expelled by hitting the rods.[94,95] Maintaining the *U/V* ratio constant, a straight mass scan line can be obtained. By increasing the DC and RF voltages simultaneously, the ions from low mass to high mass will take turns passing the quadrupole. The larger the slope of the mass scan line, the better the resolution of isolution. Specifically, the quadrupole mass analyzer can also act as a mass filter when no DC potential applied and operated in the RF-only mode. The slope of the mass scan line is zero, thus ions with many different masses can be transmitted. In the Synapt G2-S mass spectrometer, a quadrupole pre-filter is placed in the front of the quadrupole mass filter, as shown in Figure 1.5b. The application of RF-only pre-filter

improves the absolute sensitivity, peak shape and resolution by reducing the effects of fringing fields at the entrance to the quadrupole.[96]

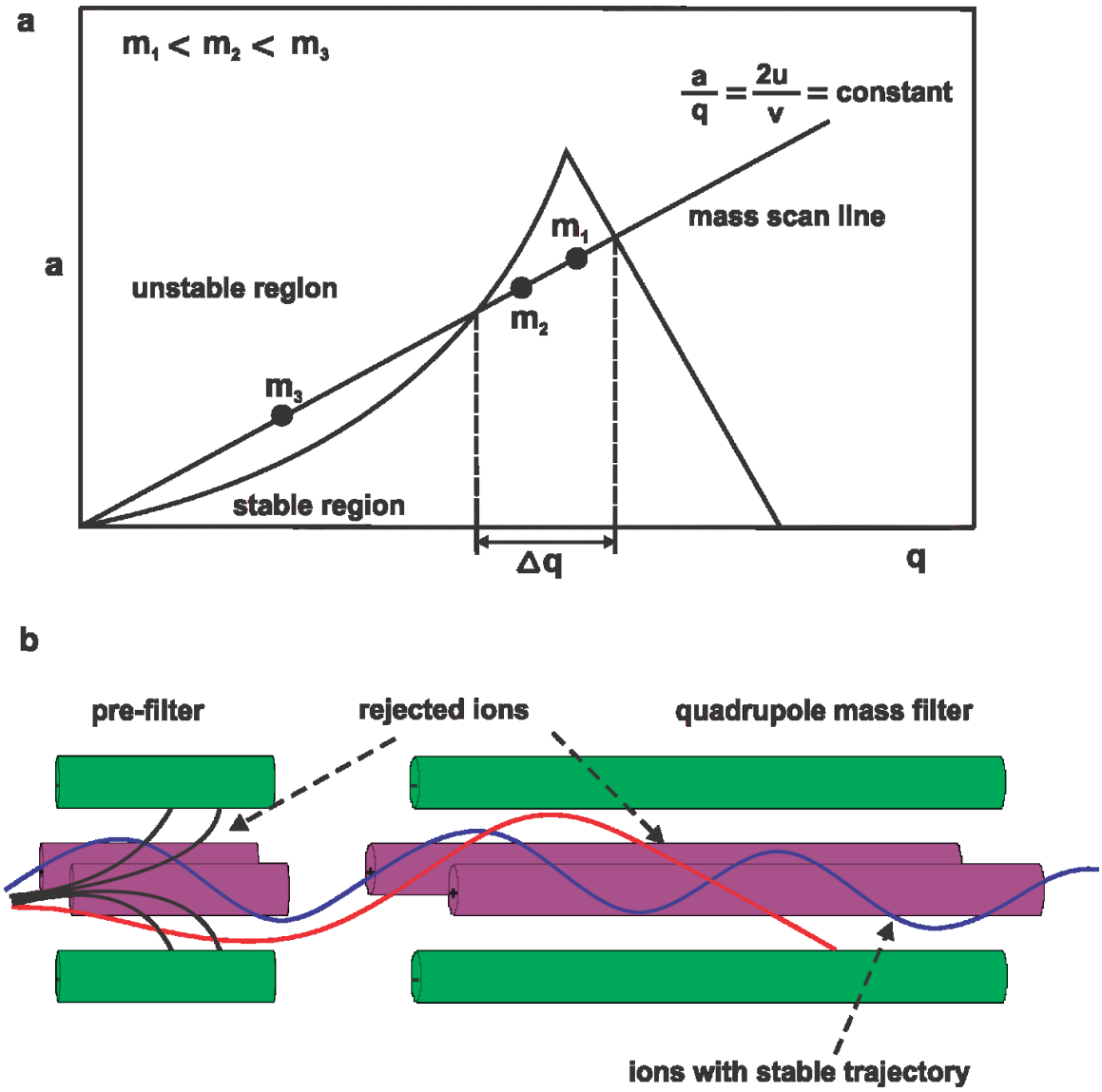

Figure 1.5. (a) Stability diagram of a quadrupole analyzer for ions with different mass (m) values ($m_1 < m_2 < m_3$), adapted from reference 95. (b) Schematic representation of the quadrupole used in Waters Synapt mass spectrometer.

1.2.4.1.2 Travelling wave

The travelling wave device in Synapt G2-S comprises three successive Triwave stacked ring ion guides (SRIGs), including Trap, IMS and Transfer Triwaves, which transfers ions from the quadrupole to the TOF with optimal efficiency. Each Triwave stacked ring ion guide consists of a series of planar electrodes arranged orthogonally to the ion transmission axis, as shown in Figure 1.6, in which adjacent electrodes have an opposite phase of RF voltage applied to them.[97,98] When a DC voltage is applied to the adjacent electrode pairs, a radially confining potential barrier is provided. Ions within this region undergo axial traps produced by the ring geometry, which will stop or slow down the ion axial motion. Accordingly, the transient DC voltage is superimposed on the confining RF applied to the next sets of electrodes downstream at given time intervals. This provides a continuous sequence of moving electric field ("travelling wave"), reducing their residence time in the cell.[98]

Meanwhile, ion mobility separation (IMS) is a gas-phase electrophoretic technique that allows ions to be distinguished according to their mobility difference, which is affected by their charge, mass and collision cross section (i.e., the size and shape of the ions), through a buffer gas (nitrogen or helium) in the presence of an electric field.[99-101] In Triwave IMS, ions are moved through Triwave cell with a combination of a reverse buffer gas (nitrogen) flow and a non-uniform, moving electrical fields and separated based on their mobility. As ions pass through the buffer gas, they are subjected to a number of collisions, which prevent them progress towards the next Triwave ion guide. Larger ions with lower mobility experience more collision than smaller ions and eventually traverse more slowly. In the Synapt Triwave IMS, a chamber filled with helium is placed prior to the main IMS cell to minimize ion losses through scattering and/or fragmentation and balance the pressure of the nitrogen.[101]

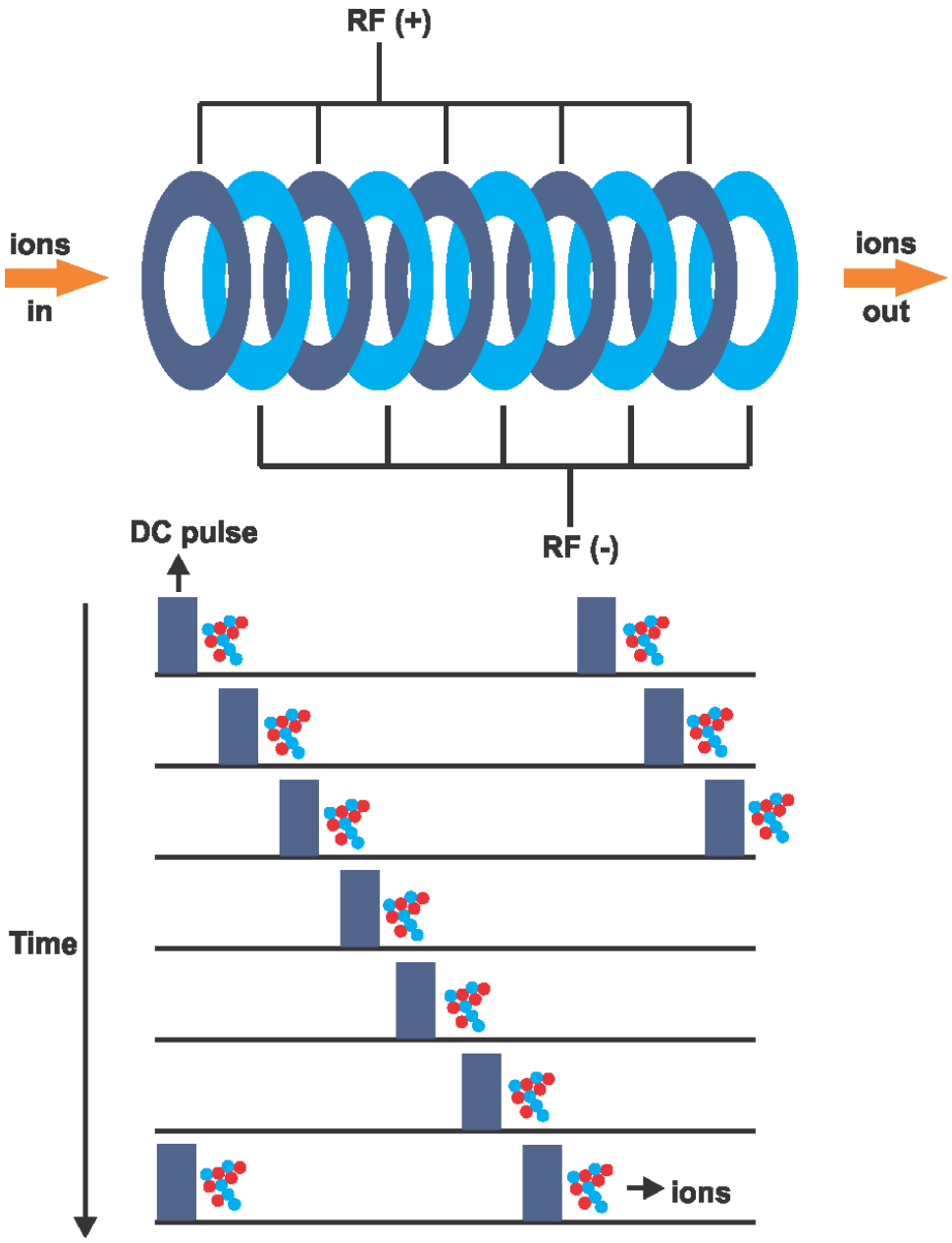

Figure 1.6. Illustration of the operation of a Triwave SRIG, adapted from reference 97.

Both Trap and Transfer Triwaves can be used as collision-cell regions for optimized fragmentation of compounds of interest. Collision-induced dissociation (CID) is the most commonly ion activation technique used in tandem mass spectrometry (MS/MS). CID occurs when the particular ions, accelerated by applying an electrical potential to increase the ion kinetic energy,

collide with neutral gas molecules (such as argon, helium and nitrogen) and a small fraction of the ion's kinetic energy is transferred into internal energy, which results in dissociation of the ions into various fragment ions. The extent of fragmentation is determined by the total internal energy content of the excited ion.[102,103] In Synapt G2-S mass spectrometer, either Trap or Transfer collision-cell region can be performed CID by simultaneously applying a constant DC voltage (collision energy) to each ring electrode and a transient DC voltage used to drive ions to the next stage of the instrument. When the selected ions of interest are transferred into the Trap/Transfer regions filled with argon as a neutral background gas, these precursor ions are subjected to collide with the Ar gas and are fragmented by CID. Eventually, the fragment ions are detected by mass analyzer. Currently, CID has been widely employed for investigating non-colvalent protein-ligand and protein-protein interactions in the gas phase.[104-106] In this thesis, the applications of CID to study noncovalent protein-carbohydrate/GL interactions are described in Chapter 2.

1.2.4.1.3 TOF mass analyzer

The time-of-flight (TOF) mass analyzer disperses ions with different *m/z* according to their flight time along a field-free drift path of known length. Ions are accelerated by an electric field with known voltage between the ion accelerator and the detector.[107-109] Assuming that the ion is initially at rest, the velocity of the ion (v) attained is dependent on the kinetic energy of the ion in an electric field, and can also be determined by the length of the flight path (L) and flight time (t), as given by eq1.4:

$$v = \sqrt{\frac{2ezU}{m_i}} = \frac{L}{t} \qquad (1.4)$$

where e is the electron charge, z is the charge number, U is the acceleration voltage and m_i is the mass of the ion. Since e, U and L are constants, *m/z* of an ion can be calculated by rearranging

eq1.4 into eq1.5. Based on this equation, the lighter ions will arrive earlier at the detector than the heavier ions, if all the ions start their journey at the same time or at least within an adequately short time interval.

$$\frac{m}{z}_{0} = t^2 \frac{2eU}{L^2} \qquad (1.5)$$

In Synapt G2-S mass spectrometer, an orthogonal-acceleration, dual-reflectron geometry of the TOF mass analyzer is used in order to provide high resolution and exact-mass capabilities. Continuous ions are filled in the orthogonal accelerator. A high voltage pulse orthogonally accelerates the ions down the flight tube, where the dual-stage reflectron comprised of a series of electric plates with increasing potential reflects the ions back toward the detector. Ions of different kinetic energy penetrate the reflector into different depths until they reach zero kinetic energy and then get ejected into the opposite direction. Fast ions have to travel a longer path and take more time to return than slow ions. Eventually, fast and slow ions are focused in time at the detector. Overall, the use of an ion reflector or ion mirror compensates the initial energy distribution and focus ions having the same *m/z* to the detector. It is worth mentioning that Synapt G2-S instrument has two operating modes: the sensitivity mode ("V" mode) and high resolution mode ("W" mode). The former can achieve maximum sensitivity using single-pass TOF, while the latter can focus the ions twice using double-pass TOF, resulting in higher resolution but less sensitivity.

1.2.4.2 Orbitrap mass spectrometer

The other mass spectrometer used in this thesis (Chapter 3) is a Q Exactive ultra-high mass range (UHMR) hybrid quadrupole-orbitrap mass spectrometer (Thermo Fisher Scientific, Waltham, US) equipped with a nanoESI source, as shown in Figure 1.7. This instrument principally combines in-source trapping, high performance quadrupole precursor ion selection (up to *m/z* 25 000), a high-

energy collisional dissociation (HCD) cell and a high resolution accurate-mass (HRAM) Orbitrap mass analyzer with optimized RF voltages for improved high mass ion transmission, which offers high mass accuracy (< 3 ppm) and resolution (up to 200 000 at *m/z* 400) in the ultra-high mass range (*m/z* 350 - 80 000). Highly charged nanodroplets containing analytes produced by nanoESI performed at atmospheric pressure are sampled into the mass spectrometer through RF lens stacked-ring radio frequency (RF) ion guide, which captures and efficiently focuses the ions into a tight beam. Then ions pass through injection flatpole region, where the controllable, high efficient desolvation and fragmentation of ions are provided by pulsing a negative voltage on injection flatapole lens. Meanwhile, the ion cloud can also be focused by maintaining a high positive potential on inter-flatapole lens for improved transmission. Afterwards, the ions are guided and focused through the bent flatapole using an axial DC field and a focusing RF field, enhancing sensitivity. A segmented Thermo Scientific^{TM} hyperbolic quadrupole (HyperQuad^{TM}) mass filter operated at a low frequency is then used to select the ions of interest for improved ion transmission in the ultra-high mass range and optimized isolation window. After passing through transfer multipole, the ions are transmitted into the C-Trap cell, serves as an external ion storage device, where ions are accumulated and thermalized via collision with nitrogen gas. Subsequently, ions are squeezed into a small cloud and efficiently injected into the Orbitrap mass analyzer for detection. To perform tandem MS, the ions of interest are subjected to HCD in the HCD cell filled with nitrogen gas, where the fragmentation of the ions are extracted.

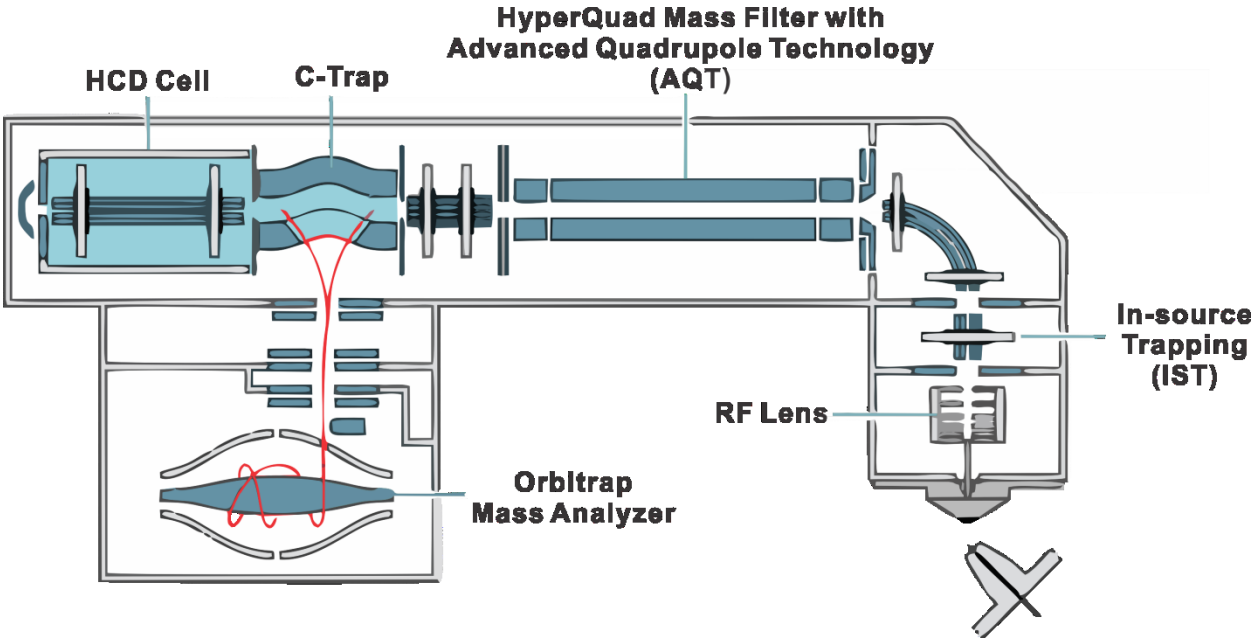

Figure 1.7. Schematic diagram of the Thermo Fisher Q Exactive ultra high mass range (UHMR) Orbitrap mass spectrometer, adapted from Thermo Fisher user's manual.

1.2.4.2.1 Orbitrap mass analyzer

The Orbitrap mass analyzer consists of a spindle-like central electrode at high voltage and a barrel-like outer electrode split in half by an insulating ceramic ring, as shown in Figure 1.8. It employs the trapping of pulsed ion beams in an electrostatic field with a quadro-logarithmic potential distribution, eq1.6:[110,111]

$$U(r, z) = \frac{k}{2}(z^2 - \frac{r^2}{2}) + \frac{k}{2}(R_m)^2 \ln[\frac{r}{R_m}] + C \qquad (1.6)$$

where r and z are cylindrical coordinates, C is a constant, k is field curvature and R_m is the characteristic radius. This electrostatic field is created between an axial central electrode and a coaxial outer electrode. Stable ion trajectories involve both orbiting motion around an axial central electrode (related to r-coordinate) and simultaneously harmonic oscillations in the z-direction. The electrostatic attraction towards the central electrode is compensated by a centrifugal force that

results from the initial tangential velocity of ions.[112] The frequency of the harmonic axial oscillation ω_z solely depends on the ratio of ionic charge q to ionic mass m and field curvature k, but is independent of the kinetic energy, tangential velocity, positions and spatial spread of the ions, as given by eq1.7: [108,112]

$$\omega_z = \sqrt{k \cdot \frac{q}{m}} \qquad (1.7)$$

The frequencies of these axial oscillations can be detected as an image current on the two split halves of the outer electrode, followed by a fast fourier transform (FFT) algorithm to convert the recorded time-domain signal into a mass-to-charge (m/z) spectrum. The ultra-high vacuum (typically < 5.0×10^{-10} mbar) is required for operating the Orbitrap mass analyzer.

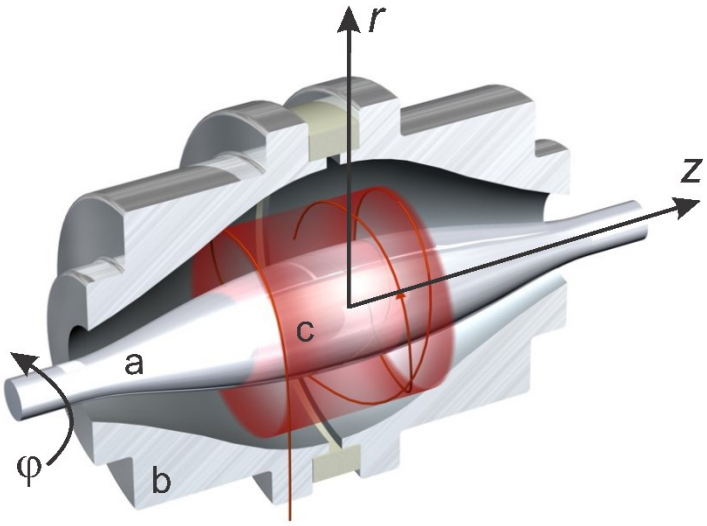

Figure 1.8. A cut-away model of the Orbitrap mass analyzer. (a) a central electrode; (b) an outer electrode, split in half by an insulating ceramic ring; (c) complex orbital path of an ion. Figure 1.8 is adapted from reference 112.

1.2.4.3 Fourier transform ion cyclotron resonance (FT-ICR) mass spectrometer

A Brucker 15 Tesla solariX-XR Fourier transform ion cyclotron resonance (FT-ICR) mass spectrometer (Bruker-Daltonics, Billerica, US) equipped with a MALDI source was used in Chapter 2, as illustrated in Figure 1.9. MALDI sample plate is introduced into the MALDI user interface load port. Ions containing analytes can be produced in this area by irradiation of a MALDI sample plate with the output of a smartbeam-II laser. The resulting ions entering the funnel stage are focused into a tight ion beam using RF voltages. The ions then enter the second funnel stage, where pressure is maintained at ~ 0.1 mbar and ions can be decelerated, accumulated in this region for a selected time or simply passed through. Subsequently, a quadrupole mass filter is used to focus and selectively transmit ions within a desired *m/z* range (1 amu - 6000 amu). The transmitted ions pass through into the collision cell where the mass-selected precursor ions can be stored for a defined time and also dissociated at an elevated pressure of ~ 1×10^{-3} mbar of typically Argon. Ions are then ejected from the collision cell by applying the DC Extract Bias voltage to the hexapole rods of the collision cell and focused by several DC lens elements. Eventually, the ions are transferred into the ICR cell via the multipole ion guide for detection. The ultra-high vacuum necessary to operate the FT-ICR mass spectrometer (typically $\leq 10^{-9}$ mbar) is maintained by differential pumping system.

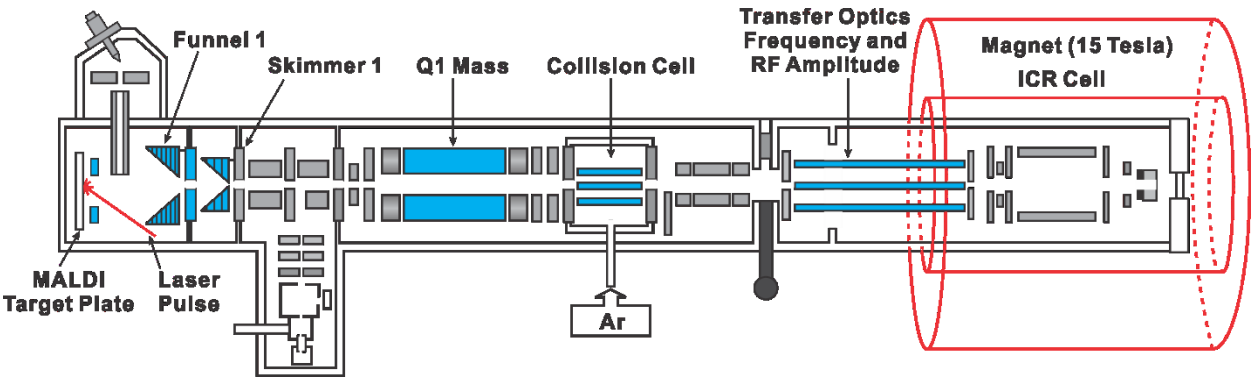

Figure 1.9. Schematic diagram of the Bruker 15 Tesla SolariX-XR FT-ICR Mass spectrometer, adapted from the Bruker user's manual.

1.2.4.3.1 FT-ICR mass analyzer

FT-ICR mass spectrometer has emerged as a prominent mass analyzer with ultra-high resolution and high mass accuracy. The general operating principle of FT-ICR mass analyzer involves in the ion cyclotron motion in a uniform magnetic field.[113] The ICR cell located inside a high-field magnetic (superconducting magnet) consists of three pairs of electrode plates, which are used for ion trapping, excitation and detection, respectively.[114-116]

The moving ions with different *m/z* generated or injected by ionization execute circular ICR orbital motion by action of the Lorentz force, when entering a uniform magnetic field perpendicular to its direction. The ion cyclotron orbital frequency, v_c, is given by eq1.8:[113]

$$v_c = \frac{\omega_c}{2\pi} = \frac{qB}{2\pi m} = \frac{zeB}{2\pi m} \qquad (1.8)$$

where ω_c is the cyclotron angular frequency, q is the ionic charge ($q = ze$, where z and e are the charge and the elementary charge, respectively), B is the magnetic field strength and m is the mass of the ion. Based on eq1.8, it is worth mentioning that all ions of a given *m/z* rotate at the same ICR frequency, independent of velocity.

When ions are generated at random time intervals or injected in the ion trap, ions of a given

initial velocity will be distributed randomly about their circle and their "incoherent" cyclotron rotation does not generate an observable electrical signal. In order to detect the ions in FT-ICR MS, ion excitation is necessary to be produced in advance by applying a spatially uniform and oscillating electric field directed perpendicular to the magnetic field direction. If the frequency of the applied field matches the cyclotron frequency of ions of a particular *m/z*, the ions are accelerated with a rotating electric field. After a few cycles, ions form a packet which spirals outward with time. As the coherently orbiting ion packet increases to larger ICR orbital radius, it induces a differential current between two opposed detection plates called image current. However, image current detection is dependent on the ion cloud repeatedly attracting (positive ions) or repelling (negative ions) the electrons of the detection electrode upon its passage.[95] The amplitude of the image current is proportional to the number of spatially coherent orbiting ions in the ICR cell. The resulting minuscule image current is then amplified, transformed into a voltage signal as long as the ion motion in the ICR cell has sufficient coherence. That voltage signal can be then amplified to yield a time domain transient free induction decay (FID) signal. Subsequently, Fourier transform converts the current from time domain signal into a frequency domain spectrum and a mass spectrum can be produced algebraically from eq1.8. The whole procedure of ion excitation, image current detection and generation of mass spectrum by FT-ICR MS is shown in Figure 1.10.[117]

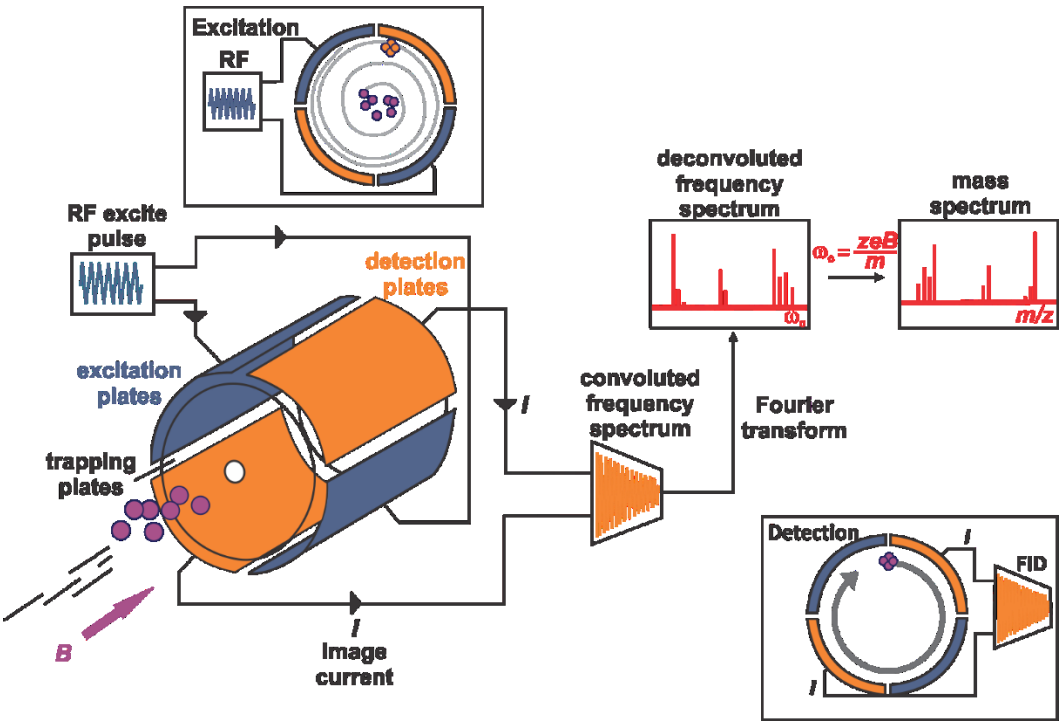

Figure 1.10. Principles of FTICR-MS illustrated in ion excitation, image current detection and generation of mass spectrum, adapted from reference 117.

1.3 ESI-MS Based Methods

1.3.1 Direct ESI-MS assay

The direct ESI-MS assay was used to detect protein-ligand interactions (including proteins, carbohydrates, lipids and small molecules) in aqueous solution and quantify their affinities.[118] This assay is based on the direct detection of free and ligand-bound protein ions by ESI-MS analysis. For a reversible interaction (eq1.9) between protein (P) with a single binding site and a monovalent ligand (L), the abundance (*Ab*) ratio (*R*) of the ligand-bound protein (PL) to free protein (P) ions measured by ESI-MS is taken to be equal to the equilibrium concentration ratio in the solution (as shown in eq1.10).

$$P + L \rightleftharpoons PL \qquad (1.9)$$

$$R = \frac{\sum Ab(\mathrm{PL})}{\sum Ab(\mathrm{P})} = \frac{[\mathrm{PL}]}{[\mathrm{P}]} \qquad (1.10)$$

The apparent association constant (K_a) can be calculated from eq1.11 the known initial concentrations of protein ($[P]_0$) and ligand ($[L]_0$) in solution and the relative abundance of the corresponding bound and unbound protein ions measured in the mass spectrum in the positive ion mode. Here, [P], [L] and [PL] are equilibrium concentrations of the protein, ligand and protein-ligand complex in solution, respectively.

$$K_a = \frac{[\mathrm{PL}]}{[\mathrm{P}][\mathrm{L}]} = \frac{R}{[\mathrm{L}]_0 - \frac{R}{1+R}[\mathrm{P}]_0} \qquad (1.11)$$

Normally, an accurate affinity (K_a) is determined by measurements performed from a titration experiments, where the initial concentration of protein ($[P]_0$) is kept constant and the initial concentration of ligand ($[L]_0$) is varied. In this cases, nonlinear regression analysis of the experimentally determined concentration-dependence of the fraction of ligand-bound protein, $[R/(R+1)]$, is used to determine K_a, eq1.12.[119]

$$\frac{R}{R+1} = \frac{1 + K_a[\mathrm{L}]_0 + K_a[\mathrm{P}]_0 - \sqrt{4K_a[\mathrm{L}]_0 + (1 - K_a[\mathrm{L}]_0 + K_a[\mathrm{P}]_0)^2}}{2K_a[\mathrm{P}]_0} \qquad (1.12)$$

Experimentally, the values of K_a that can be accurately determined with the direct ESI-MS assay range from ~ 10^2 to ~ 10^7 M^{-1}, which fits to investigate most protein-ligand interactions.

For a protein with multiple binding sites that can sequentially bind up to i ligand molecules, the abundance ratio (R_q) of ligand (L)-bound (q ligands) to free P (PL_q and P, respectively) ions measured by ESI-MS was taken to be equal to the equilibrium concentration ratio in solution, eq1.13.[26]

$$R_q = \frac{\sum Ab(\mathrm{PL_q})}{\sum Ab(\mathrm{P})} = \frac{[\mathrm{PL_q}]}{[\mathrm{P}]} \tag{1.13}$$

The apparent association constant ($K_{a,q}$) for the q^{th} ligand binding to the protein can be expressed in terms of R_q, R_{q-1}, the initial P ($[P]_0$) and ligand ($[L]_0$) concentrations, eq1.14.[26]

$$K_{a,q} = \frac{\frac{R_q}{R_{q-1}}}{([L]_0 - \frac{[P]_0 \sum_{q=1}^{h} qR_q}{1 + \sum_{q=1}^{h} R_q})} \tag{1.14}$$

In addition, a complete description of the data analysis method employed to calculate the intrinsic association constants ($K_{a,int}$) can be found elsewhere.[118,26] Assuming the protein has i independent and identical binding sites, $K_{a,int}$ can be expressed by eq1.15.[120]

$$K_{a,int} = \frac{1}{(\frac{1}{f} - 1)([L]_0 - i[P]_0 f)} \tag{1.15}$$

where $[P]_0$ and $[L]_0$ are the initial concentrations of the protein and ligand, respectively, and f is the fraction of occupied ligand binding sites, eq1.16.

$$f = \frac{\sum qR_q}{i(1 + \sum R_q)} \tag{1.16}$$

In the case of the protein possessing two equivalent binding sites, $K_{a,int}$ can be found using eq1.17:

$$K_{a,int} = \frac{R_1 + 2R_2}{(R_1 + 2)([L]_0 - \frac{[P]_0(R_1 + 2R_2)}{1 + R_1 + R_2})} \tag{1.17}$$

To correct the influence or contribution of the nonspecific interactions in ESI process, the most straightforward method is the reference protein approach,[121] which is applied in chapter 2 and chapter 3 for quantitatively and qualitatively nonspecific binding correction of protein-carbohydrate interactions. This approach involves the introduction of a proper reference protein (P_{ref}), which doesn't specifically bind to any of the target ligands, to the ESI solution. The

underlying assumption of the reference protein method is that the distribution on ligands bound nonspecifically to proteins and specific protein complexes is dependent on the number of free ligand molecules in the nanodroplets that produce gaseous ions and is not affected by the size and structure of the protein or protein complex.[121,122] The true abundance of q-ligand-bound to free protein ($Ab(PL_q)$) that doesn't involve nonspecific binding can be expressed from the apparent abundance of PL_q complexes ($Ab_{app}(PL_q)$) measured by ESI-MS and the distribution of nonspecific $P_{ref}L_q$ species using eq1.18:[121]

$$Ab(PL_q) = [Ab_{app}(PL_q) - f_{1,P_{ref}} Ab(PL_{q-1}) - \cdots - f_{q,P_{ref}} Ab(P)]/f_{0,P_{ref}} \qquad (1.18)$$

where $f_{q,Pref}$ is the fractional abundance of P_{ref} bound to q molecules of L. Remarkably, this reference protein method for correction of nonspecific binding has been successfully employed on binding measurements performed on many protein-ligand interactions, including protein-divalent metal ion, protein-carbohydrate and protein-amino acid complexes.[122-124]

1.3.2 *Proxy Ligand* ESI-MS assay

Although direct ESI-MS assay is capable of quantifying protein-ligand interactions (most protein-carbohydrate interactions), the application of direct ESI-MS assay is still limited in the case of protein (P) binding to the GL ligand (L) incorporated into MMs (such as ND and PD). Since the detected PL complexes containing GL originate from dissociation of the protein-GL-MM complexes in the gas phase, any differences in the ESI response factors for the bound and unbound protein ions will introduce errors into the affinity measurements.[125] Given these limitations, the indirect ESI-MS methods such as *proxy ligand* ESI-MS assays, which combine competitive ligand binding and direct ESI-MS analysis, have been applied to quantify the affinity of protein for MMs containing GL. This assay relies on a proxy ligand (L_{proxy}), which binds to target protein (P) with known affinity ($K_{a,proxy}$) and competes with the GL ligand (L).[125] For competitive binding, as P

binds to L, the concentration of free P in solution decreases and thus an increase in the concentration of PL_{proxy} complex relative to P. Consequently, the extent of PL binding can be deduced by monitoring the relative abundance of PL_{proxy} using ESI-MS measurements. In cases where target P possesses a single binding site, the relative equilibrium expressions are established as (eq1.19 and eq1.20):

$$K_a = \frac{[PL]}{[P][L]} = \frac{R}{[L]} \tag{1.19}$$

$$K_{a,proxy} = \frac{[PL_{proxy}]}{[P][L_{proxy}]} = \frac{R_{proxy}}{[L_{proxy}]} \tag{1.20}$$

where R is the concentration ratio of L-bound P to free P in solution (as shown in eq1.21). Meanwhile, R_{proxy} is corresponding to the abundance ratio of PL_{proxy} to free P ions, which is taken to be equal to the equilibrium concentration ratio in solution, eq1.22:

$$R = \frac{[PL]}{[P]} \tag{1.21}$$

$$R_{proxy} = \frac{\sum Ab(PL_{proxy})}{\sum Ab(P)} = \frac{[PL_{proxy}]}{[P]} \tag{1.22}$$

Accordingly, the association constant (K_a) for L binding to target P was calculated from the abundance ratio (R_{proxy}) measured with initial concentrations of P ($[P]_0$), L ($[L]_0$) and L_{proxy} ($[L_{proxy}]_0$). The expression is as follows eq1.23:

$$K_a = \frac{R}{[L]_0 - \frac{R}{1+R+R_{proxy}}[P]_0} = \frac{1}{\frac{[L]_0}{R} - \frac{[P]_0}{1+R_{proxy}+R}} \tag{1.23}$$

$$= \frac{1}{\left([L_{proxy}]_0 - \frac{R_{proxy}}{K_{a,proxy}}\right)\left(\frac{[L]_0}{R_{proxy}[P]_0 - (R_{proxy}+1)\left([L_{proxy}]_0 - \frac{R_{proxy}}{K_{a,proxy}}\right)} - \frac{1}{R_{proxy}}\right)}$$

Rearranging eq1.23 allows $[L]_0$ to be expressed as eq1.23. The K_a was determined by fitting eq1.24

to the experimentally measured R_{proxy} over a range of $[L]_0$.

$$[L]_0 = \left(\frac{R_{proxy}[P]_0}{[L_{proxy}]_0 - \frac{R_{proxy}}{K_{a,proxy}}} - R_{proxy} - 1 \right) \left(\frac{1}{K_a} + \frac{[L_{proxy}]_0}{R_{proxy}} - \frac{1}{K_{a,proxy}} \right) \quad (1.24)$$

1.3.3 Catch and Release (CaR)-ESI-MS assay

The CaR-ESI-MS assay was performed to screen libraries of ligands against a target protein to detect their specific interactions.[126] The "catch" step involves the transfer of free protein and ligand-bound protein into gas phase by ESI. The identity of ligand-bound protein complexes can be determined from molecular weight (MW) of protein-ligand complexes, in cases where they cannot be precisely determined by ESI-MS due to size or heterogeneity (i.e., antibodies and glycoproteins) of the protein or the size of the ligand. Ions corresponding to ligand-bound protein are isolated using the quadrupole mass filter. After that, the bound ligands are released from complexes by CID. The released ligand can be further determined based on the MW of the released ligands or in conjunction with IMS which is used to separate the isomeric ligands or another stage of CID for fragmentation pattern.

However, the CaR-ESI-MS assay combined with MMs can be implemented to screen the libraries of GLs against target protein to identify specific P-GL interactions.[44] Briefly, a mixture of GLs are incorporated into MMs and then incubated with target protein. The intact P-GL-MM complexes will be transferred into the gas phase by ESI and the P-GL complexes are spontaneously released from the MM ions in source for MS detection. The bound GL ligands can be released from the P-GL complexes by subjecting the complexes to CID, which facilitates to confirm the identity of GL ligands, and further analyzed by IMS and CID fragmentation.

1.4 The Present Work

The work described in this thesis focuses on the development and application of ESI-MS based techniques to study water-soluble protein interactions with carbohydrates or GLs in MM (e.g. NDs). In Chapter 2, binding properties and specificities of anti-GD2 antibodies were quantitatively investigated. Chapter 3 describes the development of a new membrane anchor-assisted CaR-ESI-MS assay for detecting low affinity interactions between GBPs and GSLs presented in NDs.

The goal of Chapter 2 was to implement an analytical method, based on native ESI-MS, to evaluate the glycan binding properties of a series of anti-GD2 monoclonal antibodies (mAbs) and their antigen binding fragments (Fabs). First, direct ESI-MS assay was employed to quantitatively evaluate the interactions between anti-GD2 antibodies and a library of fourteen ganglioside oligosaccharides. The CaR-ESI-MS assay, implemented with NDs to solubilize gangliosides, was used to screen mixtures of gangliosides against different types of anti-GD2 mAbs to detect specific interactions. Finally, the influence of ganglioside GD2 content on antibody-GD2 mAb and Fabs interactions was quantified by application of competitive binding ESI-MS assays combined with NDs.

In Chapter 3, we developed a new analytical method to tackle the challenge of detecting GBP interactions with low affinity GSL ligands. The basic idea is to covalently tether the GBP to GSL-containing MM by introducing a modified lipid (i.e., membrane anchor) to the MM. The resulting membrane anchor serves to enhance the local concentration of GBP on the surface of the membrane and enhance binding to GSL ligands. A notable feature of this membrane anchor approach is that it can be applied to any GBPs. To demonstrate the feasibility of the membrane anchor-assisted CaR-ESI-MS assay combined with MM to detect weak GBP-GSL interactions, three human galectins and their interactions with gangliosides presented in NDs are used. The

results were validated using binding data measured for the corresponding ganglioside oligosaccharides.

In Chapter 4, a summary of this thesis and some future work that should be carried out and preliminary data is presented.

1.5 References

(1) Fahy, E.; Subramaniam, S.; Brown, H. A.; Glass, C. K.; Merrill, A. H.; Murphy, R. C.; Raetz, C. R. H.; Russell, D. W.; Seyama, Y.; Shaw, W.; et al. A Comprehensive Classification System for Lipids. *J. Lipid Res.* **2005**, *46* (5), 839–862.

(2) van Meer, G.; Voelker, D. R.; Feigenson, G. W. Membrane Lipids: Where They Are and How They Behave. *Nat. Rev. Mol. Cell Biol.* **2008**, *9* (2), 112–124.

(3) Saliba, A.-E.; Vonkova, I.; Gavin, A.-C. The Systematic Analysis of Protein–lipid Interactions Comes of Age. *Nat. Rev. Mol. Cell Biol.* **2015**, *16* (12), 753–761.

(4) Merrill, A. H.; Wang, M. D.; Park, M.; Sullards, M. C. (Glyco)Sphingolipidology: An Amazing Challenge and Opportunity for Systems Biology. *Trends Biochem. Sci.* **2007**, *32* (10), 457–468.

(5) Lodish H, Berk A, Zipursky SL, et al. Biomembranes: Structural Organization and Basic Functions. Molecular Cell Biology. 4th edition. **2000**

(6) Dé Rick De Meyer, F.; Smit, B.; Klein, M. L. *Effect of Cholesterol on the Structure of a Phospholipid Bilayer*. **2009**, *10*.

(7) Lopez, P. H. H.; Schnaar, R. L. Determination of Glycolipid–Protein Interaction Specificity. **2006**, 205–220.

(8) LIPID MAPS Lipidomics Gateway http://www.lipidmaps.org.

(9) Cummings, R. D. The Repertoire of Glycan Determinants in the Human Glycome. *Mol. Biosyst.* **2009**, *5* (10), 1087.

(10) Alberts, B.; Johnson, A.; Lewis, J.; Raff, M.; Roberts, K.; Walter, P. *Molecular Biology of the Cell, 4th Edition. Garland Science: New York*. **2002**.

(11) Schulze, H.; Sandhoff, K. Sphingolipids and Lysosomal Pathologies. *Biochim. Biophys.*

Acta - Mol. Cell Biol. Lipids. **2014**, *1841* (5), 799–810.

(12) Malhotra, R. Membrane Glycolipids: Functional Heterogeneity: A Review. *Biochem. Anal. Biochem.* **2012**, *1* (2).

(13) Doronin, I. I.; Vishnyakova, P. A.; Kholodenko, I. V; Ponomarev, E. D.; Ryazantsev, D. Y.; Molotkovskaya, I. M.; Kholodenko, R. V. Ganglioside GD2 in Reception and Transduction of Cell Death Signal in Tumor Cells. *BMC Cancer.* **2014**, *14* (1), 295.

(14) Weis, W. I. Structural Basis of Lectin-Carbohydrate Recognition. *Annu. Rev. Biochem.* **1996**, *65* (1), 441–473.

(15) Dam, T. K.; Brewer, C. F. Effects of Clustered Epitopes in Multivalent Ligand−Receptor Interactions †. *Biochemistry.* **2008**, *47* (33), 8470–8476.

(16) Weis, W. I.; Drickamer, K. Structural basis of recognition lectin-carbohydrate. *Anna Rev Biochem*. **1996**, *65*.

(17) Zhang, T.; de Waard, A. A.; Wuhrer, M.; Spaapen, R. M. The Role of Glycosphingolipids in Immune Cell Functions. *Front. Immunol.* **2019**, *10* (1), 1–22.

(18) Larsen, K.; Thygesen, M. B.; Guillaumie, F.; Willats, W. G. T.; Jensen, K. J. Solid-Phase Chemical Tools for Glycobiology. *Carbohydr. Res.* **2006**, *341* (10), 1209–1234.

(19) Linman, M. J.; Taylor, J. D.; Yu, H.; Chen, X.; Cheng, Q. Surface Plasmon Resonance Study of Protein−Carbohydrate Interactions Using Biotinylated Sialosides. *Anal. Chem.* **2008**, *80* (11), 4007–4013.

(20) Smith, D. F.; Song, X.; Cummings, R. D. Use of Glycan Microarrays to Explore Specificity of Glycan-Binding Proteins. In *Methods in Enzymology*; Academic Press Inc. **2010**, *480*, 417–444.

(21) Grant, O. C.; Smith, H. M. K.; Firsova, D.; Fadda, E.; Woods, R. J. Presentation,

Presentation, Presentation! Molecular-Level Insight into Linker Effects on Glycan Array Screening Data. *Glycobiology.* **2014**, *24* (1), 17–25.

(22) Fais, M.; Karamanska, R.; Russell, D. A.; Field, R. A. Lectin and Carbohydrate Microarrays: New High-Throughput Methods for Glycoprotein, Carbohydrate-Binding Protein and Carbohydrate-Active Enzyme Analysis. *J. Cereal Sci.* **2009**, *50* (3), 306–311.

(23) Utsuno, K.; Uludağ, H. Thermodynamics of Polyethylenimine-DNA Binding and DNA Condensation. *Biophys. J.* **2010**, *99* (1), 201–207.

(24) Wilcox, D. E. Isothermal Titration Calorimetry of Metal Ions Binding to Proteins: An Overview of Recent Studies. *Inorganica Chim. Acta.* **2008**, *361* (4), 857–867.

(25) Ganem, B.; Li, Y. T.; Henion, J. D. Detection of Noncovalent Receptor-Ligand Complexes by Mass Spectrometry. *J. Am. Chem. Soc.* **1991**, *113* (16), 6294–6296.

(26) Kitova, E. N.; Kitov, P. I.; Paszkiewicz, E.; Kim, J.; Mulvey, G. L.; Armstrong, G. D.; Bundle, D. R.; Klassen, J. S. Affinities of Shiga Toxins 1 and 2 for Univalent and Oligovalent Pk-Trisaccharide Analogs Measured by Electrospray Ionization Mass Spectrometry. *Glycobiology.* **2007**, *17* (10), 1127–1137.

(27) Wang, W.; Kitova, E. N.; Klassen, J. S. Influence of Solution and Gas Phase Processes on Protein−Carbohydrate Binding Affinities Determined by Nanoelectrospray Fourier Transform Ion Cyclotron Resonance Mass Spectrometry. *Anal. Chem.* **2003**, *75* (19), 4945–4955.

(28) Kitova, E. N.; El-Hawiet, A.; Schnier, P. D.; Klassen, J. S. Reliable Determinations of Protein–Ligand Interactions by Direct ESI-MS Measurements. Are We There Yet? *J. Am. Soc. Mass Spectrom.* **2012**, *23* (3), 431–441.

(29) Song, X.; Lasanajak, Y.; Xia, B.; Heimburg-Molinaro, J.; Rhea, J. M.; Ju, H.; Zhao, C.;

Molinaro, R. J.; Cummings, R. D.; Smith, D. F. Shotgun Glycomics: A Microarray Strategy for Functional Glycomics. *Nat. Methods.* **2011**, *8* (1), 85–90.

(30) Suetake, K.; Yu, R. K. Thin-Layer Chromatography; Immunostaining of Glycolipid Antigens; and Interpretation of False-Positive Findings with Acidic Lipids. *Methods in Enzymology*. **2003**, 363, 312–319.

(31) Bolla, J. R.; Agasid, M. T.; Mehmood, S.; Robinson, C. V. Membrane Protein–Lipid Interactions Probed Using Mass Spectrometry. *Annu. Rev. Biochem.* **2019**, *88* (1), 85–111.

(32) Nath, A.; Atkins, W. M.; Sligar, S. G. Applications of Phospholipid Bilayer Nanodiscs in the Study of Membranes and Membrane Proteins †. *Biochemistry.* **2007**, *46* (8), 2059–2069.

(33) Bayburt, T. H.; Sligar, S. G. Membrane Protein Assembly into Nanodiscs. *FEBS Lett.* **2010**, *584* (9), 1721–1727.

(34) Popovic, K.; Holyoake, J.; Pomes, R.; Prive, G. G. Structure of Saposin A Lipoprotein Discs. *Proc. Natl. Acad. Sci.* **2012**, *109* (8), 2908–2912.

(35) Sanghera, N.; Correia, B. E. F. S.; Correia, J. R. S.; Ludwig, C.; Agarwal, S.; Nakamura, H. K.; Kuwata, K.; Samain, E.; Gill, A. C.; Bonev, B. B.; et al. Deciphering the Molecular Details for the Binding of the Prion Protein to Main Ganglioside GM1 of Neuronal Membranes. *Chem. Biol.* **2011**, *18* (11), 1422–1431.

(36) Shi, J.; Yang, T.; Kataoka, S.; Zhang, Y.; Diaz, A. J.; Cremer, P. S. GM 1 Clustering Inhibits Cholera Toxin Binding in Supported Phospholipid Membranes. *J. Am. Chem. Soc.* **2007**, *129* (18), 5954–5961.

(37) Borch, J.; Torta, F.; Sligar, S. G.; Roepstorff, P. Nanodiscs for Immobilization of Lipid Bilayers and Membrane Receptors: Kinetic Analysis of Cholera Toxin Binding to a Glycolipid Receptor. *Anal. Chem.* **2008**, *80* (16), 6245–6252.

(38) Chen, W. C.; Kawasaki, N.; Nycholat, C. M.; Han, S.; Pilotte, J.; Crocker, P. R.; Paulson, J. C. Antigen Delivery to Macrophages Using Liposomal Nanoparticles Targeting Sialoadhesin/CD169. *PLoS One.* **2012**, *7* (6), e39039.

(39) Krishnan, P.; Singla, A.; Lee, C.; Weatherston, J. D.; Worstell, N. C.; Wu, H. Colloids and Surfaces B : Biointerfaces Hetero-Multivalent Binding of Cholera Toxin Subunit B with Glycolipid Mixtures. **2017**, *160*, 281–288.

(40) Sherry, L. J.; Chang, S.; Schatz, G. C.; Van Duyne, R. P.; Wiley, B. J.; Xia, Y. Localized Surface Plasmon Resonance Spectroscopy of Single Silver Nanocubes. *Nano Lett.* **2005**, *5* (10), 2034–2038.

(41) Han, L.; Morales, L. C.; Richards, M. R.; Kitova, E. N.; Sipione, S.; Klassen, J. S. Investigating the Influence of Membrane Composition on Protein–Glycolipid Binding Using Nanodiscs and Proxy Ligand Electrospray Ionization Mass Spectrometry. *Anal. Chem.* **2017**, *89* (17), 9330–9338.

(42) Han, L.; Kitova, E. N.; Li, J.; Nikjah, S.; Lin, H.; Pluvinage, B.; Boraston, A. B.; Klassen, J. S. Protein–Glycolipid Interactions Studied in Vitro Using ESI-MS and Nanodiscs: Insights into the Mechanisms and Energetics of Binding. *Anal. Chem.* **2015**, *87* (9), 4888–4896.

(43) Leney, A. C.; Fan, X.; Kitova, E. N.; Klassen, J. S. Nanodiscs and Electrospray Ionization Mass Spectrometry: A Tool for Screening Glycolipids Against Proteins. *Anal. Chem.* **2014**, *86* (11), 5271–5277.

(44) Li, J.; Fan, X.; Kitova, E. N.; Zou, C.; Cairo, C. W.; Eugenio, L.; Ng, K. K. S.; Xiong, Z. J.; Privé, G. G.; Klassen, J. S. Screening Glycolipids Against Proteins in Vitro Using Picodiscs and Catch-and-Release Electrospray Ionization-Mass Spectrometry. *Anal. Chem.* **2016**, *88*

(9), 4742–4750.

(45) Dole, M.; Mack, L. L.; Hines, R. L.; Mobley, R. C.; Ferguson, L. D.; Alice, M. B. Molecular Beams of Macroions. *J. Chem. Phys.* **1968**, *49* (5), 2240–2249.

(46) Yamashita1', M.; Fenn, J. B. Negative Ion Production with the Electrospray Ion Source. *J. Phys. Chem.* **1984**, *88*, 4671-4675.

(47) Fenn, J. B. Electrospray Wings for Molecular Elephants (Nobel Lecture). *Angew. Chemie Int. Ed.* **2003**, *42* (33), 3871–3894.

(48) Sarkar, P. K.; Prajapati, P. K.; Shukla, V. J.; Ravishankar, B.; Choudhary, A. K. Toxicity and Recovery Studies of Two Ayurvedic Preparations of Iron. *Indian J. Exp. Biol.* **2009**, *47* (12), 987–992.

(49) Covey, T. R.; Thomson, B. A.; Schneider, B. B. Atmospheric Pressure Ion Sources. *Mass Spectrom. Rev.* **2009**, *28* (6), 870–897.

(50) Kebarle, P.; Tang, L. From Ions in Solution to Ions in the Gas Phase - the Mechanism of Electrospray Mass Spectrometry. *Anal. Chem.* **1993**, *65* (22), 972A–986A.

(51) Kebarle, P. A Brief Overview of the Present Status of the Mechanisms Involved in Electrospray Mass Spectrometry. *J. Mass Spectrom.* **2000**, *35* (7), 804–817.

(52) Kebarle, P.; Verkerk, U. H. Electrospray: From Ions in Solution to Ions in the Gas Phase, What We Know Now. *Mass Spectrom. Rev.* **2009**, *28* (6), 898–917.

(53) De La Mora, J. F.; Loscertales, I. G. The Current Emitted by Highly Conducting Taylor Cones. *J. Fluid Mech.* **1994**, *260*, 155–184.

(54) Fernandez de la Mora, J. Electrospray Ionization of Large Multiply Charged Species Proceeds via Dole's Charged Residue Mechanism. *Anal. Chim. Acta.* **2000**, *406* (1), 93–104.

(55) Wu, X.; Oleschuk, R. D.; Cann, N. M. Characterization of Microstructured Fibre Emitters:

In Pursuit of Improved Nano Electrospray Ionization Performance. *Analyst* **2012**, *137* (18), 4150.

(56) Benesch, J. L. P.; Ruotolo, B. T.; Simmons, D. A.; Robinson, C. V. Protein Complexes in the Gas Phase: Technology for Structural Genomics and Proteomics. *Chem. Rev.* **2007**, *107* (8), 3544–3567.

(57) Rayleigh, Lord. XX. On the Equilibrium of Liquid Conducting Masses Charged with Electricity. *London, Edinburgh, Dublin Philos. Mag. J. Sci.* **1882**, *14* (87), 184–186.

(58) Fernandez de la Mora, J. Electrospray Ionization of Large Multiply Charged Species Proceeds via Dole's Charged Residue Mechanism. *Anal. Chim. Acta.* **2000**, *406* (1), 93–104.

(59) Gomez, A.; Tang, K. Charge and Fission of Droplets in Electrostatic Sprays. *Phys. Fluids.* **1994**, *6* (1), 404–414.

(60) Kebarle, P.; Peschke, M. On the Mechanisms by Which the Charged Droplets Produced by Electrospray Lead to Gas Phase Ions. *Anal. Chim. Acta.* **2000**, *406* (1), 11–35.

(61) Iribarne, J. V. On the Evaporation of Small Ions from Charged Droplets. *J. Chem. Phys.* **1976**, *64* (6), 2287.

(62) Thomson, B. A.; Iribarne, J. V. Field Induced Ion Evaporation from Liquid Surfaces at Atmospheric Pressure. *J. Chem. Phys.* **1979**, *71* (11), 4451–4463.

(63) Konermann, L.; Ahadi, E.; Rodriguez, A. D.; Vahidi, S. Unraveling the Mechanism of Electrospray Ionization. *Anal. Chem.* **2013**, *85* (1), 2–9.

(64) Iavarone, A. T.; Williams, E. R. Mechanism of Charging and Supercharging Molecules in Electrospray Ionization. *J. Am. Chem. Soc.* **2003**, *125* (8), 2319–2327.

(65) Peschke, M.; Verkerk, U. H.; Kebarle, P. Features of the ESI Mechanism That Affect the Observation of Multiply Charged Noncovalent Protein Complexes and the Determination

of the Association Constant by the Titration Method. *J. Am. Soc. Mass Spectrom.* **2004**, *15* (10), 1424–1434.

(66) Metwally, H.; Duez, Q.; Konermann, L. Chain Ejection Model for Electrospray Ionization of Unfolded Proteins: Evidence from Atomistic Simulations and Ion Mobility Spectrometry. *Anal. Chem.* **2018**, *90* (16), 10069–10077.

(67) Konermann, L.; Rodriguez, A. D.; Liu, J. On the Formation of Highly Charged Gaseous Ions from Unfolded Proteins by Electrospray Ionization. *Anal. Chem.* **2012**, *84* (15), 6798–6804.

(68) Ahadi, E.; Konermann, L. Modeling the Behavior of Coarse-Grained Polymer Chains in Charged Water Droplets: Implications for the Mechanism of Electrospray Ionization. *J. Phys. Chem. B.* **2012**, *116* (1), 104–112.

(69) Nohmi, T.; Fenn, J. B. Electrospray Mass Spectrometry of Poly(Ethylene Glycols) with Molecular Weights up to Five Million. *J. Am. Chem. Soc.* **1992**, *114* (9), 3241–3246.

(70) Fenn, J. B. Ion Formation from Charged Droplets: Roles of Geometry, Energy, and Time. *J. Am. Soc. Mass Spectrom.* **1993**, *4* (7), 524–535.

(71) Wilm, M. S.; Mann, M. Electrospray and Taylor-Cone Theory, Dole's Beam of Macromolecules at Last? *Int. J. Mass Spectrom. Ion Process.* **1994**, *136* (2–3), 167–180.

(72) Wilm, M.; Mann, M. Analytical Properties of the Nanoelectrospray Ion Source. *Anal. Chem.* **1996**, *68* (1), 1–8.

(73) Karas, R. M.; Bahr, U.; Dülcks, T. Nano-Electrospray Ionization Mass Spectrometry: Addressing Analytical Problems beyond Routine. *Fresenius' J. Anal. Chem.* **2000**, *366* (6), 669-676.

(74) El-Faramawy, A.; Siu, K. W. M.; Thomson, B. A. Efficiency of Nano-Electrospray

Ionization. *J. Am. Soc. Mass Spectrom.* **2005**, *16* (10), 1702–1707.

(75) Juraschek, R.; Dülcks, T.; Karas, M. Nanoelectrospray—More than Just a Minimized-Flow Electrospray Ionization Source. *J. Am. Soc. Mass Spectrom.* **1999**, *10* (4), 300–308.

(76) Jecklin, M. C.; Touboul, D.; Bovet, C.; Wortmann, A.; Zenobi, R. Which Electrospray-Based Ionization Method Best Reflects Protein-Ligand Interactions Found in Solution? A Comparison of ESI, NanoESI, and ESSI for the Determination of Dissociation Constants with Mass Spectrometry. *J. Am. Soc. Mass Spectrom.* **2008**, *19* (3), 332–343.

(77) Karas, M.; Bachmann, D.; Hillenkamp, F. Influence of the Wavelength in High-Irradiance Ultraviolet Laser Desorption Mass Spectrometry of Organic Molecules. *Anal. Chem.* **1985**, *57* (14), 2935–2939.

(78) Karas, M.; Bachmann, D.; Bahr, U.; Hillenkamp, F. Matrix-Assisted Ultraviolet Laser Desorption of Non-Volatile Compounds. *Int. J. Mass Spectrom. Ion Process.* **1987**, *78* (C), 53–68.

(79) Hillenkamp, F.; Karas, M.; Ronald, G.; Beavis1, C.; Chait, B. T. Matrix-Assisted Laser Desorption/Ionization Mass Spectrometry of Biopolymers. *Anal. Chem.* **1991**, *63* (24), 1193A-1203A.

(80) Karas, M.; Hillenkamp, F. Laser Desorption Ionization of Proteins with Molecular Masses Exceeding 10,000 Daltons. *Anal. Chem.* **1988**, *60* (20), 2299–2301.

(81) Karas, M.; Krüger, R. Ion Formation in MALDI: The Cluster Ionization Mechanism. *Chem. Rev.* **2003**, *103* (2), 427–440.

(82) Liang, C. W.; Lee, C. H.; Lin, Y.-J.; Lee, Y. T.; Ni, C. K. MALDI Mechanism of Dihydroxybenzoic Acid Isomers: Desorption of Neutral Matrix and Analyte. *J. Phys. Chem. B.* **2013**, *117* (17), 5058–5064.

(83) Trimpin, S.; Wang, B.; Inutan, E. D.; Li, J.; Lietz, C. B.; Harron, A.; Pagnotti, V. S.; Sardelis, D.; McEwen, C. N. A Mechanism for Ionization of Nonvolatile Compounds in Mass Spectrometry: Considerations from MALDI and Inlet Ionization. *J. Am. Soc. Mass Spectrom.* **2012**, *23* (10), 1644–1660.

(84) Singhal, N.; Kumar, M.; Kanaujia, P. K.; Virdi, J. S. MALDI-TOF Mass Spectrometry: An Emerging Technology for Microbial Identification and Diagnosis. *Front. Microbiol.* **2015**, *6* (8), 791.

(85) Trimpin, S.; Inutan, E. D.; Herath, T. N.; McEwen, C. N. Laserspray Ionization, a New Atmospheric Pressure MALDI Method for Producing Highly Charged Gas-Phase Ions of Peptides and Proteins Directly from Solid Solutions. *Mol. Cell. Proteomics.* **2010**, *9* (2), 362–367.

(86) Knochenmuss, R. Ion Formation Mechanisms in UV-MALDI. *Analyst.* **2006**, *131* (9), 966.

(87) University of Bristol, School of Chemistry Mass Spectrometry Facility, MALDI.

(88) Karas, M.; Bahr, U.; Ingendoh, A.; Nordhoff, E.; Stahl, B.; Strupat, K.; Hillenkamp, F. Principles and Applications of Matrix-Assisted UV-Laser Desorption/Ionization Mass Spectrometry. *Anal. Chim. Acta.* **1990**, *241* (2), 175–185.

(89) Suzuki, Y. Adjustment of Matrix-Assisted Laser Desorption/Ionization for Glycolipids. *J. Anal. Bioanal. Tech.* **2015**, *6* (5).

(90) Penn, S.; Cancilla, M.; Green, M.; Lebrilla, C. Direct Comparison of Matrix-Assisted Laser Desorption/Ionisation and Electrospray Ionisation in the Analysis of Gangliosides by Fourier Transform Mass Spectrometry. *Eur. J. Mass Spectrom.* **1997**, *3* (1), 67.

(91) Jessome, L.; Hsu, N.-Y.; Wang, Y.-S.; Chen, C.-H. Matrix-Assisted Laser Desorption/Ionization Mechanism Study with Dihydroxybenzoic Acid Isomers as Matrices.

Rapid Commun. Mass Spectrom. **2008**, *22* (2), 130–134.

(92) Matta, A.; Ralhan, R.; DeSouza, L. V.; Siu, K. W. M. Mass Spectrometry-Based Clinical Proteomics: Head-and-Neck Cancer Biomarkers and Drug-Targets Discovery. *Mass Spectrom. Rev.* **2010**, *29* (6), 945–961.

(93) Kero, F. A.; Pedder, R. E.; Yost, R. A. Quadrupole Mass Analyzers: Theoretical and Practical Considerations. *Encyclopedia of Genetics, Genomics, Proteomics and Bioinformatics*. John Wiley & Sons, Ltd: Chichester, **2005**.

(94) Miller, P. E.; Denton, M. B. The Quadrupole Mass Filter: Basic Operating Concepts. *J. Chem. Educ.* **1986**, *63* (7), 617.

(95) Gross, J. H. *Mass Spectrometry A Textbook, Third Edition. Springer International Publishing*. **2017**.

(96) Pedder, R. E. Practical Quadrupole Characteristics Theory : Quadrupole Acceptance Characteristics. *Ardara Technol. Tech. Note.* **2009**, *412*, 1–5.

(97) Pringle, S. D.; Giles, K.; Wildgoose, J. L.; Williams, J. P.; Slade, S. E.; Thalassinos, K.; Bateman, R. H.; Bowers, M. T.; Scrivens, J. H. An Investigation of the Mobility Separation of Some Peptide and Protein Ions Using a New Hybrid Quadrupole/Travelling Wave IMS/Oa-ToF Instrument. *Int. J. Mass Spectrom.* **2007**, *261* (1), 1–12.

(98) Giles, K.; Pringle, S. D.; Worthington, K. R.; Little, D.; Wildgoose, J. L.; Bateman, R. H. Applications of a Travelling Wave-Based Radio-Frequency-Only Stacked Ring Ion Guide. *Rapid Commun. Mass Spectrom.* **2004**, *18* (20), 2401–2414.

(99) Creaser, C. S.; Griffiths, J. R.; Bramwell, C. J.; Noreen, S.; Hill, C. A.; Thomas, C. L. P. Ion Mobility Spectrometry: A Review. Part 1. Structural Analysis by Mobility Measurement. *Analyst.* **2004**, *129* (11), 984.

(100) Karasek, F. W. Plasma Chromatography. *Anal. Chem.* **1974**, *46* (8), 710A–720a.

(101) Giles, K.; Williams, J. P.; Campuzano, I. Enhancements in Travelling Wave Ion Mobility Resolution. *Rapid Commun. Mass Spectrom.* **2011**, *25* (11), 1559–1566.

(102) Shukla, A. K.; Futrell, J. H. Tandem Mass Spectrometry: Dissociation of Ions by Collisional Activation. *J. Mass Spectrom.* **2000**, *35* (9), 1069–1090.

(103) Mcluckey, S. A. Principles of Collisional Activation in Analytical Mass Spectrometry. *J. Am. Soc. Mass Spectrom.* **1992**, *3* (6), 599-614.

(104) Wyttenbach, T.; Bowers, M. T. Intermolecular Interactions in Biomolecular Systems Examined by Mass Spectrometry. *Annu. Rev. Phys. Chem.* **2007**, *58* (1), 511–533.

(105) Rezaei Darestani, R.; Winter, P.; Kitova, E. N.; Tuszynski, J. A.; Klassen, J. S. Screening Anti-Cancer Drugs against Tubulin Using Catch-and-Release Electrospray Ionization Mass Spectrometry. *J. Am. Soc. Mass Spectrom.* **2016**, *27* (5), 876–885.

(106) Benesch, J. L. P.; Aquilina, J. A.; Ruotolo, B. T.; Sobott, F.; Robinson, C. V. Tandem Mass Spectrometry Reveals the Quaternary Organization of Macromolecular Assemblies. *Chem. Biol.* **2006**, *13* (6), 597–605.

(107) Guilhaus, M.; Selby, D.; Mlynski, V. Orthogonal Acceleration Time-of-Flight Mass Spectrometry. *Mass Spectrom. Rev.* **2000**, *19* (2), 65–107.

(108) Burlingame, A. L.; Whitney, J. O.; Russell, D. H. Mass Spectrometry. *Anal. Chem.* **1984**, *56* (5), 417–467.

(109) Mamyrin, B. A. Time-of-Flight Mass Spectrometry (Concepts, Achievements, and Prospects). *Int. J. Mass Spectrom.* **2001**, *206* (3), 251–266.

(110) Hardman, M.; Makarov, A. A. Interfacing the Orbitrap Mass Analyzer to an Electrospray Ion Source. *Anal. Chem.* **2003**, *75* (7), 1699–1705.

(111) Makarov, A. Electrostatic Axially Harmonic Orbital Trapping: A High-Performance Technique of Mass Analysis. *Anal. Chem.* **2000**, *72* (6), 1156–1162.

(112) Scigelova, M.; Makarov, A. Orbitrap Mass Analyzer – Overview and Applications in Proteomics. *Proteomics* **2006**, *6* (S2), 16–21.

(113) Marshall, A. G.; Hendrickson, C. L. Fourier Transform Ion Cyclotron Resonance Detection: Principles and Experimental Configurations. *Int. J. Mass Spectrom.* **2002**, *215* (1–3), 59–75.

(114) Marshall, A. G.; Hendrickson, C. L.; Jackson, G. S. Fourier Transform Ion Cyclotron Resonance Mass Spectrometry: A Primer. *Mass Spectrom. Rev.* **1998**, *17* (1), 1–35.

(115) Marshall, A. G. Fourier Transform Mass Spectrometry. *Spectrosc. Biomed. Sci.* **2018**, 87–105.

(116) Marshall, A. G.; Grosshans, P. B. Fourier Transform Ion Cyclotron Resonance Mass Spectrometry: The Teenage Years. *Anal. Chem.* **1991**, *63* (4), 215A–229A.

(117) Johnson Lab. Fourier Trans Form Ion Cyclotron Resonance Mass Spectrometry.

(118) Kitova, E. N.; El-Hawiet, A.; Schnier, P. D.; Klassen, J. S. Reliable Determinations of Protein–Ligand Interactions by Direct ESI-MS Measurements. Are We There Yet? *J. Am. Soc. Mass Spectrom.* **2012**, *23* (3), 431–441.

(119) Sun, J.; Kitova, E. N.; Klassen, J. S. Method for Stabilizing Protein−Ligand Complexes in Nanoelectrospray Ionization Mass Spectrometry. *Anal. Chem.* **2007**, *79* (2), 416–425.

(120) Han, L.; Tan, M.; Xia, M.; Kitova, E. N.; Jiang, X.; Klassen, J. S. Gangliosides Are Ligands for Human Noroviruses. *J. Am. Chem. Soc.* **2014**, *136* (36), 12631–12637.

(121) Sun, J.; Kitova, E. N.; Wang, W.; Klassen, J. S. Method for Distinguishing Specific from Nonspecific Protein−Ligand Complexes in Nanoelectrospray Ionization Mass Spectrometry.

Anal. Chem. **2006**, *78* (9), 3010–3018.

(122) Sun, N.; Soya, N.; Kitova, E. N.; Klassen, J. S. Nonspecific Interactions between Proteins and Charged Biomolecules in Electrospray Ionization Mass Spectrometry. *J. Am. Soc. Mass Spectrom.* **2010**, *21* (3), 472–481.

(123) Rademacher, C.; Shoemaker, G. K.; Kim, H.-S.; Zheng, R. B.; Taha, H.; Liu, C.; Nacario, R. C.; Schriemer, D. C.; Klassen, J. S.; Peters, T.; et al. Ligand Specificity of CS-35, a Monoclonal Antibody That Recognizes Mycobacterial Lipoarabinomannan: A Model System for Oligofuranoside−Protein Recognition. *J. Am. Chem. Soc.* **2007**, *129* (34), 10489–10502.

(124) Deng, L.; Sun, N.; Kitova, E. N.; Klassen, J. S. Direct Quantification of Protein−Metal Ion Affinities by Electrospray Ionization Mass Spectrometry. *Anal. Chem.* **2010**, *82* (6), 2170–2174.

(125) Han, L.; Kitova, E. N.; Li, J.; Nikjah, S.; Lin, H.; Pluvinage, B.; Boraston, A. B.; Klassen, J. S. Protein–Glycolipid Interactions Studied in Vitro Using ESI-MS and Nanodiscs: Insights into the Mechanisms and Energetics of Binding. *Anal. Chem.* **2015**, *87* (9), 4888–4896.

(126) El-Hawiet, A.; Kitova, E. N.; Klassen, J. S. Quantifying Protein Interactions with Isomeric Carbohydrate Ligands Using a Catch and Release Electrospray Ionization-Mass Spectrometry Assay. *Anal. Chem.* **2013**, *85* (16), 7637–7644.

Chapter 2

Glycan Binding Properties of Anti-GD2 Antibodies Studied by Electrospray Ionization Mass Spectrometry

2.1 Introduction

Gangliosides, which are sialic acid-containing glycosphingolipids (GSLs), are promising targets for cancer immunotherapy.[1] They not only play important roles in many normal physiological processes, such as cell growth, differentiation as well as cell adhesion and recognition, but also in pathological events like cellular malignancy and metastasis.[2,3] Altered glycosylation is a hallmark of cancer and many gangliosides, including GM1, GM2, GM3, GD2 and GD3, are overexpressed in the plasma membrane of tumor cells of neuroectodermal origin such as neuroblastomas (NBs).[4] The disialoganglioside GD2 is particularly attractive as a target antigen for anti-tumor immunotherapy of NBs because it is the most highly expressed ganglioside on the cell surface of almost all types of the primary neuroblastomas but has low expression levels in normal cells (1 - 2% of total ganglioside content).[5-7] Moreover, anti-GD2 antibodies have been shown to interfere with proliferation and invasiveness, as well as to directly induce apoptosis of tumour cells.[8]

A variety of anti-GD2 antibodies have been developed and undergone clinical trials for the treatment of NBs. These include the mouse immunoglobulin G3 (IgG3) antibody 3F8 (m3F8) and its humanized version (hu3F8), and the mouse immunoglobulin G2a (IgG2a) antibody 14G2a and its chimeric (ch14.18) or humanized forms (hu14.18).[9-11] Of these, ch14.18 (Dinutuximab, United Therapeutics), a human-mouse chimeric monoclonal antibody, received Food and Drug Administration (FDA) approved in 2015 for the treatment of pediatric NB patients.[12] The administration of anti-GD2 monoclonal antibodies (mAbs) to NB patients with GD2 expressing

neuroblastoma have yielded promising outcomes when compared to standard therapies, such as chemotherapy and radiotherapy.[13] Despite the promising anti-tumour activity of anti-GD2 mAbs, there have been no systematic investigations into their ganglioside binding properties or their cross-reactivity with other classes of human glycans.

In previous study, Gildersleeve and coworkers have used glycan microarrays, which has sufficient throughput screening approach, to evaluate specificity of therapeutic anti-GD2 antibodies (such as ch14.18, hu3F8 and ch3F8) as well as apparent K_d values for carbohydrate-antibody interactions.[14] The results reveal that these antibodies are remarkably high selectivity for GD2 on the glycan microarray. Only GT2 and GQ2 have measurable levels of interaction with these antibodies, with > 250-fold reduced affinity compared with GD2. However, no other glycans demonstrated significant binding levels (at least 1000-fold reduced affinities for GD2). Cheung and coworkers evaluated the binding kinetics of m3F8, ch3F8, hu3F8 and 14G2a by surface plasmon resonance (SPR) and further investigated the cross-reactivity with other gangliosides (GM2, GD1a, GD1b, GT1b, GD3 and GQ1b) by enzyme-linked immunosorbent assay (ELISA).[15,16] The SPR binding data showed that hu3F8 and ch3F8 had comparable affinities (K_d = 11 nM and K_d = 13 nM, respectively) as m3F8 for GD2 (K_d = 5 nM) and better affinities than 14G2a (K_d = 77 nM). In their cross-reactivity studies, hu3F8 had similar profile as ch3F8 and m3F8. There was low level of cross-reactivity with GD1b relative to GD2, while no cross-reactivity of 14G2a with other gangliosides was observed. To some degree, these surface-based techniques have advanced current understanding of antibody-ganglioside recognition. However, immobilization of gangliosides on a surface may create some potential problems, since the presentation of gangliosides is significantly different from that in the native lipid environment of cell membranes. The ganglioside density and the lack of fluidity of the gangliosides may affect the

binding.[17] Moreover, due to the extremely limited availability of purified GSLs (only twenty purified GSLs are commercially available), the abilities of anti-GD2 antibodies to bind to other gangliosides has not been comprehensively analyzed.

The goal of the present study was to investigate the glycan binding properties of a series of anti-GD2 mAbs and their antigen binding fragments (Fabs) - hu3F8 and its double mutant E1K/D32H (E1K: (L-FR1) and D32H: (L-CDR1)), and 14G2a mAb. We employed electrospray ionization-mass spectrometry (ESI-MS) to quantitatively evaluate the interactions between the anti-GD2 antibodies and fourteen ganglioside oligosaccharides. Using the catch-and-release (CaR) ESI-MS assay and nanodiscs (NDs), the antibodies were screened against libraries of gangliosides. Finally, affinities of the hu3F8 and its double mutant E1K/D32H Fabs and the 14G2a mAb for GD2 incorporated into a nanodisc (ND) were measured using competitive ligand binding ESI-MS assays.

2.2 Experimental Section

2.2.1 Proteins

The mouse monoclonal anti-GD2 antibody (clone 14G2a mAb, MW 149 251 Da) was purchased from Millipore Canada Ltd. (Etobicoke, Canada). The humanized 3F8 wild type (hu3F8) and its double mutant 3F8 E1K/D32 (hu3F8 E1K/D32H) mAbs were a gift from Prof. Nai-Kong Cheung (Memorial Sloan Kettering Cancer Centre, New York, NY). The Fab fragments for hu3F8 (MW 46 392 Da) and hu3F8 E1K/D32H (MW 47 190 Da) were a gift from Prof. Kenneth K.S. Ng (University of Calgary, Calgary, Alberta). The single chain variable fragment (scFv, MW 26 537 Da) of the monoclonal antibody (mAb) Se155-4 were expressed in Escherichia coli and purified as described previously.[1] Eqyine heart cytochrome c (cytoc, MW 12 384 Da) was purchased from Sigma-Aldrich Canada (Oakville, Canada). The P dimer of the Saga strain (GII.4 genotype, MW:

69 734 Da) was produced from the P domain of human noroviruse (huNoV) Saga.[18] The scFv, cytoc and huNoV Saga P dimer were used as reference protein (P_{ref}) for the binding measurements. The recombinant membrane scaffold protein (MSP) MSP1E1 (MW 27 494 Da) used for the ND preparation was expressed from the plasmid pMSP1E1 (Addgene, Cambridge, MA) and purified using a reported protocol.[2] Human carbonic anhydrase (hCA, type 1, MW 28 848 Da) was purchased from Sigma-Aldrich Canada (Oakville, Canada). Stock solutions of all proteins except MSP1E1 were dialyzed into an aqueous 200 mM ammonium acetate solution (pH 6.8) using Amicon 0.5 mL microconcentrator (EMD Millipore, Billerica, MA) with a MW cutoff of 3 kDa (cytoc) or 10 kDa (hu3F8 Fab, hu3F8 E1K/D32H Fab, scFv, huNoV Saga P dimer and hCA) or 30 kDa (14G2a, hu3F8 and hu3F8 E1K/D32H mAbs) and stored at -80 °C until used. The concentrations of the protein stock solutions were estimated by UV absorption at 280 nm.

2.2.2 Lipids and Glycolipids

The gangliosides β-D-Gal-(1 → 3)-β-D-GalNAc-(1 → 4)-[α-D-Neu5Ac-(2 → 3)]-β-D-Gal-(1 → 4)-D-Glc-ceramide (GM1, major isoforms d18:1−18:0 and d20:1−18:0 have MWs 1545.8 Da, 1573.9 Da), β-D-GalNAc-(1 → 4)-[α-D-Neu5Ac-(2 → 3)]-β-D-Gal-(1 → 4)-D-Glc-ceramide (GM2, major isoforms d18:1−18:0 and d20:1−18:0 have MWs 1383.7 Da, 1411.7 Da) and α-D-Neu5Ac-(2 → 3)-β-D-Gal-(1 → 4)-D-Glc-ceramide (GM3, major isoforms d18:1−18:0 and d20:1−18:0 have MWs 1180.5 Da, 1208.5 Da) were purchased from Cedarlane Laboratories (Burlington, Canada); α-D-Neu5Ac-(2 → 3)-β-D-Gal-(1 → 3)-β-D-GalNAc-(1 → 4)-[α-D-Neu5Ac-(2 → 3)]-β-D-Gal-(1 → 4)-D-Glc-ceramide (GD1a, major isoforms d18:1−18:0 and d20:1−18:0 have MWs 1836.1 Da, 1864.1 Da), β-D-Gal-(1 → 3)-β-D-GalNAc-(1 → 4)-[α-D-Neu5Ac-(2 → 8)-α-D-Neu5Ac-(2 → 3)]-β-D-Gal-(1 → 4)-D-Glc-ceramide (GD1b, major isoforms d18:1−18:0 and d20:1−18:0 have MWs 1836.1 Da, 1864.1 Da), α-D-Neu5Ac-(2−3)-β-

D-Gal-(1−3)-β-D-Gal-NAc-(1−4)-[α-D-Neu5Ac-(2−8)-α-D-Neu5Ac-(2−3)]-β-D-Gal-(1−4)-D-Glc-ceramide (GT1b, major isoforms d18:1−18:0 and d20:1−18:0 have MWs 2126.4 Da, 2154.4 Da) were purchased from Sigma-Aldrich Canada (Oakville, Canada), and β-D-GalNAc-(1 → 4)-[α-D-Neu5Ac-(2 → 8)-α-D-Neu5Ac-(2 → 3)]-β-D-Gal-(1 → 4)-D-Glc-ceramide (GD2, major isoforms d18:1−18:0 and d20:1−18:0 have MWs 1674.0 Da, 1702.0 Da), α-D-Neu5Ac-(2 → 3)-β-D-Gal-ceramide (GM4), α-L-Fuc-(1 → 2)-β-D-Gal-(1 → 3)-β-D-GalNAc-(1 → 4)-[α-D-Neu5Ac-(2 → 3)]-β-D-Gal-(1 → 4)-D-Glc-ceramide (fucosyl GM1), α-D-Neu5Ac-(2 → 8)-α-D-Neu5Ac-(2 → 3)-β-D-Gal-(1 → 4)-D-Glc-ceramide (GD3) and α-D-Neu5Ac-(2−8)-α-D-Neu5Ac-(2−3)-β-D-Gal-(1−3)-β-D-GalNAc-(1−4)-[α-D-Neu5Ac-(2−3)]-β-D-Gal-(1−4)-D-Glc-ceramide (GT1a, major isoforms d18:1−18:0 and d20:1−18:0 have MWs 2126.4 Da, 2154.4 Da) were purchased from MyBioSource Inc. (San Diego, CA). The phospholipid 1-palmitoyl-2-oleoyl-sn-glycero-3-phosphocholine (POPC) was purchased from Avanti Polar Lipids Inc. (Alabaster, AL). The structures of the gangliosides and POPC were shown in Figure 2.1.

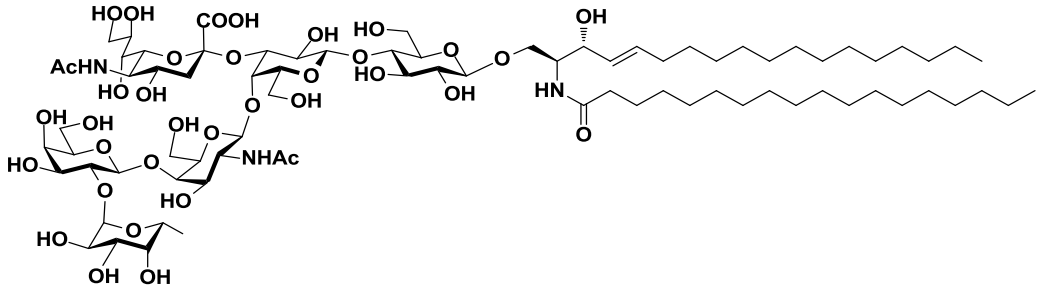

Fucosyl-GM1 (*d*18:1-18:0)

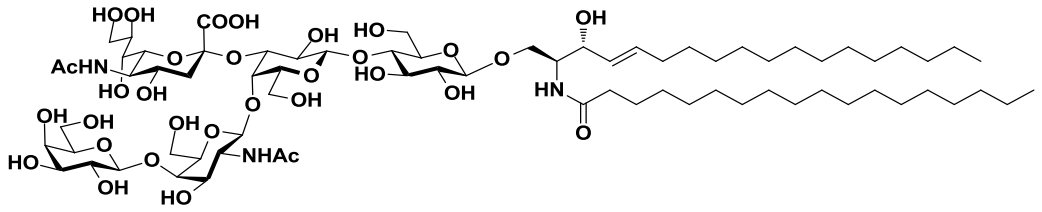

GM1 (*d*18:1-18:0)

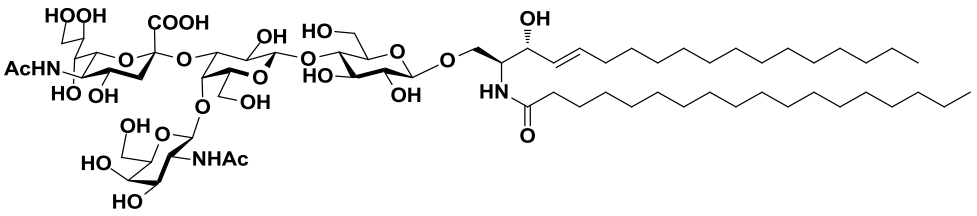

GM2 (*d*18:1-18:0)

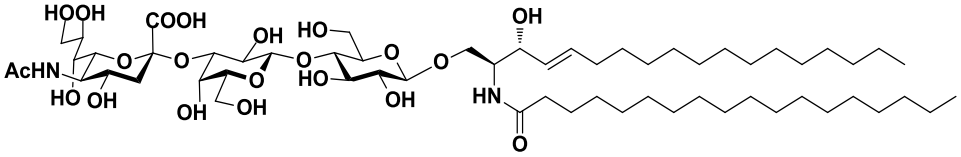

GM3 (*d*18:1-18:0)

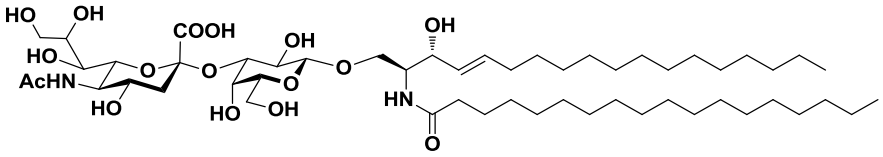

GM4 (*d*18:1-18:0)

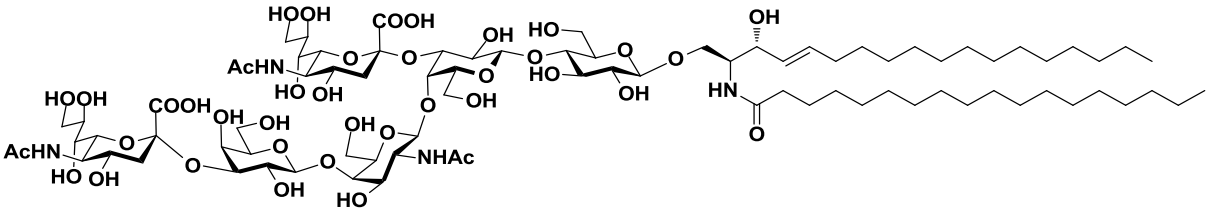

GD1a (*d*18:1-18:0)

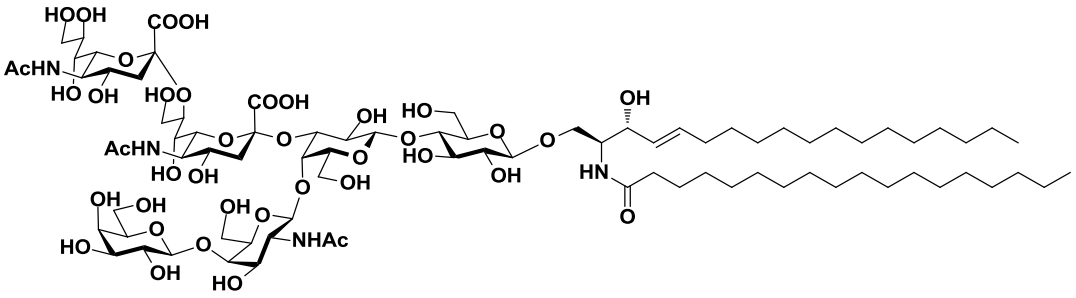

GD1b (*d*18:1-18:0)

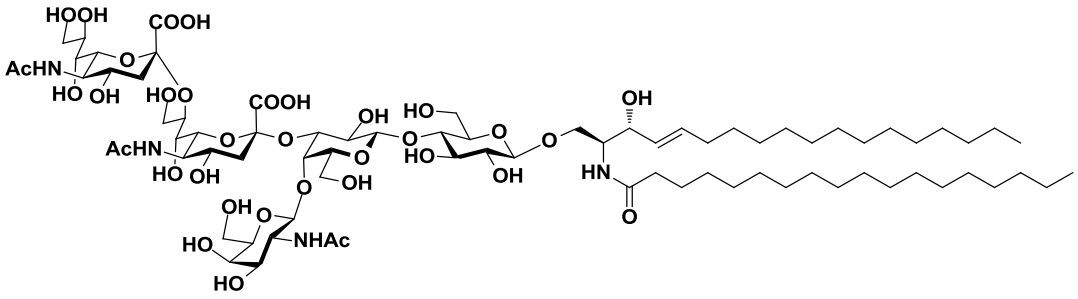

GD2 (*d*18:1-18:0)

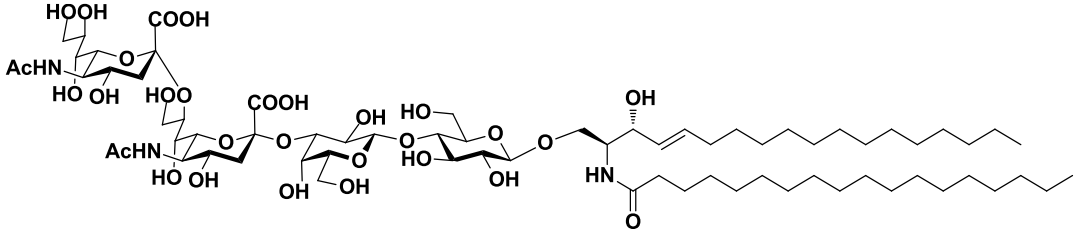

GD3 (*d*18:1-18:0)

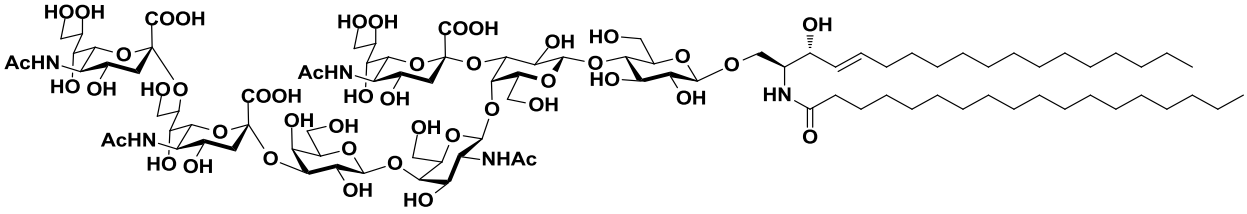

GT1a (*d*18:1-18:0)

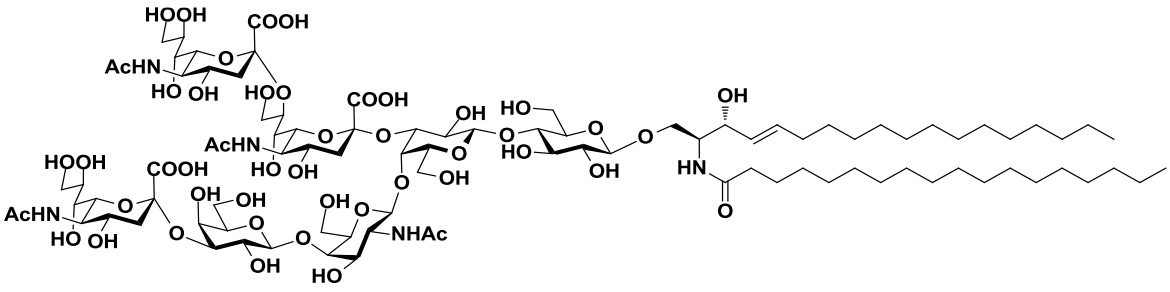

GT1b (*d*18:1-18:0)

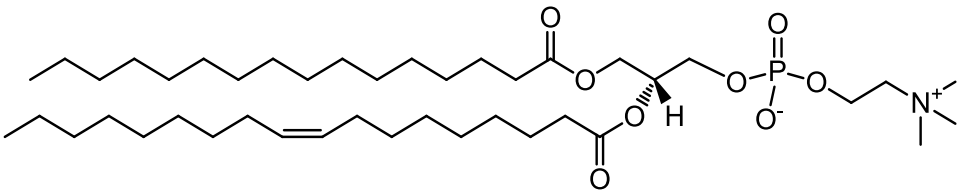

POPC (16:0/18:1(9Z))

Figure 2.1. Structures of the gangliosides Fucosyl GM1, GM1, GM2, GM3, GM4, GD1a, GD1b, GD2, GD3, GT1a, GT1b and POPC.

2.2.3 Oligosaccharides

The ganglioside oligosaccharides β-D-Gal-(1 → 3)-β-D-GalNAc-(1 → 4)-[α-D-Neu5Ac-(2 → 3)]-β-D-Gal-(1 → 4)-D-Glc ($GM1a_{os}$, MW 998.34 Da); α-D-Neu5Ac-(2 → 3)-β-D-Gal-(1 → 3)-β-D-GalNAc-(1 → 4)-β-D-Gal-(1 → 4)-D-Glc ($GM1b_{os}$, MW 998.34 Da); β-D-GalNAc-(1 → 4)-[α-D-Neu5Ac-(2 → 3)]-β-D-Gal-(1 → 4)-D-Glc ($GM2_{os}$, MW 836.29 Da); α-D-Neu5Ac-(2 → 3)-β-D-Gal-(1 → 4)-D-Glc ($GM3_{os}$, MW 633.21 Da); α-D-Neu5Ac-(2 → 3)-β-D-Gal-(1 → 3)-β-D-GalNAc-(1 → 4)-[α-D-Neu5Ac-(2 → 3)]-β-D-Gal-(1 → 4)-D-Glc ($GD1a_{os}$, MW 1289.44 Da); β-D-Gal-(1 → 3)-β-D-GalNAc-(1 → 4)-[α-D-Neu5Ac-(2 → 8)-α-D-Neu5Ac-(2 → 3)]-β-D-Gal-(1 → 4)-D-Glc ($GD1b_{os}$, MW 1289.44 Da); β-D-GalNAc-(1 → 4)-[α-D-Neu5Ac-(2 → 8)-α-D-Neu5Ac-(2 → 3)]-β-D-Gal-(1 → 4)-D-Glc ($GD2_{os}$, MW 1127.39 Da); α-D-Neu5Ac-(2 → 8)-α-D-Neu5Ac-(2 → 3)]-β-D-Gal-(1 → 4)-D-Glc ($GD3_{os}$, MW 924.31 Da); α-D-Neu5Ac-(2−8)-α-D-Neu5Ac-(2−3)-β-D-Gal-(1−3)-β-D-GalNAc-(1−4)-[α-D-Neu5Ac(2−3)]-β-D-Gal-(1−4)-D-Glc ($GT1a_{os}$, MW 1580.53 Da); α-D-Neu5Ac-(2−3)-β-D-Gal-(1−3)-β-D-Gal-NAc-(1−4)-[α-D-Neu5Ac-(2−8)-α-D-Neu5Ac-(2−3)]-β-D-Gal-(1−4)-D-Glc ($GT1b_{os}$, MW 1580.53 Da); β-D-Gal-(1,3)-β-D-GalNAc-(1,4)-[α-D-Neu5Ac-(2,8)-α-D-Neu5Ac-(2,8)-α-D-Neu5Ac-(2,3)]-β-D-Gal(1,4)-D-Glc ($GT1c_{os}$, MW 1580.53 Da); β-D-GalNAc-(1,4)-[α-D-Neu5Ac-(2,8)-α-D-Neu5Ac-(2,8)-α-D-Neu5Ac-(2,3)]-β-D-Gal-(1,4)-D-Glc ($GT2_{os}$, MW 1418.5 Da) and α-D-Neu5Ac-(2,8)-

α-D-Neu5Ac-(2,8)-α-D-Neu5Ac-(2,3)-β-D-Gal-(1,4)-D-Glc ($GT3_{os}$, MW 1215.4) were purchased from Elicityl SA (Crolles, France). α-D-Neu5Ac-(2 → 3)-β-D-Gal-O$(CH2)_8N_3$ ($GM4_{os}$, MW 624.3 Da) was a gift from Prof. Todd L. Lowary (University of Alberta). Modified $GM2_{os}$-CUPRA, $GM3_{os}$-CUPRA, $GM4_{os}$-CUPRA, $GD2_{os}$-CUPRA and $GD3_{os}$-CUPRA compounds were synthesized, which consisted of corresponding oligosaccharides linked to a benzene sulfonamide affinity tag. The structures of the ganglioside oligosaccharides were shown in Figure 2.2. Stock solutions (1 mM in Milli-Q water (Millipore, MA)) of each of the oligosaccharides were prepared and stored at −20 °C until needed.

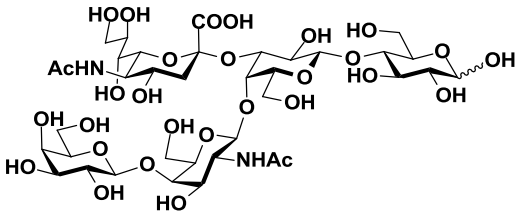

$GM1a_{os}$

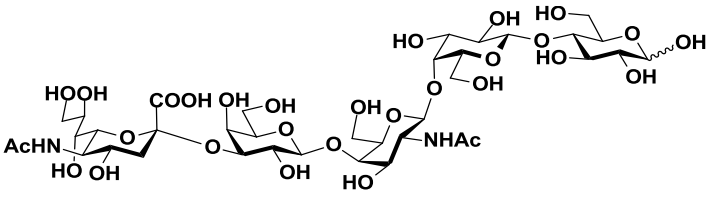

$GM1b_{os}$

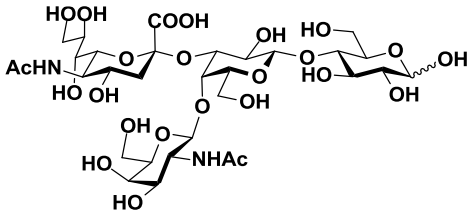

$GM2_{os}$

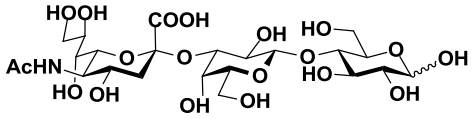

$GM3_{os}$

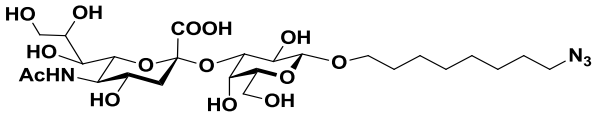

$GM4_{os}$

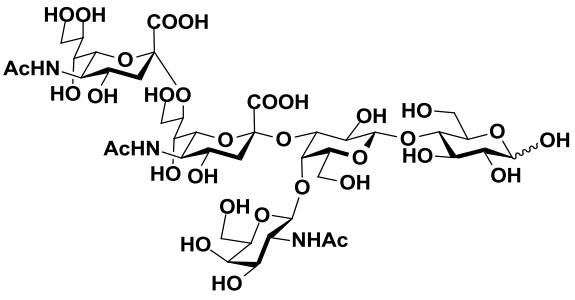

$GD2_{os}$

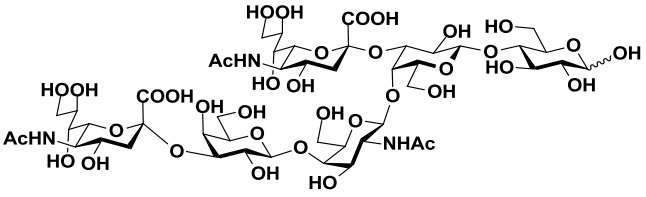

GD1a$_{os}$

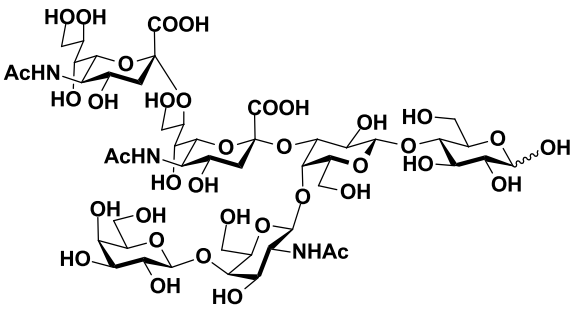

GD1b$_{os}$

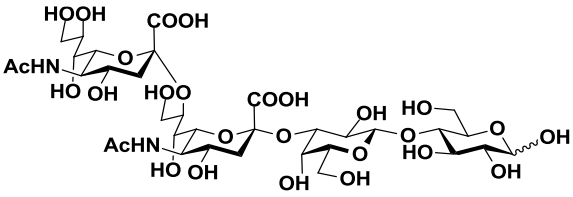

GD3$_{os}$

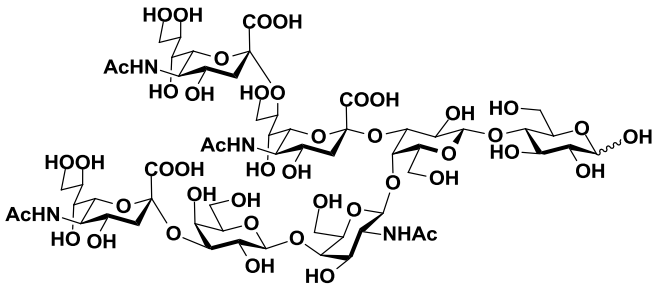

GT1b$_{os}$

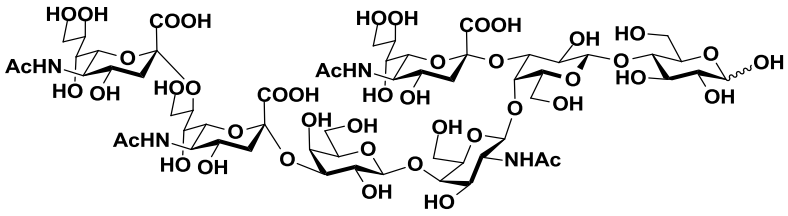

GT1a$_{os}$

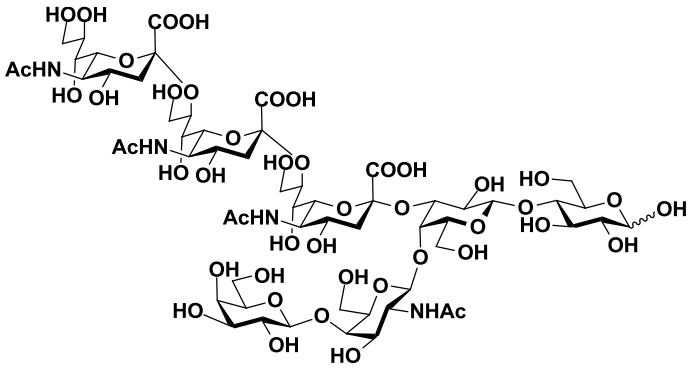

GT1c$_{os}$

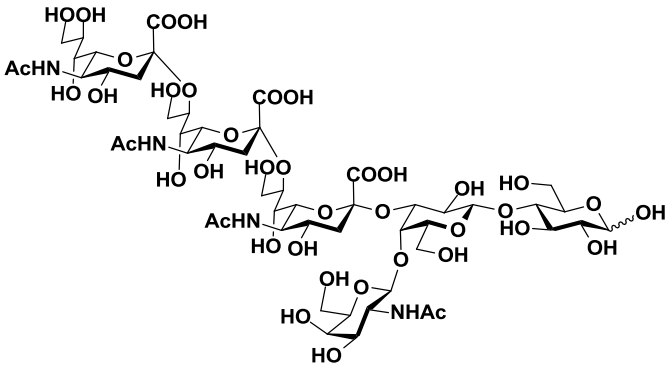

$GT2_{os}$

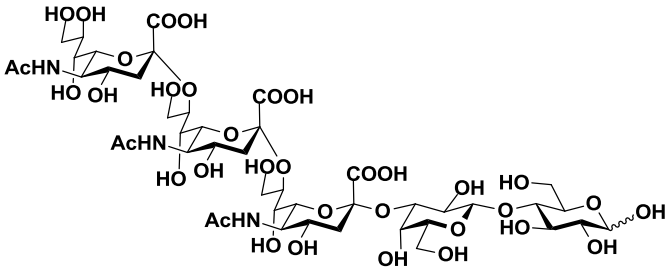

$GT3_{os}$

Figure 2.2. Structures of the gangliosides oligosaccharides $GM1a_{os}$, $GM1b_{os}$, $GM2_{os}$, $GM3_{os}$, $GM4_{os}$, $GD2_{os}$, $GD1a_{os}$, $GD1b_{os}$, $GD3_{os}$, $GT1b_{os}$, $GT1a_{os}$, $GT1c_{os}$, $GT2_{os}$ and $GT3_{os}$.

2.2.4 Preparation of nanodiscs

Nanodiscs (NDs) composed of phospholipid POPC and different amounts of gangliosides were prepared using a protocol reported previously by Sligar and coworkers.[19,20] Briefly, the POPC, dissolved in methanol, was mixed with either an individual ganglioside or a mixture of three gangliosides (fucosyl-GM1, GM1, GM2, GM3, GM4, GD1a, GD1b, GD2, GD3, GT1a, GT1b) at the desired molar ratios. The lipids were dried under a gentle stream of nitrogen to form a lipid film and kept in a vacuum desiccator overnight. The lipids were then dissolved in 20 mM TrisHCl, 0.5 mM EDTA, 100 mM NaCl, and 25 mM sodium cholate (pH 7.4) and sonicated for 15 mins. The MSP1E1 protein was added to the mixture at a MSP1E1-to-total lipid molar ratio of 1:100,

followed by incubation at 4 °C for 20 mins. The ND formation process was initiated by adding an equal volume of pre-washed Biobeads (Bio-Rad Laboratories Ltd., Mississauga, Canada), and then solution was incubated at 4 °C for 4 h on an orbital shaker to remove all detergents. The supernatant was then recovered, and a Superdex 200 10/300 size-exclusion column (GE-Healthcare Bio-Sciences, Uppsala, Sweden), which was equilibrated with a 200 mM aqueous ammonium acetate solution (pH 6.8) at room temperature, was used for NDs purification. Finally, the ND fractions were pooled, concentrated, and buffer exchanged into a 200 mM aqueous ammonium acetate solution (pH 6.8) using an Amicon microconcentrator (EMD Millipore, Billerica, MA) with a 30 kDa MW cutoff. The concentrations of the ND stock solutions were determined from on the concentration of MSP1E1 dimer, measured by UV absorption at 280 nm. All NDs stock solutions were stored at −80 °C until used.

2.2.5 Nanodisc concentration determination

Each nanodisc (ND) composed of two copies of MSP1E1 and the concentration of ND was estimated by measuring the UV absorbance of MSP1E1 at 280 nm ([ND] = 1/2 [MSP1E1]).[19] Since the molar ratio of MSP1E1-to-total lipid was 1:100 for all preparation, the nominal concentration of glycolipid ($[GL]_{nominal}$) in ND solution was calculated from the mole percentages (total lipid content) of GL (%GL) used for each ND preparation, eq.2.1:

$$[GL]_{nominal} \approx [ND] \times 2 \times \%GL \qquad (2.1)$$

2.2.6 Mass spectrometry

All ESI-MS and CaR-ESI-MS measurements were carried out using a Synapt G2S quadrupole-ion mobility separation-time-of-flight (Q-IMS-TOF) mass spectrometer (Waters, Manchester, U.K.) equipped with a nanoflow ESI (nanoESI) source. The ESI-MS binding measurements were performed in positive ion mode, whereas the CaR-ESI-MS assay was implemented in negative ion

mode. The direct ESI-MS assay,[21,22] *proxy ligand* ESI-MS method[23] and competitive universal proxy receptor assay (CUPRA)-*proxy ligand* method were used to measure the affinities of the protein-ligand interactions. Each sample solution was prepared in 200 mM aqueous ammonium acetate buffer (pH 6.8, 25 °C). A brief description of these assays was given below. The ESI solutions were loaded into nanoESI tips, produced from borosilicate capillaries using a P-1000 micropipette puller (Sutter Instruments, Novato,CA). To carry out nanoESI, a platinum wire was inserted into the nanoESI tip and a capillary voltage of ~ 0.80 kV (in negative ion mode) or 0.90 kV (in positive ion mode) was applied. The source temperature was 60°C for both two ion modes. The Cone, Trap and Transfer voltages were set to 30 V, 5 V and 2 V, respectively, unless otherwise indicated. All other instrumental conditions were set to the default parameters. Data acquisition and processing were performed using MassLynx software (version 4.1). In addition, the average number of ganglioside molecules per ND in a given preparation were quantified using matrix-assisted laser desorption ionization (MALDI)-mass spectrometer (solariX 15 Tesla FT-ICR, Bruker-Daltonics, Billerica, MA). MS data were acquired in the m/z range between 0 and 3000 in the negative ion mode by averaging signals from 1000 laser shots with a frequency of 200 Hz. The laser power was 40% with medium laser focus. All other instrumental conditions were set to the default parameters. Data acquisition and processing were performed using the FtmsControl and Compass DataAnalysis softwares, respectively (version 2.2, Bruker-Daltonics).

2.2.6.1 Direct ESI-MS assay

The direct ESI-MS assay was used to quantify the affinities of the ganglioside oligosaccharides for hu3F8 and its double mutant E1K/D32H Fabs and the 14G2a mAb. The reference protein (P_{ref}) method was used to correct the mass spectra for the occurrence of nonspecific protein-carbohydrate binding during ESI process.[24] The scFv, huNoV Saga P dimer and cytoc, which don't

bind to the oligosaccharides tested, served as P_{ref}. To analyze the data, K_a for a 1:1 PL complex was calculated from the abundance (*Ab*) ratio (*R,* eq1.10) of ligand bound (PL) to free protein (P) ions measured by ESI-MS in positive ion mode (after correction for nonspecific binding) and the known initial concentrations of protein ($[P]_0$) and ligand ($[L]_0$) in solution using eq1.11. The nanoESI process typically produces P^{n+} and PL^{n+} ions with a distribution of charge states. Therefore, the abundances of free and ligand-bound proteins were obtained from the sum of the peak areas for each species over all observed charge states. In order to get reliable affinity (K_a), a titration approach was employed, whereby the initial concentration of protein was fixed and the ligand concentration was varied.[25] In this cases, nonlinear regression analysis of the experimentally determined concentration-dependence of the fraction of ligand-bound protein, [R/(R+1)], was used to determine K_a, as shown in eq1.12.[21]

In cases where a multivalent protein that can sequentially bind up to q ligand molecules, the association constant ($K_{a,q}$) of the q^{th} ligand binding to protein can be expressed by eq1.14. Here, R_q was the abundance ratio of the protein bound to q molecules of ligand (PL_q) to free P ions measured by ESI-MS, which was shown in eq1.13. Additionally, the intrinsic association constant, $K_{a,int}$ (per binding site) can be calculated by eq1.15 and eq1.16, assuming all the i ligand binding sites of the protein were identical and independent. In the case of the 14G2a mAb which has two equivalent binding sites, the expressions for the apparent K_a values for the sequential binding of one and two ligand molecules, i.e., $K_{a,1}$ and $K_{a,2}$, are given in eq2.2 and eq2.3; $K_{a,int}$ can be found using eq2.4.

$$K_{a,1} = \frac{R_1}{([L]_0 - \frac{[P]_0(R_1 + 2R_2)}{1 + R_1 + R_2})} \quad (2.2)$$

$$K_{a,2} = \frac{R_2/R_1}{([L]_0 - \frac{[P]_0(R_1 + 2R_2)}{1 + R_1 + R_2})} \quad (2.3)$$

$$K_{a,int} = \frac{R_1 + 2R_2}{(R_1 + 2)([L]_0 - \frac{[P]_0(R_1 + 2R_2)}{1 + R_1 + R_2})} \quad (2.4)$$

2.2.6.2 *Proxy Ligand* ESI-MS assay

The *proxy ligand* ESI-MS assay, which was based on competitive ligand binding and direct ESI-MS measurements, was used to quantify the apparent affinity (K_a) of GD2, incorporated into a nanodisc (ND), for hu3F8 and hu3F8 E1K/D32H Fabs. This assay employs a proxy ligand (L_{proxy}), which binds to target P with known affinity ($K_{a,proxy}$) and competes with the glycolipid ligand (L).[23] In cases where target P possesses a single ligand binding site, the extent of PL binding can be deduced by monitoring the relative abundance of PL_{proxy} using direct ESI-MS measurements. The association constant (K_a) for L binding to target P was calculated from eq2.5:

$$K_a = \frac{1}{\left([L_{proxy}]_0 - \frac{R_{proxy}}{K_{a,proxy}}\right)\left(\frac{[L]_0}{R_{proxy}[P]_0 - (R_{proxy}+1)\left([L_{proxy}]_0 - \frac{R_{proxy}}{K_{a,proxy}}\right)} - \frac{1}{R_{proxy}}\right)} \quad (2.5)$$

where R_{proxy} corresponded to the abundance ratio of PL_{proxy} to free P ions measured by ESI-MS, which was taken to be equal to the equilibrium concentration ratio in solution (as shown in eq2.6), and $[P]_0$, $[L]_0$ and $[L_{proxy}]_0$ were the initial concentrations of P, L and L_{proxy}, respectively.

$$R_{\text{proxy}} = \frac{\sum Ab(\text{PL}_{\text{proxy}})}{\sum Ab(\text{P})} = \frac{[\text{PL}_{\text{proxy}}]}{[\text{P}]} \qquad (2.6)$$

2.2.6.3 Competitive universal proxy receptor assay (CUPRA)-*Proxy Ligand* ESI-MS method

The competitive CUPRA-*proxy ligand* ESI-MS assay was applied to quantify the apparent affinity (K_a) of GD2 incorporated into nanodiscs (NDs) for 14G2a mAb, since the measurements of anti-GD2 antibody binding to GD2. This assay relies on CUPRA as a proxy ligand which binds to target protein (P) with known affinity ($K_{a,int,PL_{proxy}}$, per binding site) and competes with GL ligand (L). The extent of PL binding can be deduced by monitoring the relative abundance of $P_{proxy}L_{proxy}$ by ESI-MS. The schematic for competitive CUPRA-*proxy ligand* ESI-MS assay was as follows Figure 2.3.

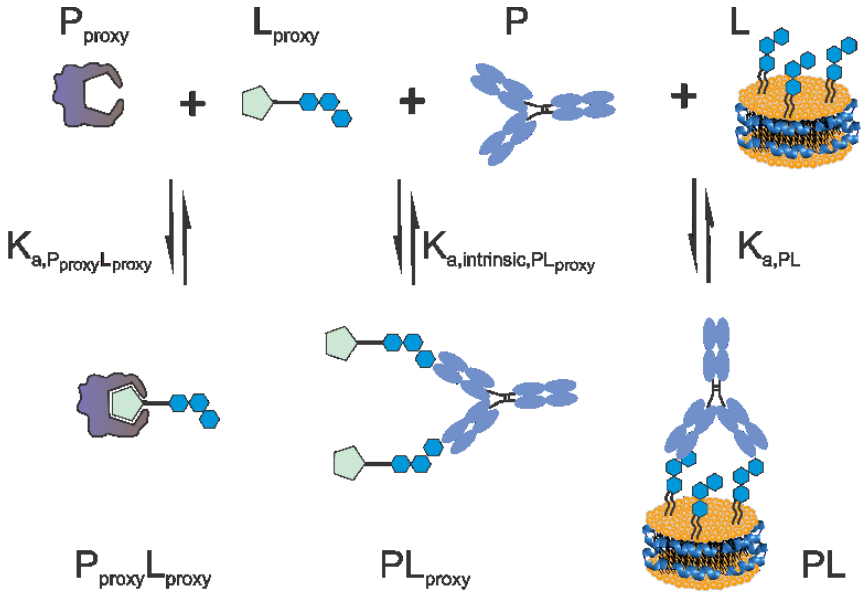

Figure 2.3. Schematic for competitive CUPRA-*proxy ligand* ESI-MS assay.

Briefly, the CUPRA was applied to quantify binding affinity of a heterobifunctional compound consisting of GD2 oligosaccharide linked to a common affinity tag (L_{proxy}, $GD2_{os}$-CUPRA ligand, $GD2_{os}$-CL) for a universal proxy protein receptor human carbonic anhydrase

(P_{proxy}, hCA) which binds $GD2_{os}$-CL through the affinity tag. For competitive binding of L and L_{proxy} to a target P, the relevant equilibrium expressions were given by eq2.7-2.9. In cases where the 14G2a mAb has two equivalent binding sites, $K_{a,int,PLproxy}$ (per binding site) was calculated in this study.

$$K_{a,PproxyLproxy} = \frac{[P_{proxy}L_{proxy}]}{[P_{proxy}][L_{proxy}]} = \frac{R_{proxy}}{[L_{proxy}]} \quad (2.7)$$

$$K_{a,int,PLproxy} = \frac{[PL_{proxy}]}{[P][L_{proxy}]} \quad (2.8)$$

$$K_{a,PL} = \frac{[PL]}{[P][L]} \quad (2.9)$$

$$R_{proxy} = \frac{\sum Ab(PL_{proxy})}{\sum Ab(P)} = \frac{[PL_{proxy}]}{[P]} \quad (2.10)$$

Where R_{proxy} corresponds to the abundance ratio of L_{proxy}-bound P_{proxy} ($P_{proxy}L_{proxy}$) to free P_{proxy} ions which is taken to be equal to the corresponding concentration ratio in solution, eq2.10. The value of K_a for L binding to P can be found from the experimentally determined R_{proxy} and the following equations of mass balance, eq2.11-2.14, and $K_{a,PproxyLproxy}$, $K_{a,int,PLproxy}$ and the initial concentrations of P ($[P]_0$), L ($[L]_0$), P_{proxy} ($[P_{proxy}]_0$) and L_{proxy} ($[L_{proxy}]_0$).

$$[P]_0 = [P] + [PL] + [PL_{proxy}] \quad (2.11)$$

$$[L]_0 = [L] + [PL] \quad (2.12)$$

$$[P_{proxy}]_0 = [P_{proxy}L_{proxy}] + [P_{proxy}] \quad (2.13)$$

$$[L_{proxy}]_0 = [P_{proxy}L_{proxy}] + [PL_{proxy}] + [L_{proxy}] \quad (2.14)$$

Dividing both sides of eq2.12 by $[P_{proxy}]$, gave eq2.15:

$$\frac{[P_{proxy}]_0}{[P_{proxy}]} = \frac{[P_{proxy}L_{proxy}] + [P_{proxy}]}{[P_{proxy}]} = R_{proxy} + 1 \quad (2.15)$$

It followed that $[P_{proxy}]$, $[PL_{proxy}]$ and $[P_{proxy}L_{proxy}]$ can be expressed as eqs2.16-2.18, respectively:

$$[P_{proxy}] = \frac{[P_{proxy}]_0}{1 + R_{proxy}} \quad (2.16)$$

$$[PL_{proxy}] = [L_{proxy}]_0 - \frac{R_{proxy}}{K_{a,PproxyLproxy}} - \frac{[P_{proxy}]_0}{1 + R_{proxy}} \times R_{proxy} \quad (2.17)$$

$$[P_{proxy}L_{proxy}] = \frac{[P_{proxy}]_0}{1 + R_{proxy}} \times R_{proxy} \quad (2.18)$$

and [P], [L] and [PL] can be expressed as eqs2.19-2.21, respectively:

$$[P] = \frac{[PL_{proxy}]}{K_{a,int,PLproxy}[L_{proxy}]} = \frac{[L_{proxy}]_0 - \frac{R_{proxy}}{K_{a,PproxyLproxy}} - \frac{[P_{proxy}]_0}{1+R_{proxy}} \times R_{proxy}}{K_{a,int,PLproxy} \times \frac{R_{proxy}}{K_{a,PproxyLproxy}}} \quad (2.19)$$

$$[L] = [L]_0 - ([P]_0 + [L_{proxy}]_0 + \frac{R_{proxy}}{K_{a,PproxyLproxy}} + \frac{[P_{proxy}]_0}{1+R_{proxy}} \times R_{proxy} - \frac{[L_{proxy}]_0 - \frac{R_{proxy}}{K_{a,PproxyLproxy}} - \frac{[P_{proxy}]_0}{1+R_{proxy}} \times R_{proxy}}{K_{a,int,PLproxy} \times \frac{R_{proxy}}{K_{a,PproxyLproxy}}}) \quad (2.20)$$

$$[PL] = [P]_0 + [L_{proxy}]_0 + \frac{R_{proxy}}{K_{a,PproxyLproxy}} + \frac{[P_{proxy}]_0}{1+R_{proxy}} \times R_{proxy} - \frac{[L_{proxy}]_0 - \frac{R_{proxy}}{K_{a,PproxyLproxy}} - \frac{[P_{proxy}]_0}{1+R_{proxy}} \times R_{proxy}}{K_{a,int,PLproxy} \times \frac{R_{proxy}}{K_{a,PproxyLproxy}}} \quad (2.21)$$

2.2.6.4 Catch and Release (CaR)-ESI-MS assay

The CaR-ESI-MS assay was performed to screen libraries of gangliosides against antibodies including 14G2a, hu3F8 and hu3F8 E1K/D32H mAbs. Ions corresponding to ligand-bound protein were isolated using the quadrupole mass filter which was set to transmit ions with a range of mass-to-charge ratios (m/z) window (approximately ranges from 100 to 150 m/z units). It allows for the passage of ligand-bound protein complexes of interest at a given charge state. Protein-ligand complexes were subjected to collision-induced dissociation (CID) in the Trap region using collision energies of 50 - 120 V. The deprotonated ligands released from the complexes were identified from their measured molecular weight (MW).

2.2.6.5 Quantifying ganglioside content of nanodiscs using MALDI-MS

The amount of GD2 in a given ND preparation was quantified using MALDI-MS and an internal standard (IS) approach. The matrix compound 2,5-Dihydroxybenzoic acid (2,5-DHB, purchased

from Sigma-Aldrich Canada) was dissolved in methanol solution at concentrations of 10 mg/mL. The ammonium citrate was also dissolved in water as 25 mg/mL solution. The matrix solutions were prepared by mixing 2,5-DHB solution with ammonium citrate solution at 9:1 volume ratio. After that, the matrix solution was mixed with a given GD2-ND and a known amount of GD1b as an IS in a tube and then placed on the target plate for crystallization. Crystallization was accelerated by a gentle stream of cold air. All samples were detected by MALDI-MS.

2.3 Results and Discussion

2.3.1 Affinities of ganglioside oligosaccharides for anti-GD2 antibodies

In order to determine whether anti-GD2 antibody non-specifically binds to other gangliosides that remain in the human cell, the direct ESI-MS binding measurements were carried out to quantify binding between a library of fourteen ganglioside oligosaccharides ($GM1a_{os}$, $GM1b_{os}$, $GM2_{os}$, $GM3_{os}$, $GM4_{os}$, $GD1a_{os}$, $GD1b_{os}$, $GD2_{os}$, $GD3_{os}$, $GT1a_{os}$, $GT1b_{os}$, $GT1c_{os}$, $GT2_{os}$, $GT3_{os}$) and the hu3F8 and hu3F8 E1K/D32H Fabs and 14G2a mAb. Shown in Figure 2.4a, 2.5a and 2.6a are representative ESI mass spectra acquired for aqueous (200 mM ammonium acetate, pH 6.8, 25°C) solutions of hu3F8 Fab (4 μM), hu3F8 E1K/D32H Fab (3.5 μM) and 14G2a mAb (3 μM), respectively. The measured MWs of hu3F8 and hu3F8 E1K/D32H Fabs and 14G2a mAb are 46 392 ± 3 608 Da, 47 190 ± 2 810 Da and 149 251 ± 749 Da, respectively, which was approximately in agreement with the theoretical values (Fab: theoretical MW 50 000 Da; mAb: theoretical MW 150 000 Da).

Representative ESI mass spectra measured for an aqueous ammonium acetate solution (200 mM ammonium acetate, pH 6.8, 25°C) containing hu3F8 Fab with $GD2_{os}$, $GD3_{os}$ and $GT3_{os}$ are shown in Figure 2.4b-d. The scFv (4 μM), which served as P_{ref}, was present in the solutions used to correct for nonspecific ligand binding in weak binding events ($K_a < 10^4\ M^{-1}$). Based on the ESI-

MS data, the hu3F8 Fab which possessed single binding site binds with one ganglioside oligosaccharide molecule (i.e., $(P + L)^{n+}$, where n= 13-16). In the meantime, signals corresponding to unbound and bound P_{ref} ions were also detected for $GD3_{os}$ and $GT3_{os}$, (i.e., $(P_{ref} + L)^{n+}$, where n= 9-11), which indicated that nonspecific binding of hu3F8 Fab to $GD3_{os}$ and $GT3_{os}$ occurred during the ESI process. Similarly, shown in Figure 2.5b-d are representative ESI mass spectra acquired for an aqueous ammonium acetate solution (200 mM ammonium acetate, pH 6.8, 25°C) of hu3F8 E1K/D32H Fab with $GD2_{os}$, $GD3_{os}$ and $GT3_{os}$, respectively.

Subsequently, the stepwise binding of 14G2a mAb with $GD2_{os}$ was evaluated. ESI-MS measurements were performed in aqueous ammonium acetate solutions (200 mM, pH 6.8) of 14G2a mAb (1.5 μM) and $GD2_{os}$ at concentrations ranging from 0 to 20 μM. As illustrated in Figure 2.6b, the 14G2a mAb binds up to two molecules of $GD2_{os}$ (i.e., $(P + qGD2_{os})^{n+}$ ions where q = 1-2 and n = 23-28). Additionally, shown in Figure 2.6c-d are representative mass spectra acquired in the solution of 14G2a mAb with $GM1a_{os}$ and $GT2_{os}$, respectively. According to the ESI-MS spectra, ions corresponding to 14G2a mAb predominantly bound to one molecule of $GM1a_{os}$ or $GT2_{os}$ were detected, in cases where the huNoV Saga P dimer was used as the P_{ref} to correct nonspecific binding during the ESI process.

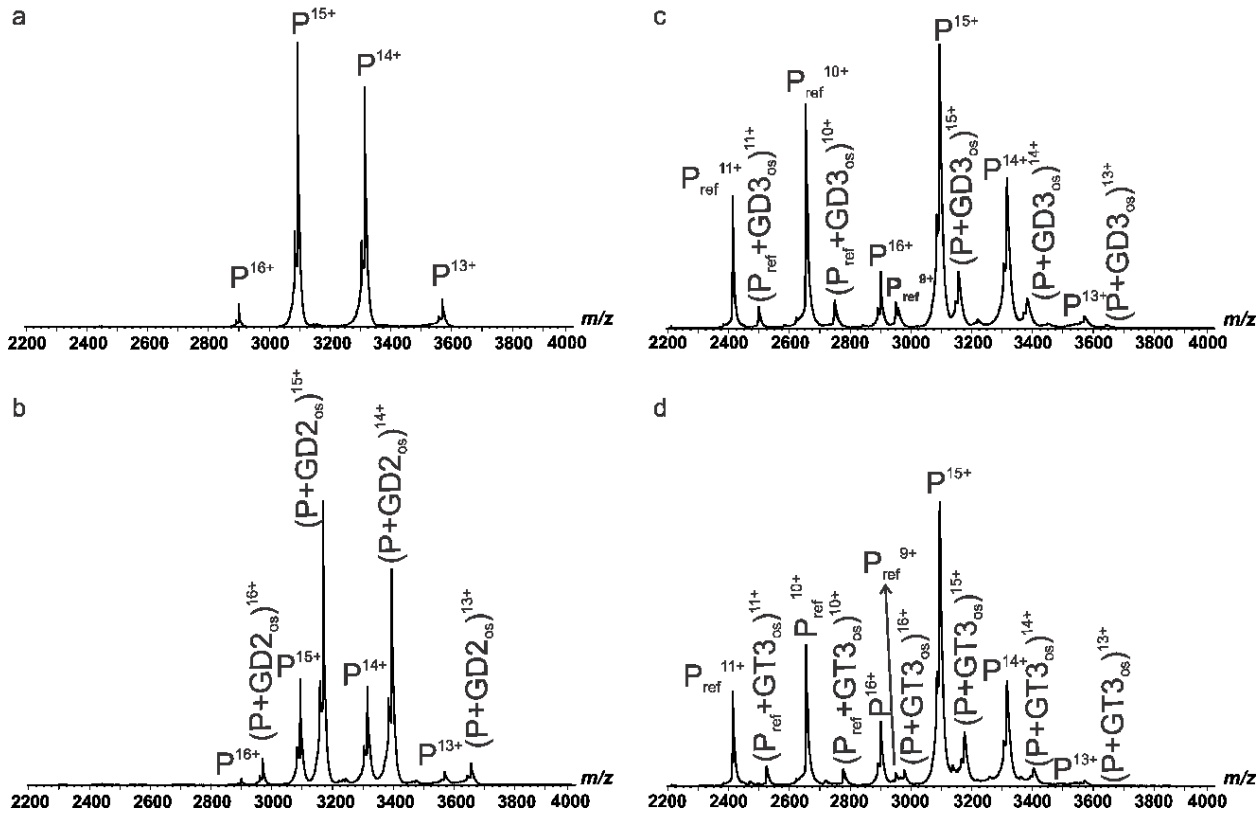

Figure 2.4. ESI mass spectra in positive ion mode for a 200 mM aqueous ammonium acetate solution (pH 6.8, 25 °C) of (a) hu3F8 Fab (4 μM) and with (b) $GD2_{os}$ (8 μM), (c) $GD3_{os}$ (50 μM) and (d) $GT3_{os}$ (70 μM) using scFv as P_{ref}.

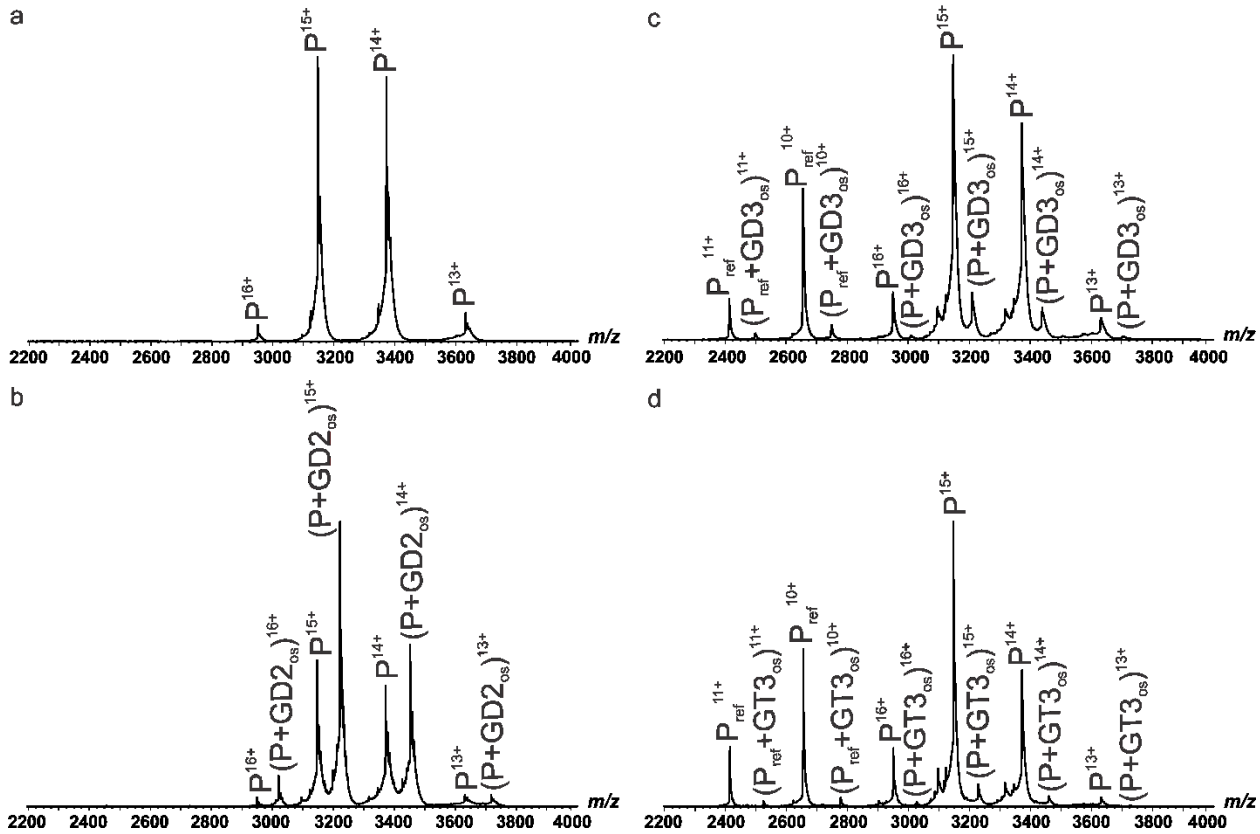

Figure 2.5. ESI mass spectra in positive ion mode for a 200 mM aqueous ammonium acetate solution (pH 6.8, 25 °C) of (a) hu3F8 E1K/D32H Fab (3.5 μM) and with (b) $GD2_{os}$ (3 μM), (c) $GD3_{os}$ (50 μM) and (d) $GT3_{os}$ (50 μM) using scFv as P_{ref}.

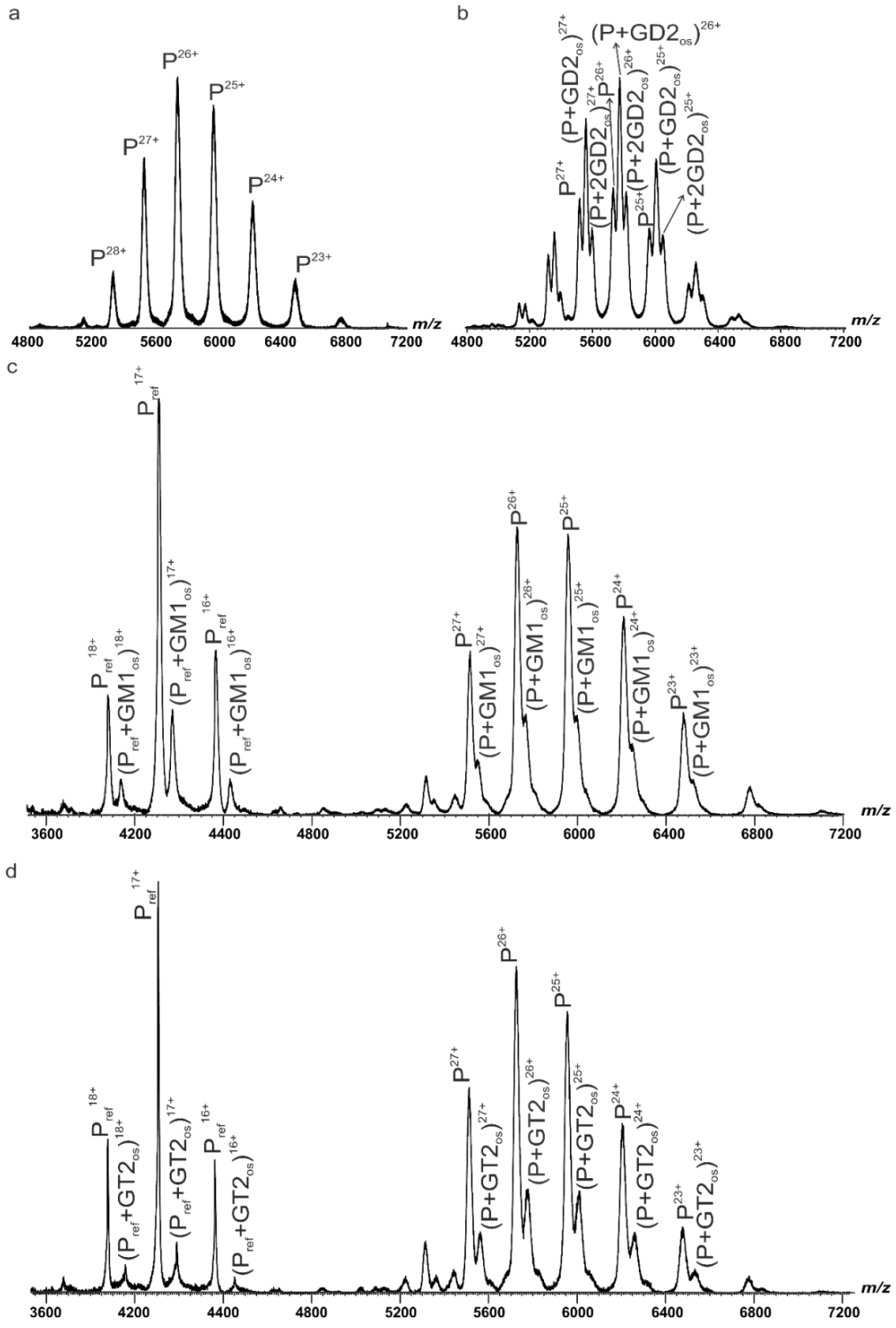

Figure 2.6. ESI mass spectra in positive ion mode for a 200 mM aqueous ammonium acetate solution (pH 6.8, 25 °C) of (a) 14G2a mAb (1.5 μM) and with (b) $GD2_{os}$ (15 μM), (c) $GM1a_{os}$ (35 μM) and (d) $GT2_{os}$ (25 μM) using huNoV Saga P dimer as P_{ref}.

The binding affinities of anti-GD2 antibodies, including hu3F8 and hu3F8 E1K/D32H Fabs and 14G2a mAb binding to the fourteen ganglioside oligosaccharides, were quantified by direct ESI-MS analysis. For hu3F8 Fab binding measurements, direct ESI-MS titration experiments were performed. At least three different initial ligand concentrations ranging from 5 to 100 μM were used for each oligosaccharide tested, and the binding measurements were carried out in triplicate. The K_a values obtained by fitting eq1.12 to the fraction of ligand-bound protein measured experimentally as shown in Figure 2.7. The K_a values for hu3F8 E1K/D32H Fab and 14G2a mAb were determined from direct ESI-MS measurements carried out at two different ligand concentrations due to the limited availability of anti-GD2 antibodies, except $GD2_{os}$ ligand at a minimum of four different concentrations. A summary of the K_a values (per binding site) is shown in Table 2.1. Inspection of the K_a values revealed that, among the tested oligosaccharides, $GD2_{os}$ exhibited the high affinities for different types of anti-GD2 antibodies. The anti-GD2 antibodies were ranked in order of affinity: hu3F8 E1K/D32H Fab ($K_{a,GD2os} = (22 \pm 1.5) \times 10^5\ M^{-1}$) > hu3F8 Fab ($K_{a,GD2os} = (4.3 \pm 0.1) \times 10^5\ M^{-1}$) > 14G2a mAb ($K_{a1,app} = (1.2 \pm 0.9) \times 10^5\ M^{-1}$, $K_{a2,app} = (4.1 \pm 0.4) \times 10^4\ M^{-1}$ and $K_{a,int,GD2os} = (7.0 \pm 0.2) \times 10^4\ M^{-1}$ (per binding site)). Measurements performed on other oligosaccharides proved that they were also recognized by these antibodies, although with lower affinities, in the $2.0 \times 10^2\ M^{-1} – 5.8 \times 10^3\ M^{-1}$ range. Interestingly, these antibodies exhibited relative high binding affinities for $GT2_{os}$ compared with other oligosaccharides, which was consistent with reported glycan microarray data.[26] Moreover, the 14G2a mAb with very malleable antigen binding site was capable of recognizing some oligosaccharides with relative low affinities. It not only binds predominantly to $GD2_{os}$, but also has the potential to respond to a variety of foreign antigens, such as $GM1a_{os}$, $GD1b_{os}$, which are also present on several neuroectodermal tumors including melanoma or renal carcinoma.[26] In contrast, the hu3F8 Fab exhibits relatively

excellent specificity to $GD2_{os}$. Taken together, since the affinities of these antibodies to other ganglioside oligosaccharides were uniformly weak relative to $GD2_{os}$, there are not going to be competitive for equal amount of oligosaccharides on the cells.

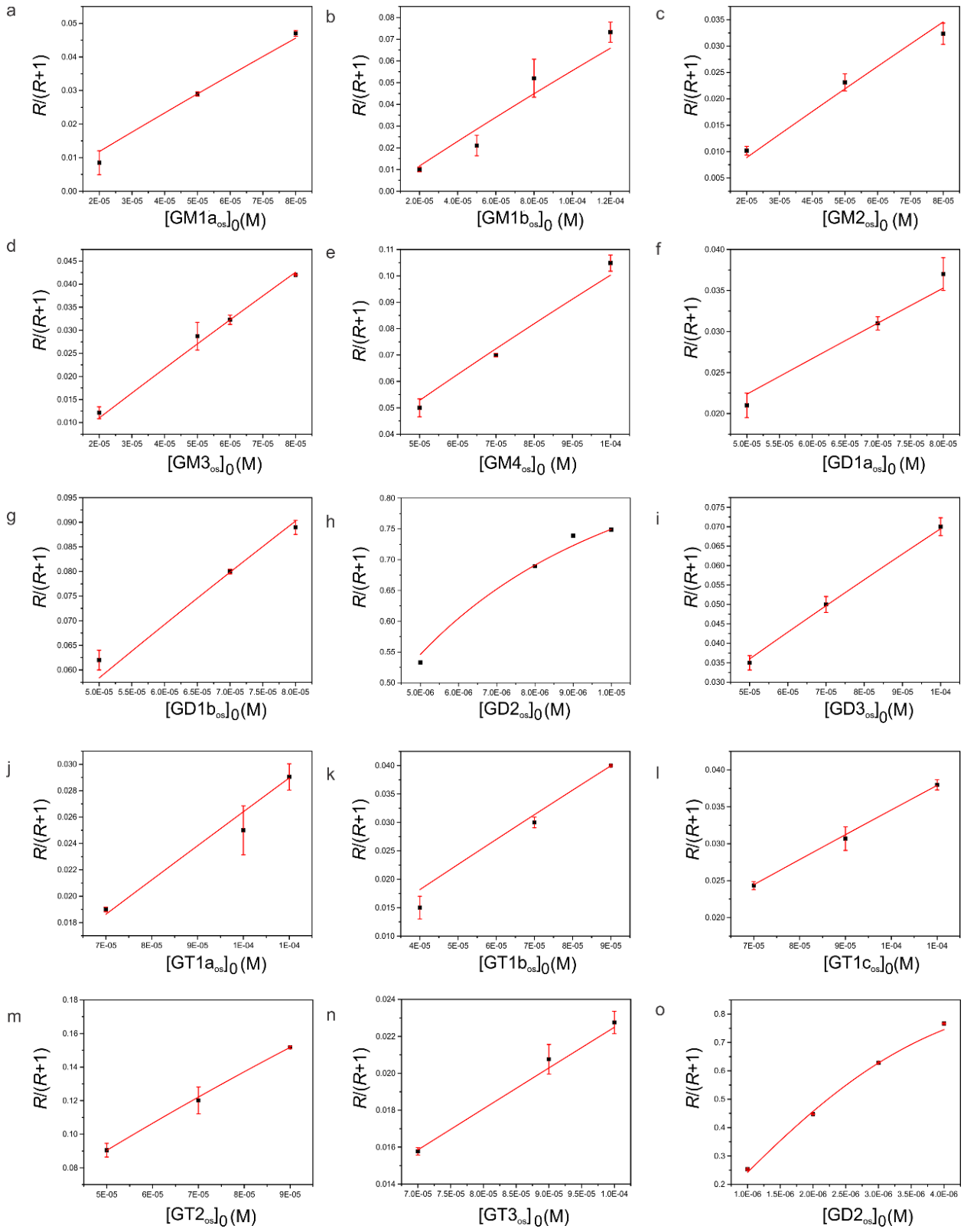

Figure 2.7. Plots of fraction of ligand-bound hu3F8 Fab versus ligand concentration measured for

(a) $GM1a_{os}$, (b) $GM1b_{os}$, (c) $GM2_{os}$, (d) $GM3_{os}$, (e) $GM4_{os}$, (f) $GD1a_{os}$, (g) $GD1b_{os}$, (h) $GD2_{os}$, (i) $GD3_{os,}$ (j) $GT1a_{os,}$ (k) $GT1b_{os}$, (l) $GT1c_{os,}$ (m) $GT2_{os}$ and (n) $GT3_{os}$. Plot of fraction of ligand-bound hu3F8 E1K/D32H Fab versus ligand concentration measured for (o) $GD2_{os}$. The solid curves correspond to the best fit of eq1.12 to the experimental data and the error bars correspond to one standard derivation.

Table 2.1. Association constants K_a (M^{-1}) for anti-GD2 antibodies binding to ganglioside oligosaccharides measured by ESI-MS in 200 mM aqueous ammonium acetate solutions (pH 6.8, 25 °C).

Oligosaccharide	K_a ($\times 10^2$ M^{-1}) hu3F8 Fab	K_a ($\times 10^2$ M^{-1}) hu3F8 E1K/D32H Fab	$K_{a,int}$ ($\times 10^2$ M^{-1}) 14G2a mAb
$GM1a_{os}$	6.0 ± 0.4	9.8 ± 1.9	10.1 ± 1.6
$GM1b_{os}$	5.9 ± 0.5	4.1 ± 1.6	9.0 ± 1.4
$GM2_{os}$	4.5 ± 0.2	9.9 ± 3.4	4.6 ± 0.2
$GM3_{os}$	5.6 ± 0.02	6.3 ± 3.0	5.7 ± 0.7
$GM4_{os}$	11.2 ± 0.3	43.0 ± 0.3	5.9 ± 1.0
$GD1a_{os}$	4.6 ± 0.1	7.0 ± 0.6	3.6 ± 0.8
$GD1b_{os}$	12.5 ± 0.3	17.0 ± 1.1	12.7 ± 1.2
$GD2_{os}$	4271.7 ± 143.1	22000.0 ± 1500.0	700.0 ± 23.0
$GD3_{os}$	7.5 ± 0.1	12.9 ± 5.9	2.0 ± 0.2
$GT1a_{os}$	2.7 ± 0.05	3.7 ± 0.09	2.7 ± 0.3
$GT1b_{os}$	4.6 ± 0.04	8.8 ± 1.8	11.6 ± 3.0
$GT1c_{os}$	3.6 ± 0.02	8.8 ± 1.5	4.8 ± 0.7
$GT2_{os}$	20.0 ± 0.1	58.3 ± 7.6	28.7 ± 2.7
$GT3_{os}$	2.3 ± 0.04	3.1 ± 1.2	7.0 ± 1.8

2.3.2 Screening ganglioside-containing NDs against anti-GD2 antibodies

Next, the CaR-ESI-MS assay, implemented using NDs, was used to screen gangliosides (Fucosyl-GM1, GM1, GM2, GM3, GM4, GD1a, GD1b, GD2, GD3, GT1a and GT1b) against the hu3F8, hu3F8 E1K/D32H and 14G2a mAbs. Ten small libraries of ganglioside-containing NDs were prepared. Each library contained three different gangliosides and always included GD2. *Library 1-5* consisted of a single ND prepared from an equimolar (1%) mixture of the three gangliosides, while *Library 6-10* contained an equimolar (1%) mixture of three different NDs, each prepared with a single ganglioside. The compositions of lipids and gangliosides in *Library 1-10* are shown in Table 2.2.

Table 2.2. Composition of lipids including phospholipid and glycolipid in *Library 1-10*.

Library	Phospholipid	Glycolipids
Library 1	POPC	GM3, GD1a and GD2
Library 2	POPC	GM4, GT1b and GD2
Library 3	POPC	GM1, GM2 and GD2
Library 4	POPC	Fucosyl-GM1, GD3 and GD2
Library 5	POPC	GT1a, GD1b and GD2
Library 6	POPC	GM3, GD1a and GD2
Library 7	POPC	GM4, GT1b and GD2
Library 8	POPC	GM1, GM2 and GD2
Library 9	POPC	Fucosyl-GM1, GD3 and GD2
Library 10	POPC	GT1a, GD1b and GD2

To confirm that all three gangliosides were incorporated into the NDs, the libraries were analyzed by ESI-MS and the ND ions were subjected to CID. Shown in Figure 2.8a is a representative ESI mass spectrum acquired for an aqueous ammonium acetate solution (200 mM, pH 6.8) of *Library 1* (8 μM, 1% of each ganglioside). A broad unresolved peak centered at m/z ~ 11000 was detected. This feature was attributed to intact ND. The quadrupole mass filter was set to pass ions with m/z > 6400, which were then subjected to CID in the Trap region with a collision energy of 150 V. Signal corresponding to all three deprotonated ganglioside ions was detected, which confirmed that all three gangliosides were successfully incorporated into the NDs (Figure 2.8b). Similar results were obtained for *Library 2-5* (Figure 2.8c-f).

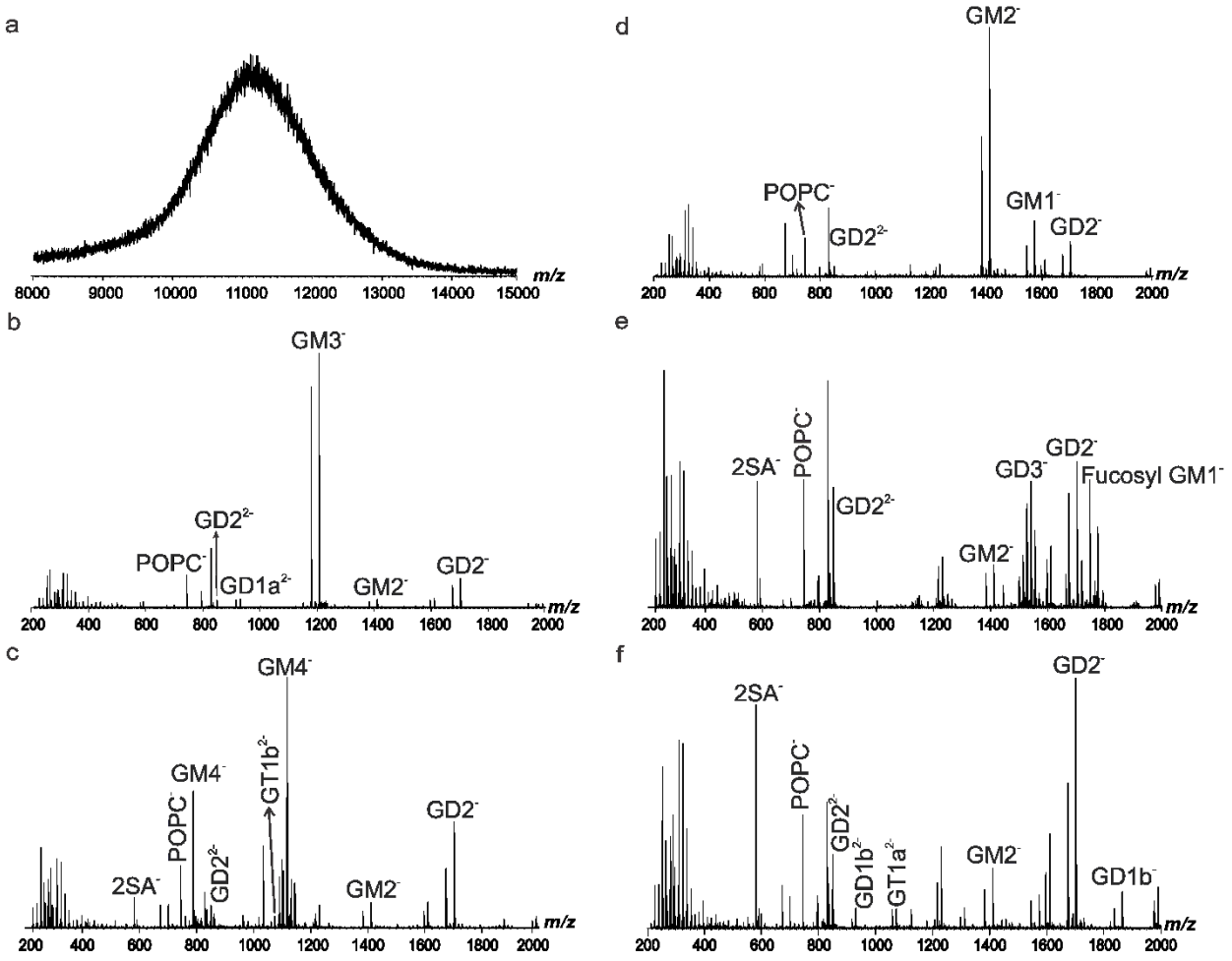

Figure 2.8. (a) ESI mass spectrum acquired in negative ion mode for an aqueous ammonium

acetate solution (200 mM, pH 6.8) of *Library 1* (8 μM, 1% of each ganglioside). (b) - (f) CID mass spectra of ions with m/z > 6400, produced by ESI in negative ion mode for aqueous ammonium acetate solutions (200 mM, pH 6.8) of *Library 1* to *Library 5*, respectively, using a collision energy (in Trap) of 150 V.

Shown in Figure 2.9a and 2.9b are the representative ESI mass spectra acquired in negative ion mode for an aqueous ammonium acetate solution (200 mM, pH 6.8) of 14G2a mAb (2.5 μM) and either *Library 1* or *Library 2* (1.5 μM of each ganglioside), respectively. Signal corresponding to the -21 to -24 charge states of the deprotonated ions of 14G2a mAb and 14G2a mAb bound to one or two ganglioside ligands (i.e., $(P + L)^{n-}$ and $(P + 2L)^{n-}$) was detected. To assess the extent of 14G2a mAb binding to the three gangliosides in a given library, CID in the Trap region was performed on the $(P + L)^{n-}$ and $(P + 2L)^{n-}$ ions at charge state -22. Using a collision energy of 100 V, CID resulted predominantly in the release of singly and doubly deprotonated GD2 ions. Notably, deprotonated GM3 (*Library 1*) and GM4 (*Library 2*) ions were detected, albeit at much lower abundances than for GD2 (5% and 14%, respectively), as shown in Figure 2.9c and 2.9d. These results are, perhaps, surprising given the low affinities measured for the corresponding oligosaccharides. Measurements performed on solutions containing *Library 3*, *4* or *5* revealed only the release of singly and doubly deprotonated GD2 ions (data not shown).

Analogous CaR-ESI-MS measurements were also carried out on the aqueous ammonium acetate solutions (200 mM, pH 6.8) of 14G2a mAb (2.5 μM) and one of *Library 6-10* (1.5 μM of each ganglioside). Representative ESI mass spectra acquired in negative ion mode for 14G2a mAb and either *Library 6* or *Library 7* are shown in Figure 2.10a and 2.10b. These are found to be qualitatively similar to those measured for solutions of *Library 1* or *Library 2*. CID of $(P + L)^{n-}$ and $(P + 2L)^{n-}$ ions at charge states -22 in the Trap region using a collision energy of 100 V led to

primarily the appearance of singly and doubly deprotonated GD2 ions, with singly deprotonated GM3 or GM4 also detected, although at low relative abundances (2% GM3 and 4% GM4, Figure 2.10c and 2.10d, respectively). Only singly and doubly deprotonated GD2 ions were released for the other libraries (data not shown).

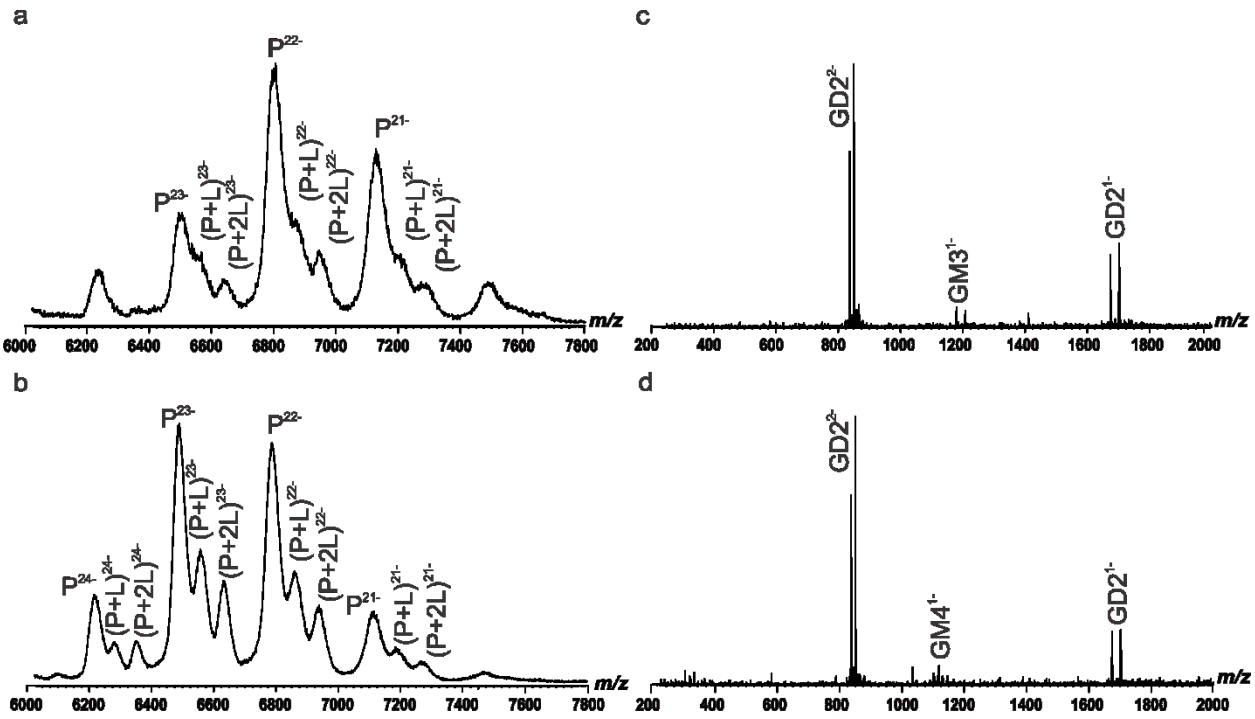

Figure 2.9. ESI mass spectra acquired in negative ion mode for a 200 mM aqueous ammonium acetate solution (pH 6.8) containing 14G2a mAb (2.5 μM) and (a) *Library 1* (1.5 μM of each ganglioside) and (b) *Library 2* (1.5 μM of each ganglioside). (c) and (d) CID mass spectra acquired in the Trap region for the $(P + L)^{22-}$ ions using a collision energy of 100 V.

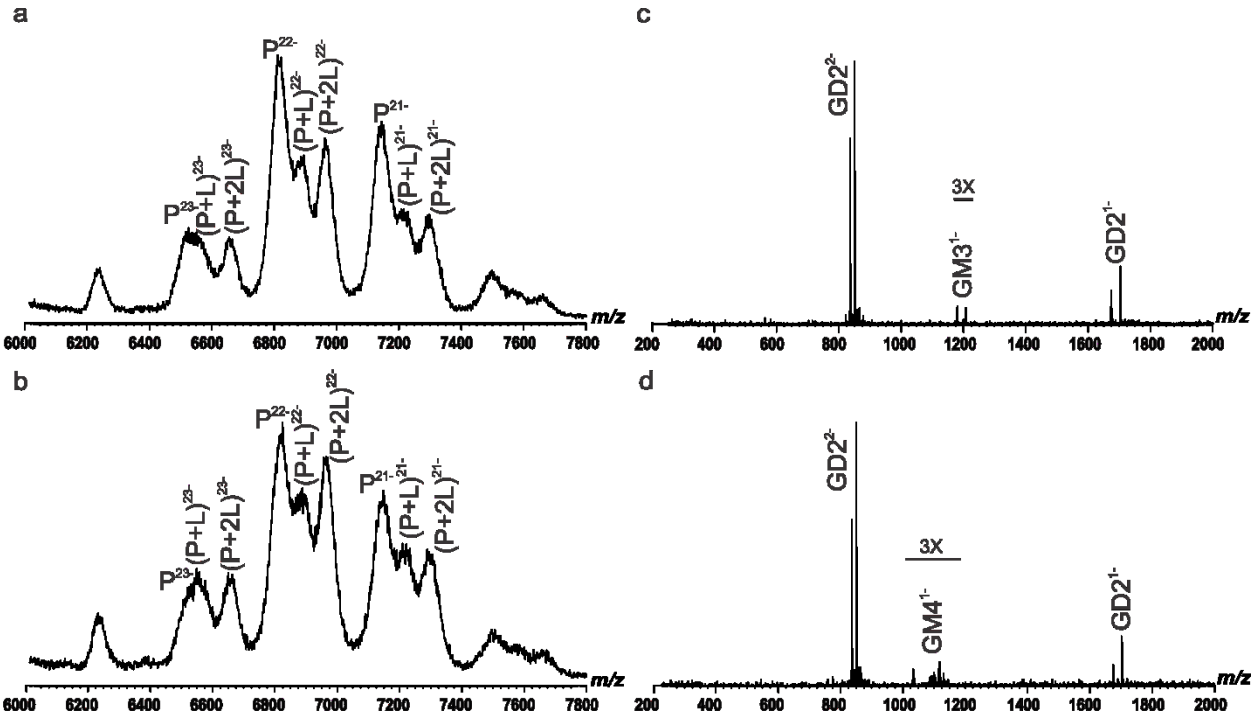

Figure 2.10. ESI mass spectra acquired in negative ion mode for a 200 mM aqueous ammonium acetate solution (pH 6.8) containing 14G2a mAb (2.5 μM) and (a) *Library 6* (1.5 μM of each ganglioside) and (b) *Library 7* (1.5 μM of each ganglioside). (c) and (d) CID mass spectra acquired in the Trap region for the $(P + L)^{22-}$ ions using a collision energy of 100 V.

The CaR-ESI-MS measurements were also carried out on using a higher concentration of *Library 1* to *Library 10*. Shown in Figure 2.11a and 2.11b are the representative ESI mass spectra acquired in negative ion mode for an aqueous ammonium acetate solution (200 mM, pH 6.8) of 14G2a mAb (2.5 μM) and *Library 1* or *Library 2* (4 μM of each ganglioside), respectively. As expected, the higher library concentrations led to more abundant $(P + L)^{n-}$ and $(P + 2L)^{n-}$ ions. CID of $(P + L)^{n-}$ and $(P + 2L)^{n-}$ ions at charge states -22 under a collision energy of 100 V resulted primarily in the appearance of singly and doubly deprotonated GD2 ions, with GM3 and GM4 ions also detected (Figure 2.11c and 2.11d, respectively). Notably, the relative abundances of the released GM3 and GM4 ions were higher than those measured at the lower library concentration

(13% and 16%, respectively). Importantly, only GD2 ions were detected when at the higher *Library 3-5* concentrations (data not shown). Shown in Figure 2.12 are the ESI mass spectra acquired in negative ion mode for 14G2a mAb (2.5 μM) and *Library 6* or *Library 7* (4 μM of each ganglioside). The CID results are consistent with those obtained for *Library 1-2*, with singly and doubly deprotonated GD2 ions dominating, and GM3 and GM4 ions present at lower abundance (5% and 12%, respectively). Only GD2 ions were released for *Library 8-10* (data not shown).

Taken together, the CaR-ESI-MS data suggest that the 14G2a mAb, although exhibiting a strong preference for GD2, has a non-negligible affinity for GM3 and GM4. These results are intriguing as they are not expected based on the ganglioside oligosaccharide affinity data described above. The CaR-ESI-MS results also suggest that the mAb does not bind appreciably to fucosyl-GM1, GM1, GM2, GD1a, GD1b, GD3, GT1a and GT1b.

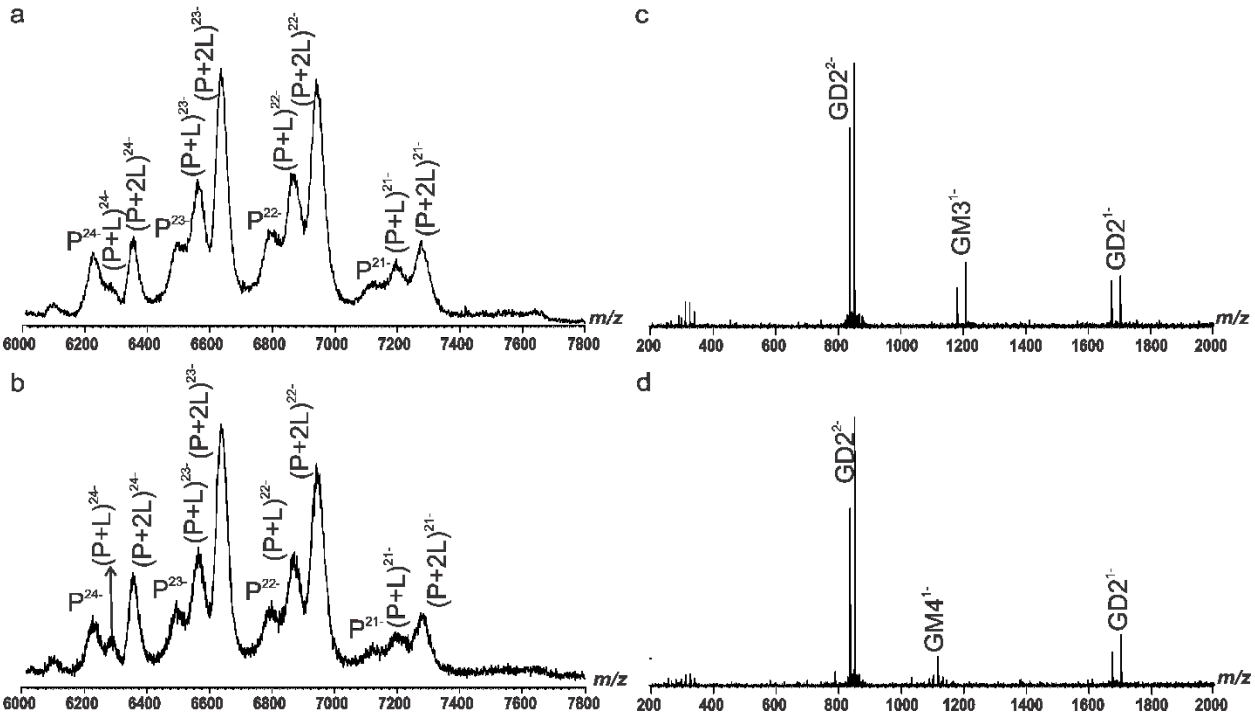

Figure 2.11. ESI mass spectra acquired in negative ion mode for a 200 mM aqueous ammonium acetate solution (pH 6.8) containing 14G2a mAb (2.5 μM) and (a) *Library 1* (4 μM of each

ganglioside) and (b) *Library 2* (4 μM of each ganglioside). (c) and (d) CID mass spectra acquired in the Trap region for the $(P + L)^{22-}$ ions using a collision energy of 100 V.

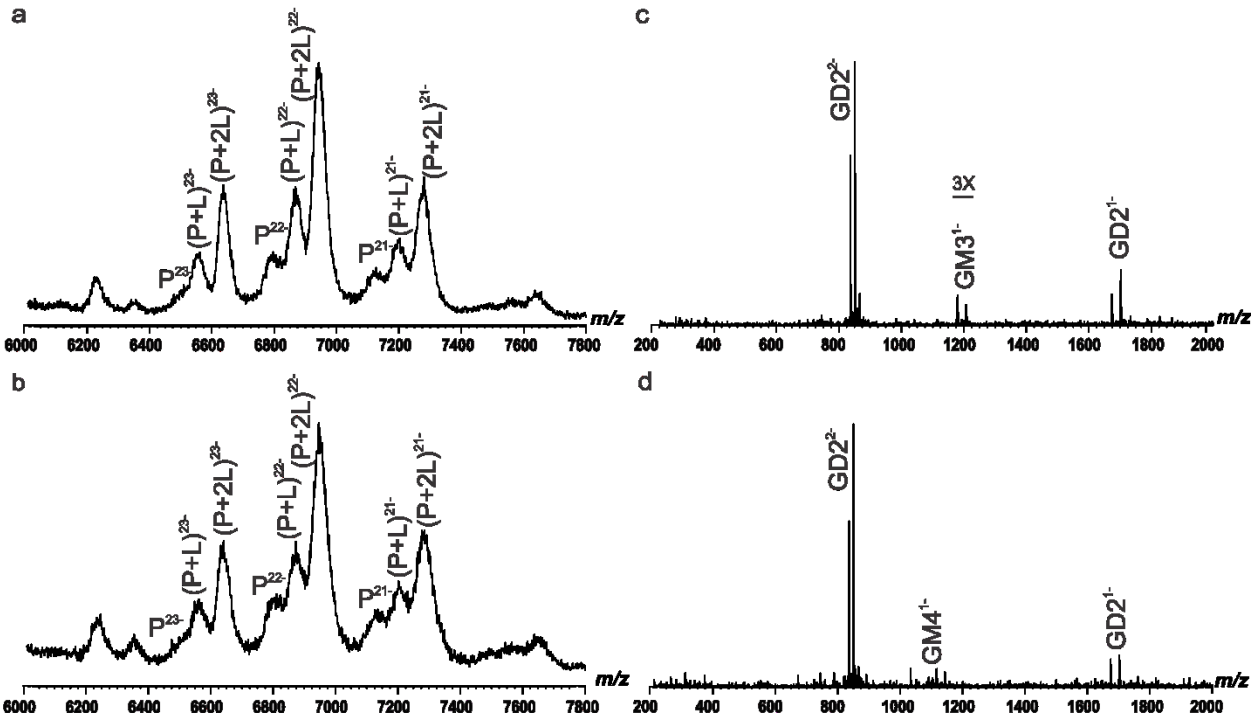

Figure 2.12. ESI mass spectra acquired in negative ion mode for a 200 mM aqueous ammonium acetate solution (pH 6.8) containing 14G2a mAb (2.5 μM) and (a) *Library 6* (4 μM of each ganglioside) or (b) *Library 7* (4 μM of each ganglioside). (c) and (d) CID mass spectra acquired in the Trap region for the $(P + L)^{22-}$ ions using a collision energy of 100 V.

Following the same procedure, the CaR-ESI-MS measurements were also carried out on the aqueous ammonium acetate solutions (200 mM, pH 6.8) of hu3F8 or hu3F8 E1K/D32H mAbs and one of *Library 1-10* (data not shown). Notably, only GD2 ions were found to be released. These results suggest that the two mAbs exhibit much higher specificity for GD2, compared to the 14G2a mAb.

2.3.3 Investigating binding properties of GD2-containing nanodiscs for anti-GD2 antibodies

2.3.3.1 Quantifying GD2 incorporation efficiency in NDs

The last part of this study involved measuring the affinity of the 14G2a mAb and the hu3F8 and hu3F8 E1K/D32H Fabs for GD2 displayed in an ND. In order to have confidence in the affinities, the average number of ganglioside GD2 molecules per ND in a given preparation must be accurately known. In the present work, an internal standard/MALDI-MS approach was applied. The amount of GD2 in a given ND preparation was determined by adding GD1b as an internal standard, mixing with 2,5-DHB matrix solutions, and carrying out MALDI-MS analysis, which were described in the Experimental Section 2.2.6.5. In this study, NDs composed of POPC and varying amounts of GD2 (1%, 5% and 10%, respectively) were prepared.

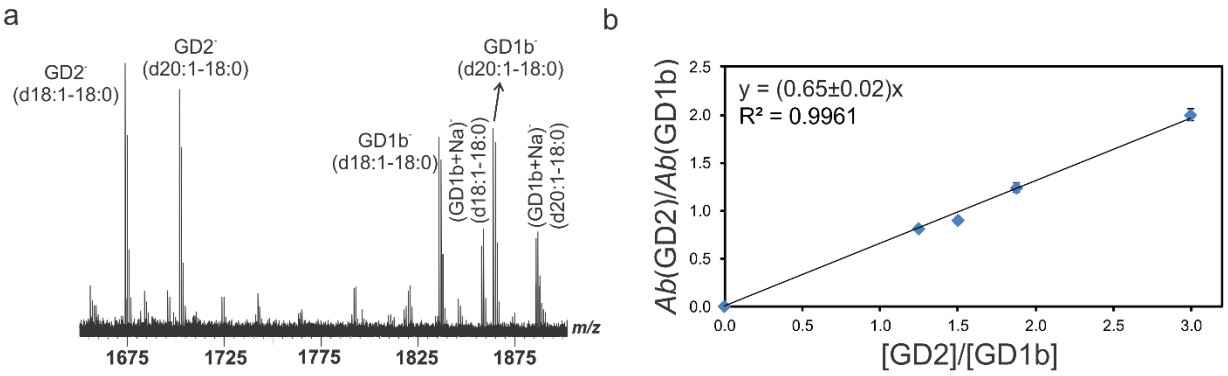

Figure 2.13. (a) Representative MALDI mass spectrum acquired in negative ion mode for mixture of ganglioside GD2 (5 μM), empty ND (1.7 μM) with GD1b (3.33 μM) after preparation with matrix. (b) Plot of the total abundance (*Ab*) ratio of GD2-to-GD1b ions versus the corresponding concentration ratio in solution; the concentration of ganglioside GD2 was 5 μM in all cases. The error bars corresponding to one standard deviation and the solid line corresponds to linear fit to the experimental data; also shown was slope and R^2 value from the linear fitting.

Shown in Figure 2.13 are representative MALDI mass spectrum acquired in negative ion mode for mixture of ganglioside GD2 (5 μM), empty ND (1.7 μM) and GD1b (3.33 μM) after preparation with matrix, as well as a plot of the total abundance (*Ab*) ratio of GD2-to-GD1b ions measured from the mass spectrum versus the corresponding concentration ratio in solution. It can be seen that both the GD2 and GD1b samples are composed primarily of two isoforms, d18:1-18:0 and d20:1-18:0 (Figure 2.13a). Additionally, linear fitting of the plot yielded a slope of 0.65 (Figure 2.13b). The concentration ratio of GD2 to GD1b in solution can be reliably determined from the measured ion abundance ratio, eq.2.22:

$$\frac{Ab(\text{GD2})}{Ab(\text{GD1b})} = 0.65\frac{[\text{GD2}]}{[\text{GD1b}]} \tag{2.22}$$

At a given ND concentration, the GD2 incorporation efficiency (IE_{GD2}) can be calculated from the ratio of the measured and expected concentration of GD2, eq. 2.23:

$$IE_{GD2} = \frac{[\text{GD2}]}{[\text{GD2}]_{\text{nominal}}} \tag{2.23}$$

which can be also expressed by eq. 2.24:

$$IE_{GD2} = \frac{[\text{GD2}]}{2 \times [\text{ND}] \times \%\text{GD2}} \tag{2.24}$$

Although IE_{GD2} can be determined at a single concentration of GD1b, it was more reliable to implement the measurements over a range of concentrations and calculate IE_{GD2} from the slope of a plot of total abundance ratio of GD2-to-GD1b ions versus ratio of the expected-to-measured GD2 concentration, eq. 2.25:

$$\frac{Ab(\text{GD2})}{Ab(\text{GD1b})} = 0.65 \times IE_{GD2} \times \frac{[\text{GD2}]_{\text{nominal}}}{[\text{GD1b}]} \tag{2.25}$$

The average number of GD2 per ND can be calculated from IE_{GD2} and %GD2, eq. 2.26:

$$(\text{GD2 per ND}) = [\text{GD2}] / [\text{ND}] = IE_{GD2} \times 2 \times \%\text{GD2} \tag{2.26}$$

Shown in Figure 2.14a-c are representative mass spectra acquired for solutions of 3.3 µM, 3.6 µM and 4 µM of ND containing 5% GD2 and 95% POPC and 5.5 µM, 5 µM and 4.4 µM of GD1b, respectively. The GD2 incorporation efficiency (IE_{GD2}) for 5% GD2 and 95% POPC ND, determined from a plot of the abundance ratio of GD2-to-GD1b ions versus expected concentration ratios measured at five different 5% GD2 and 95% POPC ND concentrations, was found to be 0.72 (Figure 2.14d), which translates to an average of 7.2 GD2 per ND. Following the same approach, the GD2 incorporation efficiency for the 1% GD2 99% POPC ND was 0.86. This value was corresponding to an average of 1.7 GD2 per ND. However, a smaller lower IE_{GD2} value was found for 10% GD2 90% POPC ND (0.6, 12 GD2 per ND).

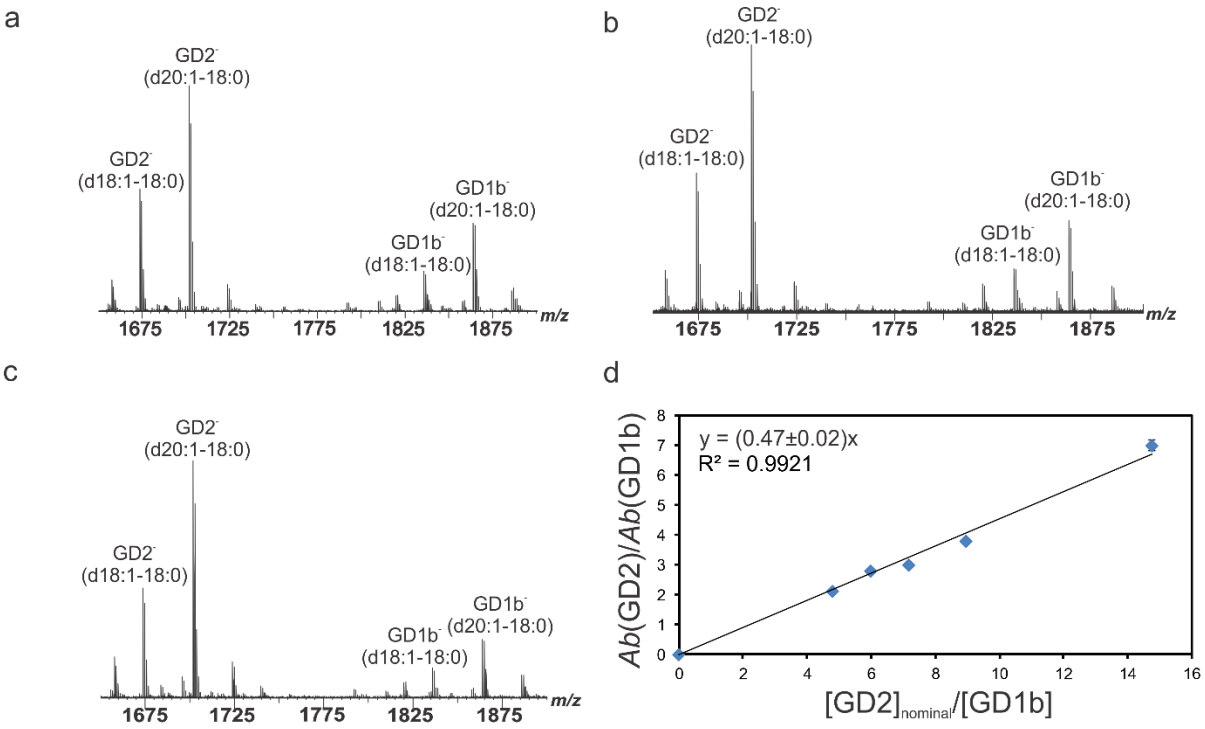

Figure 2.14. Representative MALDI mass spectra acquired in negative ion mode for (a) mixture of 3.3 µM of 5% GD2 ND with 5.5 µM GD1b, (b) mixture of 3.6 µM of 5% GD2 ND with 5 µM GD1b, (c) mixture of 4 µM of 5% GD2 ND with 4.4 µM GD1b after preparation with matrix. (d) Plot of the total abundance (*Ab*) ratio of GD2-to-GD1b ions versus the ratio of $[GD2]_{norminal}$-to-

[GD1b]. The error bars corresponding to one standard deviation and the solid line corresponds to linear fit to the experimental data; also shown is slope and R^2 value from the linear fitting.

2.3.3.2 Affinities of GD2-containing nanodiscs for hu3F8 and hu3F8 E1K/D32H Fabs

Having established the different amounts of GD2 in the GD2-containing POPC NDs (1%, 5% and 10% GD2), the *proxy ligand* ESI-MS assay was used to quantify the influence of GD2 content on the interactions between the GD2-containing POPC NDs and hu3F8 and hu3F8 E1K/D32H Fabs. Shown in Figure 2.15a is a representative ESI mass spectrum acquired in positive ion mode for a 200 mM aqueous ammonium acetate solution (pH 6.8) of hu3F8 Fab (4 μM) and $GD2_{os}$ (L_{proxy}, 8 μM). Signal corresponding to hu3F8 Fab bound to $GD2_{os}$ ions were detected (i.e.,$(P + GD2_{os})^{n+}$ ions where n = 13-16). Upon addition of 5% GD2 POPC ND (3 μM) to the solution, $(P + GD2)^{n+}$ ions, at n = 13-16, were also detected (Figure 2.15b). The $(P + GD2)^{n+}$ ions originate from the gas-phase dissociation from the ND-associated complex of GD2-bound hu3F8 Fab. Notably, the introduction of the GD2 POPC ND resulted in a measurable increase in R_{proxy}. This increase results from a fraction of the hu3F8 Fab binding to $GD2_{os}$, which effectively reduces the concentration of free hu3F8 Fab available for binding to $GD2_{os}$. Plots of measured R_{proxy} versus GD2 concentration under varying amounts of GD2 (1%, 5% and 10%) in NDs are shown in Figure 2.16a-c, respectively. Also shown are the theoretical curves corresponding to the $K_{a,GD2}$ that best describes the experimental data measured for each ND sample.

Plotted in Figure 2.16d are the measured $K_{a,GD2}$ versus the percentage of GD2 (1%, 5% and 10%) in the ND samples. Notably, there was a systematic decrease in the magnitude of $K_{a,GD2}$ with increasing GD2 content of the POPC NDs ($K_{a,1\%\ GD2} = (2.6 \pm 0.3) \times 10^5\ M^{-1}$, $K_{a,5\%\ GD2} = (1.6 \pm 0.1) \times 10^5\ M^{-1}$ and $K_{a,10\%\ GD2} = (0.7 \pm 0.07) \times 10^5\ M^{-1}$). This behavior might be correlated with the "clustering" of GD2 in the phospholipid membrane. Some of GD2 oligosaccharide moieties may

be involved in hydrogen bonding formation with neighboring GD2 molecules, which has the impact of sterically hindering GD2 binding to hu3F8 Fab.[27,28] Moreover, the binding data revealed that K_a values measured for hu3F8 Fab binding to GD2 in ND and $GD2_{os}$ were (2.6 ± 0.3) x 10^5 M^{-1} and (4.3 ± 0.1) x 10^5 M^{-1}, respectively, which indicated that membrane has no significant influence on binding affinity.

Following an analogous procedure, the *proxy ligand* ESI-MS assay was extended to investigate the affinities of hu3F8 E1K/D32H Fab for GD2 NDs (Figure 2.17). Overall, the results are very similar to those obtained for hu3F8 Fab. The affinities for hu3F8 E1K/D32H Fab binding to GD2 ($K_{a,1\%\ GD2}$ = (5.3 ± 0.4) x 10^5 M^{-1}, $K_{a,5\%\ GD2}$ = (2.5 ± 0.2) x 10^5 M^{-1} and $K_{a,10\%\ GD2}$ = (1.8 ± 0.2) x 10^5 M^{-1}) showed an obvious increase in binding efficiency relative to hu3F8 Fab, which was in good agreement with binding data measured for $GD2_{os}$ and the reported SPR data.[16] It further confirmed that two point mutations (E1K (L-FR1) and D32H (L-CDR1)) of hu3F8 Fab altered the electrostatic surface potential of the antigen binding site, allowing for an increase in the positive charge to enhance the interaction with the negatively charged GD2.[16] As observed for hu3F8 Fab, the apparent affinity of hu3F8 E1K/D32H Fab for GD2 decreased with increasing GD2 content (Figure 2.18).

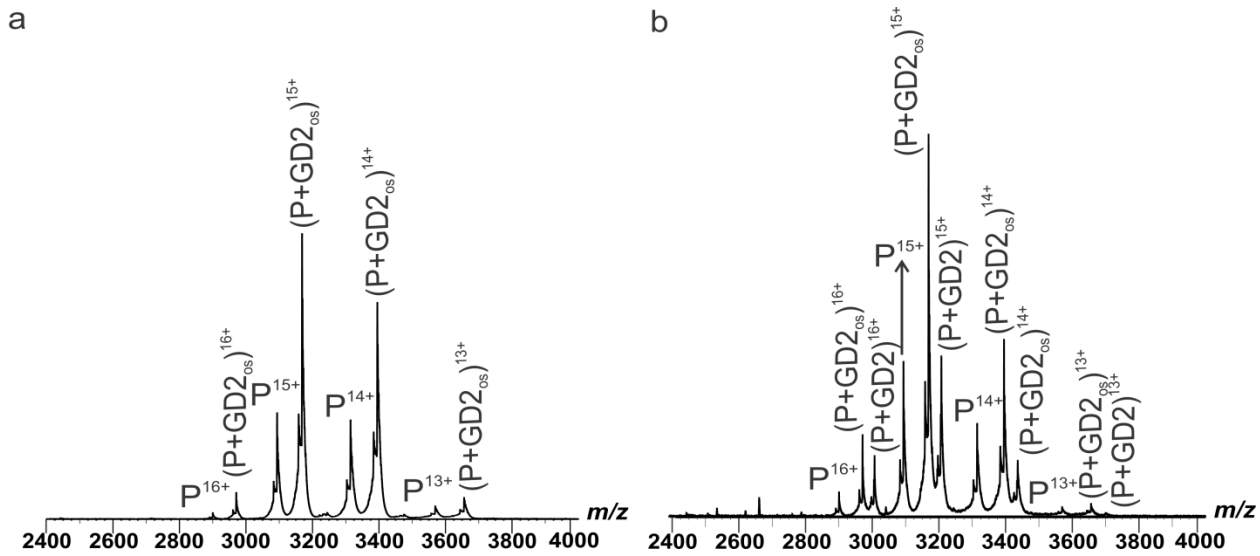

Figure 2.15. ESI mass spectra acquired in positive ion mode for hu3F8 Fab (4 μM), $GD2_{os}$ (L_{proxy}, 8 μM) without (a) and with (b) 5% GD2 POPC ND (3 μM).

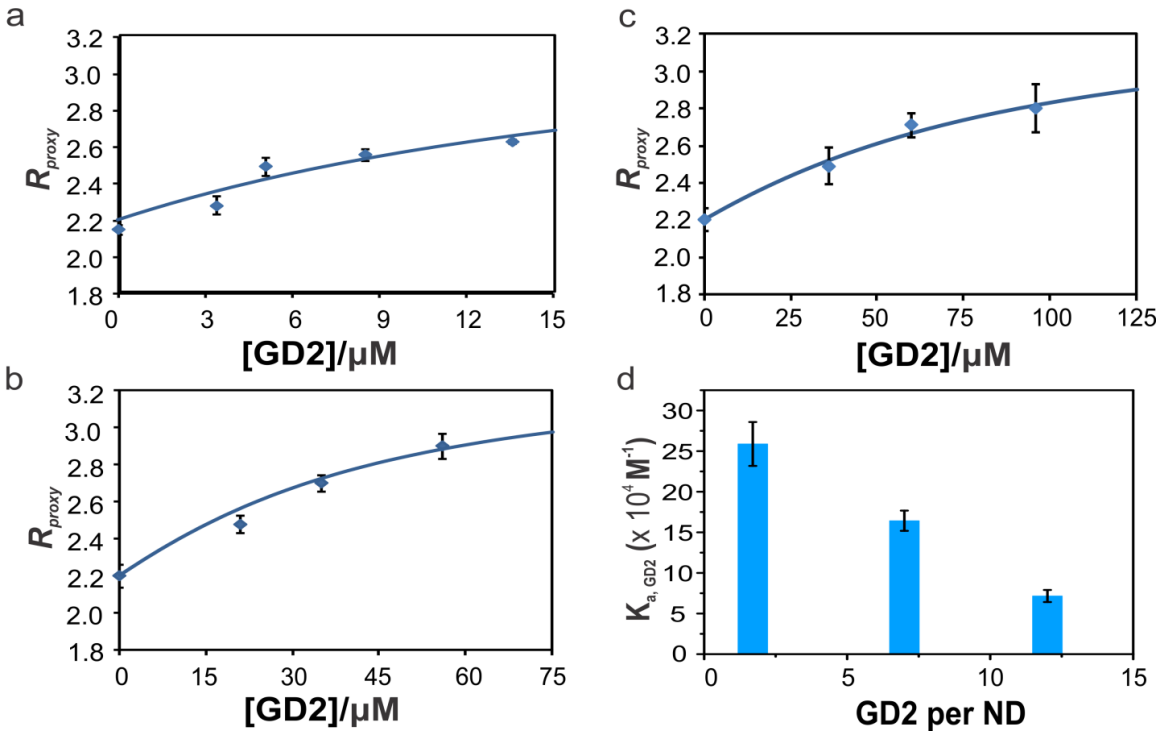

Figure 2.16. Plots of R_{proxy} (≡ *Ab*(hu3F8 Fab + $GD2_{os}$)/*Ab*(hu3F8 Fab)) versus (a) 1% GD2 POPC ND concentration, (b) 5% GD2 POPC ND concentration, (c) 10% GD2 POPC ND concentration measured by ESI-MS. (d) Bar graph of $K_{a,GD2}$ values measured for hu3F8 Fab binding to different

percentages (1%, 5% and 10%) of GD2 in NDs.

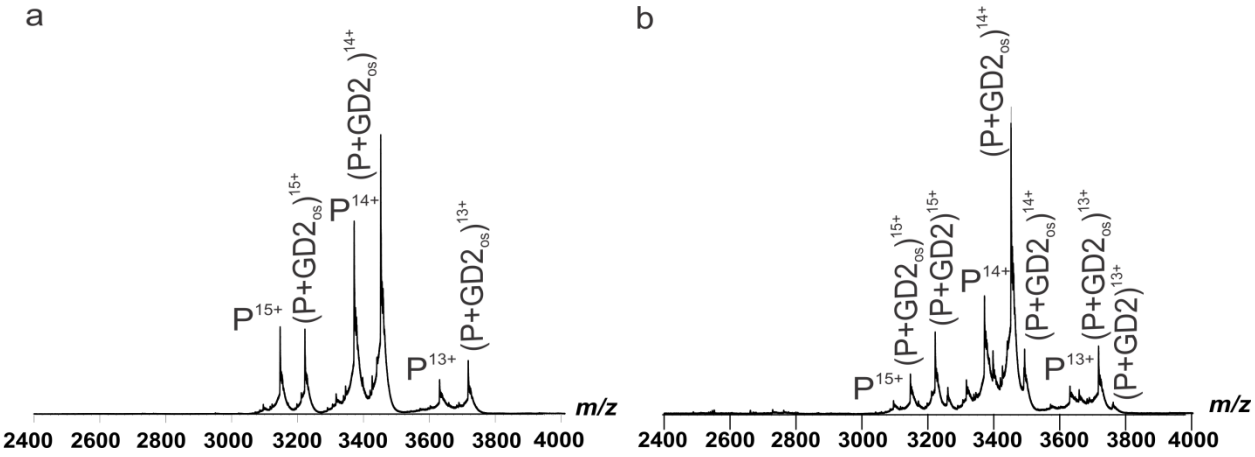

Figure 2.17. ESI mass spectra acquired in positive ion mode for hu3F8 E1K/D32H Fab (3.5 μM), GD2os (L_{proxy}, 3 μM) without (a) and with (b) 5% GD2 POPC ND (2 μM).

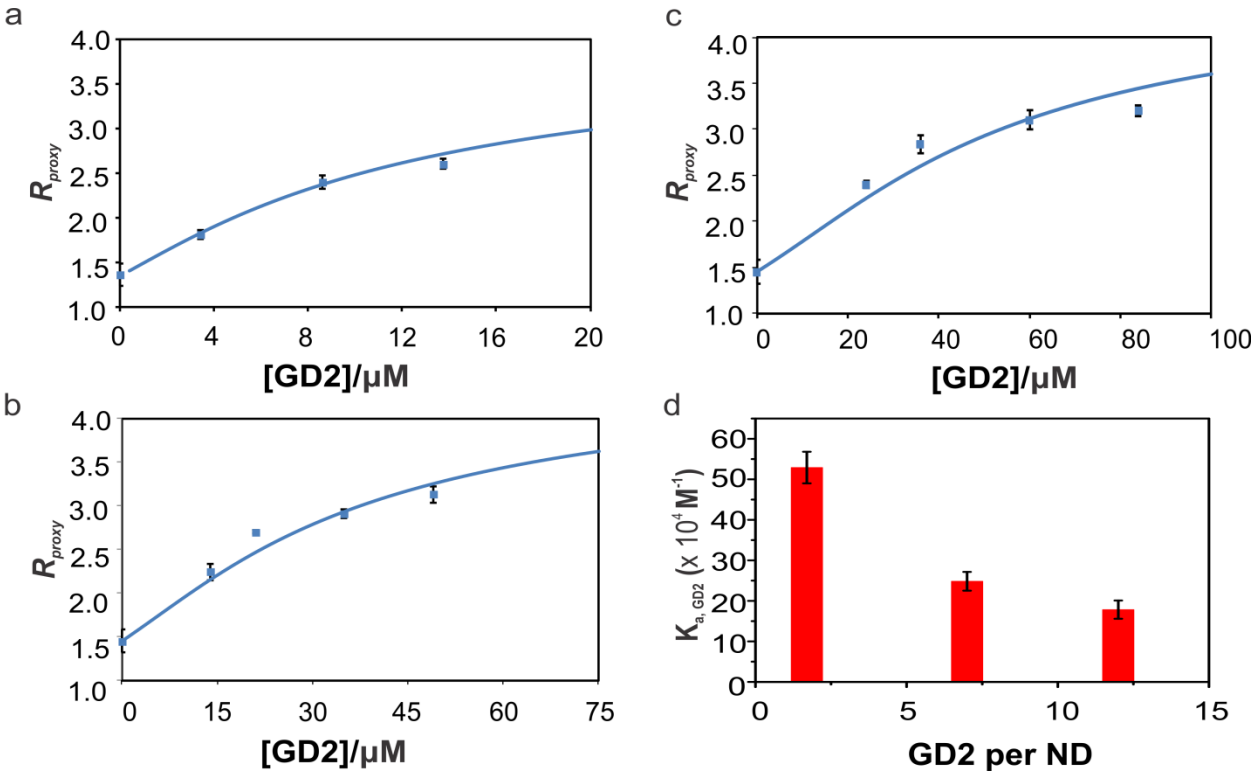

Figure 2.18. Plots of R_{proxy} (≡ *Ab*(hu3F8 E1K/D32H Fab + GD2os)/*Ab*(hu3F8 Fab)) versus (a) 1% GD2 POPC ND concentration, (b) 5% GD2 POPC ND concentration, (c) 10% GD2 POPC ND

concentration measured by ESI-MS. (d) Bar graph of K_a values measured for hu3F8 E1K/D32H Fab binding to different percentages (1%, 5% and 10%) of GD2 in NDs.

2.3.3.3 Affinities of GD2-containing nanodiscs for 14G2a mAb

To measure the affinity of 14G2a mAb for GD2 presented in NDs, the competitive CUPRA-*proxy ligand* method was used. hCA and $GD2_{os}$-CUPRA ligand ($GD2_{os}$-CL) served as P_{proxy} and L_{proxy} for these measurements, respectively. Shown in Figure 2.19b is a representative ESI mass spectrum acquired for the aqueous ammonium acetate solution (200 mM, pH 6.8) of hCA (5 μM) and $GD2_{os}$-CL (8 μM). Ions corresponding to the free hCA and hCA bound to $GD2_{os}$-CL were detected, i.e., hCA^{n+} and $(hCA + GD2_{os}\text{-}CL)^{n+}$ at n = 9-11. The affinity of $GD2_{os}$-CL for hCA was found to be $(27.5 \pm 1.7) \times 10^4\ M^{-1}$. The binding of 14G2a mAb with $GD2_{os}$-CL was then evaluated. ESI-MS measurements were performed on aqueous ammonium acetate solutions (200 mM, pH 6.8) of 14G2a mAb (1.5 μM) and $GD2_{os}$-CL at concentrations ranging from 0 to 21 μM. From the ESI-MS data, the apparent association constants ($K_{a,app}$) for the first and second $GD2_{os}$-CL binding sites were $(10 \pm 1.1) \times 10^4\ M^{-1}$ and $(3.7 \pm 0.5) \times 10^4\ M^{-1}$, respectively, giving an intrinsic association constant ($K_{a,int}$, per binding site) for the $GD2_{os}$-CL of $(5.8 \pm 0.2) \times 10^4\ M^{-1}$. Notably, this value is in good agreement with the value measured for $GD2_{os}$ ($K_{a,int,GD2os} = (7.0 \pm 0.2) \times 10^4\ M^{-1}$).

Next, binding measurements were performed on 14G2a mAb and NDs prepared with 1%, 5% and 10% POPC GD2. Shown in Figure 2.20a-c are the plots of R_{proxy} versus 14G2a mAb concentration measured for 1%, 5% and 10% GD2 POPC NDs, respectively. Also shown were the theoretical curve corresponding to the $K_{a,GD2}$ that best describes the experimental data measured for each ND sample. Since there was a competitive binding event, the relative abundance of $GD2_{os}$-CL-bound hCA decreased upon increase of 14G2a mAb to the solution. This decrease was associated with 14G2a mAb binding to $GD2_{os}$-CL, which effectively reduced the concentration of

$GD2_{os}$-CL available for binding to hCA. The $K_{a,GD2}$ values measured for the POPC NDs containing three different percentages of GD2 are plotted in Figure 2.20d. It can be seen that there was a systematic decrease in the magnitude of $K_{a,GD2}$ with increasing the GD2 content of the NDs ($K_{a,1\%\ GD2}$ = (3.3 ± 0.6) x 10^5 M^{-1}, $K_{a,5\%\ GD2}$ = (1.4 ± 0.4) x 10^5 M^{-1} and $K_{a,10\%\ GD2}$ = (0.7 ± 0.03) x 10^5 M^{-1}). This finding indicates that the extent of GD2 binding to 14G2a mAb was sensitive to the GD2 content of the NDs. According to the binding data, measurements carried out using 1% GD2 POPC ND yielded an affinity of (3.3 ± 0.6) x 10^5 M^{-1}, which was larger than the value obtained for the corresponding 14G2a mAb-$GD2_{os}$ interactions ($K_{a1,app}$ = (12 ± 0.9) x 10^4 M^{-1}, $K_{a2,app}$ = (4.1 ± 0.4) x 10^4 M^{-1} and $K_{a,int,GD2os}$ = (7.0 ± 0.2) x 10^4 M^{-1}).

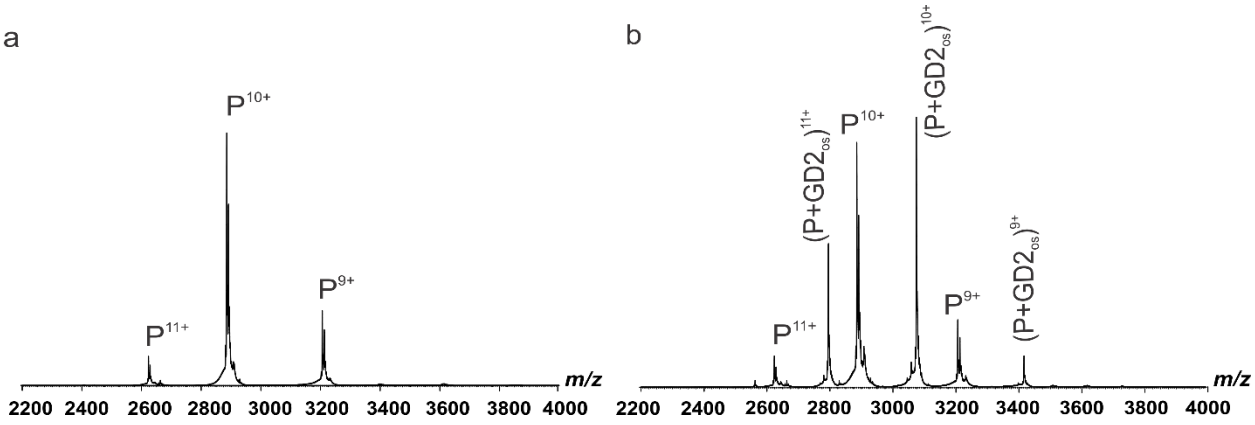

Figure 2.19. ESI mass spectra in positive ion mode of (a) hCA (5 μM) and with (b) $GD2_{os}$-CL (8 μM).

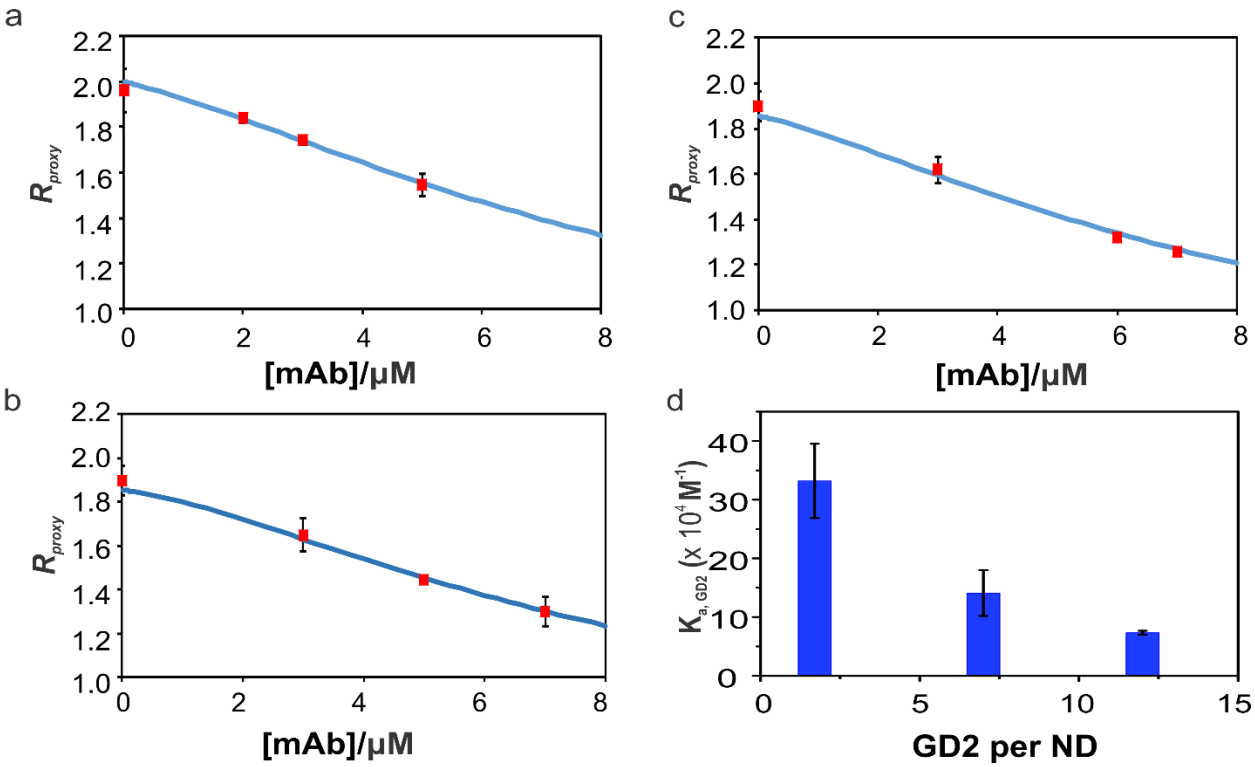

Figure 2.20. Plots of R_{proxy} (≡ *Ab*(hCA + $GD2_{os}$-CL)/*Ab*(hCA)) versus 14G2a mAb concentration measured for (a) 1% GD2 POPC ND, (b) 5% GD2 POPC ND, (c) 10% GD2 POPC ND. (d) Bar graph of $K_{a,GD2}$ values measured for 14G2a mAb binding to different percentages (1%, 5% and 10%) of GD2 in NDs.

2.4 Conclusions

In summary, the ganglioside affinities and specificities of three anti-GD2 antibodies were evaluated using ESI-MS. The affinities of fourteen ganglioside oligosaccharides for the hu3F8 and E1K/D32H Fabs, and the 14G2a mAb were measured using direct ESI-MS assay. The results of $GD2_{os}$ binding measurements revealed that the anti-GD2 antibodies were ranked in order of affinity: hu3F8 E1K/D32H Fab ($K_{a,GD2os}$ = (22 ± 1.5) x 10^5 M^{-1}) > hu3F8 Fab ($K_{a,GD2os}$ = (4.3 ± 0.1) x 10^5 M^{-1}) > 14G2a mAb ($K_{a1,app}$ = (1.2 ± 0.9) x 10^5 M^{-1}, $K_{a2,app}$ = (4.1 ± 0.4) x 10^4 M^{-1} and $K_{a,int,GD2os}$ = (7.0 ± 0.2) x 10^4 M^{-1} (per binding site). Measurements performed on other ganglioside

oligosaccharides indicated that all of them were also recognized by these antibodies, although with lower affinities, in the 2.0 x 10^2 M^{-1} - 5.8 x 10^3 M^{-1} range. Taken together, the results of direct ESI-MS are compelling to note that the hu3F8 Fab exhibits relatively excellent specificity to $GD2_{os}$ among these antibodies. The CaR-ESI-MS assay was used to screen small libraries of gangliosides in NDs against hu3F8, hu3F8 E1K/D32H and 14G2a mAbs. The results of these measurements confirmed that the mAbs exhibited a strong preference for GD2. In the case of hu3F8 and hu3F8 E1K/D32H mAbs no binding to gangliosides other than GD2 was detected. Interestingly, 14G2a mAb was found to bind to GM3 and GM4, although their relative abundances were low compared to GD2. Finally, the results of competitive ESI-MS binding assays revealed the K_a values measured for hu3F8 and hu3F8 E1K/D32H Fabs and 14G2a mAb binding to GD2 in ND and $GD2_{os}$ were similar, which indicated that membrane has no significant influence on binding affinity. Moreover, the extent of GD2 binding was found to decrease with increasing GD2 content of the NDs. This observation is attributed to GD2 clustering in the membrane at higher concentrations.

2.5 References

(1) Fredman, P.; Hedberg, K.; Brezicka, T. Gangliosides as Therapeutic Targets for Cancer. *BioDrugs.* **2003**, *17* (3), 155–167.

(2) Ahmed, M.; Cheung, N.-K. V. Engineering Anti-GD2 Monoclonal Antibodies for Cancer Immunotherapy. *FEBS Lett.* **2014**, *588* (2), 288–297.

(3) Hakomori, S. Glycosylation Defining Cancer Malignancy: New Wine in an Old Bottle. *Proc. Natl. Acad. Sci.* **2002**, *99* (16), 10231–10233.

(4) Doronin, I. I.; Vishnyakova, P. A.; Kholodenko, I. V; Ponomarev, E. D.; Ryazantsev, D. Y.; Molotkovskaya, I. M.; Kholodenko, R. V. Ganglioside GD2 in Reception and Transduction of Cell Death Signal in Tumor Cells. *BMC Cancer.* **2014**, *14* (1), 295.

(5) Lammie, G.; Cheung, N.; Gerald, W.; Rosenblum, M.; Cordoncardo, C. Ganglioside GD(2) expression in the human nervous-system and in neuroblastomas-an immunohistochemical study. *Int. J. Oncol.* **1993**, 909-915.

(6) Cheung, N.-K. V; Dyer, M. A. Neuroblastoma: Developmental Biology, Cancer Genomics and Immunotherapy. *Nat. Rev. Cancer.* **2013**, *13* (6), 397–411.

(7) Svennerholm, L.; Boström, K.; Fredman, P.; Jungbjer, B.; Lekman, A.; Månsson, J.-E.; Rynmark, B.-M. Gangliosides and Allied Glycosphingolipids in Human Peripheral Nerve and Spinal Cord. *Biochim. Biophys. Acta - Lipids Lipid Metab.* **1994**, *1214* (2), 115–123.

(8) Aixinjueluo, W.; Furukawa, K.; Zhang, Q.; Hamamura, K.; Tokuda, N.; Yoshida, S.; Ueda, R.; Furukawa, K. Mechanisms for the Apoptosis of Small Cell Lung Cancer Cells Induced by Anti-GD2 Monoclonal Antibodies. *J. Biol. Chem.* **2005**, *280* (33), 29828–29836.

(9) Cheung, N.-K. V.; Cheung, I. Y.; Kushner, B. H.; Ostrovnaya, I.; Chamberlain, E.; Kramer, K.; Modak, S. Murine Anti-GD2 Monoclonal Antibody 3F8 Combined With Granulocyte-

Macrophage Colony-Stimulating Factor and 13- Cis -Retinoic Acid in High-Risk Patients With Stage 4 Neuroblastoma in First Remission. *J. Clin. Oncol.* **2012**, *30* (26), 3264–3270.

(10) Cheung, N.-K. V.; Guo, H.; Hu, J.; Tassev, D. V; Cheung, I. Y. Humanizing Murine IgG3 Anti-GD2 Antibody M3F8 Substantially Improves Antibody-Dependent Cell-Mediated Cytotoxicity While Retaining Targeting in Vivo. *Oncoimmunology.* **2012**, *1* (4), 477–486.

(11) Shusterman, S.; London, W. B.; Gillies, S. D.; Hank, J. A.; Voss, S. D.; Seeger, R. C.; Reynolds, C. P.; Kimball, J.; Albertini, M. R.; Wagner, B.; et al. Antitumor Activity of Hu14.18-IL2 in Patients With Relapsed/Refractory Neuroblastoma: A Children's Oncology Group (COG) Phase II Study. *J. Clin. Oncol.* **2010**, *28* (33), 4969–4975.

(12) Ari, P.; Kars, M.; Meany, H.; Pestieau, S. Treatment of Transient Peripheral Neuropathy During Chimeric 14.18 Antibody Therapy in Children With Neuroblastoma. *J. Pediatr. Hematol. Oncol.* **2018**, *40* (2), e113–e116.

(13) Sait, S.; Modak, S. Anti-GD2 Immunotherapy for Neuroblastoma. *Expert Rev. Anticancer Ther.* **2017**, *17* (10), 889–904.

(14) Sterner, E.; Peach, M. L.; Nicklaus, M. C.; Gildersleeve, J. C. Therapeutic Antibodies to Ganglioside GD2 Evolved from Highly Selective Germline Antibodies. *Cell Rep.* **2017**, *20* (7), 1681–1691.

(15) Cheung, N.-K. V.; Guo, H.; Hu, J.; Tassev, D. V; Cheung, I. Y. Humanizing Murine IgG3 Anti-GD2 Antibody M3F8 Substantially Improves Antibody-Dependent Cell-Mediated Cytotoxicity While Retaining Targeting in Vivo. *Oncoimmunology.* **2012**, *1* (4), 477–486.

(16) Zhao, Q.; Ahmed, M.; Guo, H.; Cheung, I. Y.; Cheung, N.-K. V. Alteration of Electrostatic Surface Potential Enhances Affinity and Tumor Killing Properties of Anti-Ganglioside GD2 Monoclonal Antibody Hu3F8. *J. Biol. Chem.* **2015**, *290* (21), 13017–13027.

(17) Grant, O. C.; Smith, H. M.; Firsova, D.; Fadda, E.; Woods, R. J. Presentation, Presentation, Presentation! Molecular-Level Insight into Linker Effects on Glycan Array Screening Data. *Glycobiology.* **2014**, *24* (1), 17–25.

(18) Mallagaray, A.; Lockhauserbäumer, J.; Hansman, G.; Uetrecht, C.; Peters, T. Attachment of Norovirus to Histo Blood Group Antigens: A Cooperative Multistep Process. *Angew. Chemie Int. Ed.* **2015**, *54* (41), 12014–12019.

(19) Ritchie, T. K.; Grinkova, Y. V.; Bayburt, T. H.; Denisov, I. G.; Zolnerciks, J. K.; Atkins, W. M.; Sligar, S. G. Reconstitution of Membrane Proteins in Phospholipid Bilayer Nanodiscs. In *Methods in Enzymology*. **2009**, *464*, 211–231.

(20) Denisov, I. G.; Grinkova, Y. V.; Lazarides, A. A.; Sligar, S. G. Directed Self-Assembly of Monodisperse Phospholipid Bilayer Nanodiscs with Controlled Size. *J. Am. Chem. Soc.* **2004**, *126* (11), 3477–3487.

(21) Kitova, E. N.; El-Hawiet, A.; Schnier, P. D.; Klassen, J. S. Reliable Determinations of Protein–Ligand Interactions by Direct ESI-MS Measurements. Are We There Yet? *J. Am. Soc. Mass Spectrom.* **2012**, *23* (3), 431–441.

(22) Kitova, E. N.; Kitov, P. I.; Paszkiewicz, E.; Kim, J.; Mulvey, G. L.; Armstrong, G. D.; Bundle, D. R.; Klassen, J. S. Affinities of Shiga Toxins 1 and 2 for Univalent and Oligovalent Pk-Trisaccharide Analogs Measured by Electrospray Ionization Mass Spectrometry. *Glycobiology.* **2007**, *17* (10), 1127–1137.

(23) Han, L.; Kitova, E. N.; Li, J.; Nikjah, S.; Lin, H.; Pluvinage, B.; Boraston, A. B.; Klassen, J. S. Protein–Glycolipid Interactions Studied in Vitro Using ESI-MS and Nanodiscs: Insights into the Mechanisms and Energetics of Binding. *Anal. Chem.* **2015**, *87* (9), 4888–4896.

(24) Sun, J.; Kitova, E. N.; Wang, W.; Klassen, J. S. Method for Distinguishing Specific from Nonspecific Protein−Ligand Complexes in Nanoelectrospray Ionization Mass Spectrometry. *Anal. Chem.* **2006**, *78* (9), 3010–3018.

(25) Daniel, J. M.; Friess, S. D.; Rajagopalan, S.; Wendt, S.; Zenobi, R. Quantitative Determination of Noncovalent Binding Interactions Using Soft Ionization Mass Spectrometry. *Int. J. Mass Spectrom.* **2002**, *216* (1), 1–27.

(26) Sterner, E.; Peach, M. L.; Nicklaus, M. C.; Gildersleeve, J. C. Therapeutic Antibodies to Ganglioside GD2 Evolved from Highly Selective Germline Antibodies. *Cell Rep.* **2017**, *20* (7), 1681–1691.

(27) Shi, J.; Yang, T.; Kataoka, S.; Zhang, Y.; Diaz, A. J.; Cremer, P. S. GM 1 Clustering Inhibits Cholera Toxin Binding in Supported Phospholipid Membranes. *J. Am. Chem. Soc.* **2007**, *129* (18), 5954–5961.

(28) Yuan, C.; Johnston, L. J. Atomic Force Microscopy Studies of Ganglioside GM1 Domains in Phosphatidylcholine and Phosphatidylcholine/Cholesterol Bilayers. *Biophys. J.* **2001**, *81* (2), 1059–1069.

Chapter 3

Elusive Protein-Glycosphingolipid Interactions Revealed by Membrane Anchor-Assisted Catch-and-Release Electrospray Ionization Mass Spectrometry

3.1 Introduction

Interactions between glycosphingolipids (GSLs) and glycan-binding proteins (GBPs) are involved in many human cellular processes, including cell recognition, signaling and the immune response, and are implicated in a variety of pathophysiological processes, such as cancer progression, neurodegeneration and bacterial and viral infections.[1-3] Identifying these interactions and elucidating their biological roles is fundamentally important and improves human health by guiding development of new diagnostics and therapeutics to detect and treat diseases.[4,5] However, owing to shortcomings in existing analytical methods, uncovering these interactions remains challenging and, although the GSL ligands of some GBPs are known, it is widely believed that the full repertoire of cellular GSL receptors of the vast majority of GBPs have yet to be identified.[6-8] Among the key challenges hindering the discovery of GSL ligands are the low affinities (dissociation constant (K_d) of ~ 1 mM) typical of most monovalent GBP-GSL interactions, the extremely limited availability of purified GSLs and the influence of membrane composition, in particular the 'glycan' environment, on GSL recognition.[8,9] As discussed in more detail below, none of the established binding assays possess the versatility, sensitivity and specificity needed to comprehensively map the GSL receptors in different cells and tissue that are recognized by a given GBP. Consequently, advancement in this important area of functional glycomics critically depends

on the development of new analytical methods.

Surface plasmon spectroscopy-based supported-lipid bilayer nanocube biosensors have recently emerged as a promising technique for identifying GBP-GSL binding and quantifying the kinetics of the interactions.[10,11] The sensitivity of the assay allows for the detection of very weak GBP-GSL complexes. However, because the identity and number of bound ligands can't be determined, the assay is of limited use for screening GSL mixtures. Nevertheless, by comparing binding data acquired for membranes of different lipid/GSL compositions, some insights into factors affecting GBP-GSL binding have been inferred.[12] Most notably, Wu and co-workers reported a significant enhancement in the binding of GBPs with multiple binding sites to low affinity GSL ligands when they are presented together with a high affinity ligand in the bilayer.[10,11] These observations were explained in terms of reduced dimensionality, wherein binding to a high affinity ligand increases the lifetime of the GBP at the surface of the membrane and, thereby, allowing the recruitment of low affinity GSL ligands and the formation of hetero-multivalent complexes.[11] These findings, if shown to be general valid, have important implications for the design of GSL screening assays. In particular, they point to the need for assays that allow for GSLs to be screened as mixtures, rather than individually, and that enable direct identification of GSL ligands involved in binding.

Recently, a microarray-based shotgun glycomics screening method, which overcomes the challenge of the limited availability of purified GSLs, was developed.[13] This technique uses a microarray constructed from GSLs extracted from cells or tissue, derivatized with a hetero-bifunctional fluorescent tag, fractionated and printed on a glass slide.[13] The GSL array is then screened against a target GBP to identify ligands. This approach, however, is limited by the unnatural presentation and the lack of mobility of modified GSLs on the slide, and the general

inability to detect low affinity interactions.[14,15] Moreover, to enable ligand identification, the purified glycans are spatially separated in the GSL microarray (and glycan microarrays in general). As a result, low affinity GSL ligands that contribute to cellular recognition through hetero-multivalent binding would go undetected.

Native mass spectrometry (MS), electrospray ionization (ESI)-MS analysis using native-like solution conditions, is routinely used to detect and quantify GBP-oligosaccharide interactions *in vitro*.[16,17] When implemented using a catch-and-release (CaR) strategy, it also enables the high-throughput screening of oligosaccharide libraries.[18-20] Recently, CaR-ESI-MS performed using model membranes, such as nanodiscs (NDs) and picodiscs, containing GSLs, has shown promise for the discovery of GBP-GSL interactions.[21] Membrane-bound GSLs 'caught' by a GBP in solution are transferred to the gas phase by ESI.[22] During desolvation, intact GBP-GSL complexes dissociate from the model membranes in a process that is presumably driven by Coulombic repulsion between the charged GBP and membrane.[22] In some cases, the GSL ligands can be identified directly from the molecular weights (MWs) of the gaseous GBP-GSL complex ions. However, for large or heterogeneous GBPs, or for GBPs with multiple binding sites (and can bind to different GSLs), the GSLs are 'released', as ions, from the gaseous GBP-GSL complexes and identified from their MWs and, if needed, diagnostic fragment ions produced by collision-induced dissociation (CID).[21,22]

An attractive feature of CaR-ESI-MS is that it can be carried out using model membranes produced from natural libraries of GSLs extracted from cells or tissue and, thus, has tremendous potential for the discovery of GSL receptors.[21] However, the detection of low affinity GSL ligands by CaR-ESI-MS remains challenging, particularly for GBPs with a single binding site.[23] In principle, the detection of thermodynamically weak GBP-GSL interactions can be enhanced by

increasing the concentration of GSL in solution. Unfortunately, high concentrations of model membranes generally hinder the GBP detection due to ion suppression effects in ESI. Moreover, model membranes with high GSL content are generally unstable.[12,24]

Here, we describe a new CaR-ESI-MS strategy, which we refer to as membrane anchor-assisted CaR-ESI-MS assay, that enhances the detection of low affinity interactions between GBPs and GSLs in model membranes. The method, which was inspired by the recent findings that a high affinity GSL ligand can enhance GBP binding to low affinity ligands in membrane, involves covalent cross-linking of the GBP to the membrane through a modified lipid. Anchoring the GBP on the surface of the membrane enhances its local concentration and binding to GSL ligands. A notable feature of this approach is that it can, in principle, be applied to any GBP, including those possessing a single binding site. We demonstrate the reliability of this new approach using three human galectins and their interactions with gangliosides presented in NDs.

3.2 Experimental Section

3.2.1 Proteins

The recombinant fragment of the C-terminal carbohydrate recognition domain (residues 107–250) of human galectin-3 (hGal-3C, MW 16 327 Da) was a gift from Prof. C. Cairo (University of Alberta). S-Carboxyamidomethylated oxidation resistant (C2S substituted to improve stability) recombinant hGal-1 (dimer MW 29 580 Da) was a gift from Prof. S. Sato (Université Laval, Quebec).[25] Recombinant hGal-7 (dimer MW 29 887 Da) was a gift from Prof. Yves St-Pierre (INRS-Institut Armand-Frappier). Bovine carbonic anhydrase (BCA, MW 27 000 Da), purchased from Sigma-Aldrich Canada (Oakville, Canada), served as reference protein (P_{ref}) to correct the mass spectra for the formation of nonspecific interactions during the ESI process.[26] The recombinant membrane scaffold protein (MSP) MSP1E1 (MW 27 494 Da) used to prepare the

NDs, was expressed from the plasmid pMSP1E1 (Addgene, Cambridge, MA) and purified using a reported protocol.[27] Stock solutions of all proteins except MSP1E1 were concentrated and dialyzed into an aqueous 200 mM ammonium acetate solution (pH 6.8) using Amicon 0.5 mL microconcentrator (EMD Millipore, Billerica, MA) with a MW cutoff of 3 kDa (hGal-3C) or 10 kDa (hGal-1, BCA and hGal-7) and stored at -80 °C until needed. The concentrations of the protein stock solutions were estimated by UV absorption at 280 nm.

3.2.2 Lipids and Glycospingolipids

The gangliosides β-D-Gal-(1 → 3)-β-D-GalNAc-(1 → 4)-[α-D-Neu5Ac-(2 → 3)]-β-D-Gal-(1 → 4)-D-Glc-ceramide (GM1, major isoforms d18:1−18:0 and d20:1−18:0 have MWs 1545.8 Da, 1573.9 Da), β-D-GalNAc-(1 → 4)-[α-D-Neu5Ac-(2 → 3)]-β-D-Gal-(1 → 4)-D-Glc-ceramide (GM2, major isoforms d18:1−18:0 and d20:1−18:0 have MWs 1383.7 Da, 1411.7 Da) and α-D-Neu5Ac-(2 → 3)-β-D-Gal-(1 → 4)-D-Glc-ceramide (GM3, major isoforms d18:1−18:0 and d20:1−18:0 have MWs 1180.5 Da, 1208.5 Da) were purchased from Cedarlane Laboratories (Burlington, Canada); α-D-Neu5Ac-(2 → 3)-β-D-Gal-(1 → 3)-β-D-GalNAc-(1 → 4)-[α-D-Neu5Ac-(2 → 3)]-β-D-Gal-(1 → 4)-D-Glc-ceramide (GD1a, major isoforms d18:1−18:0 and d20:1−18:0 have MWs 1836.1 Da, 1864.1 Da), β-D-Gal-(1 → 3)-β-D-GalNAc-(1 → 4)-[α-D-Neu5Ac-(2 → 8)-α-D-Neu5Ac-(2 → 3)]-β-D-Gal-(1 → 4)-D-Glc-ceramide (GD1b, major isoforms d18:1−18:0 and d20:1−18:0 have MWs 1836.1 Da, 1864.1 Da), α-D-Neu5Ac-(2−3)-β-D-Gal-(1−3)-β-D-Gal-NAc-(1−4)-[α-D-Neu5Ac-(2−8)-α-D-Neu5Ac-(2−3)]-β-D-Gal-(1−4)-D-Glc-ceramide (GT1b, major isoforms d18:1−18:0 and d20:1−18:0 have MWs 2126.4 Da, 2154.4 Da) were purchased from Sigma-Aldrich Canada (Oakville, Canada), and β-D-GalNAc-(1 → 4)-[α-D-Neu5Ac-(2 → 8)-α-D-Neu5Ac-(2 → 3)]-β-D-Gal-(1 → 4)-D-Glc-ceramide (GD2, major isoforms d18:1−18:0 and d20:1−18:0 have MWs 1674.0 Da, 1702.0 Da) and α-D-Neu5Ac-(2−8)-

α-D-Neu5Ac-(2−3)-β-D-Gal-(1−3)-β-D-GalNAc-(1−4)-[α-D-Neu5Ac-(2−3)]-β-D-Gal-(1−4)-D-Glc-ceramide (GT1a, major isoforms d18:1−18:0 and d20:1−18:0 have MWs 2126.4 Da, 2154.4 Da) were purchased from MyBioSource Inc. (San Diego, CA). The phospholipid 1-palmitoyl-2-oleoyl-sn-glycero-3-phosphocholine (POPC), 1,2-dipalmitoyl-sn-glycero-3-phosphoethanolamine-N-(6-azidohexanoyl) (16:0 azidocaproyl PE, azide-PE) were purchased from Avanti Polar Lipids Inc. (Alabaster, AL). The structures of the gangliosides used in this study, as well as those of POPC, azide-PE are shown in Figure 3.1.

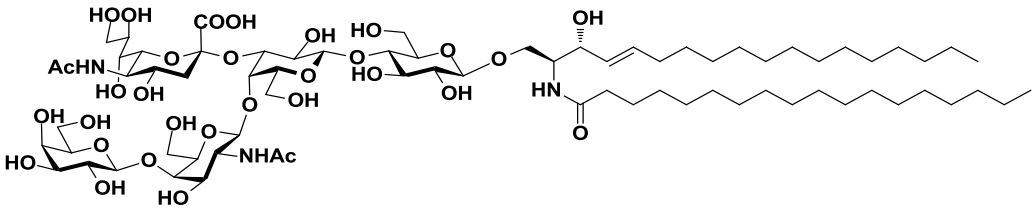

GM1 (*d*18:1-18:0)

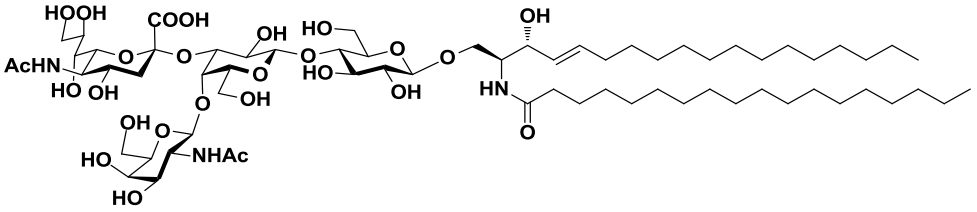

GM2 (*d*18:1-18:0)

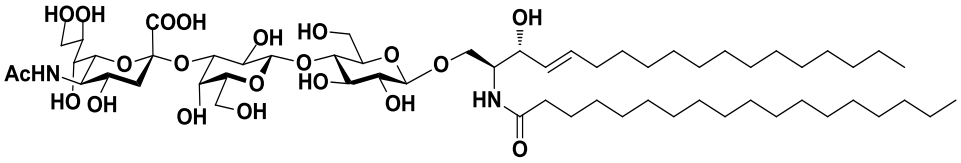

GM3 (*d*18:1-18:0)

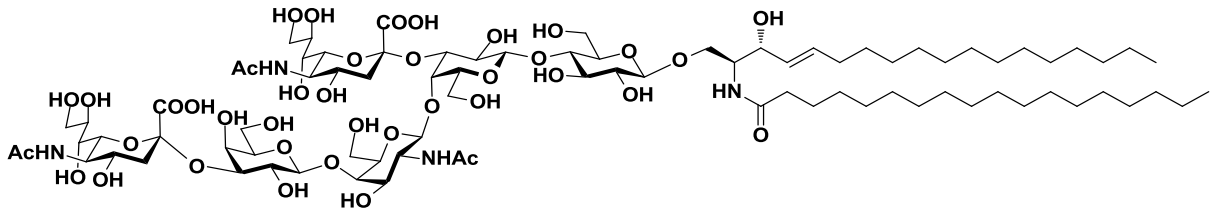

GD1a (*d*18:1-18:0)

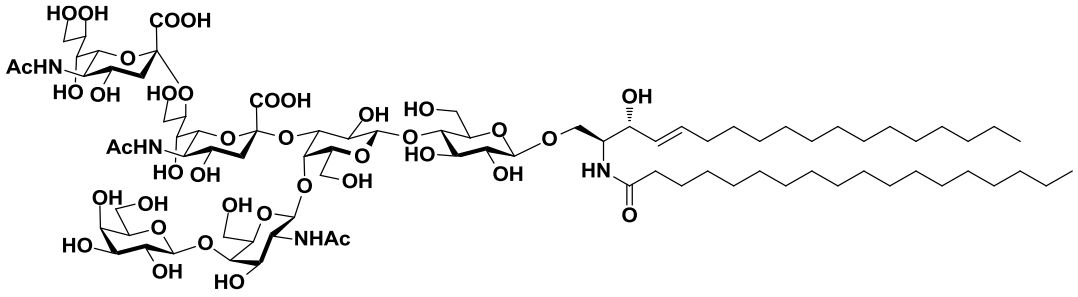

GD1b (*d*18:1-18:0)

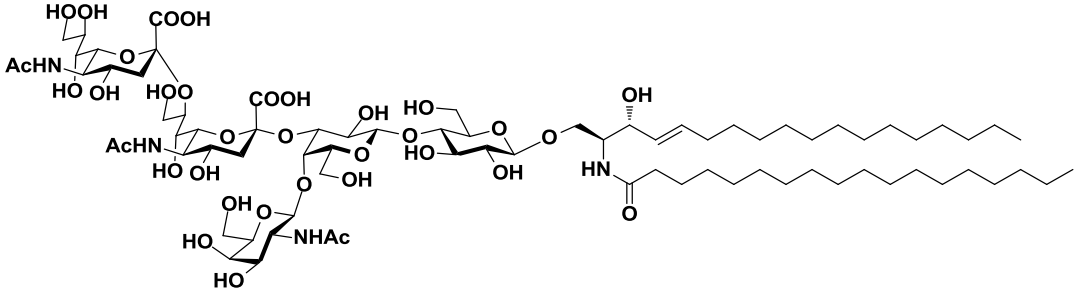

GD2 (*d*18:1-18:0)

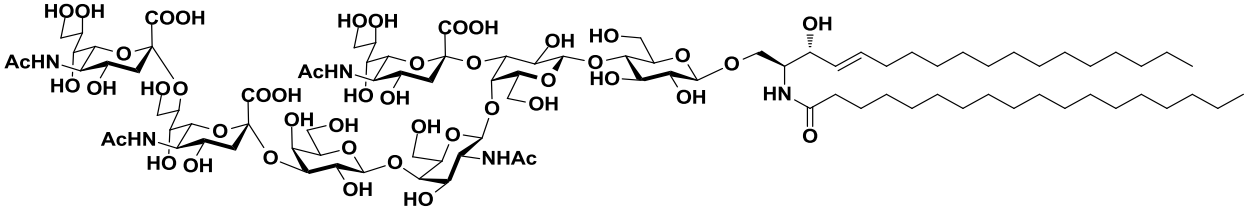

GT1a (*d*18:1-18:0)

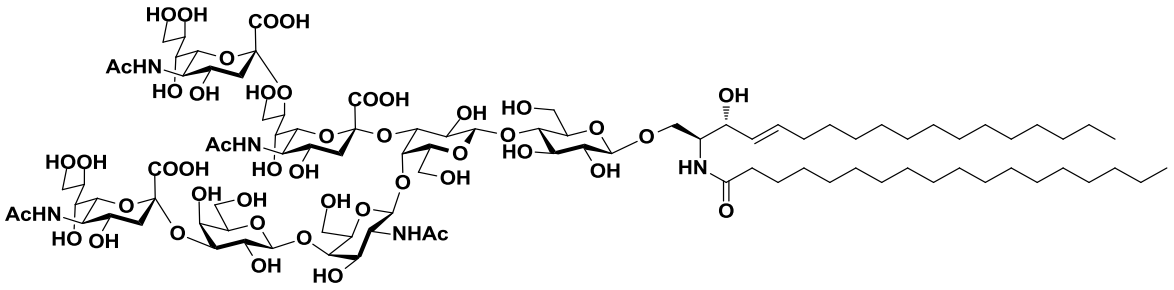

GT1b (*d*18:1-18:0)

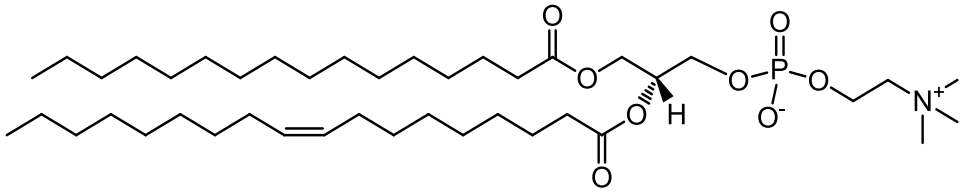

POPC (16:0/18:1(9Z))

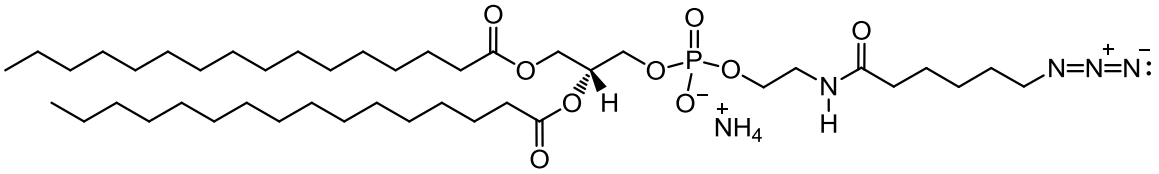

azidocaproyl PE (16:0)

Figure 3.1. Structures of the gangliosides GM1, GM2, GM3, GD1a, GD1b, GD2, GT1a, GT1b, POPC and azidocaproyl PE.

3.2.3 Oligosaccharides

The ganglioside oligosaccharides β-D-Gal-(1 → 3)-β-D-GalNAc-(1 → 4)-[α-D-Neu5Ac-(2 → 3)]-β-D-Gal-(1 → 4)-D-Glc ($GM1_{os}$, MW 998.34 Da); β-D-GalNAc-(1 → 4)-[α-D-Neu5Ac-(2 → 3)]-β-D-Gal-(1 → 4)-D-Glc ($GM2_{os}$, MW 836.29 Da); α-D-Neu5Ac-(2 → 3)-β-D-Gal-(1 → 4)-D-Glc ($GM3_{os}$, MW 633.21 Da); α-D-Neu5Ac-(2 → 3)-β-D-Gal-(1 → 3)-β-D-GalNAc-(1 → 4)-[α-D-Neu5Ac-(2 → 3)]-β-D-Gal-(1 → 4)-D-Glc ($GD1a_{os}$, MW 1289.44 Da); β-D-Gal-(1 → 3)-β-D-GalNAc-(1 → 4)-[α-D-Neu5Ac-(2 → 8)-α-D-Neu5Ac-(2 → 3)]-β-D-Gal-(1 → 4)-D-Glc ($GD1b_{os}$,

MW 1289.44 Da); β-D-GalNAc-(1 → 4)-[α-D-Neu5Ac-(2 → 8)-α-D-Neu5Ac-(2 → 3)]-β-D-Gal-(1 → 4)-D-Glc ($GD2_{os}$, MW 1127.39 Da); α-D-Neu5Ac-(2−8)-α-D-Neu5Ac-(2−3)-β-D-Gal-(1−3)-β-D-GalNAc-(1−4)-[α-D-Neu5Ac(2−3)]-β-D-Gal-(1−4)-D-Glc ($GT1a_{os}$, MW 1580.53 Da); α-D-Neu5Ac-(2−3)-β-D-Gal-(1−3)-β-D-Gal-NAc-(1−4)-[α-D-Neu5Ac-(2−8)-α-D-Neu5Ac-(2−3)]-β-D-Gal-(1−4)-D-Glc ($GT1b_{os}$, MW 1580.53 Da) were purchased from Elicityl SA (Crolles, France). The structures of the ganglioside oligosaccharides used in this work were shown in Figure 3.2. Stock solutions (1 mM in Milli-Q water (Millipore, MA)) of each of the oligosaccharides were prepared and stored at −20 °C until needed.

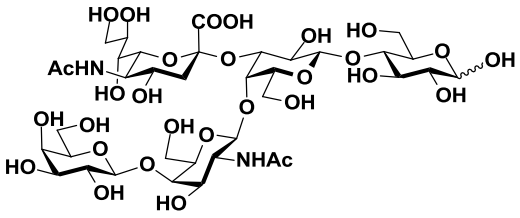

$GM1_{os}$

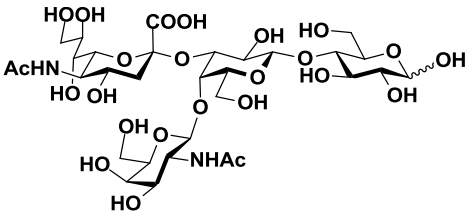

$GM2_{os}$

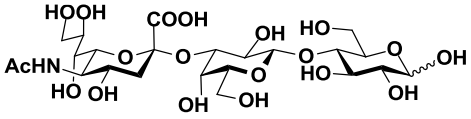

$GM3_{os}$

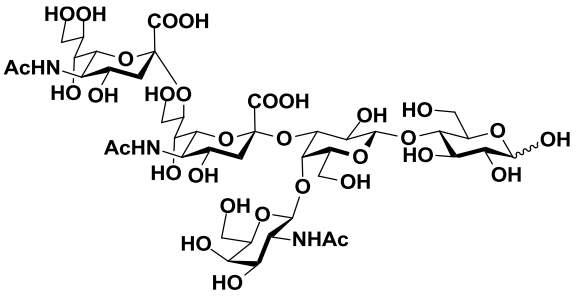

$GD2_{os}$

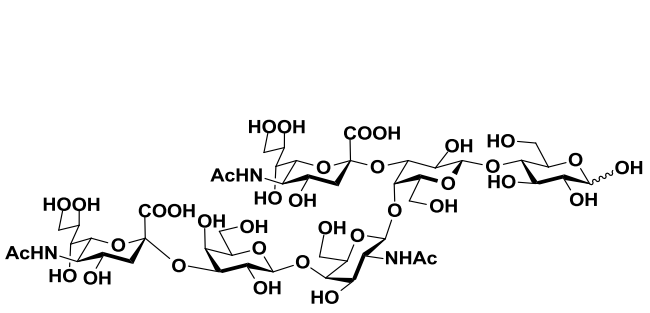

$GD1a_{os}$

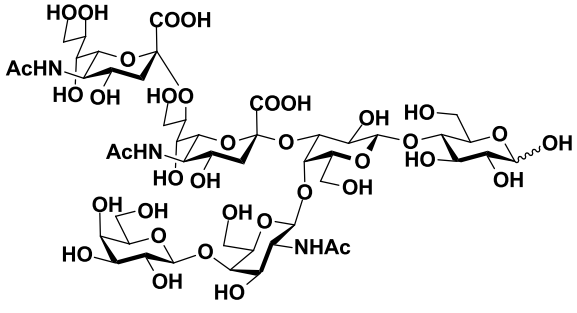

$GD1b_{os}$

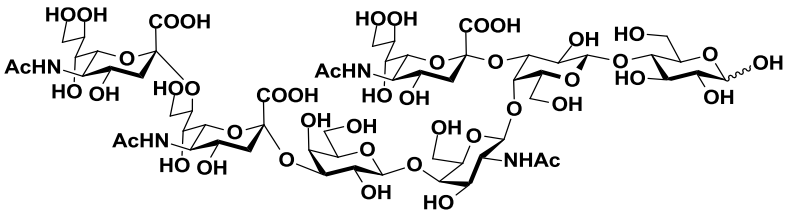

GT1a$_{os}$

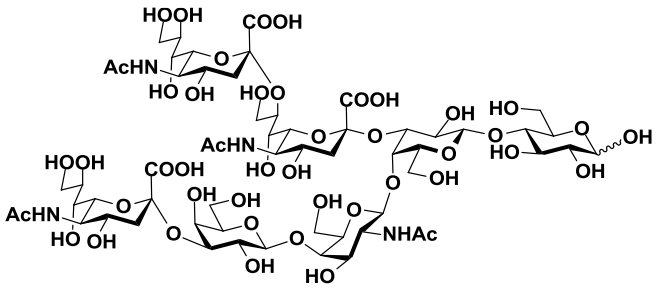

GT1b$_{os}$

Figure 3.2. Structures of the gangliosides oligosaccharides GM1$_{os}$, GM2$_{os}$, GM3$_{os}$, GD2$_{os}$, GD1a$_{os}$, GD1b$_{os}$, GT1a$_{os}$, GT1b$_{os}$.

3.2.4 Preparation of nanodiscs

Nanodiscs composed of POPC, azide-PE and one ganglioside (GM1, GM2, GM3, GD1a, GD1b, GD2, GT1a and GT1b) were prepared using a protocol reported previously.[28,29] Briefly, the POPC and azide-PE, dissolved in methanol, were mixed with ganglioside at the desired molar ratios. The lipids were dried under a stream of nitrogen to form a lipid film and kept in a vacuum desiccator overnight. The lipids were then dissolved in 20 mM TrisHCl, 0.5 mM EDTA, 100 mM NaCl, and 25 mM sodium cholate (pH 7.4) and sonicated for 15 min. The MSP1E1 protein was added to the mixture at a MSP1E1-to-total lipid molar ratio of 1:100, followed by incubation at 4 °C for 20 min. The ND formation process was initiated by adding an equal volume of prewashed Bio-beads (Bio-Rad Laboratories Ltd., Mississauga, Canada). The solution was then incubated at 4 °C for 4 h using an orbital shaker to remove all detergent. The supernatant was then recovered, and a Superdex 200 10/300 size-exclusion column (GE-Healthcare Bio-Sciences, Uppsala, Sweden), which was equilibrated with a 200 mM aqueous ammonium acetate solution (pH 6.8) at room temperature,

was used for NDs purification. Finally, the ND fractions were pooled, concentrated, and buffer exchanged into a 200 mM aqueous ammonium acetate solution (pH 6.8) using an Amicon microconcentrator (EMD Millipore, Billerica, MA) with a 30 kDa MW cutoff. The concentrations of the ND stock solutions were determined from on the concentration of MSP1E1 dimer, measured by UV absorption at 280 nm. All NDs stock solutions were stored at −80 °C until used.

3.2.5 Protein labeling (NHS ester reaction chemistry) and copper-free click chemistry reaction

The labeling reagent dibenzocyclooctyne-PEG_4-*N*-hydroxysuccinimidyl ester (DBCO-PEG_4-NHS ester), which was purchased from Sigma-Aldrich Canada (Oakville, Canada), was dissolved in DMSO to give a stock solution of 20 mg mL^{-1}. To perform GBP labeling, the protein (32 μM hGal-3C, 16 μM hGal-1 or 14 μM hGal-7) was incubated with DBCO-PEG_4-NHS ester (~ 200 μM) in 100 μL of phosphate buffered saline (PBS, pH 7.2) at 25 °C for 1 h. The non-reacted DBCO-PEG_4-NHS ester was removed by dialysis into a 200 mM ammonium acetate solution (pH 6.8) using an Amicon microconcentrator (EMD Millipore, Billerica, MA) with a 10 kDa MW cutoff. The stock solutions of labeled GBPs (hGal-3C, hGal-1 and hGal-7) were stored at -80 °C until needed.

Subsequently, the copper-free click chemistry reaction was carried out at 4 °C by mixing labeled protein (~ 3 μM) with a series of azide-PE POPC NDs containing a single ganglioside (GM1, GM2, GM3, GD1a, GD1b, GD2, GT1a and GT1b) for different incubation time. Finally, the mixed solution under a certain time was measured for detection by ESI-MS. A schematic illustration of this assay was given in Figure 3.3. In addition, the protein labeling (NHS ester reaction chemistry) and copper-free click chemistry reactions undertaken were shown in Figure 3.4.

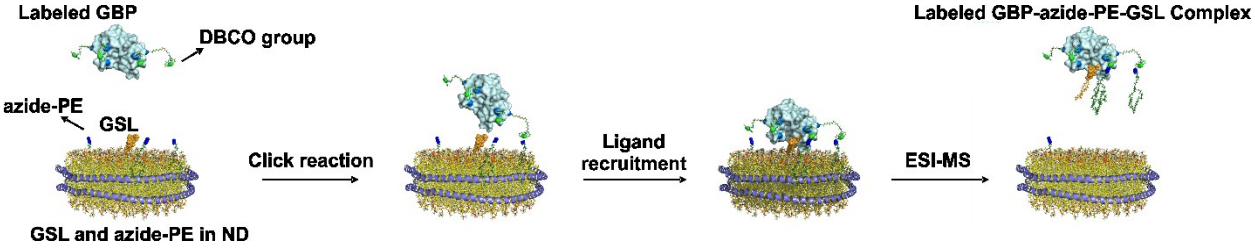

Figure 3.3. Schematic representation of the membrane anchor-assisted CaR-ESI-MS assay applied for detecting weak GBP-GSL interactions. The labeled GBP (light blue) and model membrane [e.g., nanodisc (ND) with surrounding membrane scaffold protein (purple)] containing GSL (yellow), azide-PE (dark bule/dark green) and POPC phospholipid (orange) are incubated for a certain time. Conformationally strained alkyne conjugated with receptor GBP first reacts with azide-terminated phospholipid incorporated in MM via a "click chemistry" reaction, thus, anchoring the GBP to the membrane surface. Then, non-covalent interactions between GBP and GSL becomes intramolecular and more entropically favorable. Finally, the labeled GBP-azide-PE-GSL-MM whole complexes are transferred into gas phase by ESI and the labeled GBP-azide-PE-GSL complexes are released in source for MS detection.

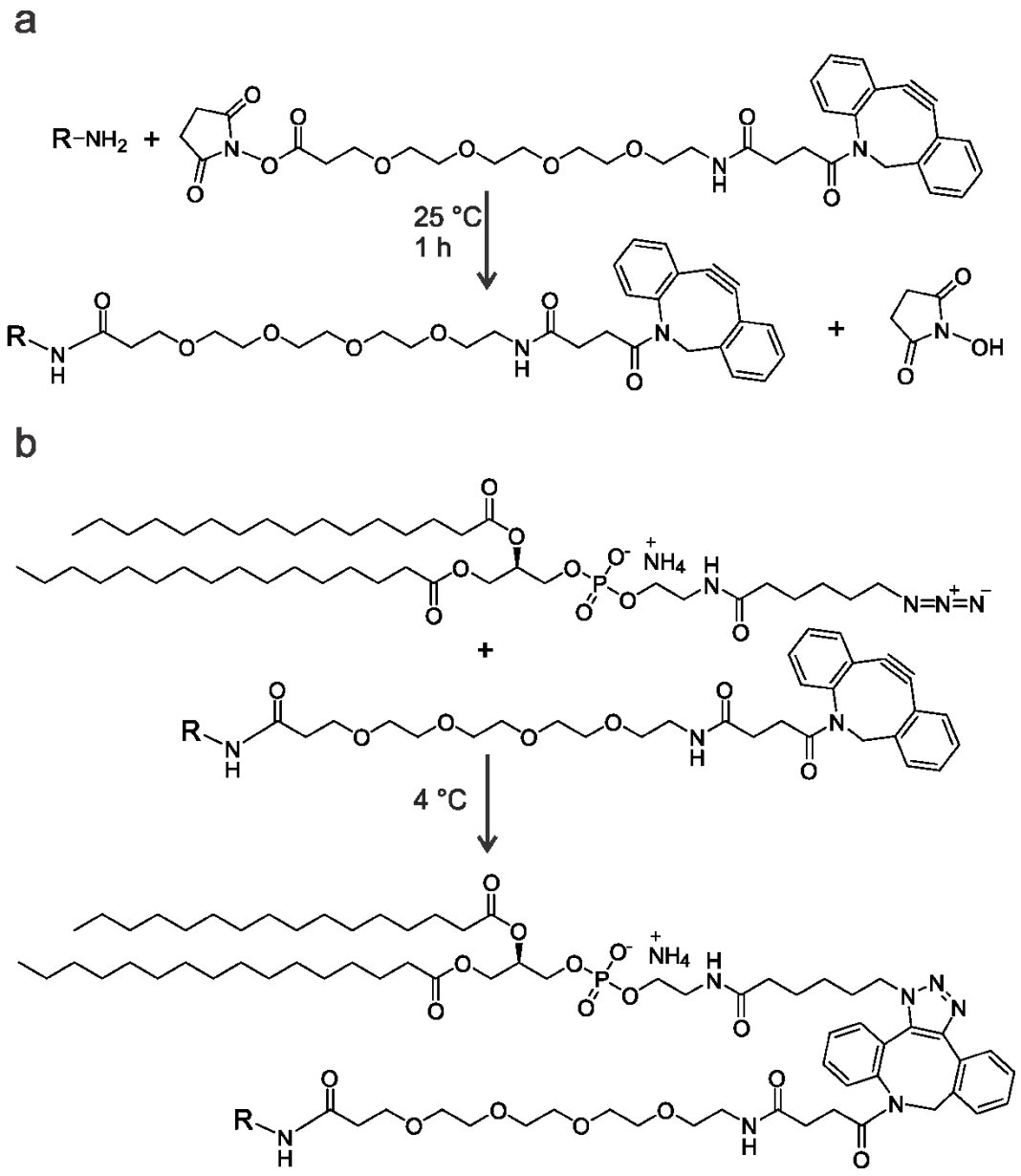

Figure 3.4. (a) Protein labeling NHS ester reaction chemistry and (b) Copper-free click chemistry.

3.2.6 Mass spectrometry

All direct ESI-MS measurements were carried out in positive ion mode using two instruments, a Q-Exactive hybrid quadrupole-orbitrap mass spectrometer (Thermo Fisher Scientific, Waltham, US) with ultra-high mass range (UHMR) and a Synapt G2S ESI quadrupole-ion mobility separation-time-of-flight (Q-IMS-TOF) mass spectrometer (Waters, Manchester, UK),

both equipped with a nanoflow ESI (nanoESI) source. All analytes solutions were loaded into a nanoESI tip produced from borosilicate capillaries using a P-1000 micropipette puller (Sutter Instruments, Novato, CA). To carry out nanoESI, a platinum wire was inserted into the back end of the tip and a voltage of 0.9 - 1.2 kV was applied. On Q-Exactive UHMR, the capillary temperature was 100 °C and mass spectra were acquired at the m/z range from 1000-8000 at a target resolution of 3125 ~ 6250 with 10 microscans summed into one scan. The maximum inject time was 100 ms and S-lens RF level was 100. The automatic gain control (AGC) target value was set to 10^6. Ultrahigh vacuum was maintained at 3.28×10^{-10} mbar. The native MS data were acquired using Thermo Q Exactive UHMR Tune software and analyzed using Thermo Xcalibur 2.2 (Thermo Fisher Scientific). Ion peak intensities were used to quantify abundance of all species of interest. For Synapt G2S, a cone voltage of 30 V was used and the source block temperature was maintained at 60 ºC. The Trap and Transfer voltages were 5 V and 2 V, respectively; argon was used in the Trap and Transfer ion guides at pressures of 3.37×10^{-4} mbar and 5.01×10^{-4} mbar, respectively. At least 180 scans were collected for each mass spectrum. Data were acquired and processed using MassLynx (Waters, version 4.1).

3.2.6.1 Direct ESI-MS assay

The direct ESI-MS assay was used to quantify ganglioside oligosaccharide affinities for hGal-3C. The reference protein (P_{ref}) method was used to correct the mass spectra for the occurrence of nonspecific protein-carbohydrate binding during ESI process, in case of the weak protein-oligosaccharide interactions ($K_a < 10^4\ M^{-1}$).[30] The BCA, which didn't bind to the oligosaccharides tested, served as P_{ref}. The details were described in Chapter 1, 1.3.1.

3.2.6.2 GSL binding measurements

To calculate the fraction of GSL complexes (f_{GSL}) consisted of GBP with qDBCO-PEG$_4$, qPE and one GSL (i.e., GBP + qDBCO-PEG$_4$ + qPE + GSL), where q was the number of GBP labeled with DBCO-PEG$_4$ and PE (for this study q ≤ 5), f_{GSL} can be determined from the abundances (*Ab*) of GSL-bound click complexes and free click complexes (i.e., GBP + qDBCO-PEG$_4$ + qPE) ions measured by ESI-MS, eq3.4:

$$f_{GSL} = \frac{\sum_{q=1}^{5} Ab(\text{GBP} + \text{qDBCO-PEG}_4 + \text{qPE} + \text{GSL})}{\sum_{q=1}^{5} Ab(\text{GBP} + \text{qDBCO-PEG}_4 + \text{qPE} + \text{GSL}) + \sum_{q=1}^{5} Ab(\text{GBP} + \text{qDBCO-PEG}_4 + \text{qPE})} \quad (3.4)$$

3.3 Results and Discussion

The objective of this study was to establish the feasibility of the membrane anchor-assisted CaR-ESI-MS assay, performed using NDs, to tackle the challenge of detecting GBPs interactions with low affinity GSL ligands. With this goal in mind, hGal-3C served as model GSL-binding protein. We first performed direct ESI-MS binding measurements on solutions of hGal-3C and a series of ganglioside oligosaccharides (GM1$_{os}$, GM2$_{os}$, GM3$_{os}$, GD1a$_{os}$, GD1b$_{os}$, GD2$_{os}$, GT1a$_{os}$ or GT1b$_{os}$). Based on these findings, the direct ESI-MS assay was then applied to several POPC-NDs containing a single ganglioside (GM1, GM2, GM3, GD1a, GD1b, GD2, GT1a or GT1b). To demonstrate the implementation and test the reliability of the membrane anchor-assisted CaR-ESI-MS assay for the detection of weak GBP-GSL interactions, measurements were carried out on solutions of labeled GBPs and a series of azide-PE POPC NDs containing a single ganglioside (GM1, GM2, GM3, GD1a, GD1b, GD2, GT1a or GT1b). In order to confirm this new assay was a general method, measurements were next extended to other two human galectins (hGal-1 and hGal-7) and their interactions with ganglioside GM3 presented in NDs.

3.3.1 Affinities of ganglioside oligosaccharides of hGal-3C

Previously, the affinity of $GM3_{os}$ for hGal-3C has been reported.[31] However, to our knowledge, the affinities to other ganglioside oligosaccharides have not been determined. Therefore, as a starting point for this study, the affinity measurements were extended to hGal-3C binding to several ganglioside oligosaccharides (e.g., $GM1_{os}$, $GM2_{os}$, $GD1a_{os}$, $GD1b_{os}$, $GD2_{os}$, $GT1a_{os}$ and $GT1b_{os}$). In addition, the affinity for $GM3_{os}$ for the hGal-3C was also re-measured and compared to the literature values ($K_a = (2.0 \pm 0.1) \times 10^4\ M^{-1}$).[31] The direct ESI-MS experiments were performed, at a fixed concentration of hGal-3C (4 μM) and three different concentrations of each ganglioside oligosaccharide ranging from 30 to 70 μM.[32] The BCA (4 μM), which served as a reference protein (p_{ref}), was present in all experiments to correct nonspecific protein-carbohydrate interactions during the ESI process.

Representative ESI mass spectra acquired for an aqueous ammonium acetate solution (200 mM, pH 6.8) containing hGal-3C (4 μM), BCA (4 μM) and each of the ganglioside oligosaccharides are shown in Figure 3.5. At the concentrations investigated, both free and oligosaccharide ligand-bound hGal-3C ions were detected, i.e., $(P+L)^{n+}$, where n = 7-9 and L = $GM1_{os}$, $GM2_{os}$, $GM3_{os}$, $GD1a_{os}$, $GD1b_{os}$, $GD2_{os}$, $GT1a_{os}$ or $GT1b_{os}$, respectively. Signals corresponding to unbound and bound P_{ref} ions were also detected, i.e., $(P_{ref}+L)^{n+}$, where n = 9-11. From the ESI-MS data, the K_a values for each oligosaccharide were calculated by fitting eq1.12 to the fraction of oligosaccharide ligand bound hGal-3C measured experimentally (Table 3.1) and the corresponding titration curves were shown in Figure 3.6. Inspection of the binding data revealed that $GM1_{os}$, $GM3_{os}$, $GD1a_{os}$, $GD1b_{os}$, $GT1a_{os}$, $GT1b_{os}$ are recognized by hGal-3C, although with low affinities, in the 6.0×10^2 to $1.5 \times 10^4\ M^{-1}$ range, while $GM2_{os}$ and $GD2_{os}$ don't bind. Among these ganglioside oligosaccharides, $GM3_{os}$ had the highest affinity for hGal-3C ($1.5 \times 10^4\ M^{-1}$),

which was in agreement with previously published value measured by ESI-MS assay.[31]

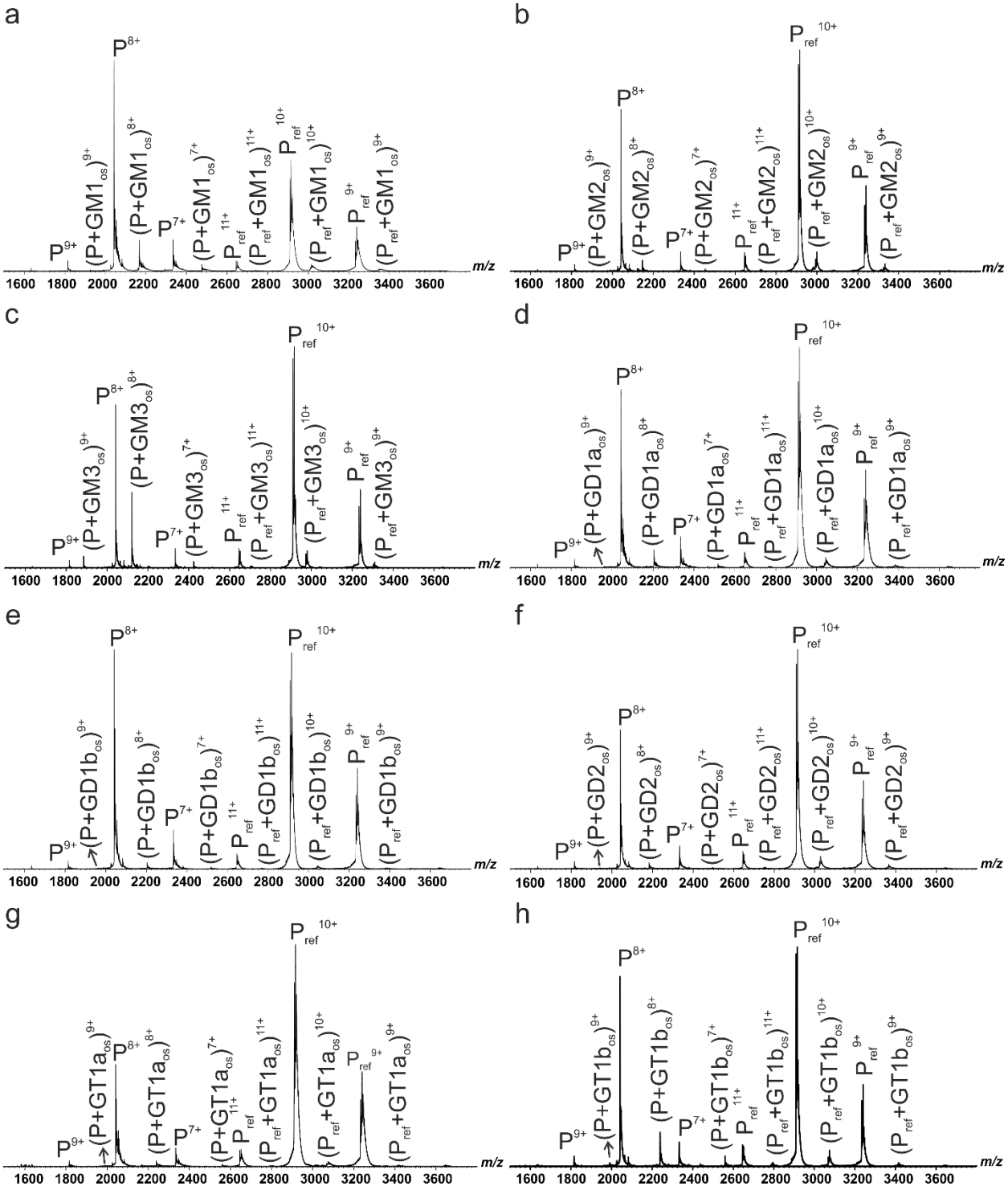

Figure 3.5. ESI mass spectra acquired in positive ion mode for aqueous ammonium acetate solutions (200 mM, pH 6.8) of hGal-3C (4 μM), BCA (P_{ref}, 4 μM), and the ganglioside

oligosaccharide (a) $GM1_{os}$ (70 μM), (b) $GM2_{os}$ (70 μM), (c) $GM3_{os}$ (30 μM), (d) $GD1a_{os}$ (50 μM), (e) $GD1b_{os}$ (30 μM), (f) $GD2_{os}$ (50 μM), (g) $GT1a_{os}$ (40 μM) and (h) $GT1b_{os}$ (30 μM).

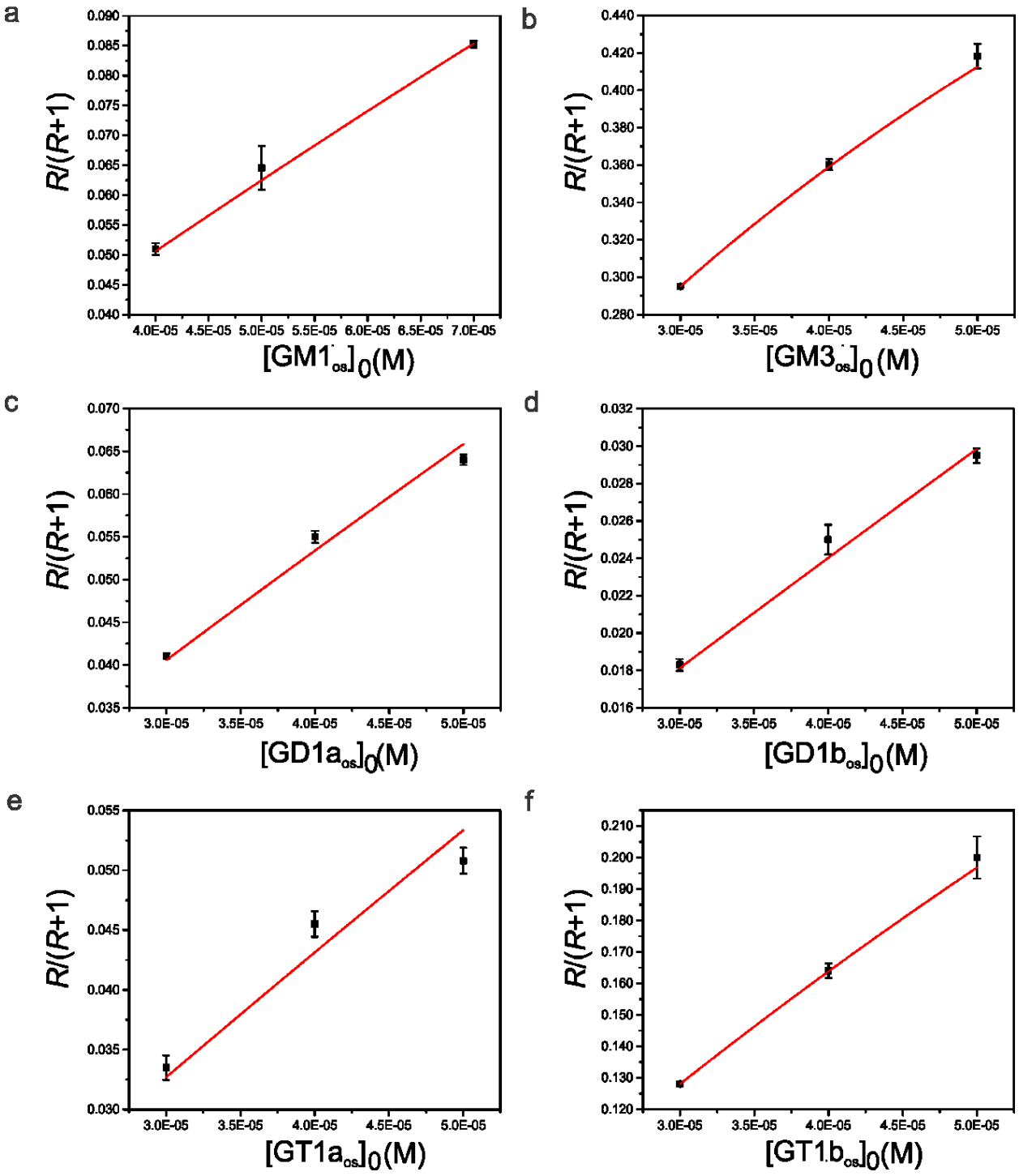

Figure 3.6. Plots of the fraction of ligand-bound hGal-3C (i.e., $R/(R+1)$) versus ligand

concentration measured for the ganglioside oligosaccharides (a) $GM1_{os}$, (b) $GM3_{os}$, (c) $GD1a_{os}$, (d) $GD1b_{os}$, (e) $GT1a_{os}$ and (f) $GT1b_{os}$. The direct ESI-MS binding measurements were carried out on 200 mM aqueous ammonium acetate solutions containing hGal-3C (4 μM), BCA (P_{ref}, 4 μM and each ganglioside oligosaccharide at three different concentrations ranging from 30 to 70 μM. The error bars correspond to one standard derivation and the solid curves corresponding to the best fit of eq1.12 to the experimental data.

Table 3.1. Association constants (K_a, units $10^3\ M^{-1}$) for hGal-3C binding to the oligosaccharides of eight gangliosides measured in an aqueous ammonium acetate solution (200 mM, pH 6.8 and 25 ºC) using the direct ESI-MS assay.

Oligosaccharide	K_a ($10^3\ M^{-1}$)
$GM1_{os}$	1.3 ± 0.01
$GM2_{os}$	NB[a]
$GM3_{os}$	14.5 ± 0.02
$GD1a_{os}$	1.4 ± 0.03
$GD1b_{os}$	0.6 ± 0.01
$GD2_{os}$	NB[a]
$GT1a_{os}$	1.1 ± 0.04
$GT1b_{os}$	5.0 ± 0.01

a. NB: No binding detected.

3.3.2 hGal-3C binding to POPC NDs containing a single ganglioside

Having established the ganglioside specificities of hGal-3C, the protein was then incubated with POPC NDs, prepared from each of GM1, GM2, GM3, GD1a, GD1b, GD2, GT1a and GT1b (over a range of GSL concentrations: 20-160 μM), and the solutions analyzed by ESI-MS. Shown in Figure 3.7 are representative mass spectra acquired for aqueous ammonium acetate solutions (200 mM, pH 6.8) of hGal-3C (4 μM) and the corresponding ganglioside-containing POPC NDs. It can be seen that, while abundant signal corresponding to free hGal-3C^{n+} ions, with n = 7-8, was detected, there was no evidence of the corresponding ganglioside-bound ions at any of the concentrations tested. Therefore, according to above measurements, it indicated that all of the gangliosides tested exhibited weak or no interactions with hGal-3C. Meanwhile, it was further concluded that the direct ESI-MS assay combined with NDs couldn't be used to find these low affinity GBP-GSL interactions.

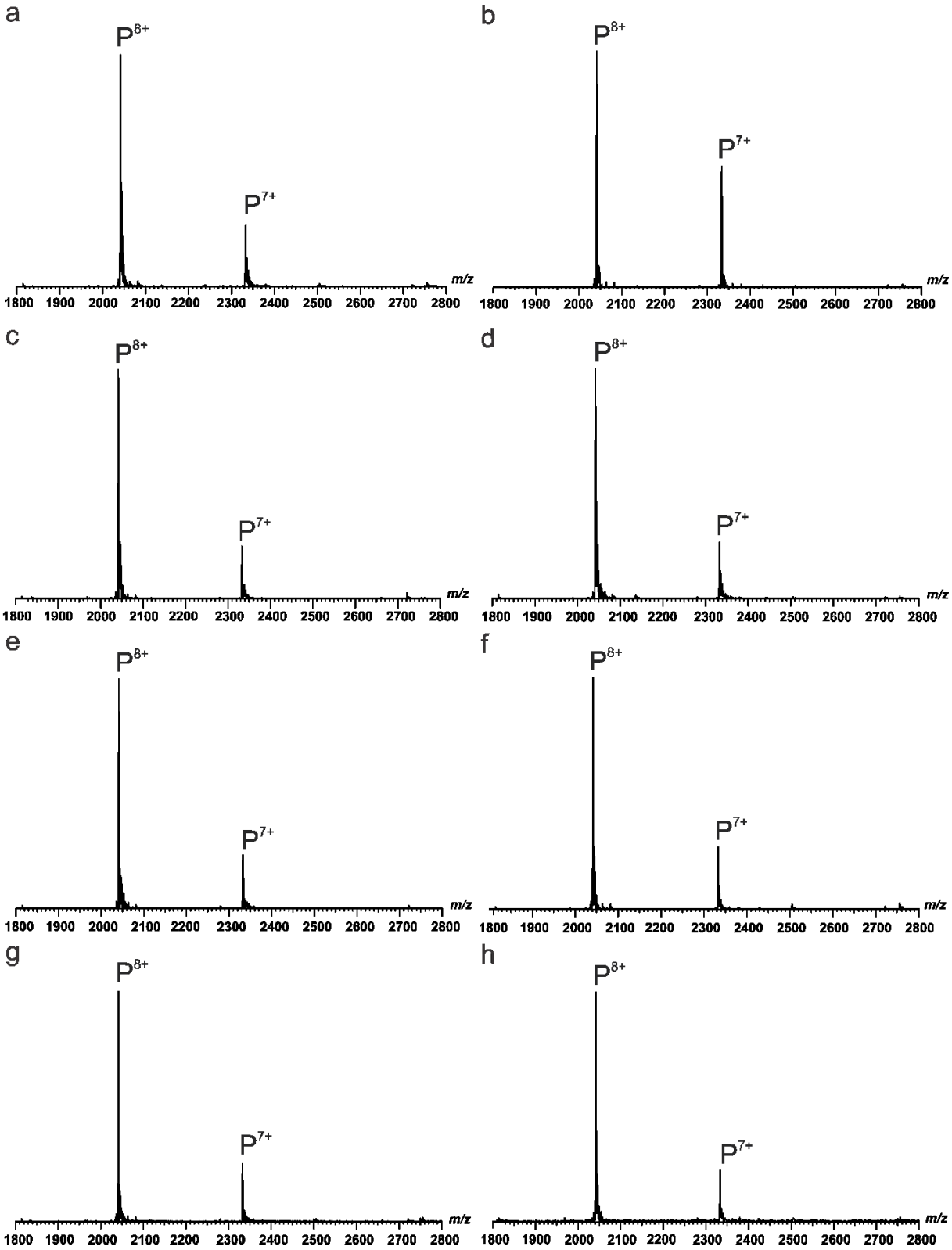

Figure 3.7. ESI mass spectra acquired in positive ion mode for aqueous ammonium acetate solutions (200 mM, pH 6.8) of hGal-3C (4 μM) with (a) 8 μM 10% GM1 POPC ND, (b) 8 μM 5%

GM2 POPC ND, (c) 8 μM 5% GM3 POPC ND (d) 10 μM 1% GD1a POPC ND, (e) 10 μM 1% GD1b POPC ND, (f) 8 μM 10% GD2 POPC ND, (g) 10 μM 1% GT1a POPC ND and (h) 10 μM 1% GT1b POPC ND.

3.3.3 Detecting hGal-3C interactions with low affinity GSL ligands by membrane anchor-assisted CaR-ESI-MS assay

To demonstrate the implementation of the membrane anchor-assisted CaR-ESI-MS assay for detection of weak GBP-GSL interactions, we labeled hGal-3C with DBCO-PEG_4 groups. hGal-3C possesses nine primary amino groups (eight lysine (Lys) residues and the N-terminus), which are the preferred sites of labeling with the DBCO-PEG_4 groups. Shown in Figure 3.8a is a representative ESI mass spectrum acquired in positive ion mode for an aqueous ammonium acetate solution (200 mM, pH 6.8, 25 °C) of hGal-3C labeled with DBCO-PEG_4 groups (2.8 μM). Ions corresponding to hGal-3C as well as (hGal-3C + qDBCO-PEG_4), with q = 1-6, were detected at charge states +7 to +9. The normalized distribution of (hGal-3C + qDBCO-PEG_4) in the inset revealed that the predominant species corresponded to hGal-3C labeled with 2 to 4 DBCO-PEG_4 groups.

This sample (2.8 μM) was then incubated with PE POPC ND (10 μM, 20% PE) in 200 mM aqueous ammonium acetate (pH 6.8) for 17 h at 4 °C. Shown in Figure 3.8b, ions corresponding to $(\text{hGal-3C + qDBCO-PEG}_4\text{ + qPE})^{n+}$, with q = 0-5 and n = 7-9, as well as MSP1E1^{n+}, with n = 10 and 11, were detected. As expected, $(\text{hGal-3C + qDBCO-PEG}_4)^{n+}$ ions, with q = 1-5 and n = 7-9, disappeared, indicating that click chemistry reaction occurred and was almost completed after 17h incubation of the labeled hGal-3C with PE POPC ND.

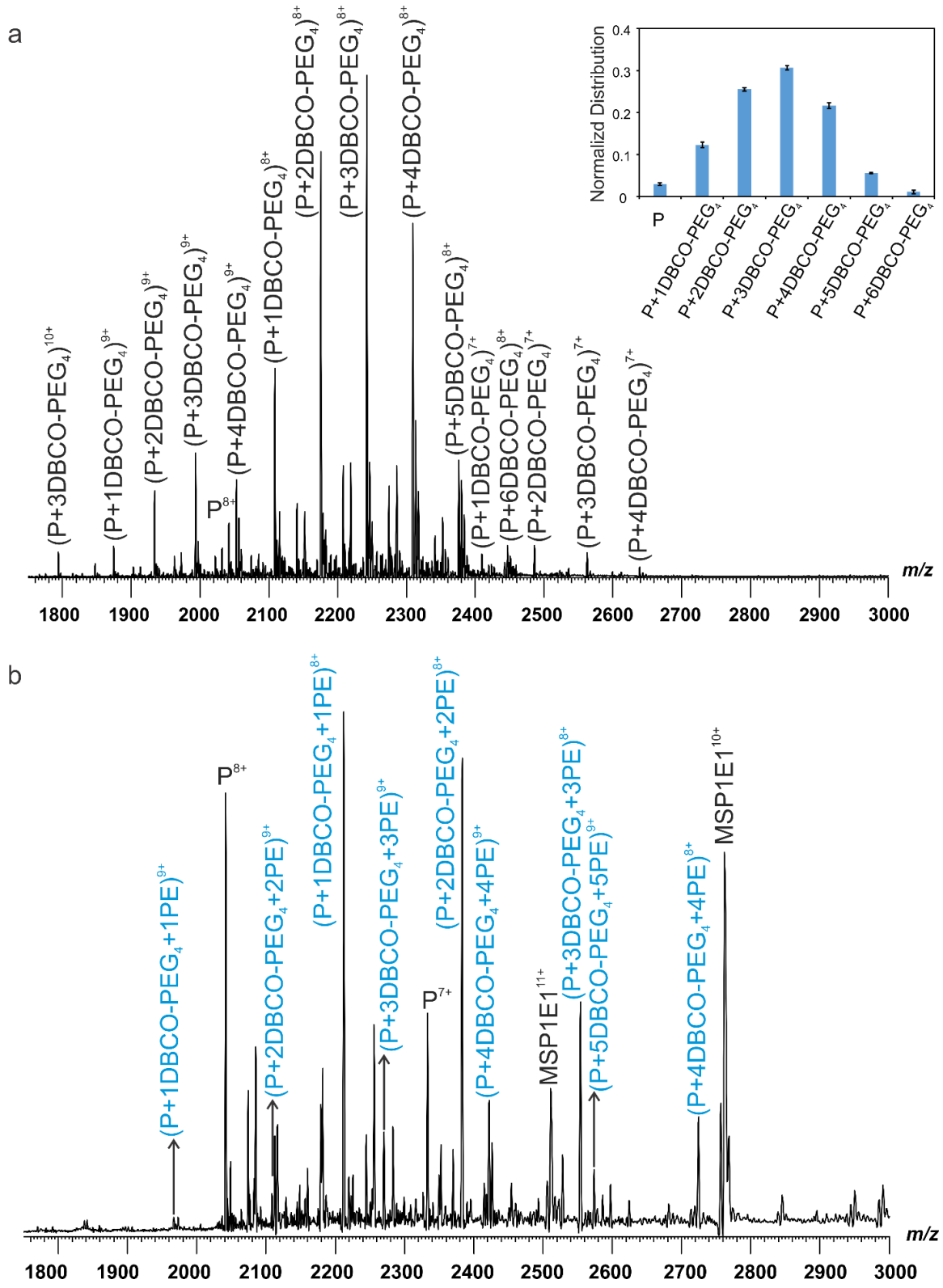

Figure 3.8. ESI mass spectra acquired in positive ion mode for aqueous ammonium acetate solutions (200 mM, 25 °C, and pH 6.8) containing (a) hGal-3C labeled with DBCO-PEG4 (2.8 µM)

and (b) hGal-3C labeled with DBCO-PEG_4 (2.8 μM) with 20% PE POPC ND (10 μM) incubated for 17 h at 4 °C. Inset show the normalized distribution of (hGal-3C + qDBCO-PEG_4) measured for solutions described in (a), where q = 0-6.

The direct ESI-MS measurements were then performed on solutions of labeled hGal-3C incubated with a series of PE POPC NDs containing a single ganglioside (GM1, GM2, GM3, GD1a, GD1b, GD2, GT1a and GT1b, respectively, 10% ganglioside, 20% PE) at 4 °C for different incubation times. As discussed in 3.3.1, hGal-3C doesn't exhibit any measurable affinities for both $GM2_{os}$ and $GD2_{os}$. Consequently, GM2 and GD2 were treated as negative controls for hGal-3C study.

Shown in Figure 3.9a is a representative mass spectrum acquired in positive ion mode for aqueous ammonium acetate solutions (200 mM, 25 °C, and pH 6.8) of labeled hGal-3C (2.8 μM) with 10% GM3 20% PE POPC ND (10 μM) at 4 °C for 17 h incubation. Analysis of the mass spectrum revealed click complex ions, i.e., $(\text{hGal-3C} + q\text{DBCO-PEG}_4 + q\text{PE})^{n+}$, with q = 1-5 and n = 8-9, as well as a measurable amount of click complexes bound to one GM3, i.e., $(\text{hGal-3C} + q\text{DBCO-PEG}_4 + q\text{PE} + \text{GM3})^{n+}$, with q = 1-5 and n = 8-9. As seen in the inset, the predominant GM3 complex species corresponded to (hGal-3C + 2DBCO-PEG_4 + 2PE + GM3) and (hGal-3C + 3DBCO-PEG_4 + 3PE + GM3). Meanwhile, the fraction of click complexes bound to GM3 calculated from the abundances of the (hGal-3C + qDBCO-PEG_4 + qPE + GM3) and (hGal-3C + qDBCO-PEG_4 + qPE) ions, with q = 1-5, using eq3.4 from the mass spectrum shown in Figure 3.9a was approximately 0.39. Following the same procedure, the interactions between labeled hGal-3C and the rest of GSL PE POPC NDs were measured, individually. As shown in Figure 3.9b-3.9f, signal corresponding to click complexes ions, i.e., $(\text{hGal-3C} + q\text{DBCO-PEG}_4 + q\text{PE})^{n+}$, with q = 1-4 and n = 8-9, as well as abundant free hGal-3C ions at charge states + 7 and + 8 were

detected. Notably, inspection of the ESI mass spectra also revealed the solid evidences of low affinity GSL ligands (e.g., GM1, GD1a, GD1b, GT1a and GT1b) binding to labeled hGal-3C (i.e., (hGal-3C + qDBCO-PEG_4 + qPE + GSL)$^{n+}$, with q = 1-4 and n = 8-9). In contrast, signal corresponding to labeled hGal-3C with PE (i.e., (hGal-3C + qDBCO-PEG_4 + qPE)$^{n+}$, with q = 0-5 and n = 8-9) was detected for both GM2/GD2 PE POPC NDs tested, while no evidence of GM2 or GD2 binding to labeled hGal-3C (i.e., (hGal-3C + qDBCO-PEG_4 + qPE + GM2/GD2)$^{n+}$, where n = 8-9) was observed (Figure 3.9g and 3.9h). These results confirmed that hGal-3C didn't bind to GM2, as well as GD2, which was consistent with binding data measured for hGal-3C and the oligosaccharides of these two gangliosides. Taken together, the implementation of membrane anchor-assisted CaR-ESI-MS assay revealed that by covalently tethering hGal-3C to the GSL-containing PE POPC NDs enabled the detection of low affinity GSL receptors.

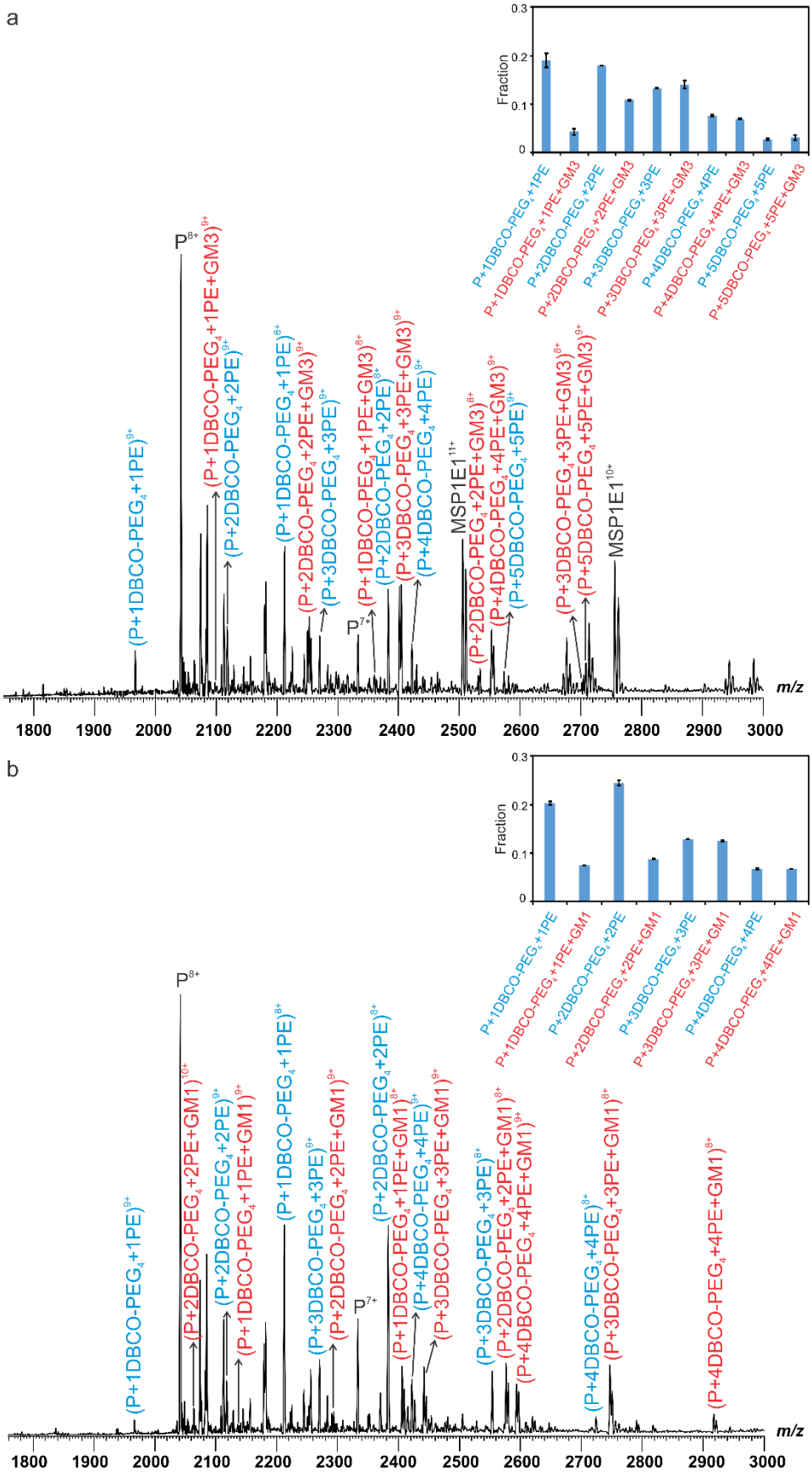
a
Fraction
0.3
0.2
0.1
0
P+1DBCO-PEG4+1PE
P+1DBCO-PEG4+1PE+GM3
P+2DBCO-PEG4+2PE
P+2DBCO-PEG4+2PE+GM3
P+3DBCO-PEG4+3PE
P+3DBCO-PEG4+3PE+GM3
P+4DBCO-PEG4+4PE
P+4DBCO-PEG4+4PE+GM3
P+5DBCO-PEG4+5PE
P+5DBCO-PEG4+5PE+GM3
P8+
P7+
(P+1DBCO-PEG4+1PE)9+
(P+1DBCO-PEG4+1PE+GM3)9+
(P+2DBCO-PEG4+2PE)9+
(P+1DBCO-PEG4+1PE)8+
(P+2DBCO-PEG4+2PE+GM3)9+
(P+3DBCO-PEG4+3PE)9+
(P+1DBCO-PEG4+1PE+GM3)8+
(P+2DBCO-PEG4+2PE)8+
(P+3DBCO-PEG4+3PE+GM3)9+
(P+4DBCO-PEG4+4PE)9+
MSP1E1 11+
(P+2DBCO-PEG4+2PE+GM3)8+
(P+4DBCO-PEG4+4PE+GM3)9+
(P+5DBCO-PEG4+5PE)9+
(P+3DBCO-PEG4+3PE+GM3)8+
(P+5DBCO-PEG4+5PE+GM3)9+
MSP1E1 10+
m/z
1800 1900 2000 2100 2200 2300 2400 2500 2600 2700 2800 2900 3000
b
Fraction
0.3
0.2
0.1
0
P+1DBCO-PEG4+1PE
P+1DBCO-PEG4+1PE+GM1
P+2DBCO-PEG4+2PE
P+2DBCO-PEG4+2PE+GM1
P+3DBCO-PEG4+3PE
P+3DBCO-PEG4+3PE+GM1
P+4DBCO-PEG4+4PE
P+4DBCO-PEG4+4PE+GM1
P8+
P7+
(P+1DBCO-PEG4+1PE)9+
(P+2DBCO-PEG4+2PE+GM1)10+
(P+2DBCO-PEG4+2PE)9+
(P+1DBCO-PEG4+1PE+GM1)9+
(P+1DBCO-PEG4+1PE)8+
(P+3DBCO-PEG4+3PE)9+
(P+2DBCO-PEG4+2PE+GM1)9+
(P+2DBCO-PEG4+2PE)8+
(P+1DBCO-PEG4+1PE+GM1)8+
(P+4DBCO-PEG4+4PE)9+
(P+3DBCO-PEG4+3PE+GM1)9+
(P+3DBCO-PEG4+3PE)8+
(P+2DBCO-PEG4+2PE+GM1)8+
(P+4DBCO-PEG4+4PE+GM1)9+
(P+4DBCO-PEG4+4PE)8+
(P+3DBCO-PEG4+3PE+GM1)8+
(P+4DBCO-PEG4+4PE+GM1)8+
m/z
1800 1900 2000 2100 2200 2300 2400 2500 2600 2700 2800 2900 3000

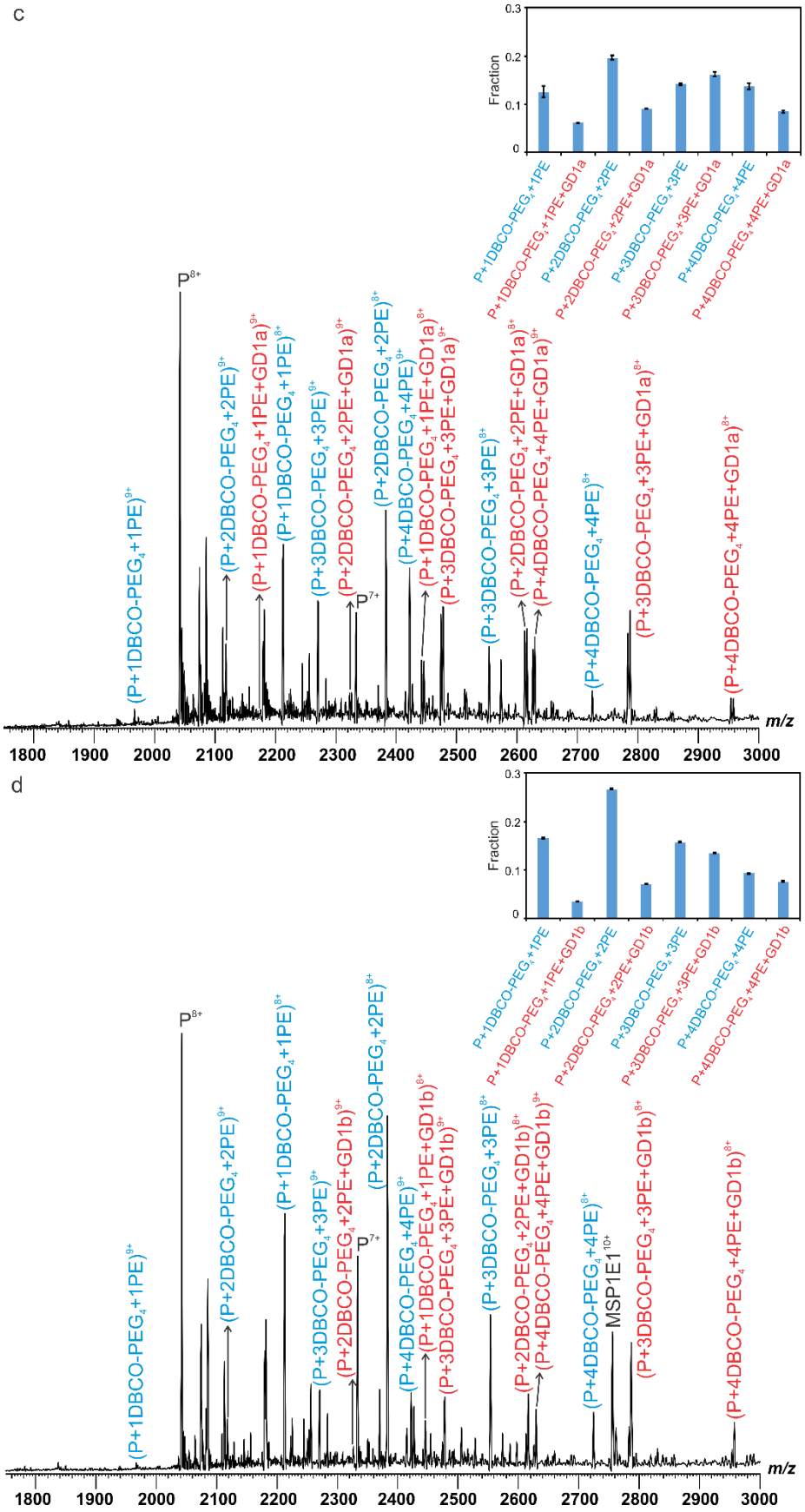
c
d
Fraction
P+1DBCO-PEG4+1PE
P+1DBCO-PEG4+1PE+GD1a
P+2DBCO-PEG4+2PE
P+2DBCO-PEG4+2PE+GD1a
P+3DBCO-PEG4+3PE
P+3DBCO-PEG4+3PE+GD1a
P+4DBCO-PEG4+4PE
P+4DBCO-PEG4+4PE+GD1a
P+1DBCO-PEG4+1PE+GD1b
P+2DBCO-PEG4+2PE+GD1b
P+3DBCO-PEG4+3PE+GD1b
P+4DBCO-PEG4+4PE+GD1b
P8+
P7+
(P+1DBCO-PEG4+1PE)9+
(P+2DBCO-PEG4+2PE)9+
(P+1DBCO-PEG4+1PE+GD1a)9+
(P+1DBCO-PEG4+1PE)8+
(P+3DBCO-PEG4+3PE)9+
(P+2DBCO-PEG4+2PE+GD1a)9+
(P+2DBCO-PEG4+2PE)8+
(P+4DBCO-PEG4+4PE)9+
(P+1DBCO-PEG4+1PE+GD1a)8+
(P+3DBCO-PEG4+3PE+GD1a)9+
(P+3DBCO-PEG4+3PE)8+
(P+2DBCO-PEG4+2PE+GD1a)8+
(P+4DBCO-PEG4+4PE+GD1a)9+
(P+4DBCO-PEG4+4PE)8+
(P+3DBCO-PEG4+3PE+GD1a)8+
(P+4DBCO-PEG4+4PE+GD1a)8+
(P+1DBCO-PEG4+1PE)9+
(P+2DBCO-PEG4+2PE)9+
(P+1DBCO-PEG4+1PE)8+
(P+3DBCO-PEG4+3PE)9+
(P+2DBCO-PEG4+2PE+GD1b)9+
(P+2DBCO-PEG4+2PE)8+
(P+4DBCO-PEG4+4PE)9+
(P+1DBCO-PEG4+1PE+GD1b)8+
(P+3DBCO-PEG4+3PE+GD1b)9+
(P+3DBCO-PEG4+3PE)8+
(P+2DBCO-PEG4+2PE+GD1b)8+
(P+4DBCO-PEG4+4PE+GD1b)9+
(P+4DBCO-PEG4+4PE)8+
MSP1E1 10+
(P+3DBCO-PEG4+3PE+GD1b)8+
(P+4DBCO-PEG4+4PE+GD1b)8+
m/z

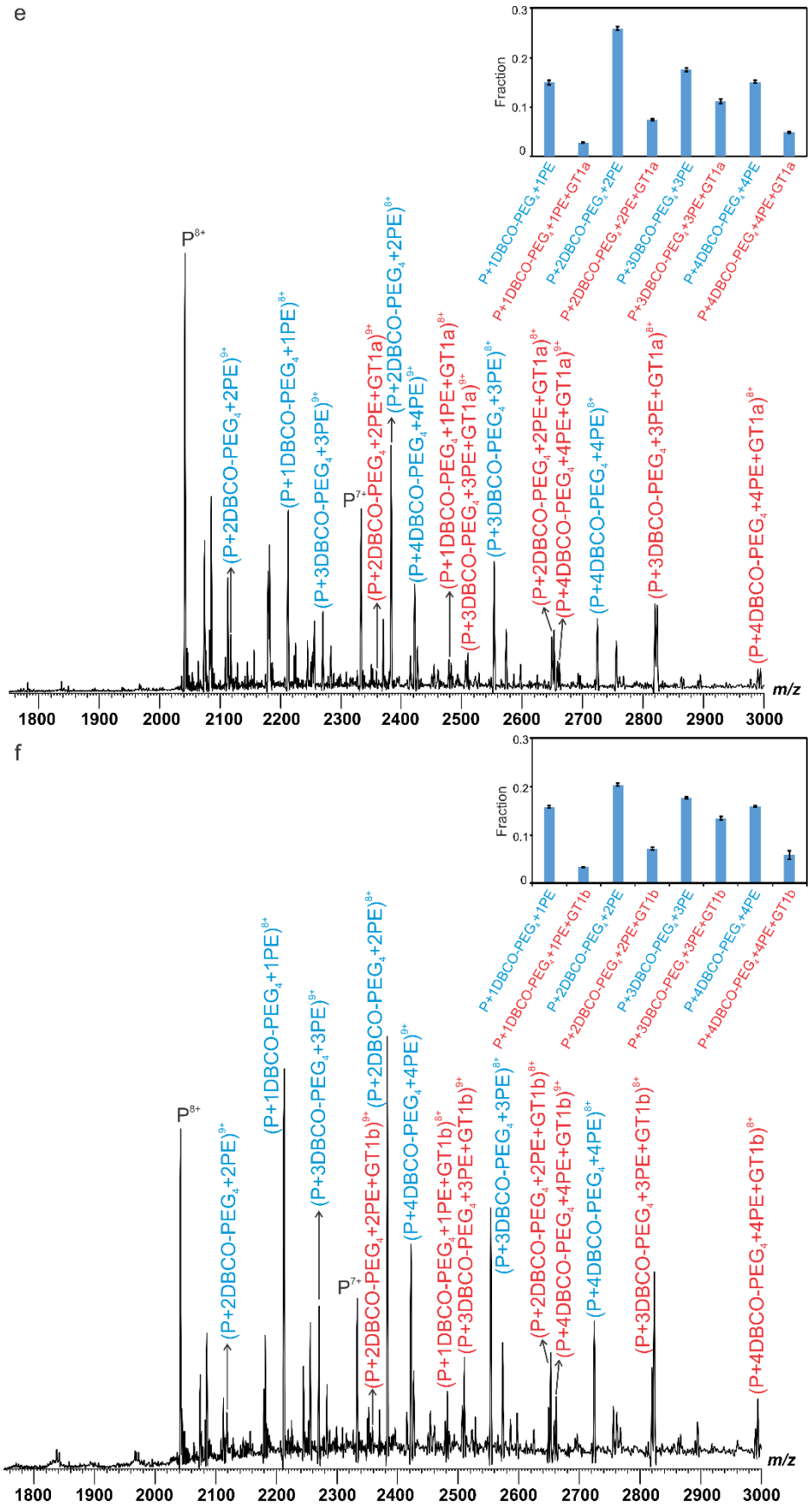
e
Fraction
P+1DBCO-PEG4+1PE
P+1DBCO-PEG4+1PE+GT1a
P+2DBCO-PEG4+2PE
P+2DBCO-PEG4+2PE+GT1a
P+3DBCO-PEG4+3PE
P+3DBCO-PEG4+3PE+GT1a
P+4DBCO-PEG4+4PE
P+4DBCO-PEG4+4PE+GT1a
P8+
(P+2DBCO-PEG4+2PE)9+
(P+1DBCO-PEG4+1PE)8+
(P+3DBCO-PEG4+3PE)9+
P7+
(P+2DBCO-PEG4+2PE+GT1a)9+
(P+2DBCO-PEG4+2PE)8+
(P+4DBCO-PEG4+4PE)9+
(P+1DBCO-PEG4+1PE+GT1a)8+
(P+3DBCO-PEG4+3PE+GT1a)9+
(P+3DBCO-PEG4+3PE)8+
(P+2DBCO-PEG4+2PE+GT1a)8+
(P+4DBCO-PEG4+4PE+GT1a)9+
(P+4DBCO-PEG4+4PE)8+
(P+3DBCO-PEG4+3PE+GT1a)8+
(P+4DBCO-PEG4+4PE+GT1a)8+
m/z
1800 1900 2000 2100 2200 2300 2400 2500 2600 2700 2800 2900 3000
f
Fraction
P+1DBCO-PEG4+1PE
P+1DBCO-PEG4+1PE+GT1b
P+2DBCO-PEG4+2PE
P+2DBCO-PEG4+2PE+GT1b
P+3DBCO-PEG4+3PE
P+3DBCO-PEG4+3PE+GT1b
P+4DBCO-PEG4+4PE
P+4DBCO-PEG4+4PE+GT1b
P8+
(P+2DBCO-PEG4+2PE)9+
(P+1DBCO-PEG4+1PE)8+
(P+3DBCO-PEG4+3PE)9+
P7+
(P+2DBCO-PEG4+2PE+GT1b)9+
(P+2DBCO-PEG4+2PE)8+
(P+4DBCO-PEG4+4PE)9+
(P+1DBCO-PEG4+1PE+GT1b)8+
(P+3DBCO-PEG4+3PE+GT1b)9+
(P+3DBCO-PEG4+3PE)8+
(P+2DBCO-PEG4+2PE+GT1b)8+
(P+4DBCO-PEG4+4PE+GT1b)9+
(P+4DBCO-PEG4+4PE)8+
(P+3DBCO-PEG4+3PE+GT1b)8+
(P+4DBCO-PEG4+4PE+GT1b)8+
m/z
1800 1900 2000 2100 2200 2300 2400 2500 2600 2700 2800 2900 3000

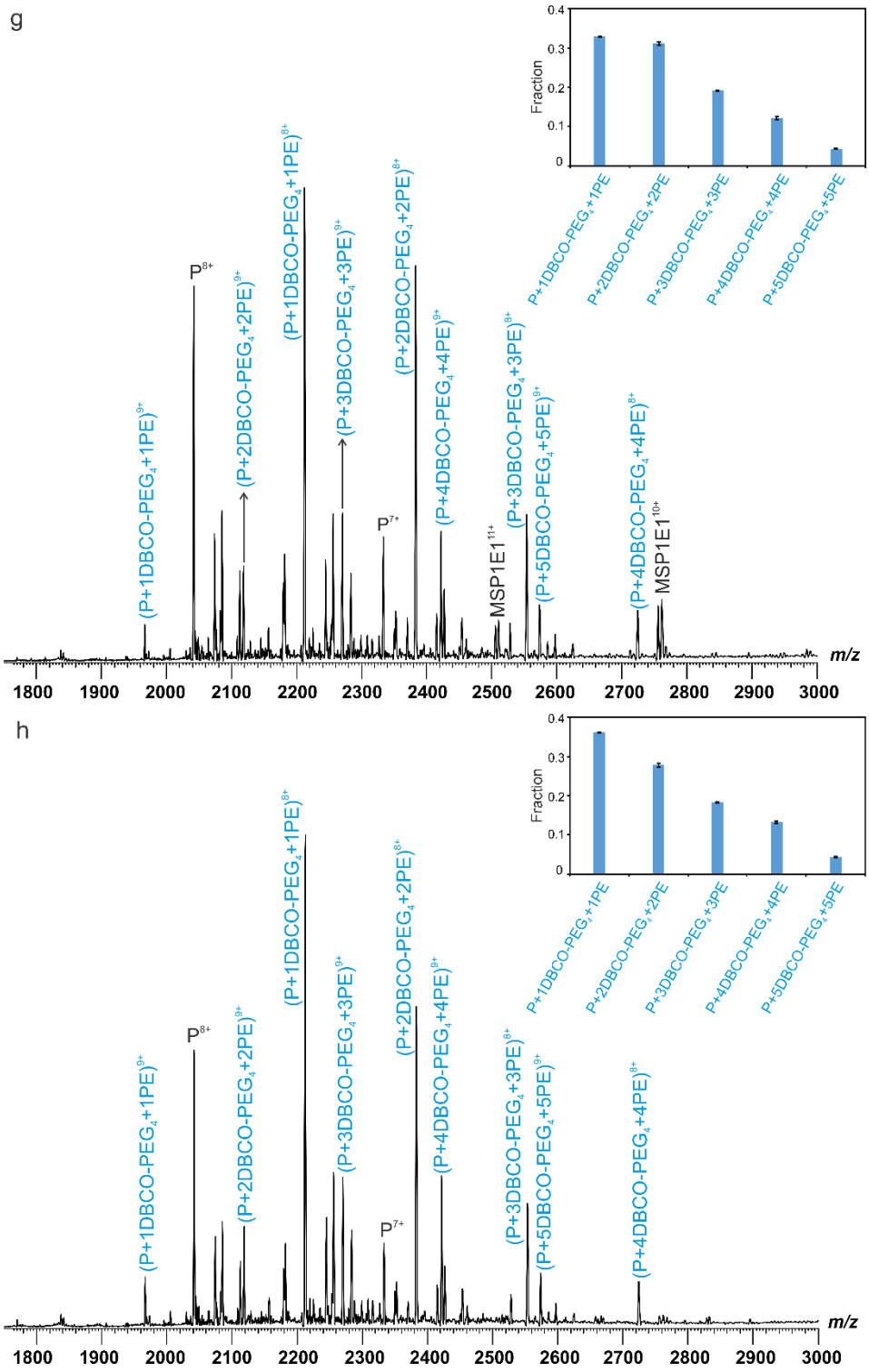

Figure 3.9. ESI mass spectra acquired in positive ion mode for aqueous ammonium acetate solutions (200 mM, 25 °C, and pH 6.8) containing labeled hGal-3C (2.8 μM) with (a) 10% GM3 20% PE POPC ND (10 μM), (b) 10% GM1 20% PE POPC ND (10 μM) (c) 10% GD1a 20% PE

POPC ND (10 μM), (d) 10% GD1b 20% PE POPC ND (10 μM), (e) 10% GT1a 20% PE POPC ND (10 μM), (f) 10% GT1b 20% PE POPC ND (10 μM) and (g) 10% GM2 20% PE POPC ND (10 μM) and (h) 10% GD2 20% PE POPC ND (10 μM) incubated for 17 h at 4 °C. Insets show the corresponding fractions of (hGal-3C + qDBCO-PEG_4 + qPE) and (hGal-3C + qDBCO-PEG_4 + qPE + GSL) measured for solutions described in (a) to (h), where q = 0-5.

To further investigate this phenomenon and monitor the dependence of low affinity GSL ligands-containing PE POPC NDs binding on incubation time, the ESI-MS measurements were performed on solutions of labeled hGal-3C (2.8 μM) incubated with a series of 10 μM 20% PE POPC NDs containing a single ganglioside (GM1, GM2, GM3, GD1a, GD1b, GD2, GT1a or GT1b, 10% ganglioside) at 4 °C for 7 h, 17 h and 40 h. Plotted in Figure 3.10 is the time-dependent fraction of GSL complexes obtained from the mass spectra. With increasing incubation time from 7 to 17 h, the amount of GSL complexes (e.g., GM1, GM3, GD1a, GD1b, GT1a and GT1b) gradually increased as well. Specially, the fractions of GM3 and GT1b complexes reached a plateau longer than 17 h, which was 0.39 and 0.3, respectively. However, based on oligosaccharides binding results, for other relatively low affinity GSL receptors such as GT1a, GD1b, the amount of formation of GSL complexes seems to reach a maximum at approximately 40 h. As expected, for the solution of labeled hGal-3C incubated with 10% GM2 20% PE POPC ND or 10% GD2 20% PE POPC ND, neither GM2 complex nor GD2 complex was detected, even at longer incubation time, which was consistent with binding results measured for hGal-3C and soluble ganglioside oligosaccharides. Overall, these results revealed that the amount of formation of GSL complexes was related to incubation time. Additionally, it also suggested that the relatively low affinity GSL ligands binding required a longer incubation time to reach equilibrium states.

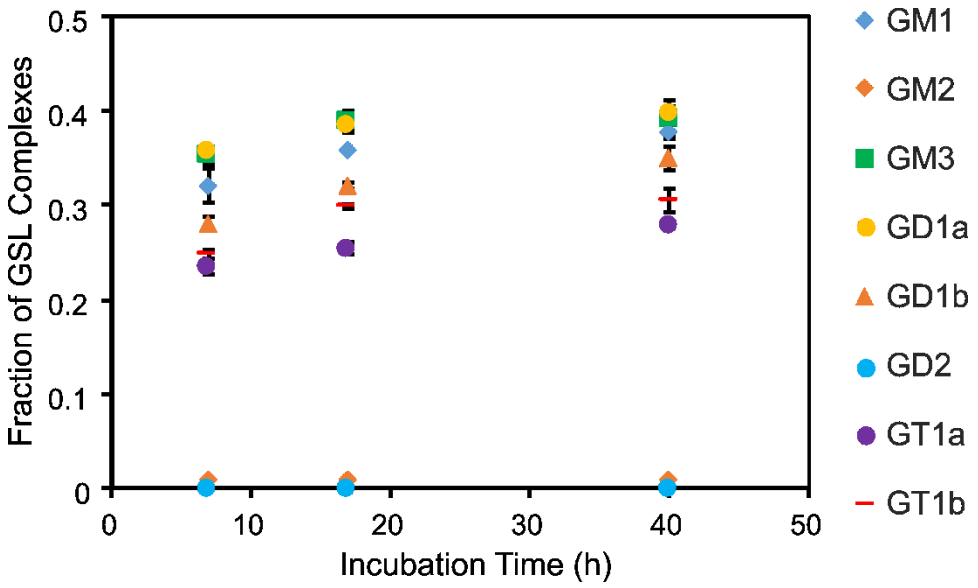

Figure 3.10. Plots of fraction of GSL complexes versus incubation time (7 h, 17 h and 40 h) measured by ESI-MS for solutions of labeled hGal-3C (2.8 μM) and NDs produced from: 10% GM1 20% PE POPC ND (10 μM); 10% GM2 20% PE POPC ND (10 μM); 10% GM3 20% PE POPC ND (10 μM); 10% GD1a 20% PE POPC ND (10 μM); 10% GD1b 20% PE POPC ND (10 μM); 10% GD2 20% PE POPC ND (10 μM); 10% GT1a 20% PE POPC ND (10 μM) and 10% GT1b 20% PE POPC ND (10 μM). The error bars correspond to one standard deviation.

In an effort to explore which factors in solution could affect the formation of GSL complexes, measurements were also performed on solutions of labeled hGal-3C (2.8 μM) with a series of 20% PE POPC NDs prepared with 10% single ganglioside (GM1, GM2, GM3, GD1a, GD1b, GD2, GT1a and GT1b, respectively) at 4 °C for 17h under different solution conditions ranging from 3 μM to 10 μM. The dependence of the fraction of GSL complexes on 10% GSL 20% PE POPC ND concentrations is shown in Figure 3.11. From low to high ND concentrations, the fraction of click complexes bound to one GSL, i.e., $f_{(\text{hGal-3C + qDBCO-PEG4 + qPE+GSL})}$, with q = 1-4, gradually increased except GM2 and GD2 ligands even at a high concentration of POPC NDs. These results revealed that the formation of GSL complexes was sensitive to the concentration of GSL PE POPC NDs.

Once the concentration of GSL PE POPC NDs increased to above 10 μM, it was difficult to acquire signal due to ion suppression effects of NDs in ESI.

Taken together, the present data provide the direct evidence that the membrane anchor assay was successfully developed to discover weak GBP-GSL interactions. Moreover, the novel feature of this assay was that it could be applied to a monovalent GBP such as hGal-3C.

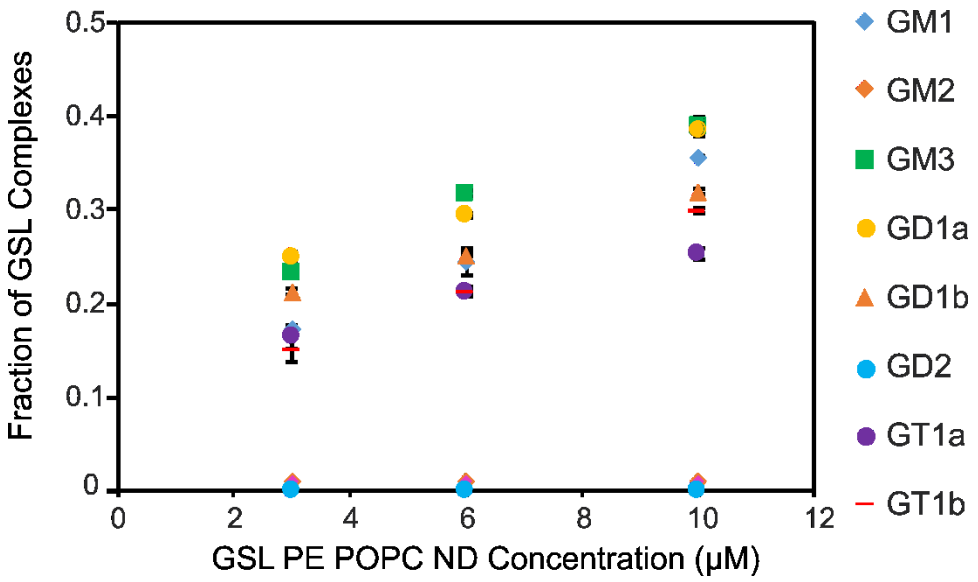

Figure 3.11. Plots of fraction of GSL complexes versus GSL PE POPC ND concentrations (3 μM, 6 μM and 10 μM) measured by ESI-MS for solutions of labeled hGal-3C (2.8 μM) and NDs produced from: 10% GM1 20% PE POPC ND; 10% GM2 20% PE POPC ND; 10% GM3 20% PE POPC ND; 10% GD1a 20% PE POPC ND; 10% GD1b 20% PE POPC ND; 10% GD2 20% PE POPC ND; 10% GT1a 20% PE POPC ND and 10% GT1b 20% PE POPC ND incubated for 17 h. The error bars correspond to one standard deviation.

3.3.4 Detecting hGal-1 and hGal-7 interactions with low affinity GM3 ligand by membrane anchor-assisted CaR-ESI-MS assay

In order to confirm that membrane anchor-assisted CaR-ESI-MS assay is a general method, we are extending measurements to other two human galectins which are hGal-1 and hGal-7. Since the affinities of $GM3_{os}$ for hGal-1 and hGal-7 have been previously reported,[31] proteins of two human galectins and their interactions with ganglioside GM3 presented in NDs were also measured using this new approach. The results showed direct evidence of GM3 binding for hGal-1 and hGal-7. We summarized the results as follows:

The prototype hGal-1 and hGal-7, which are known to exist as noncovalent dimer in neutral solution, contain eighteen primary amino groups (dimer: sixteen Lys residues and two N-termini) and only eight primary amino groups (dimer: six Lys residues and two N-termini), respectively. Shown in Figure 3.12a and 3.12b are representative ESI mass spectra acquired in positive ion mode for aqueous ammonium acetate solutions (200 mM, pH 6.8) of modified hGal-1 (3 μM) and hGal-7 (8 μM), respectively. Labeled hGal-1 and hGal-7 were found to contain ions corresponding to labeled proteins with 0 to 4 DBCO-PEG_4 groups (i.e., $(P_2 + q\text{DBCO-PEG}_4)^{n+}$, where q = 0-4 and n = 9-11). The normalized distributions of $(P_2 + q\text{DBCO-PEG}_4)$ in the insets revealed that the mainly modified hGal-1 species corresponded to dimeric hGal-1 (i.e., hGal-1_2^{n+} at charge states +9 and +10), as well as hGal-1 labeled with one DBCO-PEG_4 group (i.e., $(\text{hGal-1}_2 + 1\text{DBCO-PEG}_4)^{n+}$, where n = 9-10), while hGal-7 was predominantly labeled with one DBCO-PEG_4 group (i.e., $(\text{hGal-7}_2 + 1\text{DBCO-PEG}_4)^{n+}$, where n = 10-11) under the solution condition.

To confirm that click chemistry reaction happened, the direct ESI-MS measurements were performed on aqueous ammonium acetate solutions (200 mM, pH 6.8) containing labeled hGal-1 (3 μM) with 20% PE POPC ND (12 μM) and modified hGal-7 (8 μM) with 20% PE POPC ND (5

μM) for 15 h at 4 °C, respectively (Figure 3.13a and 3.13b). Inspection of the representative mass spectra revealed ion signal corresponding to (P_2 + qDBCO-PEG_4 + qPE) at charge state +10 to +11, where q = 1-2, as well as free P_2^{n+}, with n = 9-11. In contrast, proteins labeled with DBCO-PEG_4 species were consumed completely after 15h incubation, which indicated click chemistry reaction occurred in the bulk solution.

Shown in Figure 3.14a and Figure 3.14b are representative mass spectra acquired in positive ion mode for aqueous solutions of labeled hGal-1 (3 μM) with 10% GM3 20% PE POPC ND (13 μM) incubated for 15 h and labeled hGal-7 (3.5 μM) incubated with the 10% GM3 20% PE POPC ND (3 μM) for 3.5 h. Signal corresponding to click complexes ions, i.e., (P_2 + qDBCO-PEG_4 + qPE) $^{n+}$, where q = 1-2 and n = 10-11, as well as predominantly free P_2^{n+}, with n = 9-11 were identified from the spectra. Notably, inspection of the mass spectra also revealed a measurable amount of click complexes bound to one GM3 ions, i.e., (P_2 + 1DBCO-PEG_4 + 1PE + GM3)$^{n+}$, with n = 10-11. As seen in the inset, the fractions of click complexes bound to GM3 for hGal-1 or hGal-7 were approximately 0.32 and 0.25, respectively. These results further demonstrated that the membrane anchor-assisted CaR-ESI-MS assay can be also applied to multivalent GBPs for detection of low affinity GBP-GSL interactions.

Subsequently, measurements were extended to explore the dependence of GM3 binding on ND concentration. Plotted in Figure 3.15a and 3.15b are fractions of GM3 complexes (f_{GM3}) as a function of 10% GM3 20% PE POPC ND concentration for hGal-1 and hGal-7, respectively. It can be seen that the fraction of GM3 complexes firstly increased with GM3 PE POPC ND concentration, reaching a maximum, and then dropped off slightly with increasing GM3 PE POPC ND concentration. These results suggested that the formation of GM3 complexes was predominantly controlled by GM3 PE POPC ND concentrations in the solution, which was

consistent with the result measured for hGal-3C. However, the data also showed that the addition of relatively high concentration of GM3 PE POPC ND to the solution mightn't facilitate the formation of GM3 complexes due to clustering of GM3.

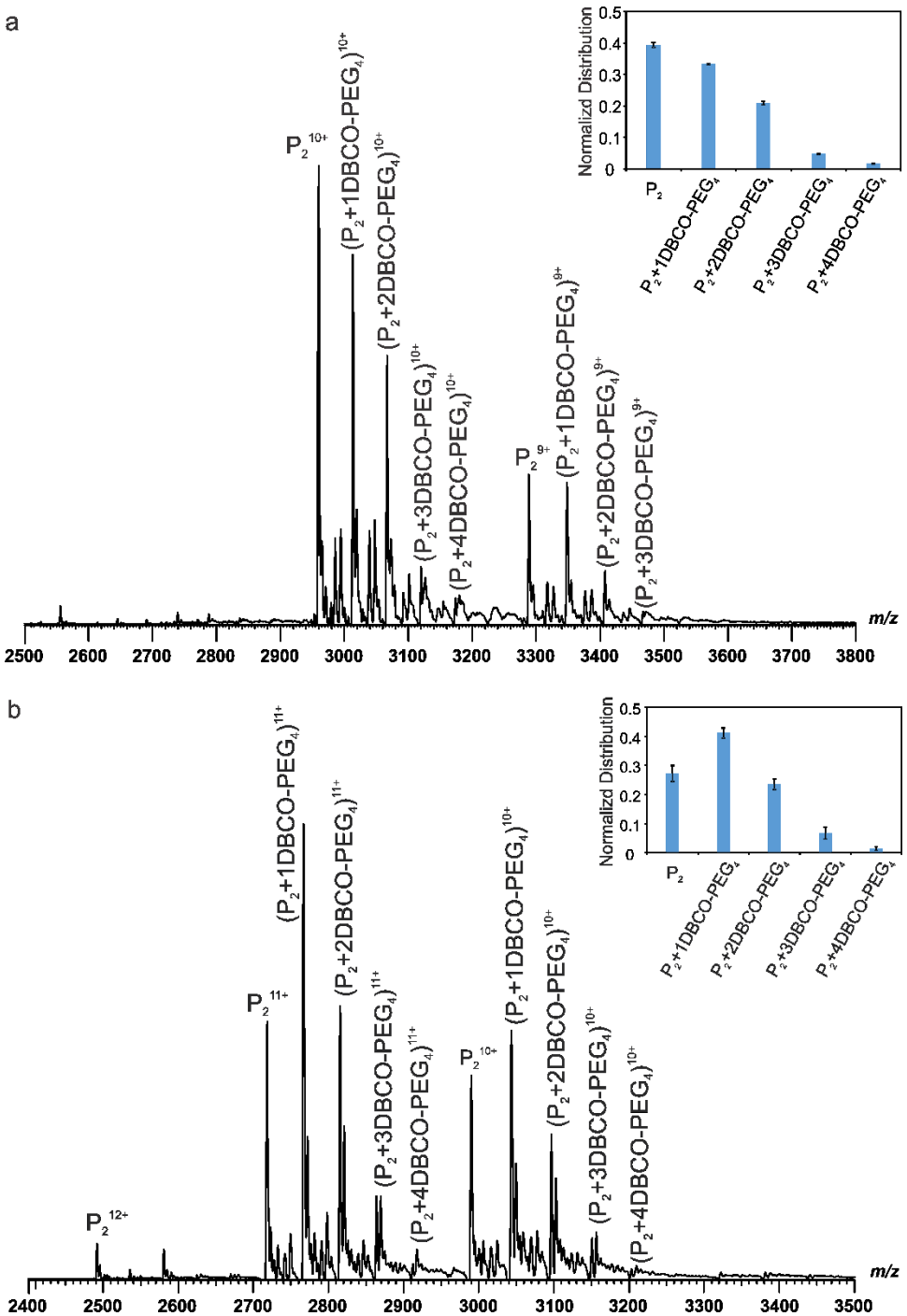

Figure 3.12. ESI mass spectra acquired in positive ion mode for aqueous ammonium acetate

solutions (200 mM, 25 °C, and pH 6.8) containing (a) hGal-1 labeled with DBCO-PEG$_4$ (3 μM) and (b) hGal-7 labeled with DBCO-PEG$_4$ (8 μM). Insets show the normalized distributions of (P_2 + qDBCO-PEG$_4$) measured for solutions described in (a) and (b), where q = 0-4.

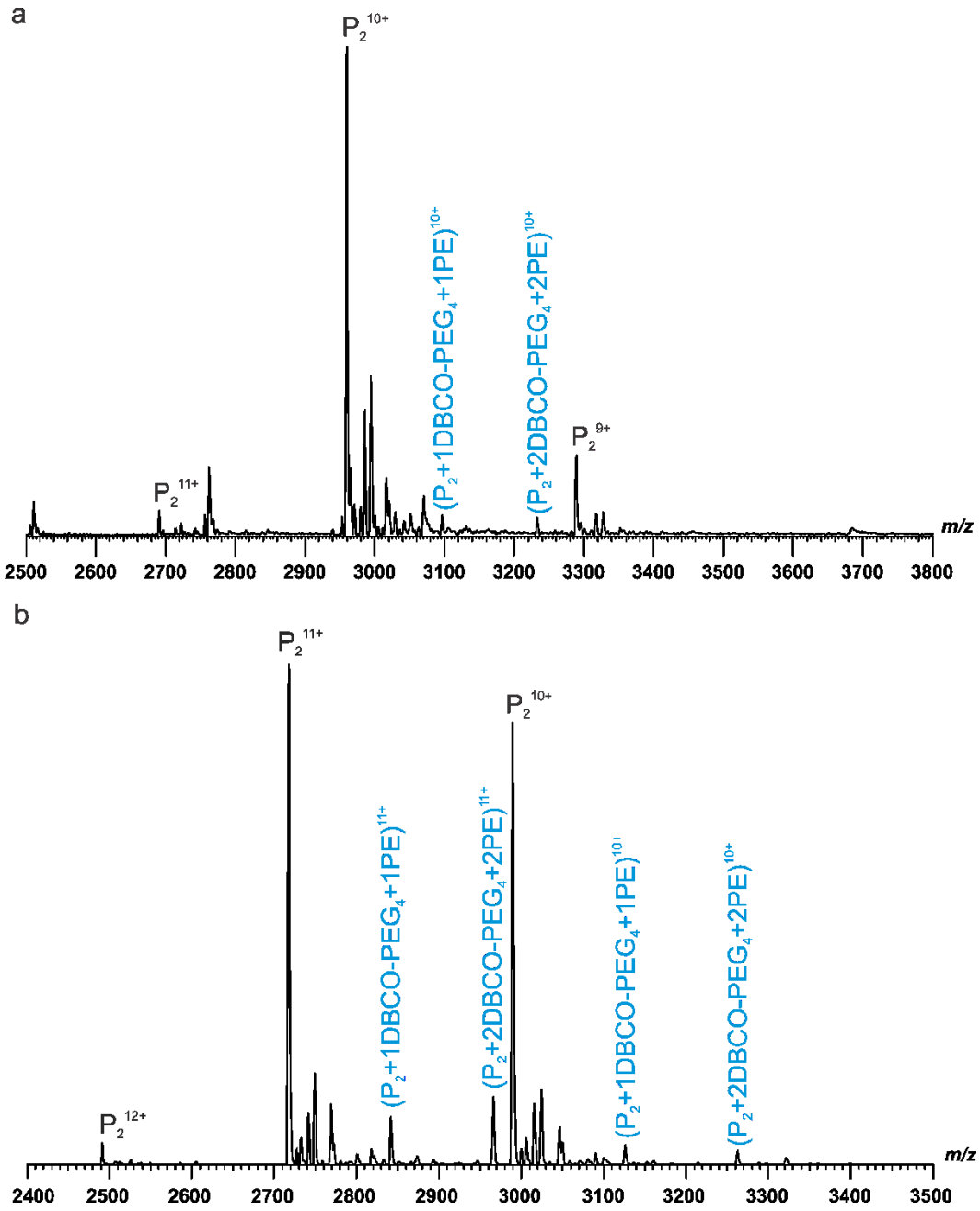

Figure 3.13. ESI mass spectra acquired in positive ion mode for aqueous ammonium acetate solutions (200 mM, 25 °C, and pH 6.8) containing (a) hGal-1 labeled with DBCO-PEG$_4$ (3 μM)

with 20% PE POPC ND (12 μM) and (b) hGal-7 labeled with DBCO-PEG$_4$ (8 μM) with 20% PE POPC ND (5 μM) incubated for 15 h at 4 °C.

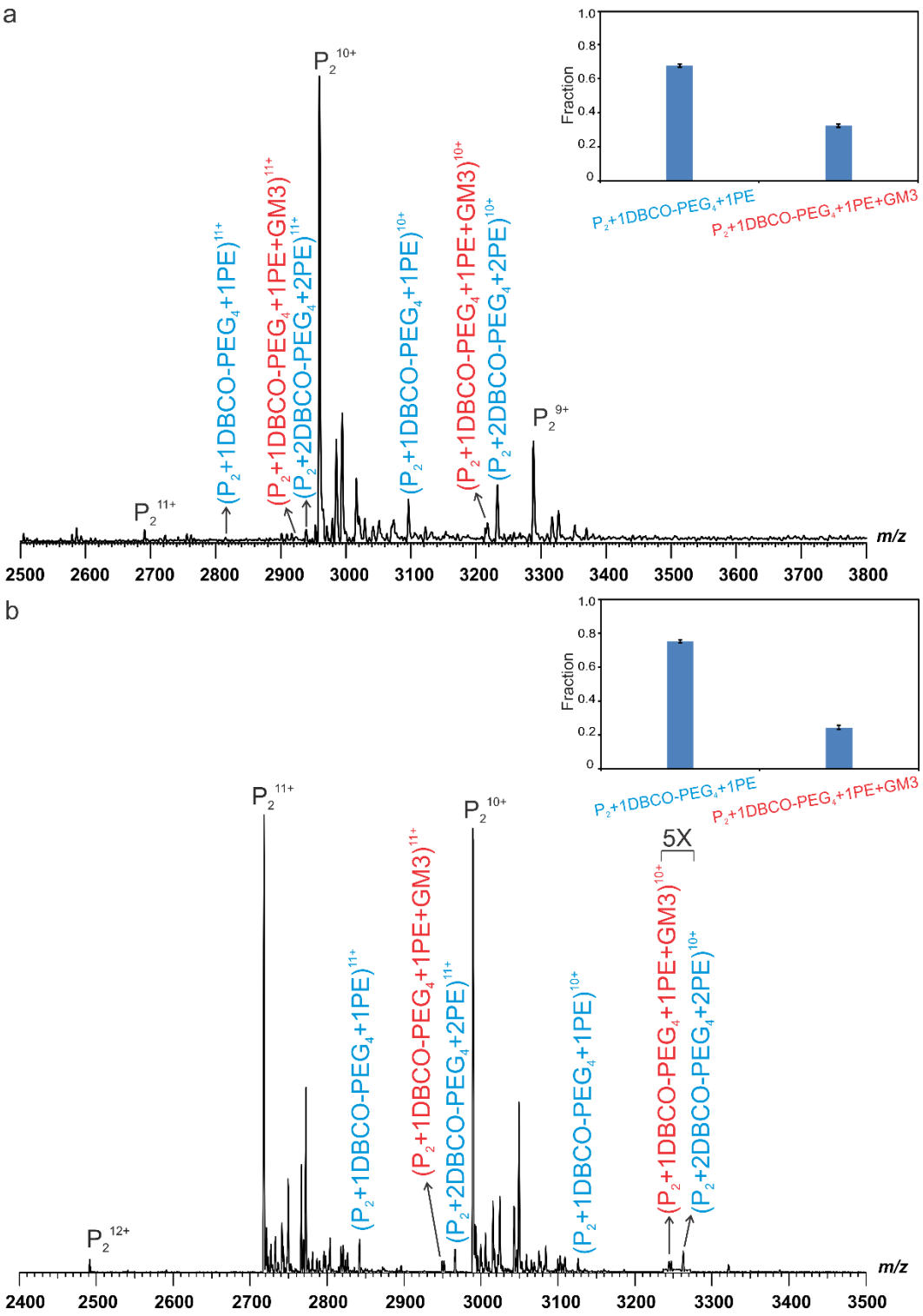

Figure 3.14. ESI mass spectrum acquired in positive ion mode for aqueous ammonium acetate

solutions (200 mM, 25 °C, and pH 6.8) containing (a) labeled hGal-1 (3 μM) with 10% GM3 20% PE POPC ND (13 μM) incubated for 15 h and (b) labeled hGal-7 (3.5 μM) with 10% GM3 20% PE POPC ND (3 μM) incubated for 3.5 h. Insets show the corresponding fractions of (P_2 + 1DBCO-PEG_4 + 1PE) and (P_2 + 1DBCO-PEG_4 + 1PE + GM3) measured for solutions described in (a) and (b).

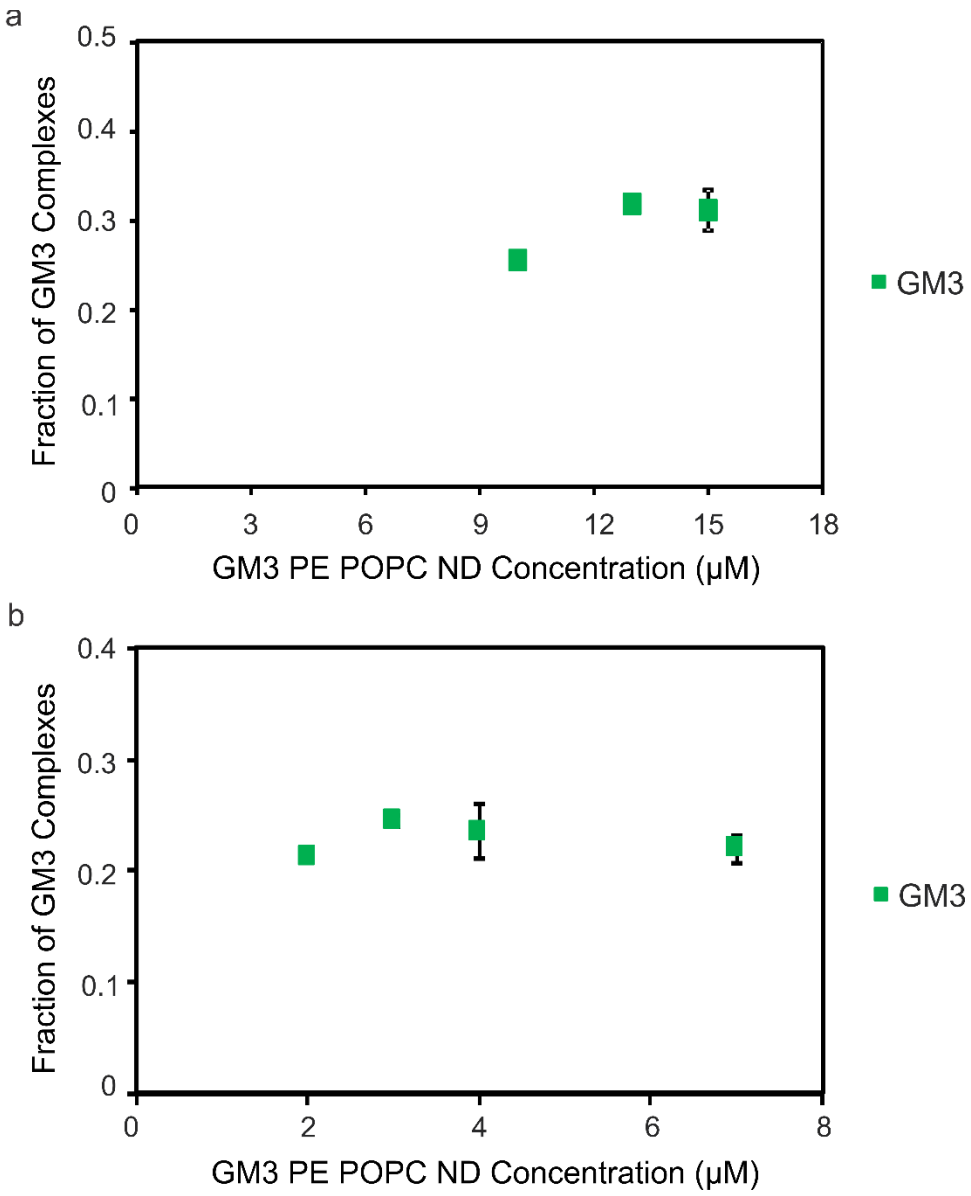

Figure 3.15. Plots of fraction of GM3 complexes versus GM3 PE POPC ND concentration measured by ESI-MS for solutions of (a) labeled hGal-1 (3 μM) and 10% GM3 20% PE POPC

ND (10 μM, 13 μM and 15 μM) incubated for 15h; (b) labeled hGal-7 (3.5 μM) and 10% GM3 20% PE POPC ND (2 μM, 3 μM, 4 μM and 7 μM). The error bars correspond to one standard deviation.

3.4 Conclusions

In summary, the results of the present study demonstrated the implementation and reliability of the new membrane anchor-assisted CaR-ESI-MS assay to enhance the detection of low affinity interactions between GBPs and GSLs presented in model membranes. The implementation of this assay using human galectins (i.e., hGal-3C, hGal-1 and hGal-7) and their interactions with gangliosides ligands presented in NDs revealed that low affinity interactions can be successfully detected by covalently cross-linking the GBP to the ganglioside-containing NDs through a modified lipid served as membrane anchor. The results of this study were validated using binding data measured for the corresponding ganglioside oligosaccharides. A notable feature of this approach was that it can, in principle, be applied to any GBP, including those possessing a single binding site. Moreover, the present results revealed that the formation of GBP-GSL complexes not only was predominantly controlled by the ND concentrations in the solution, but also was dependent on incubation time. Future measurements will be carried out using hGal-1 and hGal-7 and their interactions with other ganglioside ligands in NDs to highlight the utility of this new approach. Overall, these data of the membrane anchor-assisted CaR-ESI-MS assay provide important guidance for discovering new GSL receptors of GBPs in native-like membrane environments.

3.5 References

(1) Daniotti, J. L.; Lardone, R. D.; Vilcaes, A. A. Dysregulated Expression of Glycolipids in Tumor Cells: From Negative Modulator of Anti-Tumor Immunity to Promising Targets for Developing Therapeutic Agents. *Front. Oncol.* **2016**, *5*, 300.

(2) Malhotra, R. Membrane Glycolipids: Functional Heterogeneity: A Review. *Biochem. Anal. Biochem.* **2012**, *1* (2).

(3) Saliba, A.-E.; Vonkova, I.; Gavin, A.-C. The Systematic Analysis of Protein–lipid Interactions Comes of Age. *Nat. Rev. Mol. Cell Biol.* **2015**, *16* (12), 753–761.

(4) Zuverink, M.; Barbieri, J. T. Protein Toxins That Utilize Gangliosides as Host Receptors. *Progress in Molecular Biology and Translational Science*. **2018**, 156, 325–354.

(5) Ledeen, R. W.; Kopitz, J.; Abad-Rodríguez, J.; Gabius, H.-J. Glycan Chains of Gangliosides: Functional Ligands for Tissue Lectins (Siglecs/Galectins). *Progress in Molecular Biology and Translational Science*. **2018**, 156, 289–324.

(6) Zhang, T.; de Waard, A. A.; Wuhrer, M.; Spaapen, R. M. The Role of Glycosphingolipids in Immune Cell Functions. *Front. Immunol.* **2019**, *10* (1), 1–22.

(7) Merrill, A. H.; Wang, M. D.; Park, M.; Sullards, M. C. (Glyco)Sphingolipidology: An Amazing Challenge and Opportunity for Systems Biology. *Trends Biochem. Sci.* **2007**, *32* (10), 457–468.

(8) Cummings, R. D.; Pierce, J. M. The Challenge and Promise of Glycomics. *Chem. Biol.* **2014**, *21* (1), 1–15.

(9) Cummings, R. D. The Repertoire of Glycan Determinants in the Human Glycome. *Mol. Biosyst.* **2009**, *5* (10), 1087.

(10) Worstell, N. C.; Singla, A.; Saenkham, P.; Galbadage, T.; Sule, P.; Lee, D.; Mohr, A.; Kwon,

J. S.; Cirillo, J. D.; Wu, H. Hetero-Multivalency of Pseudomonas Aeruginosa Lectin LecA Binding to Model Membranes. *Sci. Rep.* **2018**, *8* (1), 8419.

(11) Krishnan, P.; Singla, A.; Lee, C.-A.; Weatherston, J. D.; Worstell, N. C.; Wu, H.-J. Hetero-Multivalent Binding of Cholera Toxin Subunit B with Glycolipid Mixtures. *Colloids Surfaces B Biointerfaces.* **2017**, *160*, 281–288.

(12) Han, L.; Morales, L. C.; Richards, M. R.; Kitova, E. N.; Sipione, S.; Klassen, J. S. Investigating the Influence of Membrane Composition on Protein–Glycolipid Binding Using Nanodiscs and Proxy Ligand Electrospray Ionization Mass Spectrometry. *Anal. Chem.* **2017**, *89* (17), 9330–9338.

(13) Song, X.; Lasanajak, Y.; Xia, B.; Heimburg-Molinaro, J.; Rhea, J. M.; Ju, H.; Zhao, C.; Molinaro, R. J.; Cummings, R. D.; Smith, D.F. Shotgun Glycomics: A Microarray Strategy for Functional Glycomics. *Nature Methods.* **2011**, *8* (1), 85–90.

(14) Grant, O. C.; Smith, H. M. K.; Firsova, D.; Fadda, E.; Woods, R. J. Presentation, Presentation, Presentation! Molecular-Level Insight into Linker Effects on Glycan Array Screening Data. *Glycobiology.* **2014**, *24* (1), 17–25.

(15) Fais, M.; Karamanska, R.; Russell, D. A.; Field, R. A. Lectin and Carbohydrate Microarrays: New High-Throughput Methods for Glycoprotein, Carbohydrate-Binding Protein and Carbohydrate-Active Enzyme Analysis. *J. Cereal Sci.* **2009**, *50* (3), 306–311.

(16) Yao, Y.; Shams-Ud-Doha, K.; Daneshfar, R.; Kitova, E. N.; Klassen, J. S. Quantifying Protein-Carbohydrate Interactions Using Liquid Sample Desorption Electrospray Ionization Mass Spectrometry. *J. Am. Soc. Mass Spectrom.* **2015**, *26* (1), 98–106.

(17) Lin, H.; Kitova, E. N.; Klassen, J. S. Measuring Positive Cooperativity Using the Direct ESI-MS Assay. Cholera Toxin B Subunit Homopentamer Binding to GM1 Pentasaccharide.

J. Am. Soc. Mass Spectrom. **2014**, *25* (1), 104–110.

(18) El-Hawiet, A.; Shoemaker, G. K.; Daneshfar, R.; Kitova, E. N.; Klassen, J. S. Applications of a Catch and Release Electrospray Ionization Mass Spectrometry Assay for Carbohydrate Library Screening. *Anal. Chem.* **2012**, *84* (1), 50–58.

(19) Han, L.; Kitova, E. N.; Tan, M.; Jiang, X.; Klassen, J. S. Identifying Carbohydrate Ligands of a Norovirus P Particle Using a Catch and Release Electrospray Ionization Mass Spectrometry Assay. *J. Am. Soc. Mass Spectrom.* **2014**, *25* (1), 111–119.

(20) Abzalimov, R. R.; Dubin, P. L.; Kaltashov, I. A. Glycosaminoglycans as Naturally Occurring Combinatorial Libraries: Developing a Mass Spectrometry-Based Strategy for Characterization of Anti-Thrombin Interaction with Low Molecular Weight Heparin and Heparin Oligomers. *Anal. Chem.* **2007**, *79* (16), 6055–6063.

(21) Li, J.; Fan, X.; Kitova, E. N.; Zou, C.; Cairo, C. W.; Eugenio, L.; Ng, K. K. S.; Xiong, Z. J.; Privé, G. G.; Klassen, J. S. Screening Glycolipids Against Proteins in Vitro Using Picodiscs and Catch-and-Release Electrospray Ionization-Mass Spectrometry. *Anal. Chem.* **2016**, *88* (9), 4742–4750.

(22) Leney, A. C.; Fan, X.; Kitova, E. N.; Klassen, J. S. Nanodiscs and Electrospray Ionization Mass Spectrometry: A Tool for Screening Glycolipids Against Proteins. *Anal. Chem.* **2014**, *86* (11), 5271–5277.

(23) Cohen, M.; Varki, A. Modulation of Glycan Recognition by Clustered Saccharide Patches. *International Review of Cell and Molecular Biology*. **2014**, *308*, 75–125.

(24) Overduin, M.; Esmaili, M. Native Nanodiscs and the Convergence of Lipidomics, Metabolomics, Interactomics and Proteomics. *Appl. Sci.* **2019**, *9* (6), 1230.

(25) Ouellet, M.; Mercier, S.; Pelletier, I.; Bounou, S.; Roy, J.; Hirabayashi, J.; Sato, S.; Tremblay,

M. J. Galectin-1 Acts as a Soluble Host Factor That Promotes HIV-1 Infectivity through Stabilization of Virus Attachment to Host Cells. *J. Immunol.* **2005**, *174* (7), 4120–4126.

(26) Sun, J.; Kitova, E. N.; Wang, W.; Klassen, J. S. Method for Distinguishing Specific from Nonspecific Protein−Ligand Complexes in Nanoelectrospray Ionization Mass Spectrometry. *Anal. Chem.* **2006**, *78* (9), 3010–3018.

(27) Bayburt, T. H.; Grinkova, Y. V.; Sligar, S. G. Self-Assembly of Discoidal Phospholipid Bilayer Nanoparticles with Membrane Scaffold Proteins. *Nano Lett.* **2002**, *2* (8), 853–856.

(28) Denisov, I. G.; Grinkova, Y. V.; Lazarides, A. A.; Sligar, S. G. Directed Self-Assembly of Monodisperse Phospholipid Bilayer Nanodiscs with Controlled Size. *J. Am. Chem. Soc.* **2004**, *126* (11), 3477–3487.

(29) Ritchie, T. K.; Grinkova, Y. V.; Bayburt, T. H.; Denisov, I. G.; Zolnerciks, J. K.; Atkins, W. M.; Sligar, S. G. Chapter 11 Reconstitution of Membrane Proteins in Phospholipid Bilayer Nanodiscs. *Methods in Enzymology*. **2009**, 211–231.

(30) Sun, J.; Kitova, E. N.; Wang, W.; Klassen, J. S. Method for Distinguishing Specific from Nonspecific Protein−Ligand Complexes in Nanoelectrospray Ionization Mass Spectrometry. *Anal. Chem.* **2006**, *78* (9), 3010–3018.

(31) Shams-Ud-Doha, K.; Kitova, E. N.; Kitov, P. I.; St-Pierre, Y.; Klassen, J. S. Human Milk Oligosaccharide Specificities of Human Galectins. Comparison of Electrospray Ionization Mass Spectrometry and Glycan Microarray Screening Results. *Anal. Chem.* **2017**, *89* (9), 4914–4921.

(32) Kitova, E. N.; El-Hawiet, A.; Schnier, P. D.; Klassen, J. S. Reliable Determinations of Protein–Ligand Interactions by Direct ESI-MS Measurements. Are We There Yet? *J. Am. Soc. Mass Spectrom.* **2012**, *23* (3), 431–441.

Chapter 4

Conclusions and Future Work

4.1 Conclusions

The work describes the development and application of electrospray ionization mass spectrometry (ESI-MS) based techniques to discovery water-soluble proteins interactions with carbohydrates or glycolipids (GLs) in model membranes (MMs). The first project (Chapter 2) focuses on the implementation of the native ESI-MS based direct/competitive binding assay and catch-and-release electrospray ionization mass spectrometry (CaR-ESI-MS) assay to quantitatively investigate the ganglioside binding properties of three anti-GD2 antibodies. The second project (Chapter 3) describes the development of a new CaR-ESI-MS assay for detecting low affinity interactions between glycan binding proteins (GBPs) and glycosphingolipids (GSLs) presented in nanodiscs (NDs).

In Chapter 2, as a starting point, the direct ESI-MS assay was employed to quantitatively evaluate the interactions between the hu3F8 and its double mutant E1K/D32H antigen binding fragments (Fabs) and 14G2a monoclonal antibody (mAb), and fourteen ganglioside oligosaccharides. The results of the binding measurements showed that the $GD2_{os}$ affinities followed the order: hu3F8 E1K/D32H Fab ($K_{a,GD2os}$ = (22 ± 1.5) x 10^5 M^{-1}) > hu3F8 Fab ($K_{a,GD2os}$ = (4.3 ± 0.1) x 10^5 M^{-1}) > 14G2a mAb ($K_{a1,app}$ = (1.2 ± 0.9) x 10^5 M^{-1}, $K_{a2,app}$ = (4.1 ± 0.4) x 10^4 M^{-1} and $K_{a,int,GD2os}$ = (7.0 ± 0.2) x 10^4 M^{-1} (per binding site). A significant finding of this study was that all of the ganglioside oligosaccharides tested were recognized by the antibodies, although with lower affinities, in the 2.0 x 10^2 M^{-1} - 5.8 x 10^3 M^{-1} range. Subsequently, the CaR-ESI-MS assay and competitive binding ESI-MS assays, implemented with model membrane nanodiscs (NDs),

were used to detect and quantitatively investigate the ganglioside specificities of a series of anti-GD2 mAbs and their Fabs. Application of CaR-ESI-MS to screen small libraries of gangliosides against the three anti-GD2 mAbs demonstrated that, for hu3F8 and hu3F8E1K/D32H mAbs, only GD2 was recognized. However, 14G2a mAb has measurable binding to GM3 and GM4, although GD2 is preferentially recognized. Finally, the competitive ESI-MS binding data demonstrates the extent of GD2 binding to 14G2a mAb and hu3F8 and its double mutant E1K/D32H Fabs is found to be sensitive to ganglioside content of the NDs. A notable finding of this study is that the affinities for the interactions of these anti-GD2 antibodies with GD2 in NDs gradually decrease with increasing GD2 content of the NDs, which results from the occurrence of GD2 clustering in the membrane.

In Chapter 3, a new membrane anchor-assisted CaR-ESI-MS method was developed to enhance the detection of low affinity interactions between GBPs and GSLs in MMs. The membrane anchor method involves covalent cross-linking of the GBP to the GSL-containing MM by introducing a modified lipid. This membrane anchor serves to enhance the local concentration of GBP on the surface of the membrane and improve binding to GSL ligands. A notable feature of this assay is that it can be applied to any GBPs, including those with a single binding site. The reliability of this new approach was established using three human galectins and their known interactions with gangliosides presented in NDs. The implementation of this assay revealed that weak interactions between GBPs and GSLs in NDs can be successfully detected. The results of this study are further validated using binding results measured for the corresponding ganglioside oligosaccharides. Moreover, the present results indicate that the formation of GBP-GSL complexes not only is controlled by the ND concentrations in the solution, but also is dependent on incubation time.

4.2 Future work

There are various possible extensions of the current studies. As mentioned in Chapter 3, we demonstrate the implementation and reliability of membrane anchor-assisted CaR-ESI-MS approach using human galectins and their interactions with gangliosides ligands presented in NDs. In the future, we will apply this method to discover new GSL receptors of GBPs. One class of target GBPs that will be investigated are the human Siglecs, which are sialic-acid-binding immunoglobulin-like lectins that are mostly expressed by cells of the immune system.[1,2] Each Siglec has a distinct preference for binding sialylated ligands which are found on the surface of all mammalian cells and these interactions play key roles in regulating immune cell functions and pathological processes.[2,3] It is believed that all Siglecs have the potential to interact with sialylated gangliosides through their respective V-set domains.[4] Siglec-1, which serves as a pathogen recognition receptor, binds promiscuously to many sialylated molecules typically found on pathogens, including HIV and murine leukemia virus.[5,6,7] Siglec-1 can capture HIV-1 through recognition of sialylated carbohydrate head group of viral membrane gangliosides and then promote uptake and trans infection.[4,8] Although some groups have reported that gangliosides such as GM1, GM2 and GM3 present in HIV-1 membranes might be critical for the HIV/Siglec-1 interactions, the discovery of the role of Siglec-1 in capturing viruses with some gangliosides in their membranes is poorly understood.[8-10] More generally, the ganglioside binding properties of Siglec-1 have not been convincingly established.[8,11-13]

To address this deficiency, we have recently begun applying the membrane anchor-assisted CaR-ESI-MS assay to assess the ganglioside specificities of Siglec-1. Preliminary measurements carried out using a fragment of human Siglec-1 and POPC NDs containing a single ganglioside (GM1, GM2 or GM3, shown in Figure 4.1) failed to detect any ganglioside binding, even at high

concentration. However, application of the membrane anchor-assisted CaR-ESI-MS assay revealed evidence of Siglec-1 binding to all three gangliosides (Figure 4.2, Figure 4.3a-4.3c). Affinity measurements performed on the oligosaccharides of the three gangliosides confirmed that Siglec-1 recognizes these carbohydrates, albeit with low affinity GSL (K_a = ~ 10^3 M^{-1}). Future investigations will be carried to test binding to other gangliosides in order to comprehensively establish the gangliosides binding specificities of Siglec-1.

Another extension of the work in Chapter 3 is to explore other azide-containing phospholipids as membrane anchors. Recent studies by our lab into hetero-multivalent GSL binding to GBPs suggest that this process may be regulated by the relative (to the membrane surface) position of the high and low affinity GSLs. Inspired by this finding, we hypothesize the low affinity GSL ligand binding might be enhanced by varying the length of the terminal azide group of the modified lipid (membrane anchor). To explore this possibility, we will implement the membrane anchor-assisted CaR-ESI-MS method using additional azide-containing phospholipids, such as azidoethyl PC (18:0) and azidoethyl SM (16:0). The structures of the modified lipids are shown in Figure 4.4. Specifically, we will test the influence of the length of the azide-containing phospholipids to that of the GSL ligands on GBP binding.

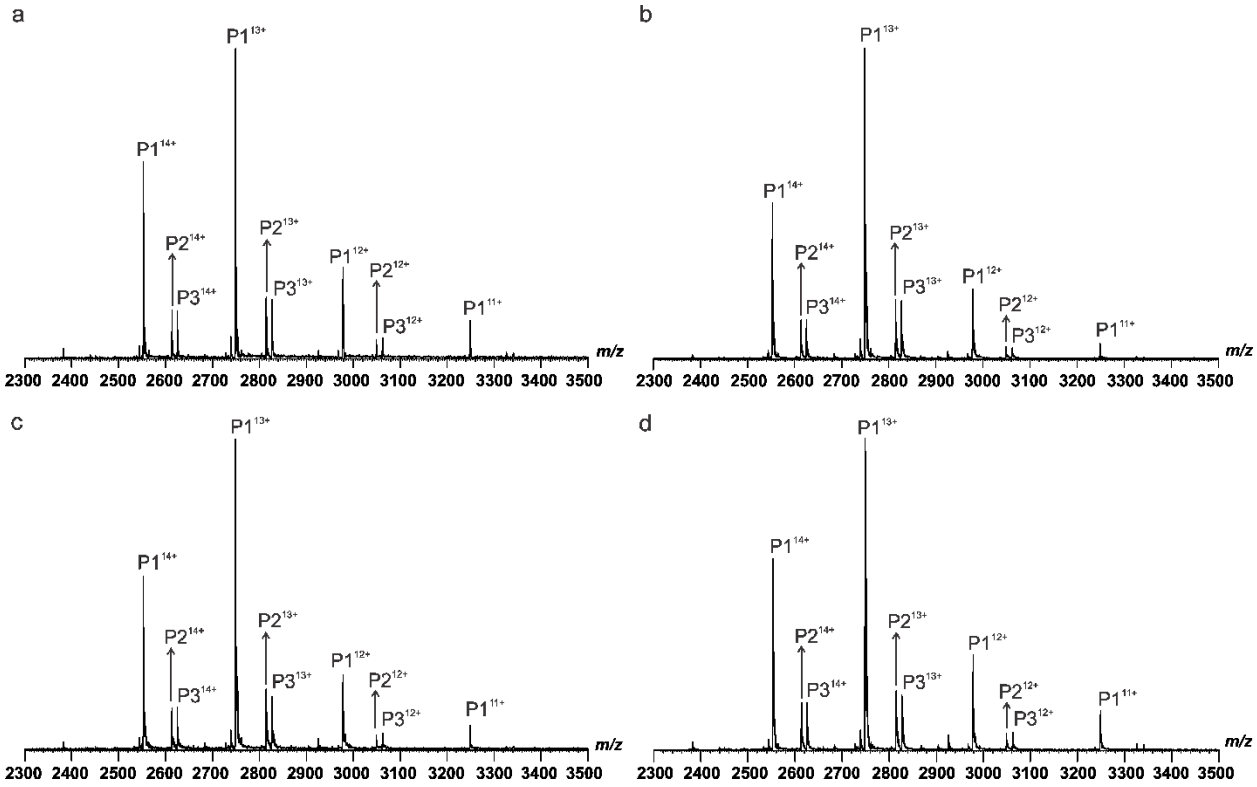

Figure 4.1. ESI mass spectra acquired in positive ion mode for aqueous ammonium acetate solutions (200 mM, pH 6.8) of (a) fragment of human Siglec-1 (3 μM) and with (b) 8 μM 10% GM1 POPC ND, (c) 8 μM 5% GM2 POPC ND, (d) 8 μM 5% GM3 POPC ND.

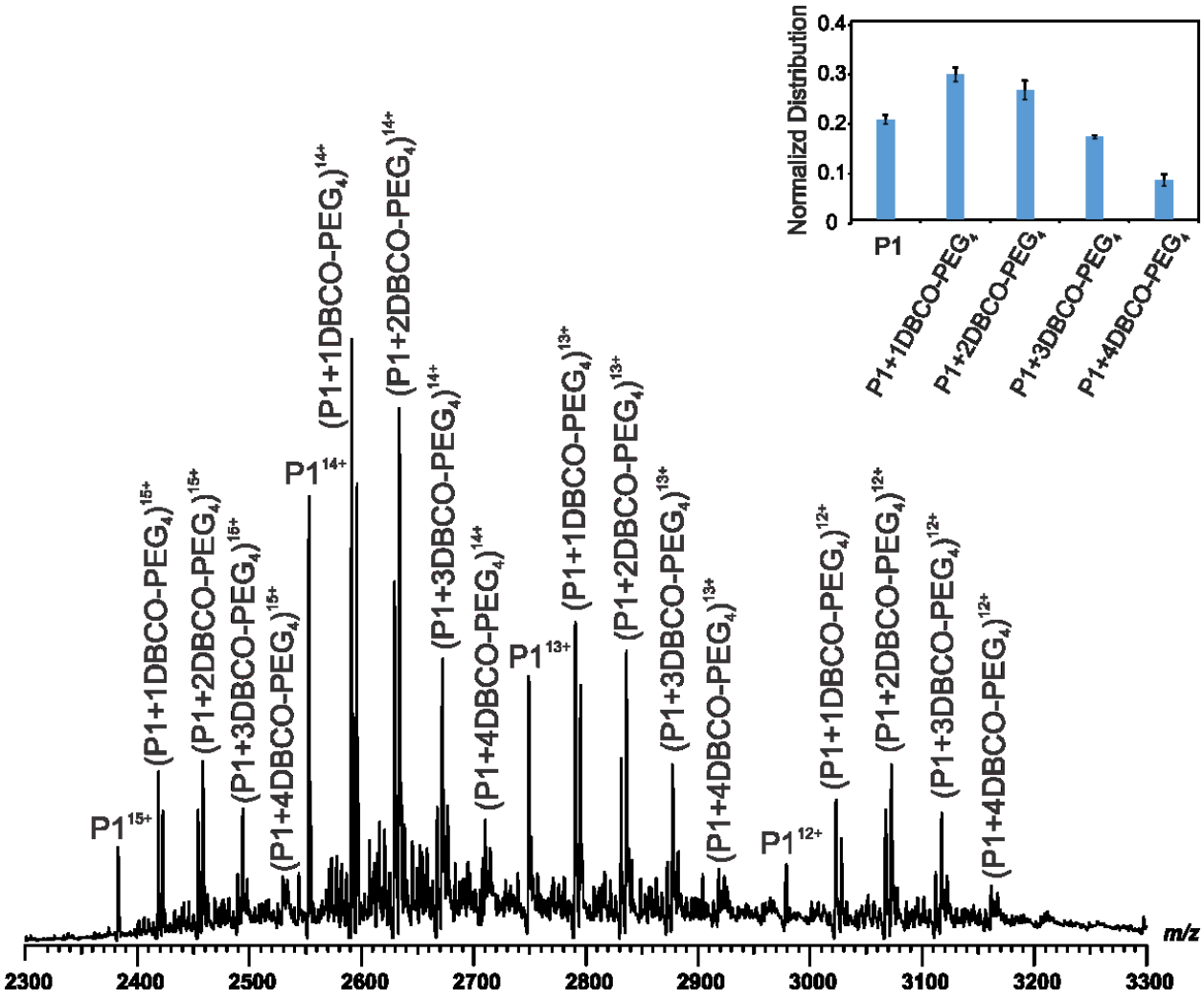

Figure 4.2. ESI mass spectra acquired in positive ion mode for aqueous ammonium acetate solutions (200 mM, 25 °C, and pH 6.8) containing fragment of human Siglec-1 labeled with DBCO-PEG$_4$ (0.5 μM). Inset show the normalized distribution of (Siglec-1 + qDBCO-PEG$_4$) measured from the mass spectrum, where q = 0-4.

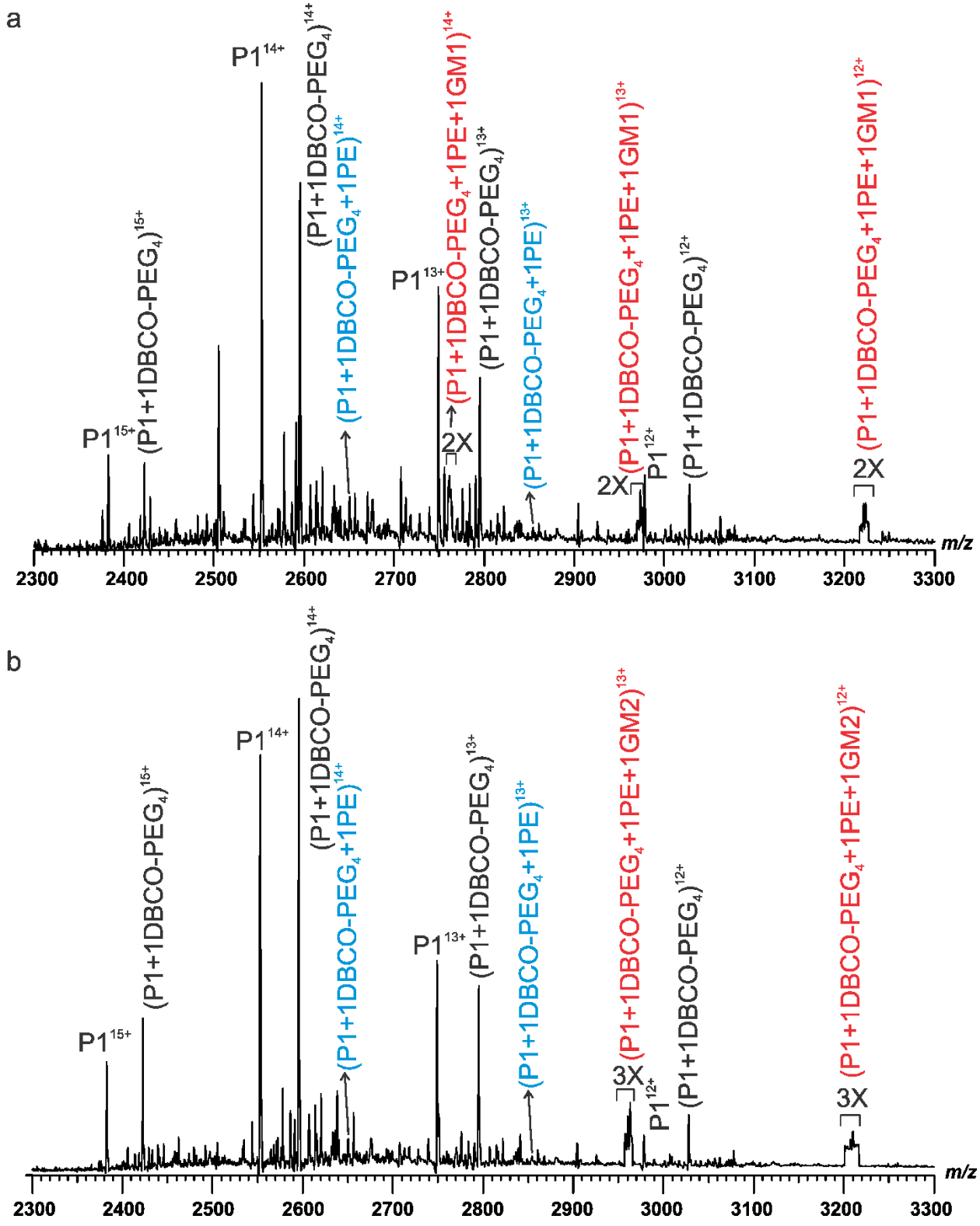
a
P1^14+
(P1+1DBCO-PEG4)^14+
P1^15+
(P1+1DBCO-PEG4)^15+
(P1+1DBCO-PEG4+1PE)^14+
P1^13+
(P1+1DBCO-PEG4+1PE+1GM1)^14+
2X
(P1+1DBCO-PEG4)^13+
(P1+1DBCO-PEG4+1PE)^13+
2X
(P1+1DBCO-PEG4+1PE+1GM1)^13+
P1^12+
(P1+1DBCO-PEG4)^12+
2X
(P1+1DBCO-PEG4+1PE+1GM1)^12+
m/z
2300 2400 2500 2600 2700 2800 2900 3000 3100 3200 3300
b
P1^14+
(P1+1DBCO-PEG4)^14+
P1^15+
(P1+1DBCO-PEG4)^15+
(P1+1DBCO-PEG4+1PE)^14+
P1^13+
(P1+1DBCO-PEG4)^13+
(P1+1DBCO-PEG4+1PE)^13+
3X
(P1+1DBCO-PEG4+1PE+1GM2)^13+
P1^12+
(P1+1DBCO-PEG4)^12+
3X
(P1+1DBCO-PEG4+1PE+1GM2)^12+
m/z
2300 2400 2500 2600 2700 2800 2900 3000 3100 3200 3300

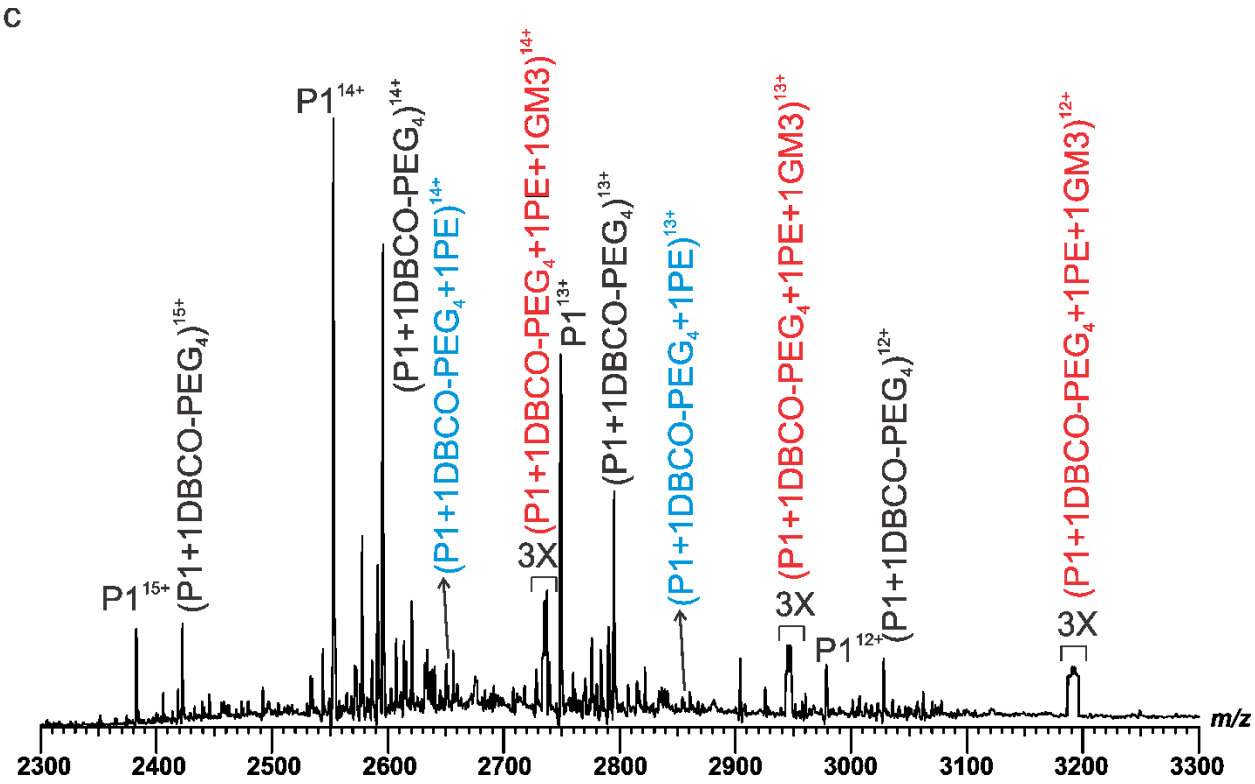

Figure 4.3. ESI mass spectra acquired in positive ion mode for aqueous ammonium acetate solutions (200 mM, 25 °C, and pH 6.8) containing labeled fragment of human Siglec-1 (0.5 μM) with (a) 10% GM1 20% PE POPC ND (3 μM), (b) 10% GM2 20% PE POPC ND (2 μM) (c) 10% GM3 20% PE POPC ND (2.5 μM) incubated for 2 h.

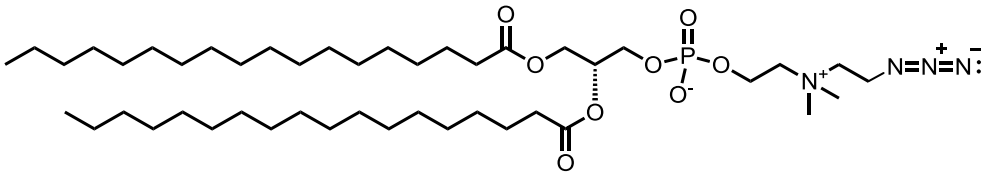

azidoethyl PC (18:0)

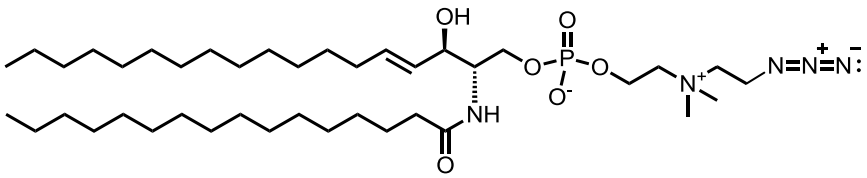

azidoethyl SM (16:0)

Figure 4.4. Structures of the modified lipids azidoethyl PC and azidoethyl SM.

4.3 References

(1) Magesh, S.; Ando, H.; Tsubata, T.; Ishida, H.; Kiso, M. High-Affinity Ligands of Siglec Receptors and Their Therapeutic Potentials. *Curr. Med. Chem.* **2011**, *18* (23), 3537–3550.

(2) Angata, T.; Nycholat, C. M.; Macauley, M. S. Therapeutic Targeting of Siglecs Using Antibody- and Glycan-Based Approaches. *Trends Pharmacol. Sci.* **2015**, *36* (10), 645–660.

(3) Macauley, M. S.; Crocker, P. R.; Paulson, J. C. Siglec-Mediated Regulation of Immune Cell Function in Disease. *Nat. Rev. Immunol.* **2014**, *14* (10), 653–666.

(4) Izquierdo-Useros, N.; Lorizate, M.; McLaren, P. J.; Telenti, A.; Kräusslich, H.-G.; Martinez-Picado, J. HIV-1 Capture and Transmission by Dendritic Cells: The Role of Viral Glycolipids and the Cellular Receptor Siglec-1. *PLoS Pathog.* **2014**, *10* (7), e1004146.

(5) Crocker, P. R.; Paulson, J. C.; Varki, A. Siglecs and Their Roles in the Immune System. *Nat. Rev. Immunol.* **2007**, *7* (4), 255–266.

(6) Izquierdo-Useros, N.; Lorizate, M.; Contreras, F.-X.; Rodriguez-Plata, M. T.; Glass, B.; Erkizia, I.; Prado, J. G.; Casas, J.; Fabriàs, G.; Kräusslich, H.-G.; et al. Sialyllactose in Viral Membrane Gangliosides Is a Novel Molecular Recognition Pattern for Mature Dendritic Cell Capture of HIV-1. *PLoS Biol.* **2012**, *10* (4), e1001315.

(7) Chan, R.; Uchil, P. D.; Jin, J.; Shui, G.; Ott, D. E.; Mothes, W.; Wenk, M. R. Retroviruses Human Immunodeficiency Virus and Murine Leukemia Virus Are Enriched in Phosphoinositides. *J. Virol.* **2008**, *82* (22), 11228–11238.

(8) Erikson, E.; Wratil, P. R.; Frank, M.; Ambiel, I.; Pahnke, K.; Pino, M.; Azadi, P.; Izquierdo-Useros, N.; Martinez-Picado, J.; Meier, C.; et al. Mouse Siglec-1 Mediates Trans -Infection of Surface-Bound Murine Leukemia Virus in a Sialic Acid N -Acyl Side Chain-Dependent Manner. *J. Biol. Chem.* **2015**, *290* (45), 27345–27359.

(9) Puryear, W. B.; Yu, X.; Ramirez, N. P.; Reinhard, B. M.; Gummuluru, S. HIV-1 Incorporation of Host-Cell-Derived Glycosphingolipid GM3 Allows for Capture by Mature Dendritic Cells. *Proc. Natl. Acad. Sci.* **2012**, *109* (19), 7475–7480.

(10) Izquierdo-Useros, N.; Lorizate, M.; Contreras, F.-X.; Rodriguez-Plata, M. T.; Glass, B.; Erkizia, I.; Prado, J. G.; Casas, J.; Fabriàs, G.; Kräusslich, H.-G.; et al. Sialyllactose in Viral Membrane Gangliosides Is a Novel Molecular Recognition Pattern for Mature Dendritic Cell Capture of HIV-1. *PLoS Biol.* **2012**, *10* (4), e1001315.

(11) Puryear, W. B.; Yu, X.; Ramirez, N. P.; Reinhard, B. M.; Gummuluru, S. HIV-1 Incorporation of Host-Cell-Derived Glycosphingolipid GM3 Allows for Capture by Mature Dendritic Cells. *Proc. Natl. Acad. Sci.* **2012**, *109* (19), 7475–7480.

(12) Collins, B. E.; Ito, H.; Sawada, N.; Ishida, H.; Kiso, M.; Schnaar, R. L. Enhanced Binding of the Neural Siglecs, Myelin-Associated Glycoprotein and Schwann Cell Myelin Protein, to Chol-1 (α-Series) Gangliosides and Novel Sulfated Chol-1 Analogs. *J. Biol. Chem.* **1999**, *274* (53), 37637–37643.

(13) Puryear, W. B.; Akiyama, H.; Geer, S. D.; Ramirez, N. P.; Yu, X.; Reinhard, B. M.; Gummuluru, S. Interferon-Inducible Mechanism of Dendritic Cell-Mediated HIV-1 Dissemination Is Dependent on Siglec-1/CD169. *PLoS Pathog.* **2013**, *9* (4), e1003291.

List of References

Chapter 1

(1) Fahy, E.; Subramaniam, S.; Brown, H. A.; Glass, C. K.; Merrill, A. H.; Murphy, R. C.; Raetz, C. R. H.; Russell, D. W.; Seyama, Y.; Shaw, W.; et al. A Comprehensive Classification System for Lipids. *J. Lipid Res.* **2005**, *46* (5), 839–862.

(2) van Meer, G.; Voelker, D. R.; Feigenson, G. W. Membrane Lipids: Where They Are and How They Behave. *Nat. Rev. Mol. Cell Biol.* **2008**, *9* (2), 112–124.

(3) Saliba, A.-E.; Vonkova, I.; Gavin, A.-C. The Systematic Analysis of Protein–lipid Interactions Comes of Age. *Nat. Rev. Mol. Cell Biol.* **2015**, *16* (12), 753–761.

(4) Merrill, A. H.; Wang, M. D.; Park, M.; Sullards, M. C. (Glyco)Sphingolipidology: An Amazing Challenge and Opportunity for Systems Biology. *Trends Biochem. Sci.* **2007**, *32* (10), 457–468.

(5) Lodish H, Berk A, Zipursky SL, et al. Biomembranes: Structural Organization and Basic Functions. Molecular Cell Biology. 4th edition. **2000**

(6) Dé Rick De Meyer, F.; Smit, B.; Klein, M. L. *Effect of Cholesterol on the Structure of a Phospholipid Bilayer*. **2009**, *10*.

(7) Lopez, P. H. H.; Schnaar, R. L. Determination of Glycolipid–Protein Interaction Specificity. **2006**, 205–220.

(8) LIPID MAPS Lipidomics Gateway http://www.lipidmaps.org.

(9) Cummings, R. D. The Repertoire of Glycan Determinants in the Human Glycome. *Mol. Biosyst.* **2009**, *5* (10), 1087.

(10) Alberts, B.; Johnson, A.; Lewis, J.; Raff, M.; Roberts, K.; Walter, P. *Molecular Biology of the Cell, 4th Edition. Garland Science: New York*. **2002**.

(11) Schulze, H.; Sandhoff, K. Sphingolipids and Lysosomal Pathologies. *Biochim. Biophys. Acta - Mol. Cell Biol. Lipids.* **2014**, *1841* (5), 799–810.

(12) Malhotra, R. Membrane Glycolipids: Functional Heterogeneity: A Review. *Biochem. Anal. Biochem.* **2012**, *1* (2).

(13) Doronin, I. I.; Vishnyakova, P. A.; Kholodenko, I. V; Ponomarev, E. D.; Ryazantsev, D. Y.; Molotkovskaya, I. M.; Kholodenko, R. V. Ganglioside GD2 in Reception and Transduction of Cell Death Signal in Tumor Cells. *BMC Cancer.* **2014**, *14* (1), 295.

(14) Weis, W. I. Structural Basis of Lectin-Carbohydrate Recognition. *Annu. Rev. Biochem.* **1996**, *65* (1), 441–473.

(15) Dam, T. K.; Brewer, C. F. Effects of Clustered Epitopes in Multivalent Ligand−Receptor Interactions †. *Biochemistry.* **2008**, *47* (33), 8470–8476.

(16) Weis, W. I.; Drickamer, K. Structural basis of recognition lectin-carbohydrate. *Anna Rev Biochem*. **1996**, *65*.

(17) Zhang, T.; de Waard, A. A.; Wuhrer, M.; Spaapen, R. M. The Role of Glycosphingolipids in Immune Cell Functions. *Front. Immunol.* **2019**, *10* (1), 1–22.

(18) Larsen, K.; Thygesen, M. B.; Guillaumie, F.; Willats, W. G. T.; Jensen, K. J. Solid-Phase Chemical Tools for Glycobiology. *Carbohydr. Res.* **2006**, *341* (10), 1209–1234.

(19) Linman, M. J.; Taylor, J. D.; Yu, H.; Chen, X.; Cheng, Q. Surface Plasmon Resonance Study of Protein−Carbohydrate Interactions Using Biotinylated Sialosides. *Anal. Chem.* **2008**, *80* (11), 4007–4013.

(20) Smith, D. F.; Song, X.; Cummings, R. D. Use of Glycan Microarrays to Explore Specificity of Glycan-Binding Proteins. In *Methods in Enzymology*; Academic Press Inc. **2010**, *480*, 417–444.

(21) Grant, O. C.; Smith, H. M. K.; Firsova, D.; Fadda, E.; Woods, R. J. Presentation, Presentation, Presentation! Molecular-Level Insight into Linker Effects on Glycan Array Screening Data. *Glycobiology.* **2014**, *24* (1), 17–25.

(22) Fais, M.; Karamanska, R.; Russell, D. A.; Field, R. A. Lectin and Carbohydrate Microarrays: New High-Throughput Methods for Glycoprotein, Carbohydrate-Binding Protein and Carbohydrate-Active Enzyme Analysis. *J. Cereal Sci.* **2009**, *50* (3), 306–311.

(23) Utsuno, K.; Uludağ, H. Thermodynamics of Polyethylenimine-DNA Binding and DNA Condensation. *Biophys. J.* **2010**, *99* (1), 201–207.

(24) Wilcox, D. E. Isothermal Titration Calorimetry of Metal Ions Binding to Proteins: An Overview of Recent Studies. *Inorganica Chim. Acta.* **2008**, *361* (4), 857–867.

(25) Ganem, B.; Li, Y. T.; Henion, J. D. Detection of Noncovalent Receptor-Ligand Complexes by Mass Spectrometry. *J. Am. Chem. Soc.* **1991**, *113* (16), 6294–6296.

(26) Kitova, E. N.; Kitov, P. I.; Paszkiewicz, E.; Kim, J.; Mulvey, G. L.; Armstrong, G. D.; Bundle, D. R.; Klassen, J. S. Affinities of Shiga Toxins 1 and 2 for Univalent and Oligovalent Pk-Trisaccharide Analogs Measured by Electrospray Ionization Mass Spectrometry. *Glycobiology.* **2007**, *17* (10), 1127–1137.

(27) Wang, W.; Kitova, E. N.; Klassen, J. S. Influence of Solution and Gas Phase Processes on Protein−Carbohydrate Binding Affinities Determined by Nanoelectrospray Fourier Transform Ion Cyclotron Resonance Mass Spectrometry. *Anal. Chem.* **2003**, *75* (19), 4945–4955.

(28) Kitova, E. N.; El-Hawiet, A.; Schnier, P. D.; Klassen, J. S. Reliable Determinations of Protein–Ligand Interactions by Direct ESI-MS Measurements. Are We There Yet? *J. Am. Soc. Mass Spectrom.* **2012**, *23* (3), 431–441.

(29) Song, X.; Lasanajak, Y.; Xia, B.; Heimburg-Molinaro, J.; Rhea, J. M.; Ju, H.; Zhao, C.; Molinaro, R. J.; Cummings, R. D.; Smith, D. F. Shotgun Glycomics: A Microarray Strategy for Functional Glycomics. *Nat. Methods.* **2011**, *8* (1), 85–90.

(30) Suetake, K.; Yu, R. K. Thin-Layer Chromatography; Immunostaining of Glycolipid Antigens; and Interpretation of False-Positive Findings with Acidic Lipids. *Methods in Enzymology*. **2003**, 363, 312–319.

(31) Bolla, J. R.; Agasid, M. T.; Mehmood, S.; Robinson, C. V. Membrane Protein–Lipid Interactions Probed Using Mass Spectrometry. *Annu. Rev. Biochem.* **2019**, *88* (1), 85–111.

(32) Nath, A.; Atkins, W. M.; Sligar, S. G. Applications of Phospholipid Bilayer Nanodiscs in the Study of Membranes and Membrane Proteins †. *Biochemistry.* **2007**, *46* (8), 2059–2069.

(33) Bayburt, T. H.; Sligar, S. G. Membrane Protein Assembly into Nanodiscs. *FEBS Lett.* **2010**, *584* (9), 1721–1727.

(34) Popovic, K.; Holyoake, J.; Pomes, R.; Prive, G. G. Structure of Saposin A Lipoprotein Discs. *Proc. Natl. Acad. Sci.* **2012**, *109* (8), 2908–2912.

(35) Sanghera, N.; Correia, B. E. F. S.; Correia, J. R. S.; Ludwig, C.; Agarwal, S.; Nakamura, H. K.; Kuwata, K.; Samain, E.; Gill, A. C.; Bonev, B. B.; et al. Deciphering the Molecular Details for the Binding of the Prion Protein to Main Ganglioside GM1 of Neuronal Membranes. *Chem. Biol.* **2011**, *18* (11), 1422–1431.

(36) Shi, J.; Yang, T.; Kataoka, S.; Zhang, Y.; Diaz, A. J.; Cremer, P. S. GM 1 Clustering Inhibits Cholera Toxin Binding in Supported Phospholipid Membranes. *J. Am. Chem. Soc.* **2007**, *129* (18), 5954–5961.

(37) Borch, J.; Torta, F.; Sligar, S. G.; Roepstorff, P. Nanodiscs for Immobilization of Lipid Bilayers and Membrane Receptors: Kinetic Analysis of Cholera Toxin Binding to a

Glycolipid Receptor. *Anal. Chem.* **2008**, *80* (16), 6245–6252.

(38) Chen, W. C.; Kawasaki, N.; Nycholat, C. M.; Han, S.; Pilotte, J.; Crocker, P. R.; Paulson, J. C. Antigen Delivery to Macrophages Using Liposomal Nanoparticles Targeting Sialoadhesin/CD169. *PLoS One.* **2012**, *7* (6), e39039.

(39) Krishnan, P.; Singla, A.; Lee, C.; Weatherston, J. D.; Worstell, N. C.; Wu, H. Colloids and Surfaces B : Biointerfaces Hetero-Multivalent Binding of Cholera Toxin Subunit B with Glycolipid Mixtures. **2017**, *160*, 281–288.

(40) Sherry, L. J.; Chang, S.; Schatz, G. C.; Van Duyne, R. P.; Wiley, B. J.; Xia, Y. Localized Surface Plasmon Resonance Spectroscopy of Single Silver Nanocubes. *Nano Lett.* **2005**, *5* (10), 2034–2038.

(41) Han, L.; Morales, L. C.; Richards, M. R.; Kitova, E. N.; Sipione, S.; Klassen, J. S. Investigating the Influence of Membrane Composition on Protein–Glycolipid Binding Using Nanodiscs and Proxy Ligand Electrospray Ionization Mass Spectrometry. *Anal. Chem.* **2017**, *89* (17), 9330–9338.

(42) Han, L.; Kitova, E. N.; Li, J.; Nikjah, S.; Lin, H.; Pluvinage, B.; Boraston, A. B.; Klassen, J. S. Protein–Glycolipid Interactions Studied in Vitro Using ESI-MS and Nanodiscs: Insights into the Mechanisms and Energetics of Binding. *Anal. Chem.* **2015**, *87* (9), 4888–4896.

(43) Leney, A. C.; Fan, X.; Kitova, E. N.; Klassen, J. S. Nanodiscs and Electrospray Ionization Mass Spectrometry: A Tool for Screening Glycolipids Against Proteins. *Anal. Chem.* **2014**, *86* (11), 5271–5277.

(44) Li, J.; Fan, X.; Kitova, E. N.; Zou, C.; Cairo, C. W.; Eugenio, L.; Ng, K. K. S.; Xiong, Z. J.; Privé, G. G.; Klassen, J. S. Screening Glycolipids Against Proteins in Vitro Using Picodiscs

and Catch-and-Release Electrospray Ionization-Mass Spectrometry. *Anal. Chem.* **2016**, *88* (9), 4742–4750.

(45) Dole, M.; Mack, L. L.; Hines, R. L.; Mobley, R. C.; Ferguson, L. D.; Alice, M. B. Molecular Beams of Macroions. *J. Chem. Phys.* **1968**, *49* (5), 2240–2249.

(46) Yamashita1', M.; Fenn, J. B. Negative Ion Production with the Electrospray Ion Source. *J. Phys. Chem.* **1984**, *88*, 4671-4675.

(47) Fenn, J. B. Electrospray Wings for Molecular Elephants (Nobel Lecture). *Angew. Chemie Int. Ed.* **2003**, *42* (33), 3871–3894.

(48) Sarkar, P. K.; Prajapati, P. K.; Shukla, V. J.; Ravishankar, B.; Choudhary, A. K. Toxicity and Recovery Studies of Two Ayurvedic Preparations of Iron. *Indian J. Exp. Biol.* **2009**, *47* (12), 987–992.

(49) Covey, T. R.; Thomson, B. A.; Schneider, B. B. Atmospheric Pressure Ion Sources. *Mass Spectrom. Rev.* **2009**, *28* (6), 870–897.

(50) Kebarle, P.; Tang, L. From Ions in Solution to Ions in the Gas Phase - the Mechanism of Electrospray Mass Spectrometry. *Anal. Chem.* **1993**, *65* (22), 972A–986A.

(51) Kebarle, P. A Brief Overview of the Present Status of the Mechanisms Involved in Electrospray Mass Spectrometry. *J. Mass Spectrom.* **2000**, *35* (7), 804–817.

(52) Kebarle, P.; Verkerk, U. H. Electrospray: From Ions in Solution to Ions in the Gas Phase, What We Know Now. *Mass Spectrom. Rev.* **2009**, *28* (6), 898–917.

(53) De La Mora, J. F.; Loscertales, I. G. The Current Emitted by Highly Conducting Taylor Cones. *J. Fluid Mech.* **1994**, *260*, 155–184.

(54) Fernandez de la Mora, J. Electrospray Ionization of Large Multiply Charged Species Proceeds via Dole's Charged Residue Mechanism. *Anal. Chim. Acta.* **2000**, *406* (1), 93–104.

(55) Wu, X.; Oleschuk, R. D.; Cann, N. M. Characterization of Microstructured Fibre Emitters: In Pursuit of Improved Nano Electrospray Ionization Performance. *Analyst* **2012**, *137* (18), 4150.

(56) Benesch, J. L. P.; Ruotolo, B. T.; Simmons, D. A.; Robinson, C. V. Protein Complexes in the Gas Phase: Technology for Structural Genomics and Proteomics. *Chem. Rev.* **2007**, *107* (8), 3544–3567.

(57) Rayleigh, Lord. XX. On the Equilibrium of Liquid Conducting Masses Charged with Electricity. *London, Edinburgh, Dublin Philos. Mag. J. Sci.* **1882**, *14* (87), 184–186.

(58) Fernandez de la Mora, J. Electrospray Ionization of Large Multiply Charged Species Proceeds via Dole's Charged Residue Mechanism. *Anal. Chim. Acta.* **2000**, *406* (1), 93–104.

(59) Gomez, A.; Tang, K. Charge and Fission of Droplets in Electrostatic Sprays. *Phys. Fluids.* **1994**, *6* (1), 404–414.

(60) Kebarle, P.; Peschke, M. On the Mechanisms by Which the Charged Droplets Produced by Electrospray Lead to Gas Phase Ions. *Anal. Chim. Acta.* **2000**, *406* (1), 11–35.

(61) Iribarne, J. V. On the Evaporation of Small Ions from Charged Droplets. *J. Chem. Phys.* **1976**, *64* (6), 2287.

(62) Thomson, B. A.; Iribarne, J. V. Field Induced Ion Evaporation from Liquid Surfaces at Atmospheric Pressure. *J. Chem. Phys.* **1979**, *71* (11), 4451–4463.

(63) Konermann, L.; Ahadi, E.; Rodriguez, A. D.; Vahidi, S. Unraveling the Mechanism of Electrospray Ionization. *Anal. Chem.* **2013**, *85* (1), 2–9.

(64) Iavarone, A. T.; Williams, E. R. Mechanism of Charging and Supercharging Molecules in Electrospray Ionization. *J. Am. Chem. Soc.* **2003**, *125* (8), 2319–2327.

(65) Peschke, M.; Verkerk, U. H.; Kebarle, P. Features of the ESI Mechanism That Affect the

Observation of Multiply Charged Noncovalent Protein Complexes and the Determination of the Association Constant by the Titration Method. *J. Am. Soc. Mass Spectrom.* **2004**, *15* (10), 1424–1434.

(66) Metwally, H.; Duez, Q.; Konermann, L. Chain Ejection Model for Electrospray Ionization of Unfolded Proteins: Evidence from Atomistic Simulations and Ion Mobility Spectrometry. *Anal. Chem.* **2018**, *90* (16), 10069–10077.

(67) Konermann, L.; Rodriguez, A. D.; Liu, J. On the Formation of Highly Charged Gaseous Ions from Unfolded Proteins by Electrospray Ionization. *Anal. Chem.* **2012**, *84* (15), 6798–6804.

(68) Ahadi, E.; Konermann, L. Modeling the Behavior of Coarse-Grained Polymer Chains in Charged Water Droplets: Implications for the Mechanism of Electrospray Ionization. *J. Phys. Chem. B.* **2012**, *116* (1), 104–112.

(69) Nohmi, T.; Fenn, J. B. Electrospray Mass Spectrometry of Poly(Ethylene Glycols) with Molecular Weights up to Five Million. *J. Am. Chem. Soc.* **1992**, *114* (9), 3241–3246.

(70) Fenn, J. B. Ion Formation from Charged Droplets: Roles of Geometry, Energy, and Time. *J. Am. Soc. Mass Spectrom.* **1993**, *4* (7), 524–535.

(71) Wilm, M. S.; Mann, M. Electrospray and Taylor-Cone Theory, Dole's Beam of Macromolecules at Last? *Int. J. Mass Spectrom. Ion Process.* **1994**, *136* (2–3), 167–180.

(72) Wilm, M.; Mann, M. Analytical Properties of the Nanoelectrospray Ion Source. *Anal. Chem.* **1996**, *68* (1), 1–8.

(73) Karas, R. M.; Bahr, U.; Dülcks, T. Nano-Electrospray Ionization Mass Spectrometry: Addressing Analytical Problems beyond Routine. *Fresenius' J. Anal. Chem.* **2000**, *366* (6), 669-676.

(74) El-Faramawy, A.; Siu, K. W. M.; Thomson, B. A. Efficiency of Nano-Electrospray Ionization. *J. Am. Soc. Mass Spectrom.* **2005**, *16* (10), 1702–1707.

(75) Juraschek, R.; Dülcks, T.; Karas, M. Nanoelectrospray—More than Just a Minimized-Flow Electrospray Ionization Source. *J. Am. Soc. Mass Spectrom.* **1999**, *10* (4), 300–308.

(76) Jecklin, M. C.; Touboul, D.; Bovet, C.; Wortmann, A.; Zenobi, R. Which Electrospray-Based Ionization Method Best Reflects Protein-Ligand Interactions Found in Solution? A Comparison of ESI, NanoESI, and ESSI for the Determination of Dissociation Constants with Mass Spectrometry. *J. Am. Soc. Mass Spectrom.* **2008**, *19* (3), 332–343.

(77) Karas, M.; Bachmann, D.; Hillenkamp, F. Influence of the Wavelength in High-Irradiance Ultraviolet Laser Desorption Mass Spectrometry of Organic Molecules. *Anal. Chem.* **1985**, *57* (14), 2935–2939.

(78) Karas, M.; Bachmann, D.; Bahr, U.; Hillenkamp, F. Matrix-Assisted Ultraviolet Laser Desorption of Non-Volatile Compounds. *Int. J. Mass Spectrom. Ion Process.* **1987**, *78* (C), 53–68.

(79) Hillenkamp, F.; Karas, M.; Ronald, G.; Beavis1, C.; Chait, B. T. Matrix-Assisted Laser Desorption/Ionization Mass Spectrometry of Biopolymers. *Anal. Chem.* **1991**, *63* (24), 1193A-1203A.

(80) Karas, M.; Hillenkamp, F. Laser Desorption Ionization of Proteins with Molecular Masses Exceeding 10,000 Daltons. *Anal. Chem.* **1988**, *60* (20), 2299–2301.

(81) Karas, M.; Krüger, R. Ion Formation in MALDI: The Cluster Ionization Mechanism. *Chem. Rev.* **2003**, *103* (2), 427–440.

(82) Liang, C. W.; Lee, C. H.; Lin, Y.-J.; Lee, Y. T.; Ni, C. K. MALDI Mechanism of Dihydroxybenzoic Acid Isomers: Desorption of Neutral Matrix and Analyte. *J. Phys. Chem.*

B. **2013**, *117* (17), 5058–5064.

(83) Trimpin, S.; Wang, B.; Inutan, E. D.; Li, J.; Lietz, C. B.; Harron, A.; Pagnotti, V. S.; Sardelis, D.; McEwen, C. N. A Mechanism for Ionization of Nonvolatile Compounds in Mass Spectrometry: Considerations from MALDI and Inlet Ionization. *J. Am. Soc. Mass Spectrom.* **2012**, *23* (10), 1644–1660.

(84) Singhal, N.; Kumar, M.; Kanaujia, P. K.; Virdi, J. S. MALDI-TOF Mass Spectrometry: An Emerging Technology for Microbial Identification and Diagnosis. *Front. Microbiol.* **2015**, *6* (8), 791.

(85) Trimpin, S.; Inutan, E. D.; Herath, T. N.; McEwen, C. N. Laserspray Ionization, a New Atmospheric Pressure MALDI Method for Producing Highly Charged Gas-Phase Ions of Peptides and Proteins Directly from Solid Solutions. *Mol. Cell. Proteomics.* **2010**, *9* (2), 362–367.

(86) Knochenmuss, R. Ion Formation Mechanisms in UV-MALDI. *Analyst.* **2006**, *131* (9), 966.

(87) University of Bristol, School of Chemistry Mass Spectrometry Facility, MALDI.

(88) Karas, M.; Bahr, U.; Ingendoh, A.; Nordhoff, E.; Stahl, B.; Strupat, K.; Hillenkamp, F. Principles and Applications of Matrix-Assisted UV-Laser Desorption/Ionization Mass Spectrometry. *Anal. Chim. Acta.* **1990**, *241* (2), 175–185.

(89) Suzuki, Y. Adjustment of Matrix-Assisted Laser Desorption/Ionization for Glycolipids. *J. Anal. Bioanal. Tech.* **2015**, *6* (5).

(90) Penn, S.; Cancilla, M.; Green, M.; Lebrilla, C. Direct Comparison of Matrix-Assisted Laser Desorption/Ionisation and Electrospray Ionisation in the Analysis of Gangliosides by Fourier Transform Mass Spectrometry. *Eur. J. Mass Spectrom.* **1997**, *3* (1), 67.

(91) Jessome, L.; Hsu, N.-Y.; Wang, Y.-S.; Chen, C.-H. Matrix-Assisted Laser

Desorption/Ionization Mechanism Study with Dihydroxybenzoic Acid Isomers as Matrices. *Rapid Commun. Mass Spectrom.* **2008**, *22* (2), 130–134.

(92) Matta, A.; Ralhan, R.; DeSouza, L. V.; Siu, K. W. M. Mass Spectrometry-Based Clinical Proteomics: Head-and-Neck Cancer Biomarkers and Drug-Targets Discovery. *Mass Spectrom. Rev.* **2010**, *29* (6), 945–961.

(93) Kero, F. A.; Pedder, R. E.; Yost, R. A. Quadrupole Mass Analyzers: Theoretical and Practical Considerations. *Encyclopedia of Genetics, Genomics, Proteomics and Bioinformatics*. John Wiley & Sons, Ltd: Chichester, **2005**.

(94) Miller, P. E.; Denton, M. B. The Quadrupole Mass Filter: Basic Operating Concepts. *J. Chem. Educ.* **1986**, *63* (7), 617.

(95) Gross, J. H. *Mass Spectrometry A Textbook, Third Edition. Springer International Publishing*. **2017**.

(96) Pedder, R. E. Practical Quadrupole Characteristics Theory : Quadrupole Acceptance Characteristics. *Ardara Technol. Tech. Note.* **2009**, *412*, 1–5.

(97) Pringle, S. D.; Giles, K.; Wildgoose, J. L.; Williams, J. P.; Slade, S. E.; Thalassinos, K.; Bateman, R. H.; Bowers, M. T.; Scrivens, J. H. An Investigation of the Mobility Separation of Some Peptide and Protein Ions Using a New Hybrid Quadrupole/Travelling Wave IMS/Oa-ToF Instrument. *Int. J. Mass Spectrom.* **2007**, *261* (1), 1–12.

(98) Giles, K.; Pringle, S. D.; Worthington, K. R.; Little, D.; Wildgoose, J. L.; Bateman, R. H. Applications of a Travelling Wave-Based Radio-Frequency-Only Stacked Ring Ion Guide. *Rapid Commun. Mass Spectrom.* **2004**, *18* (20), 2401–2414.

(99) Creaser, C. S.; Griffiths, J. R.; Bramwell, C. J.; Noreen, S.; Hill, C. A.; Thomas, C. L. P. Ion Mobility Spectrometry: A Review. Part 1. Structural Analysis by Mobility Measurement.

Analyst. **2004**, *129* (11), 984.

(100) Karasek, F. W. Plasma Chromatography. *Anal. Chem.* **1974**, *46* (8), 710A–720a.

(101) Giles, K.; Williams, J. P.; Campuzano, I. Enhancements in Travelling Wave Ion Mobility Resolution. *Rapid Commun. Mass Spectrom.* **2011**, *25* (11), 1559–1566.

(102) Shukla, A. K.; Futrell, J. H. Tandem Mass Spectrometry: Dissociation of Ions by Collisional Activation. *J. Mass Spectrom.* **2000**, *35* (9), 1069–1090.

(103) Mcluckey, S. A. Principles of Collisional Activation in Analytical Mass Spectrometry. *J. Am. Soc. Mass Spectrom.* **1992**, *3* (6), 599-614.

(104) Wyttenbach, T.; Bowers, M. T. Intermolecular Interactions in Biomolecular Systems Examined by Mass Spectrometry. *Annu. Rev. Phys. Chem.* **2007**, *58* (1), 511–533.

(105) Rezaei Darestani, R.; Winter, P.; Kitova, E. N.; Tuszynski, J. A.; Klassen, J. S. Screening Anti-Cancer Drugs against Tubulin Using Catch-and-Release Electrospray Ionization Mass Spectrometry. *J. Am. Soc. Mass Spectrom.* **2016**, *27* (5), 876–885.

(106) Benesch, J. L. P.; Aquilina, J. A.; Ruotolo, B. T.; Sobott, F.; Robinson, C. V. Tandem Mass Spectrometry Reveals the Quaternary Organization of Macromolecular Assemblies. *Chem. Biol.* **2006**, *13* (6), 597–605.

(107) Guilhaus, M.; Selby, D.; Mlynski, V. Orthogonal Acceleration Time-of-Flight Mass Spectrometry. *Mass Spectrom. Rev.* **2000**, *19* (2), 65–107.

(108) Burlingame, A. L.; Whitney, J. O.; Russell, D. H. Mass Spectrometry. *Anal. Chem.* **1984**, *56* (5), 417–467.

(109) Mamyrin, B. A. Time-of-Flight Mass Spectrometry (Concepts, Achievements, and Prospects). *Int. J. Mass Spectrom.* **2001**, *206* (3), 251–266.

(110) Hardman, M.; Makarov, A. A. Interfacing the Orbitrap Mass Analyzer to an Electrospray

Ion Source. *Anal. Chem.* **2003**, *75* (7), 1699–1705.

(111) Makarov, A. Electrostatic Axially Harmonic Orbital Trapping: A High-Performance Technique of Mass Analysis. *Anal. Chem.* **2000**, *72* (6), 1156–1162.

(112) Scigelova, M.; Makarov, A. Orbitrap Mass Analyzer – Overview and Applications in Proteomics. *Proteomics* **2006**, *6* (S2), 16–21.

(113) Marshall, A. G.; Hendrickson, C. L. Fourier Transform Ion Cyclotron Resonance Detection: Principles and Experimental Configurations. *Int. J. Mass Spectrom.* **2002**, *215* (1–3), 59–75.

(114) Marshall, A. G.; Hendrickson, C. L.; Jackson, G. S. Fourier Transform Ion Cyclotron Resonance Mass Spectrometry: A Primer. *Mass Spectrom. Rev.* **1998**, *17* (1), 1–35.

(115) Marshall, A. G. Fourier Transform Mass Spectrometry. *Spectrosc. Biomed. Sci.* **2018**, 87–105.

(116) Marshall, A. G.; Grosshans, P. B. Fourier Transform Ion Cyclotron Resonance Mass Spectrometry: The Teenage Years. *Anal. Chem.* **1991**, *63* (4), 215A–229A.

(117) Johnson Lab. Fourier Trans Form Ion Cyclotron Resonance Mass Spectrometry.

(118) Kitova, E. N.; El-Hawiet, A.; Schnier, P. D.; Klassen, J. S. Reliable Determinations of Protein–Ligand Interactions by Direct ESI-MS Measurements. Are We There Yet? *J. Am. Soc. Mass Spectrom.* **2012**, *23* (3), 431–441.

(119) Sun, J.; Kitova, E. N.; Klassen, J. S. Method for Stabilizing Protein−Ligand Complexes in Nanoelectrospray Ionization Mass Spectrometry. *Anal. Chem.* **2007**, *79* (2), 416–425.

(120) Han, L.; Tan, M.; Xia, M.; Kitova, E. N.; Jiang, X.; Klassen, J. S. Gangliosides Are Ligands for Human Noroviruses. *J. Am. Chem. Soc.* **2014**, *136* (36), 12631–12637.

(121) Sun, J.; Kitova, E. N.; Wang, W.; Klassen, J. S. Method for Distinguishing Specific from

Nonspecific Protein−Ligand Complexes in Nanoelectrospray Ionization Mass Spectrometry. *Anal. Chem.* **2006**, *78* (9), 3010–3018.

(122) Sun, N.; Soya, N.; Kitova, E. N.; Klassen, J. S. Nonspecific Interactions between Proteins and Charged Biomolecules in Electrospray Ionization Mass Spectrometry. *J. Am. Soc. Mass Spectrom.* **2010**, *21* (3), 472–481.

(123) Rademacher, C.; Shoemaker, G. K.; Kim, H.-S.; Zheng, R. B.; Taha, H.; Liu, C.; Nacario, R. C.; Schriemer, D. C.; Klassen, J. S.; Peters, T.; et al. Ligand Specificity of CS-35, a Monoclonal Antibody That Recognizes Mycobacterial Lipoarabinomannan: A Model System for Oligofuranoside−Protein Recognition. *J. Am. Chem. Soc.* **2007**, *129* (34), 10489–10502.

(124) Deng, L.; Sun, N.; Kitova, E. N.; Klassen, J. S. Direct Quantification of Protein−Metal Ion Affinities by Electrospray Ionization Mass Spectrometry. *Anal. Chem.* **2010**, *82* (6), 2170–2174.

(125) Han, L.; Kitova, E. N.; Li, J.; Nikjah, S.; Lin, H.; Pluvinage, B.; Boraston, A. B.; Klassen, J. S. Protein–Glycolipid Interactions Studied in Vitro Using ESI-MS and Nanodiscs: Insights into the Mechanisms and Energetics of Binding. *Anal. Chem.* **2015**, *87* (9), 4888–4896.

(126) El-Hawiet, A.; Kitova, E. N.; Klassen, J. S. Quantifying Protein Interactions with Isomeric Carbohydrate Ligands Using a Catch and Release Electrospray Ionization-Mass Spectrometry Assay. *Anal. Chem.* **2013**, *85* (16), 7637–7644.

Chapter 2

(1) Fredman, P.; Hedberg, K.; Brezicka, T. Gangliosides as Therapeutic Targets for Cancer. *BioDrugs.* **2003**, *17* (3), 155–167.

(2) Ahmed, M.; Cheung, N.-K. V. Engineering Anti-GD2 Monoclonal Antibodies for Cancer Immunotherapy. *FEBS Lett.* **2014**, *588* (2), 288–297.

(3) Hakomori, S. Glycosylation Defining Cancer Malignancy: New Wine in an Old Bottle. *Proc. Natl. Acad. Sci.* **2002**, *99* (16), 10231–10233.

(4) Doronin, I. I.; Vishnyakova, P. A.; Kholodenko, I. V; Ponomarev, E. D.; Ryazantsev, D. Y.; Molotkovskaya, I. M.; Kholodenko, R. V. Ganglioside GD2 in Reception and Transduction of Cell Death Signal in Tumor Cells. *BMC Cancer.* **2014**, *14* (1), 295.

(5) Lammie, G.; Cheung, N.; Gerald, W.; Rosenblum, M.; Cordoncardo, C. Ganglioside GD(2) expression in the human nervous-system and in neuroblastomas-an immunohistochemical study. *Int. J. Oncol.* **1993**, 909-915.

(6) Cheung, N.-K. V; Dyer, M. A. Neuroblastoma: Developmental Biology, Cancer Genomics and Immunotherapy. *Nat. Rev. Cancer.* **2013**, *13* (6), 397–411.

(7) Svennerholm, L.; Boström, K.; Fredman, P.; Jungbjer, B.; Lekman, A.; Månsson, J.-E.; Rynmark, B.-M. Gangliosides and Allied Glycosphingolipids in Human Peripheral Nerve and Spinal Cord. *Biochim. Biophys. Acta - Lipids Lipid Metab.* **1994**, *1214* (2), 115–123.

(8) Aixinjueluo, W.; Furukawa, K.; Zhang, Q.; Hamamura, K.; Tokuda, N.; Yoshida, S.; Ueda, R.; Furukawa, K. Mechanisms for the Apoptosis of Small Cell Lung Cancer Cells Induced by Anti-GD2 Monoclonal Antibodies. *J. Biol. Chem.* **2005**, *280* (33), 29828–29836.

(9) Cheung, N.-K. V.; Cheung, I. Y.; Kushner, B. H.; Ostrovnaya, I.; Chamberlain, E.; Kramer, K.; Modak, S. Murine Anti-GD2 Monoclonal Antibody 3F8 Combined With Granulocyte-

Macrophage Colony-Stimulating Factor and 13- Cis -Retinoic Acid in High-Risk Patients With Stage 4 Neuroblastoma in First Remission. *J. Clin. Oncol.* **2012**, *30* (26), 3264–3270.

(10) Cheung, N.-K. V.; Guo, H.; Hu, J.; Tassev, D. V; Cheung, I. Y. Humanizing Murine IgG3 Anti-GD2 Antibody M3F8 Substantially Improves Antibody-Dependent Cell-Mediated Cytotoxicity While Retaining Targeting in Vivo. *Oncoimmunology.* **2012**, *1* (4), 477–486.

(11) Shusterman, S.; London, W. B.; Gillies, S. D.; Hank, J. A.; Voss, S. D.; Seeger, R. C.; Reynolds, C. P.; Kimball, J.; Albertini, M. R.; Wagner, B.; et al. Antitumor Activity of Hu14.18-IL2 in Patients With Relapsed/Refractory Neuroblastoma: A Children's Oncology Group (COG) Phase II Study. *J. Clin. Oncol.* **2010**, *28* (33), 4969–4975.

(12) Ari, P.; Kars, M.; Meany, H.; Pestieau, S. Treatment of Transient Peripheral Neuropathy During Chimeric 14.18 Antibody Therapy in Children With Neuroblastoma. *J. Pediatr. Hematol. Oncol.* **2018**, *40* (2), e113–e116.

(13) Sait, S.; Modak, S. Anti-GD2 Immunotherapy for Neuroblastoma. *Expert Rev. Anticancer Ther.* **2017**, *17* (10), 889–904.

(14) Sterner, E.; Peach, M. L.; Nicklaus, M. C.; Gildersleeve, J. C. Therapeutic Antibodies to Ganglioside GD2 Evolved from Highly Selective Germline Antibodies. *Cell Rep.* **2017**, *20* (7), 1681–1691.

(15) Cheung, N.-K. V.; Guo, H.; Hu, J.; Tassev, D. V; Cheung, I. Y. Humanizing Murine IgG3 Anti-GD2 Antibody M3F8 Substantially Improves Antibody-Dependent Cell-Mediated Cytotoxicity While Retaining Targeting in Vivo. *Oncoimmunology.* **2012**, *1* (4), 477–486.

(16) Zhao, Q.; Ahmed, M.; Guo, H.; Cheung, I. Y.; Cheung, N.-K. V. Alteration of Electrostatic Surface Potential Enhances Affinity and Tumor Killing Properties of Anti-Ganglioside GD2 Monoclonal Antibody Hu3F8. *J. Biol. Chem.* **2015**, *290* (21), 13017–13027.

(17) Grant, O. C.; Smith, H. M.; Firsova, D.; Fadda, E.; Woods, R. J. Presentation, Presentation, Presentation! Molecular-Level Insight into Linker Effects on Glycan Array Screening Data. *Glycobiology.* **2014**, *24* (1), 17–25.

(18) Mallagaray, A.; Lockhauserbäumer, J.; Hansman, G.; Uetrecht, C.; Peters, T. Attachment of Norovirus to Histo Blood Group Antigens: A Cooperative Multistep Process. *Angew. Chemie Int. Ed.* **2015**, *54* (41), 12014–12019.

(19) Ritchie, T. K.; Grinkova, Y. V.; Bayburt, T. H.; Denisov, I. G.; Zolnerciks, J. K.; Atkins, W. M.; Sligar, S. G. Reconstitution of Membrane Proteins in Phospholipid Bilayer Nanodiscs. In *Methods in Enzymology*. **2009**, *464*, 211–231.

(20) Denisov, I. G.; Grinkova, Y. V.; Lazarides, A. A.; Sligar, S. G. Directed Self-Assembly of Monodisperse Phospholipid Bilayer Nanodiscs with Controlled Size. *J. Am. Chem. Soc.* **2004**, *126* (11), 3477–3487.

(21) Kitova, E. N.; El-Hawiet, A.; Schnier, P. D.; Klassen, J. S. Reliable Determinations of Protein–Ligand Interactions by Direct ESI-MS Measurements. Are We There Yet? *J. Am. Soc. Mass Spectrom.* **2012**, *23* (3), 431–441.

(22) Kitova, E. N.; Kitov, P. I.; Paszkiewicz, E.; Kim, J.; Mulvey, G. L.; Armstrong, G. D.; Bundle, D. R.; Klassen, J. S. Affinities of Shiga Toxins 1 and 2 for Univalent and Oligovalent Pk-Trisaccharide Analogs Measured by Electrospray Ionization Mass Spectrometry. *Glycobiology.* **2007**, *17* (10), 1127–1137.

(23) Han, L.; Kitova, E. N.; Li, J.; Nikjah, S.; Lin, H.; Pluvinage, B.; Boraston, A. B.; Klassen, J. S. Protein–Glycolipid Interactions Studied in Vitro Using ESI-MS and Nanodiscs: Insights into the Mechanisms and Energetics of Binding. *Anal. Chem.* **2015**, *87* (9), 4888–4896.

(24) Sun, J.; Kitova, E. N.; Wang, W.; Klassen, J. S. Method for Distinguishing Specific from Nonspecific Protein−Ligand Complexes in Nanoelectrospray Ionization Mass Spectrometry. *Anal. Chem.* **2006**, *78* (9), 3010–3018.

(25) Daniel, J. M.; Friess, S. D.; Rajagopalan, S.; Wendt, S.; Zenobi, R. Quantitative Determination of Noncovalent Binding Interactions Using Soft Ionization Mass Spectrometry. *Int. J. Mass Spectrom.* **2002**, *216* (1), 1–27.

(26) Sterner, E.; Peach, M. L.; Nicklaus, M. C.; Gildersleeve, J. C. Therapeutic Antibodies to Ganglioside GD2 Evolved from Highly Selective Germline Antibodies. *Cell Rep.* **2017**, *20* (7), 1681–1691.

(27) Shi, J.; Yang, T.; Kataoka, S.; Zhang, Y.; Diaz, A. J.; Cremer, P. S. GM 1 Clustering Inhibits Cholera Toxin Binding in Supported Phospholipid Membranes. *J. Am. Chem. Soc.* **2007**, *129* (18), 5954–5961.

(28) Yuan, C.; Johnston, L. J. Atomic Force Microscopy Studies of Ganglioside GM1 Domains in Phosphatidylcholine and Phosphatidylcholine/Cholesterol Bilayers. *Biophys. J.* **2001**, *81* (2), 1059–1069.

Chapter 3

(1) Daniotti, J. L.; Lardone, R. D.; Vilcaes, A. A. Dysregulated Expression of Glycolipids in Tumor Cells: From Negative Modulator of Anti-Tumor Immunity to Promising Targets for Developing Therapeutic Agents. *Front. Oncol.* **2016**, *5*, 300.

(2) Malhotra, R. Membrane Glycolipids: Functional Heterogeneity: A Review. *Biochem. Anal. Biochem.* **2012**, *1* (2).

(3) Saliba, A.-E.; Vonkova, I.; Gavin, A.-C. The Systematic Analysis of Protein–lipid Interactions Comes of Age. *Nat. Rev. Mol. Cell Biol.* **2015**, *16* (12), 753–761.

(4) Zuverink, M.; Barbieri, J. T. Protein Toxins That Utilize Gangliosides as Host Receptors. *Progress in Molecular Biology and Translational Science*. **2018**, 156, 325–354.

(5) Ledeen, R. W.; Kopitz, J.; Abad-Rodríguez, J.; Gabius, H.-J. Glycan Chains of Gangliosides: Functional Ligands for Tissue Lectins (Siglecs/Galectins). *Progress in Molecular Biology and Translational Science*. **2018**, 156, 289–324.

(6) Zhang, T.; de Waard, A. A.; Wuhrer, M.; Spaapen, R. M. The Role of Glycosphingolipids in Immune Cell Functions. *Front. Immunol.* **2019**, *10* (1), 1–22.

(7) Merrill, A. H.; Wang, M. D.; Park, M.; Sullards, M. C. (Glyco)Sphingolipidology: An Amazing Challenge and Opportunity for Systems Biology. *Trends Biochem. Sci.* **2007**, *32* (10), 457–468.

(8) Cummings, R. D.; Pierce, J. M. The Challenge and Promise of Glycomics. *Chem. Biol.* **2014**, *21* (1), 1–15.

(9) Cummings, R. D. The Repertoire of Glycan Determinants in the Human Glycome. *Mol. Biosyst.* **2009**, *5* (10), 1087.

(10) Worstell, N. C.; Singla, A.; Saenkham, P.; Galbadage, T.; Sule, P.; Lee, D.; Mohr, A.; Kwon, J. S.; Cirillo, J. D.; Wu, H. Hetero-Multivalency of Pseudomonas Aeruginosa Lectin LecA Binding to Model Membranes. *Sci. Rep.* **2018**, *8* (1), 8419.

(11) Krishnan, P.; Singla, A.; Lee, C.-A.; Weatherston, J. D.; Worstell, N. C.; Wu, H.-J. Hetero-Multivalent Binding of Cholera Toxin Subunit B with Glycolipid Mixtures. *Colloids Surfaces B Biointerfaces.* **2017**, *160*, 281–288.

(12) Han, L.; Morales, L. C.; Richards, M. R.; Kitova, E. N.; Sipione, S.; Klassen, J. S. Investigating the Influence of Membrane Composition on Protein–Glycolipid Binding Using Nanodiscs and Proxy Ligand Electrospray Ionization Mass Spectrometry. *Anal.*

Chem. **2017**, *89* (17), 9330–9338.

(13) Song, X.; Lasanajak, Y.; Xia, B.; Heimburg-Molinaro, J.; Rhea, J. M.; Ju, H.; Zhao, C.; Molinaro, R. J.; Cummings, R. D.; Smith, D.F. Shotgun Glycomics: A Microarray Strategy for Functional Glycomics. *Nature Methods.* **2011**, *8* (1), 85–90.

(14) Grant, O. C.; Smith, H. M. K.; Firsova, D.; Fadda, E.; Woods, R. J. Presentation, Presentation, Presentation! Molecular-Level Insight into Linker Effects on Glycan Array Screening Data. *Glycobiology.* **2014**, *24* (1), 17–25.

(15) Fais, M.; Karamanska, R.; Russell, D. A.; Field, R. A. Lectin and Carbohydrate Microarrays: New High-Throughput Methods for Glycoprotein, Carbohydrate-Binding Protein and Carbohydrate-Active Enzyme Analysis. *J. Cereal Sci.* **2009**, *50* (3), 306–311.

(16) Yao, Y.; Shams-Ud-Doha, K.; Daneshfar, R.; Kitova, E. N.; Klassen, J. S. Quantifying Protein-Carbohydrate Interactions Using Liquid Sample Desorption Electrospray Ionization Mass Spectrometry. *J. Am. Soc. Mass Spectrom.* **2015**, *26* (1), 98–106.

(17) Lin, H.; Kitova, E. N.; Klassen, J. S. Measuring Positive Cooperativity Using the Direct ESI-MS Assay. Cholera Toxin B Subunit Homopentamer Binding to GM1 Pentasaccharide. *J. Am. Soc. Mass Spectrom.* **2014**, *25* (1), 104–110.

(18) El-Hawiet, A.; Shoemaker, G. K.; Daneshfar, R.; Kitova, E. N.; Klassen, J. S. Applications of a Catch and Release Electrospray Ionization Mass Spectrometry Assay for Carbohydrate Library Screening. *Anal. Chem.* **2012**, *84* (1), 50–58.

(19) Han, L.; Kitova, E. N.; Tan, M.; Jiang, X.; Klassen, J. S. Identifying Carbohydrate Ligands of a Norovirus P Particle Using a Catch and Release Electrospray Ionization Mass Spectrometry Assay. *J. Am. Soc. Mass Spectrom.* **2014**, *25* (1), 111–119.

(20) Abzalimov, R. R.; Dubin, P. L.; Kaltashov, I. A. Glycosaminoglycans as Naturally

Occurring Combinatorial Libraries: Developing a Mass Spectrometry-Based Strategy for Characterization of Anti-Thrombin Interaction with Low Molecular Weight Heparin and Heparin Oligomers. *Anal. Chem.* **2007**, *79* (16), 6055–6063.

(21) Li, J.; Fan, X.; Kitova, E. N.; Zou, C.; Cairo, C. W.; Eugenio, L.; Ng, K. K. S.; Xiong, Z. J.; Privé, G. G.; Klassen, J. S. Screening Glycolipids Against Proteins in Vitro Using Picodiscs and Catch-and-Release Electrospray Ionization-Mass Spectrometry. *Anal. Chem.* **2016**, *88* (9), 4742–4750.

(22) Leney, A. C.; Fan, X.; Kitova, E. N.; Klassen, J. S. Nanodiscs and Electrospray Ionization Mass Spectrometry: A Tool for Screening Glycolipids Against Proteins. *Anal. Chem.* **2014**, *86* (11), 5271–5277.

(23) Cohen, M.; Varki, A. Modulation of Glycan Recognition by Clustered Saccharide Patches. *International Review of Cell and Molecular Biology*. **2014**, *308*, 75–125.

(24) Overduin, M.; Esmaili, M. Native Nanodiscs and the Convergence of Lipidomics, Metabolomics, Interactomics and Proteomics. *Appl. Sci.* **2019**, *9* (6), 1230.

(25) Ouellet, M.; Mercier, S.; Pelletier, I.; Bounou, S.; Roy, J.; Hirabayashi, J.; Sato, S.; Tremblay, M. J. Galectin-1 Acts as a Soluble Host Factor That Promotes HIV-1 Infectivity through Stabilization of Virus Attachment to Host Cells. *J. Immunol.* **2005**, *174* (7), 4120–4126.

(26) Sun, J.; Kitova, E. N.; Wang, W.; Klassen, J. S. Method for Distinguishing Specific from Nonspecific Protein−Ligand Complexes in Nanoelectrospray Ionization Mass Spectrometry. *Anal. Chem.* **2006**, *78* (9), 3010–3018.

(27) Bayburt, T. H.; Grinkova, Y. V.; Sligar, S. G. Self-Assembly of Discoidal Phospholipid Bilayer Nanoparticles with Membrane Scaffold Proteins. *Nano Lett.* **2002**, *2* (8), 853–856.

(28) Denisov, I. G.; Grinkova, Y. V.; Lazarides, A. A.; Sligar, S. G. Directed Self-Assembly of

Monodisperse Phospholipid Bilayer Nanodiscs with Controlled Size. *J. Am. Chem. Soc.* **2004**, *126* (11), 3477–3487.

(29) Ritchie, T. K.; Grinkova, Y. V.; Bayburt, T. H.; Denisov, I. G.; Zolnerciks, J. K.; Atkins, W. M.; Sligar, S. G. Chapter 11 Reconstitution of Membrane Proteins in Phospholipid Bilayer Nanodiscs. *Methods in Enzymology*. **2009**, 211–231.

(30) Sun, J.; Kitova, E. N.; Wang, W.; Klassen, J. S. Method for Distinguishing Specific from Nonspecific Protein−Ligand Complexes in Nanoelectrospray Ionization Mass Spectrometry. *Anal. Chem.* **2006**, *78* (9), 3010–3018.

(31) Shams-Ud-Doha, K.; Kitova, E. N.; Kitov, P. I.; St-Pierre, Y.; Klassen, J. S. Human Milk Oligosaccharide Specificities of Human Galectins. Comparison of Electrospray Ionization Mass Spectrometry and Glycan Microarray Screening Results. *Anal. Chem.* **2017**, *89* (9), 4914–4921.

(32) Kitova, E. N.; El-Hawiet, A.; Schnier, P. D.; Klassen, J. S. Reliable Determinations of Protein–Ligand Interactions by Direct ESI-MS Measurements. Are We There Yet? *J. Am. Soc. Mass Spectrom.* **2012**, *23* (3), 431–441.

Chapter 4

(1) Magesh, S.; Ando, H.; Tsubata, T.; Ishida, H.; Kiso, M. High-Affinity Ligands of Siglec Receptors and Their Therapeutic Potentials. *Curr. Med. Chem.* **2011**, *18* (23), 3537–3550.

(2) Angata, T.; Nycholat, C. M.; Macauley, M. S. Therapeutic Targeting of Siglecs Using Antibody- and Glycan-Based Approaches. *Trends Pharmacol. Sci.* **2015**, *36* (10), 645–660.

(3) Macauley, M. S.; Crocker, P. R.; Paulson, J. C. Siglec-Mediated Regulation of Immune Cell Function in Disease. *Nat. Rev. Immunol.* **2014**, *14* (10), 653–666.

(4) Izquierdo-Useros, N.; Lorizate, M.; McLaren, P. J.; Telenti, A.; Kräusslich, H.-G.; Martinez-

Picado, J. HIV-1 Capture and Transmission by Dendritic Cells: The Role of Viral Glycolipids and the Cellular Receptor Siglec-1. *PLoS Pathog.* **2014**, *10* (7), e1004146.

(5) Crocker, P. R.; Paulson, J. C.; Varki, A. Siglecs and Their Roles in the Immune System. *Nat. Rev. Immunol.* **2007**, *7* (4), 255–266.

(6) Izquierdo-Useros, N.; Lorizate, M.; Contreras, F.-X.; Rodriguez-Plata, M. T.; Glass, B.; Erkizia, I.; Prado, J. G.; Casas, J.; Fabriàs, G.; Kräusslich, H.-G.; et al. Sialyllactose in Viral Membrane Gangliosides Is a Novel Molecular Recognition Pattern for Mature Dendritic Cell Capture of HIV-1. *PLoS Biol.* **2012**, *10* (4), e1001315.

(7) Chan, R.; Uchil, P. D.; Jin, J.; Shui, G.; Ott, D. E.; Mothes, W.; Wenk, M. R. Retroviruses Human Immunodeficiency Virus and Murine Leukemia Virus Are Enriched in Phosphoinositides. *J. Virol.* **2008**, *82* (22), 11228–11238.

(8) Erikson, E.; Wratil, P. R.; Frank, M.; Ambiel, I.; Pahnke, K.; Pino, M.; Azadi, P.; Izquierdo-Useros, N.; Martinez-Picado, J.; Meier, C.; et al. Mouse Siglec-1 Mediates Trans -Infection of Surface-Bound Murine Leukemia Virus in a Sialic Acid N -Acyl Side Chain-Dependent Manner. *J. Biol. Chem.* **2015**, *290* (45), 27345–27359.

(9) Puryear, W. B.; Yu, X.; Ramirez, N. P.; Reinhard, B. M.; Gummuluru, S. HIV-1 Incorporation of Host-Cell-Derived Glycosphingolipid GM3 Allows for Capture by Mature Dendritic Cells. *Proc. Natl. Acad. Sci.* **2012**, *109* (19), 7475–7480.

(10) Izquierdo-Useros, N.; Lorizate, M.; Contreras, F.-X.; Rodriguez-Plata, M. T.; Glass, B.; Erkizia, I.; Prado, J. G.; Casas, J.; Fabriàs, G.; Kräusslich, H.-G.; et al. Sialyllactose in Viral Membrane Gangliosides Is a Novel Molecular Recognition Pattern for Mature Dendritic Cell Capture of HIV-1. *PLoS Biol.* **2012**, *10* (4), e1001315.

(11) Puryear, W. B.; Yu, X.; Ramirez, N. P.; Reinhard, B. M.; Gummuluru, S. HIV-1

Incorporation of Host-Cell-Derived Glycosphingolipid GM3 Allows for Capture by Mature Dendritic Cells. *Proc. Natl. Acad. Sci.* **2012**, *109* (19), 7475–7480.

(12) Collins, B. E.; Ito, H.; Sawada, N.; Ishida, H.; Kiso, M.; Schnaar, R. L. Enhanced Binding of the Neural Siglecs, Myelin-Associated Glycoprotein and Schwann Cell Myelin Protein, to Chol-1 (α-Series) Gangliosides and Novel Sulfated Chol-1 Analogs. *J. Biol. Chem.* **1999**, *274* (53), 37637–37643.

(13) Puryear, W. B.; Akiyama, H.; Geer, S. D.; Ramirez, N. P.; Yu, X.; Reinhard, B. M.; Gummuluru, S. Interferon-Inducible Mechanism of Dendritic Cell-Mediated HIV-1 Dissemination Is Dependent on Siglec-1/CD169. *PLoS Pathog.* **2013**, *9* (4), e1003291.